EIEлектротехніка і лектромеханіка

Electrical Engineering & Electromechanics

Електротехнічні комплекси та системи

Промислова електроніка

Електроізоляційна та кабельна техніка

Електричні станції, мережі і системи

Electrical Engineering & Electromechanics

Electrical Engineering & Electromechanics

Scientific Journal

no. 2, 2022

Table of Contents

Electrotechnical Complexes and Systems

Industrial Electronics

Electrical Insulation and Cable Engineering

Power Stations, Grids and Systems

B.I. Kuznetsov, T.B. Nikitina, I.V. Bovdui, O.V. Voloshko, V.V. Kolomiets, B.B. Kobilyanskiy

The method of limitation of dynamic loads of nonlinear electromechanical systems under state vector robust control

Aim. *Development of the method of limitation of dynamic loads of nonlinear electromechanical systems under state vector robust control.* ***Methodology.*** *Limitation of dynamic loads of nonlinear electromechanical systems is carried out using the minimum selector of choosing the minimum value of the control vector from formed with the help of local controllers and with the vector of maximum control values. Calculation of the gain coefficients of nonlinear robust controllers and observers are based on solutions of the Hamilton–Jacob–Isaacs equations.* ***Results.*** *The results of computer simulation of transitional processes of main roll drives of the rolling mill 950 of the Zaporozhye plant «Dniprospetsstal» with limitation of dynamic loads are given.* ***Originality.*** *For the first time the method of limitation of dynamic loads of nonlinear electromechanical systems under state vector robust control based on minimum selector and nonlinear robust control of state variables which is needed limitation is developed.* ***Practical value.*** *Examples of transitional processes of main roll drives of the rolling mill 950 of the Zaporozhye plant «Dniprospetsstal» with limitation of dynamic loads are given.* References 35, figures 6.
Key words: **nonlinear electromechanical systems, state vector robust control, Hamilton–Jacobi–Isaacs equations, limitation of dynamic loads, computer simulation.**

Мета. *Розробка методу обмеження динамічних навантажень нелінійних електромеханічних систем при векторному робастному управлінні.* ***Методологія.*** *Обмеження динамічних навантажень нелінійних електромеханічних систем здійснюється за допомогою селектора вибору мінімального значення вектора керування із сформованого за допомогою локальних регуляторів та вектора максимальних значень керування. Розрахунок коефіцієнтів підсилення нелінійних робастних контролерів і спостерігачів базується на рішеннях рівнянь Гамільтона–Якобі–Айзека.* ***Результати.*** *Наведено результати комп'ютерного моделювання перехідних процесів головних приводів валків прокатного стану 950 Запорізького заводу «Дніпроспецсталь» із обмеженням динамічних навантажень.* ***Оригінальність.*** *Вперше розроблено метод обмеження динамічних навантажень нелінійних електромеханічних систем при робастному управлінні за вектором стану на основі селектору мінімуму та нелінійних робастних регуляторів змінних стану, які необхідно обмежуват.* ***Практична цінність.*** *Наведено приклади перехідних процесів головних приводів прокатного стану 950 Запорізького заводу «Дніпроспецсталь» із обмеженням динамічних навантажень.* Бібл. 35, рис. 6.
Ключові слова: **нелінійні електромеханічні системи, робастне керування за вектором стану, рівняння Гамільтона–Якобі–Айзека, обмеження динамічних навантажень, комп'ютерне моделювання.**

Introduction. The use of optimal and modal controllers that implement control over the full state vector makes it possible to significantly increase the speed of electromechanical systems compared to traditional slave control systems [1, 2]. Especially effective is the use of state control for controlling electromechanical systems with the presence of elastic connections in the kinematics chain from the drive motor to the working body of the electromechanical system [3, 4].

Mathematical models of such systems are accepted in the form of two, three and more mass electro-mechanical systems. The control of such multi-mass systems becomes much more complicated if there are nonlinear elements in the bottom. In most mass electromechanical systems, it is necessary to take into account the nonlinear dependence of friction on the shafts of the drive motor, gearbox and working body. The task of control becomes even more complicated for a multi-ton electromechanical system with non-linear connections between individual motors through the control object.

To implement high-speed operation in such systems, significant torques and speeds are required, and possibly even higher derivative changes in the drive motor shafts and transmission elements. When working out the setting influences, the limitation of dynamic loads in such systems is implemented using intensity generators.

However, in the process of compensating for disturbances in the system, it is necessary to limit the dynamic loads. Note that the extremely widespread use of slave control systems is due precisely to the simplicity of

limiting dynamic loads by limiting the rate of change and current of the drive motor, as well as speed and position using slave control loops.

One example of such multi-motor electromechanical systems is rolling mills [5–7]. A characteristic feature of the operation of rolling mills is their heavy loading mode: dynamic load application during the period of metal gripping by rolls, roll slipping, impacts of heavy ingots on rolls, impacts in the gaps of the main line, heavy modes of non-stationary processes in electric drives with acceleration and deceleration acceleration and other factors. In difficult operating conditions of mills, cases of simultaneous action of the indicated loads in various combinations are possible [8, 9]. Then the dynamics of transient processes becomes rather complex, and its study is hampered by the nonlinearity of systems of differential equations describing the motion of the main lines. Experience shows that most accidents occur as a result of large dynamic vibration loads arising during transient and unstable operating modes, as well as in connection with a violation of rolling technology (rolled cold metal, excessive reduction, etc.).

Experimental studies of the ingot gripping process on the operating equipment have shown that the dynamic loads in the main line of the mill differ significantly depending on the state of the ingot surface, the shape of the front and rear ends of the ingot, gripping conditions, etc. In fact, the change in the moment of resistance during the capture of the ingot does not occur instantaneously, and in a number of works it is proposed to approximate

the change in the moment of resistance by an exponential curve. In this case, depending on the value of the exponential time constant, the excess of the current in the optimal controller can be 2–4 maximum permissible current values [5–7]. With such an excess, the coordinate limiting system is stable and reliably limits the state and control variables.

The purpose of the work is to develop the method of limitation of dynamic of loads of nonlinear electromechanical systems under state vector robust control.

Problem statement. Let us consider the limitation of loads in nonlinear multi-mass systems with robust control over the state vector. First, consider the limitation in an electromechanical system with only one single motor [10, 11].

To limit the state and control variables, consider the scheme of such a system. This system uses separate controllers for the main control coordinate and the same state variables that need to be limited. Using the minimum selector, we apply a voltage to the input of the thyristor converter, which corresponds to the minimum value of the outputs of all regulators.

Consider the limitation on the vector of output coordinates $\vec{y}(k)$ system at a given level of maximum permissible values $\vec{y}_{max}$. For this purpose, we construct optimal nonlinear controllers that minimize criteria in which the integrands $\psi(\vec{x}(k), \vec{y}(k))$ are selected from the condition of ensuring the specified requirements for the speed of operation of the controllers, with the help of which the vector of output variables $\vec{y}(k)$ maintained at the level of maximum permissible values $\vec{y}_{max}(k)$. As a result of the solution, the optimal controls are found $\vec{u}_i(k)$, ensuring the maintenance of i component $y_i(k)$ vector of output variables $\vec{y}(k)$ at the level of maximum permissible values $y_{max\,i}(k)$ vector of maximum permissible values of the output coordinates $\vec{y}_{max}(k)$. The choice of control entering the input of the system is carried out using the minimum selector, as shown in Fig. 1.

Naturally, the circuit shown in Fig. 1 for limiting the state and control variables is only an illustration of the operation of the algorithm implemented with the help of a control computer.

The control vectors defined in this way $\vec{u}(k)$ from the conditions for working out the required reference influences and compensating for disturbances, as well as maintaining the vector $\vec{y}_{max}$ the maximum permissible values of the state variables are fed to the minimum selector, with the help of which the control is formed $\vec{u}(k)$, supplied to the input of the control system. In the course of choosing the minimum value of the control components from those formed with the help of various controllers, a comparison is also made with the maximum control value $\vec{u}_{max}$ and thus, the limitation is carried out not only on the vector of state variables, but also on the control.

Let us now consider the limitation of loads in multi-channel nonlinear multi-mass systems, with robust control by the state vector with many electric drives connected through the control object [12–15]. In particular, such a problem arises in the joint control of the speeds of rotation of the upper and lower rolls with individual drive of the rolls and their mutual influence through the rolled metal. In addition, such a problem arises with joint coordinated control of the speeds of the main drives of multi-stand rolling mills with their mutual influence on each other through the rolled strip [5–7].
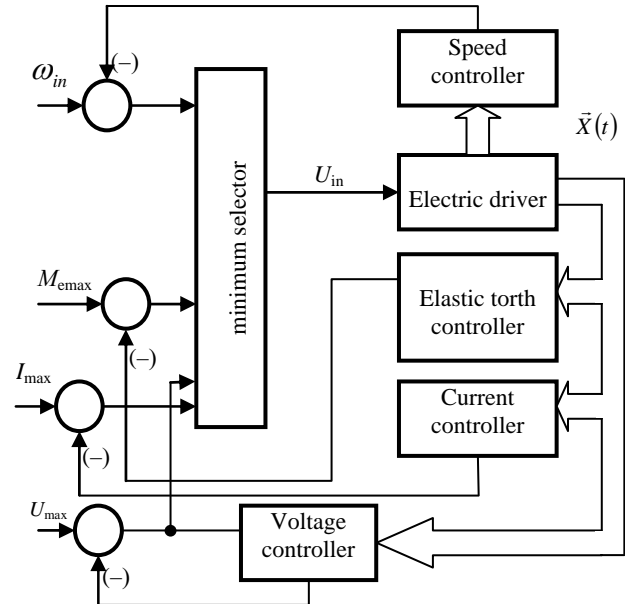
Fig. 1. Scheme of limitation of dynamic of loads of only single motor electromechanical systems

Consider the limitation on the vector of output coordinates $\vec{y}(t)$ multichannel system at a given level of maximum permissible values $\vec{y}_{max}$ [16, 17]. For this purpose, we construct optimal nonlinear controllers that minimize criteria in which the integrands $\psi(\vec{x}(t), \vec{y}(t))$ are selected from the condition of ensuring the specified requirements for the speed of operation of the controllers, with the help of which the vector of output variables $\vec{y}(t)$ maintained at the level of maximum permissible values $\vec{y}_{max}(t)$. As a result of the solution, the optimal controls are found $\vec{u}_i(t)$, ensuring the maintenance of i component $y_i(t)$ vector of output variables $\vec{y}(t)$ at the level of maximum permissible values $y_{max\,i}(t)$ vector of maximum permissible values of the output coordinates $\vec{y}_{max}(t)$. The choice of control arriving at the input of the system is carried out using the minimum selector, as shown in Fig. 2.

For this purpose, we construct robust optimal nonlinear controllers that minimize criteria in which the integrands are selected from the condition of ensuring the specified requirements for the speed of operation of the controllers, with the help of which the vector of output variables maintained at the level of maximum permissible values. As a result of the solution, the optimal controls are found, ensuring the maintenance of component vector of output variables at the level of maximum permissible values vector of maximum permissible values of the output coordinates. The choice of control arriving at the input of the system is carried out using the minimum selector, as shown in Fig. 2.
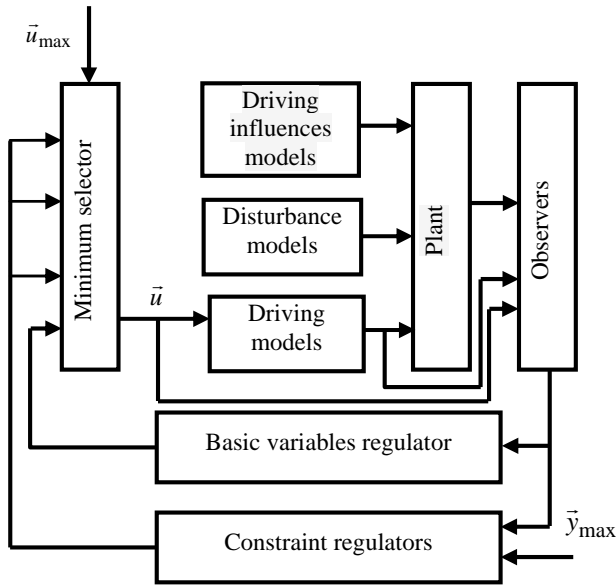
Fig. 2. Scheme of limitation of dynamic of loads of multymotor electromechanical systems

The control vectors defined in this way from the conditions of working out the required reference influences and compensation of disturbances, as well as limiting the vector of the output coordinates of the multichannel system at a given level of maximum permissible values are fed to the minimum selector, with the help of which the control vector is formed, supplied to the input of control channels. In addition, in the course of choosing the minimum value of the components of the control vector from those formed with the help of various controllers, there is also a comparison with the vector of maximum control values and thus, the limitation is carried out not only on the vector of state variables, but also on the control vector.

Method of computation of separate nonlinear robust controllers. Let us first consider the synthesis of feedback over the full state vector x, under the assumption that all components of the state vector can be measured without errors [18–20]. Then the original system takes the following form

$$\dot{x} = f(x) + g_\omega(x)\omega + g_u(x)u , \qquad (1)$$

$$z = h_z(x) + k_{uz}(x)u . \qquad (2)$$

in these expressions: x – state vector, u – control vector and ω – vector of external uncontrolled influences.

The control is formed from the state vector using some nonlinear transformation $u = l(x)$. Then the closed system takes the following form

$$\dot{x} = \tilde{f}(x) + \tilde{g}_\omega(x)\omega , \qquad (3)$$

$$z = \tilde{h}_z(x), \qquad (4)$$

where

$$\tilde{f}(x) = f(x) + g(x)l(x), \qquad (5)$$

$$\tilde{g}_\omega(x) = g_\omega(x), \qquad (6)$$

$$\tilde{h}_z(x) = h_z(x) + k_{uz}(x)g(x)l(x). \qquad (7)$$

For this initial system (5)–(7), we write the Hamilton–Jacobi–Isaacs equation in the following form

$$\frac{\partial}{\partial t}V(x) = V_x f + V_x g_u u + V_x g_\omega \omega =$$

$$= V_x f + \frac{1}{2}\left\| u + g_u^T V_x^T \right\|^2 - \ldots$$

$$\ldots - \frac{1}{2}\gamma^2 \left\| \omega - \frac{1}{\gamma^2} g_\omega^T V_x^T \right\|^2 + \ldots \qquad (8)$$

$$\ldots + \frac{1}{2}\frac{1}{\gamma^2} V_x g_\omega g_\omega^T V_x^T - \frac{1}{2}V_x g_u g_u^T V_x^T + \ldots$$

$$\ldots + \frac{1}{2}h_z^T h_z + \frac{1}{2}\gamma^2 \|\omega\|^2 - \frac{1}{2}\|h_z\|^2 - \frac{1}{2}\|u\|^2$$

This approach can be interpreted as a zero-sum differential game of two players in which one player minimizes the accepted quality criterion for control u, and the other player maximizes this criterion with respect to the vector of external variables ω. In this case, the minimization strategy for control u

$$u^* = \alpha_u(x) = -g_u^T(x)V_x^T(x), \qquad (9)$$

and the strategy of maximization along the vector of external influences ω

$$\omega^* = \alpha_\omega(x) = \frac{1}{\gamma^2} g_\omega^T(x)V_x^T(x). \qquad (10)$$

Previously, the issues of synthesis of nonlinear robust control (9)–(10) were considered under the assumption that the full state vector can be accurately measured. Usually, only some variables are available for measurement in the system, and they are measured with noise [21, 22]. Let us now consider the synthesis of such a robust control, when only a part of the state variables is available for measurement with noise. We will call such an approach control by the full state vector with an estimate of the state vector by the measured output. The output equation can be represented as the following expression

$$y = h_y(x) + k_{\omega y}(x)\omega + k_{\omega y}(x)u . \qquad (11)$$

We will estimate the total state vector from the measured output vector (11) using a dynamic system – an observer, whose equation we write in the following form

$$\dot{\xi} = f(\xi) + g_u(\xi)u + g_\omega(\xi)\omega + G(\xi)* \ldots$$
$$\ldots *\left(y - h_y(\xi) - k_{\omega y}(\xi)\omega\right) \qquad (12)$$

The synthesis of such an observer (12) consists in determining the matrix of the gains of this observer. The perturbation is clearly not applied to the output of the observer and, in the synthesis of the guaranteed estimate, is determined during the synthesis of the observer for the worst case (worst – case disturbance), when the perturbation itself is a function of the state vector of the observer ξ, so the following expression holds

$$\omega = \alpha_\omega(\xi). \qquad (13)$$

Then the original system (1)–(2), closed by the total state vector, estimated with the help of such an observer (12), together with the equation of the vector of controlled coordinates (11), will take the following form

$$\dot{x} = f(x) + g_u(x)\alpha_u(\xi) + g_\omega(x)\omega , \qquad (14)$$

$$\dot{\xi} = f(\xi) + g_u(\xi)\alpha_u(\xi) + g_\omega(\xi)\alpha_\omega(\xi) + \ldots$$
$$\ldots + G(\xi)\left(h_y(x) - h_y(\xi) - \ldots \right. \qquad (15)$$
$$\left. \ldots - k_{\omega y}(\xi)\alpha_\omega(\xi) + k_{\omega y}(x)\omega\right)$$

$$z = h_z(x) + k_{uz}(x)\alpha_u(\xi). \qquad (16)$$

This approach can be interpreted as a zero-sum differential game of two players in which one player minimizes the accepted quality criterion (2) for matrix of gains $G(\xi)$, and the other player maximizes this criterion (2) with respect to the vector of external variables ω.

In addition to synthesizing the observer in the form of a matrix of gains $G(\xi)$ of this observer, it is also necessary to synthesize the controller in the form of a matrix of gains of this controller $\alpha_u(\xi)$ by the observer state vector ξ. Calculation of the gain coefficients of nonlinear robust controllers and observers are based on solutions of the Hamilton–Jacobi–Isaacs equations [23, 24].

Mathematical models of the blooming main drives. Let us consider the control system for the individual main drives of the upper and lower rolls of a rolling mill, taking into account their mutual influences through the rolled metal. During the capture of the ingot or normal rolling, slip of the rolls relative to the rolled metal is possible. The system takes into account the nonlinear nature of the dependence of the friction torque in the slip mode on the speed of the roll slip relative to the rolled metal. In this case, various combinations of operating modes of the upper and lower rolls are possible: both rolls are in normal rolling modes: one roll is skidding, and the second roll is in normal rolling mode, and finally, both rolls are in skidding mode [25–27]. It should be noted that even in the normal rolling mode, when both rolls are in the rolling mode and there is no slip relative to the rolled metal, a deep rolling asymmetry is possible in which a significant redistribution of the rolling moments between the upper and lower rolls takes place. Cases are known when the motor of one roll operates in a motor mode, and the motor of the other roll operates in a generator mode. In some cases, such asymmetric rolling is organized specifically for technological reasons. In this case, of course, the rolls rotate at different speeds and a different advance of the rolled metal relative to the upper and lower rolls is created. The breakdown of the roll in the slip mode occurs when it exceeds the critical slip relative to the rolled metal, which depends mainly on the state of the rolled metal surface. In particular, the presence of scale even in a localized area can cause the roll to slip during normal rolling.

Let us take mathematical models of the channels for a short blooming line in the form of a two-mass system, and a long blooming line in the form of a three-mass system and take into account the presence of a cross-connection between the main drives of the rolls in the form of a moment proportional to the difference between the rotation speeds of the upper and lower rolls. The moment of mutual influence is the driving moment for the roll rotating at a lower speed, and this moment is braking for the roll rotating at a higher speed. Depending on the rolling conditions, the value of this moment, which characterizes the mutual influence of the rolls on each other through the rolled metal, can be a different fraction of the rolling moment, which is the moment of resistance for the main blooming drives [28, 29]. Transient processes in the short and long lines of the mill differ significantly from each other, and as the mutual coupling through the rolled ingot increases, the transients become significantly more oscillatory [30–35].

With a stepwise change in the magnitude of the moment of resistance, for the implementation of optimal control, more than tenfold forcing of the armature current and voltage of the thyristor converter is required. In this case, the limiting system goes into a self-oscillating mode of current limiting at the maximum positive and negative values.

The mathematical model of the disturbing effect is adopted in the form of an exponential application of the load on the roll.

To implement optimal control of the main variable and variables that must be limited in the considered electromechanical system, a complete state vector is required. In a three-mass system, the moments of elasticity are not directly measured $M_{e1}(t)$ and $M_{e2}(t)$, as well as the speed of rotation of the reducer $\omega_R(t)$ and mechanism $\omega_{mech}(t)$, in a two-mass system, the elastic moment and the rotation speed of the mechanism are not measured. To reconstruct these directly not measurable state variables, we construct an optimal observer of reduced dimension in comparison with the original system, such that the input of this observer will be the armature currents $I_M(t)$, and the measured outputs of this observer will be the rotational speeds of the motors $\omega_M(t)$.

Computer simulation. As an example, in Fig. 3 are shown transient processes on references in a nonlinear control system with limiting the output value of the motor armature circuit current and voltage at the output of the thyristor converter of the upper roll of rolling mill 950 of the Zaporozhye plant «Dniprospetsstal» with an exponential application of the load on the roll. In the figure are shown transient processes of ω_M – motor rate speed (*a*), M_e – the moment of elasticity of the shaft (*b*), ω_v – roll rotation speed (*c*) and I – motor armature current (*d*). In the figure are shown the characteristic sections of constant current, held by the current regulator at the level of maximum permissible values.

a

b
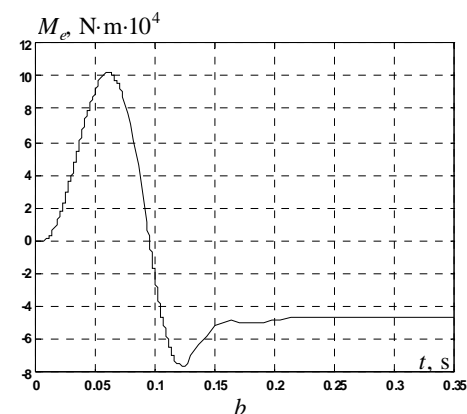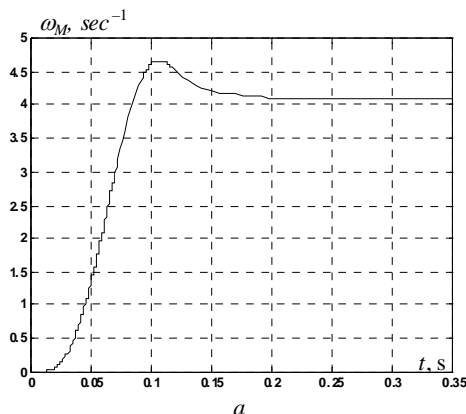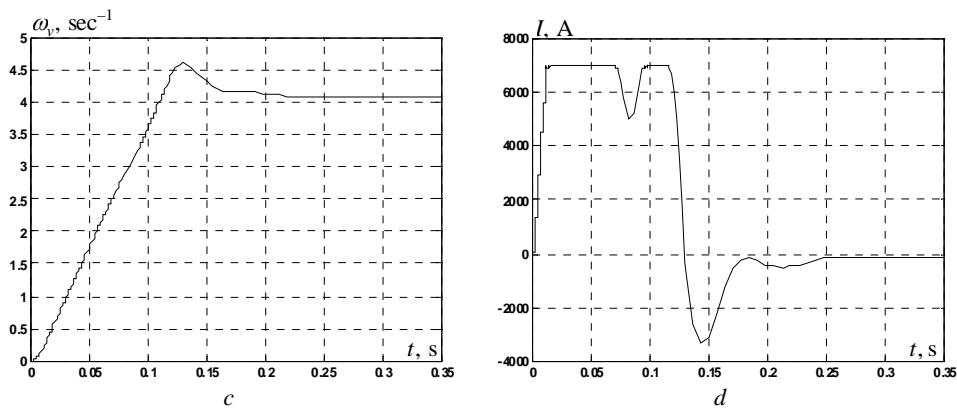
Fig. 3. Transient processes on references

As an example, in Fig. 4 are shown the transient processes on moment of resistance of the upper roll control system (dual-mass control system) with the limitation of the output value of the motor armature circuit current and the voltage at the output of the thyristor converter of the rolling mill 950 of the Zaporozhye plant «Dniprospetsstal» with an exponential application of the load on the roll due to the disturbing effect. In the figure, the following designations of the system state variables are adopted:

ω_v – roll rotation speed (*a*), M_e – the moment of elasticity of the shaft (*b*) and I – motor armature current (*c*). In the figure also are shown the characteristic sections of constant current held by the current regulators at the level of maximum permissible values.

Despite armature current limitations, the roll speed control system returns the speed mismatch to zero in steady state.
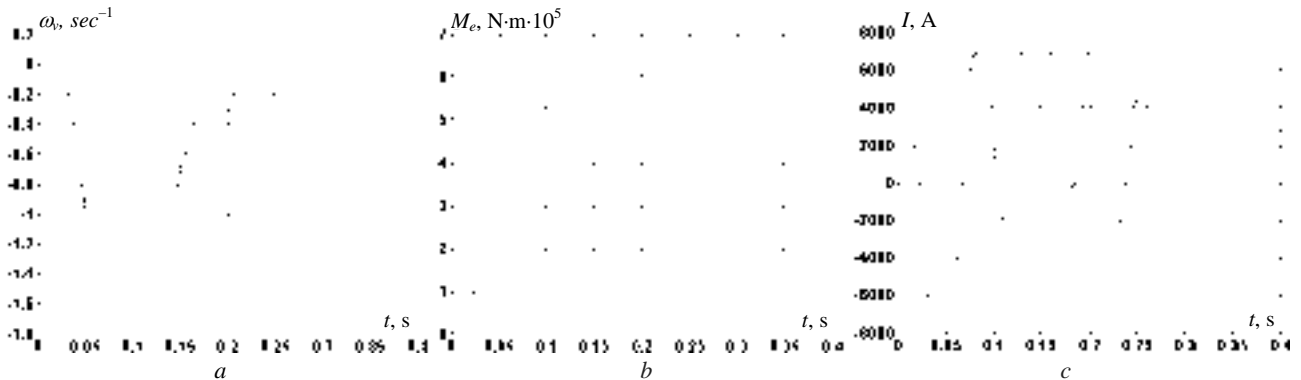
Fig. 4. Transient processes on moment of resistance

In Fig. 5 are shown the transient processes on references of the upper roll control system with simultaneous limitation of the output voltage value at the output of the thyristor converter and the current of the armature circuit of the motor of the rolling mill 950 of the Zaporozhye plant «Dniprospetsstal» by the disturbing effect are shown. In the figure, the following designations

of the system state variables are adopted: U – voltage at the output of the thyristor converter (*a*) and I – motor armature current (*b*). In the figure also are shown typical sections of constant current and voltage values, which are held by current and voltage regulators at the level of maximum permissible values.
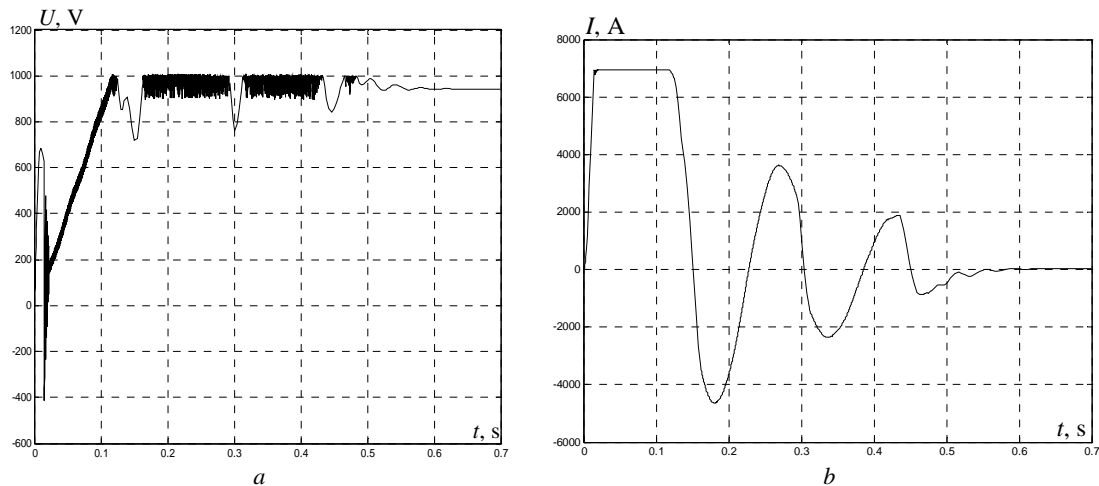
Fig. 5. Transient processes on references

In Fig. 6 are shown the transient processes of the ω_M motor rotation speed (*a*) and the *I* armature current (*b*) of the upper roll control system (dual-mass control system) with the restriction of the output value of the armature circuit current of the motor of the rolling mill 950 of the Zaporozhye plant «Dniprospetsstal» by the disturbing effect.
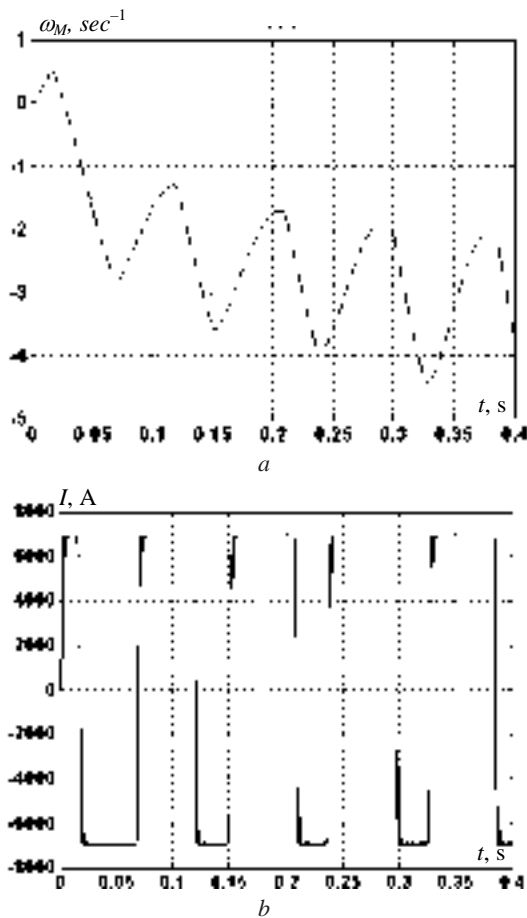
Fig. 6. Transient processes on moment of resistance

As can be seen from these graphs, using the control system, the armature current is limited at the level of maximum permissible values when the system is working out the disturbing effect when capturing the ingot.

The mathematical model of the change in the load moment in the process of gripping the ingot is assumed to be exponential. Analysis of transient processes shows that the nature of dynamic loads in the system during ingot capture depends significantly on the rate of change of the moment of resistance. The more abruptly the moment of resistance changes, the greater the dynamic loads occur in the main line of the mill. Moreover, in this example under consideration, due to the limitation of the armature current there is a drawdown in the speed of the rolling rolls in steady state.

Discussion. The nature of transient processes in such a system substantially depends on the operation of the system of constraints. If the system does not go beyond the limits, then the transient processes in it are determined by the operation of the optimal controller of the main variables. When processing large setpoints or compensating for disturbing influences, the nature of transient processes depends significantly on the operation of the constraint system. In general, when the system reaches the limits, the time of transients increases in comparison with transients in the system without restrictions. Moreover, this increase in the time of transient processes mainly depends on the duration of the system operation on the constraints. In addition, when the system is operating on constraints, the very nature of the system's operation can significantly change. Since in such a mode the system practically opens in relation to the main controlled coordinates and is on limitations, it is natural that there is no damping of oscillatory processes in the system and an increase in oscillations can begin until loss of stability.

In the course of modelling the synthesized system, in a number of cases, when adjusting the control loops, the system switched to a self-oscillating mode at the levels of the maximum permissible positive and negative values of the state variables. As studies of such a system have shown, it can also become unstable, depending on the level and form of external influences. The most dangerous is the mode of coordinate limitation under the action of the moment of resistance. The nature of the restrictions essentially depends not so much on the magnitude as on the steepness of the change in the moment of resistance. With a stepwise change in the magnitude of the moment of resistance, for the implementation of optimal control, more than tenfold forcing of the armature current and voltage of the thyristor converter is required. In this case, the limiting system goes into a self-oscillating mode of current limiting at the maximum positive and negative values.

During the simulation of the synthesized nonlinear optimal control system with the optimal limitation of the output value of the motor armature circuit current, the voltage at the output of the thyristor converter and the moments of elasticity in the shafts of the main roll drives of the rolling mill 950 of the Zaporozhye plant «Dniprospetsstal» characteristic sections of constant current values were obtained, stresses and moments of elasticity held by robust regulators of current, voltage and moments at the levels of their maximum permissible values.

It should be noted that individual autonomous controllers can be unstable: for example, a current control loop in a small one, when the effect of a change in EMF can be neglected leads to an unlimited increase in position and speed in a steady state, since in this case there are integral relationships between current and speed and between speed and position. In some cases, when adjusting the control loops, the system goes into self-oscillating mode at the levels of the maximum permissible positive and negative values of the state variables.

As studies of such a system have shown, it can also become unstable, depending on the level and form of external influences. The most dangerous is the mode of coordinate limitation when the moment of resistance is applied. The nature of the restrictions essentially depends not so much on the magnitude as on the steepness of the change in the moment of resistance.

Conclusions.

1. For the first time the method of limitation of dynamic loads of nonlinear electromechanical systems under state vector robust control is developed. Limitation of control and state variables of nonlinear electromechanical systems is carried out using the minimum selector of choosing the

minimum value of the control vector from formed with the help of local controllers and with the vector of maximum control values.

2. To limit the state and control variables the separate robust controllers for the main control coordinate and the same state variables that need to be limited are used. Using the minimum selector, we apply a voltage to the input of the thyristor converter, which corresponds to the minimum value of the outputs of all separate regulators. The separate robust controllers are calculated based on solutions of the Hamilton–Jacobi–Isaacs equations.

3. Examples of transitional processes with limitation of dynamic loads of nonlinear electromechanical systems of main roll drives of the rolling mill 950 of the Zaporozhye plant «Dniprospetsstal» are given.

4. It is shown, that when the system reaches the limits, the time of transients increases in comparison with transients in the system without restrictions. Moreover, this increase in the time of transient processes mainly depends on the duration of the system operation on the constraints. In addition, when the system is operating on constraints, the very nature of the system's operation can significantly change.

Conflict of interest. The authors declare that they have no conflicts of interest.

REFERENCES
1. Ostroverkhov M., Chumack V., Monakhov E., Ponomarev A. Hybrid Excited Synchronous Generator for Microhydropower Unit. *2019 IEEE 6th International Conference on Energy Smart Systems (ESS)*, Kyiv, Ukraine, 2019, pp. 219-222. doi: https://doi.org/10.1109/ess.2019.8764202.
2. Ostroverkhov M., Chumack V., Monakhov E. Ouput Voltage Stabilization Process Simulation in Generator with Hybrid Excitation at Variable Drive Speed. *2019 IEEE 2nd Ukraine Conference on Electrical and Computer Engineering (UKRCON)*, Lviv, Ukraine, 2019, pp. 310-313. doi: https://doi.org/10.1109/ukrcon.2019.8879781.
3. Shmatko O., Volosyuk V., Zhyla S., Pavlikov V., Ruzhentsev N., Tserne E., Popov A., Ostroumov I., Kuzmenko N., Dergachov K., Sushchenko O., Averyanova Y., Zaliskyi M., Solomentsev O., Havrylenko O., Kuznetsov B., Nikitina T. Synthesis of the optimal algorithm and structure of contactless optical device for estimating the parameters of statistically uneven surfaces. *Radioelectronic and Computer Systems*, 2021, no. 4, pp. 199-213. doi: https://doi.org/10.32620/reks.2021.4.16.
4. Volosyuk V., Zhyla S., Pavlikov V., Ruzhentsev N., Tserne E., Popov A., Shmatko O., Dergachov K., Havrylenko O., Ostroumov I., Kuzmenko N., Sushchenko O., Averyanova Yu., Zaliskyi M., Solomentsev O., Kuznetsov B., Nikitina T. Optimal Method for Polarization Selection of Stationary Objects Against the Background of the Earth's Surface. *International Journal of Electronics and Telecommunications*, 2022, vol. 68, no. 1, pp. 83-89. doi: https://doi.org/10.24425/ijet.2022.139852.
5. Cuzzola F.A., Parisini T. *Automation and Control Solutions for Flat Strip Metal Processing. The Control Handbook. 2nd Edition*, 2010, pp. 18-36. doi: https://doi.org/10.1201/b10382-22.
6. Kozhevnikov A., Kozhevnikova I., Bolobanova N., Smirnov A. Chatter prevention in stands of continuous cold rolling mills. *Metalurgija*, 2020, vol. 59, no. 1, pp. 55-58. Available at: https://hrcak.srce.hr/224759 (accessed 06 October 2021).
7. Šinik V., Despotović Ž., Prvulović S., Desnica E., Pekez J., Tolmač J., Palinkaš I. Higher harmonics of current caused by the operation of rolling mill. *IX International Conference Industrial engineering and Environmental Protection 2019 (IIZS 2019)*, 3-4 October 2019, Zrenjanin, Serbia, pp. 50-57. Available at: https://www.researchgate.net/publication/336262031_HIGHER

_HARMONICS_OF_CURRENT_CAUSED_BY_THE_OPER ATION_OF_ROLLING_MILL (accessed 06 October 2021).
8. Krot P.V., Korennoy V.V. Nonlinear Effects in Rolling Mills Dynamics. *Proceedings of the 5th International Conference on Nonlinear Dynamics ND-KhPI2016*, September 27-30, 2016, Kharkov, Ukraine. Available at: https://www.researchgate.net/publication/308901445_Nonlinear_Ef fects_in_Rolling_Mills_Dynamics (accessed 06 October 2021).
9. Kugi A., Schlacher K., Novak R. Nonlinear control in rolling mills: a new perspective. *IEEE Transactions on Industry Applications*, 2001, vol. 37, no. 5, pp. 1394-1402. doi: https://doi.org/10.1109/28.952515.
10. Martynenko G. Practical application of the analytical method of electromagnetic circuit analysis for determining magnetic forces in active magnetic bearings. *2020 IEEE Problems of Automated Electrodrive. Theory and Practice (PAEP)*, 2020, pp. 1-4, doi: https://doi.org/10.1109/paep49887.2020.9240774.
11. Martynenko G., Martynenko V. Modeling of the dynamics of rotors of an energy gas turbine installation using an analytical method for analyzing active magnetic bearing circuits. *2020 IEEE KhPI Week on Advanced Technology (KhPIWeek)*, 2020, pp. 92-97 .doi: https://doi.org/10.1109/KhPIWeek51551.2020.9250156.
12. Buriakovskyi S.G., Maslii A.S., Pasko O.V., Smirnov V.V. Mathematical modelling of transients in the electric drive of the switch – the main executive element of railway automation. *Electrical Engineering & Electromechanics*, 2020, no. 4, pp. 17-23. doi: https://doi.org/10.20998/2074-272X.2020.4.03.
13. Tytiuk V., Chornyi O., Baranovskaya M., Serhiienko S., Zachepa I., Tsvirkun L., Kuznetsov V., Tryputen N. Synthesis of a fractional-order $PI^{\lambda}D^{\mu}$-controller for a closed system of switched reluctance motor control. *Eastern-European Journal of Enterprise Technologies*, 2019, no. 2 (98), pp. 35-42. doi: https://doi.org/10.15587/1729-4061.2019.160946.
14. Zagirnyak M., Chornyi O., Zachepa I. The autonomous sources of energy supply for the liquidation of technogenic accidents. *Przeglad Elektrotechniczny*, 2019, no. 5, pp. 47-50. doi: https://doi.org/10.15199/48.2019.05.12.
15. Chornyi O., Serhiienko S. A virtual complex with the parametric adjustment to electromechanical system parameters. *Technical Electrodynamics*, 2019, pp. 38-41. doi: https://doi.org/10.15407/techned2019.01.038.
16. Shchur I., Kasha L., Bukavyn M. Efficiency Evaluation of Single and Modular Cascade Machines Operation in Electric Vehicle. *2020 IEEE 15th International Conference on Advanced Trends in Radioelectronics, Telecommunications and Computer Engineering (TCSET)*, Lviv-Slavske, Ukraine, 2020, pp. 156-161. doi: https://doi.org/10.1109/tcset49122.2020.235413.
17. Shchur I., Turkovskyi V. Comparative Study of Brushless DC Motor Drives with Different Configurations of Modular Multilevel Cascaded Converters. *2020 IEEE 15th International Conference on Advanced Trends in Radioelectronics, Telecommunications and Computer Engineering (TCSET)*, Lviv-Slavske, Ukraine, 2020, pp. 447-451. doi: https://doi.org/10.1109/tcset49122.2020.235473.
18. Ostroumov I., Kuzmenko N., Sushchenko O., Pavlikov V., Zhyla S., Solomentsev O., Zaliskyi M., Averyanova Y., Tserne E., Popov A., Volosyuk V., Ruzhentsev N., Dergachov K., Havrylenko O., Kuznetsov B., Nikitina T., Shmatko O. Modelling and simulation of DME navigation global service volume. *Advances in Space Research*, 2021, vol. 68, no. 8, pp. 3495-3507. doi: https://doi.org/10.1016/j.asr.2021.06.027.
19. Averyanova Y., Sushchenko O., Ostroumov I., Kuzmenko N., Zaliskyi M., Solomentsev O., Kuznetsov B., Nikitina T., Havrylenko O., Popov A., Volosyuk V., Shmatko O., Ruzhentsev N., Zhyla S., Pavlikov V., Dergachov K., Tserne E. UAS cyber security hazards analysis and approach to qualitative assessment. In: Shukla S., Unal A., Varghese Kureethara J., Mishra D.K., Han D.S. (eds) *Data Science and Security. Lecture Notes in Networks and Systems*, 2021, vol. 290, pp. 258-265.

Springer, Singapore. doi: https://doi.org/10.1007/978-981-16-4486-3_28.

20. Zaliskyi M., Solomentsev O., Shcherbyna O., Ostroumov I., Sushchenko O., Averyanova Y., Kuzmenko N., Shmatko O., Ruzhentsev N., Popov A., Zhyla S., Volosyuk V., Havrylenko O., Pavlikov V., Dergachov K., Tserne E., Nikitina T., Kuznetsov B. Heteroskedasticity analysis during operational data processing of radio electronic systems. In: Shukla S., Unal A., Varghese Kureethara J., Mishra D.K., Han D.S. (eds) *Data Science and Security. Lecture Notes in Networks and Systems*, 2021, vol. 290, pp. 168-175. Springer, Singapore. doi: https://doi.org/10.1007/978-981-16-4486-3_18.

21. Sushchenko O.A. Robust control of angular motion of platform with payload based on H_∞-synthesis. *Journal of Automation and Information Sciences*, 2016, vol. 48, no. 12, pp. 13-26. doi: https://doi.org/10.1615/jautomatinfscien.v48.i12.20.

22. Chikovani V., Sushchenko O. Self-compensation for disturbances in differential vibratory gyroscope for space navigation. *International Journal of Aerospace Engineering*, 2019, vol. 2019, Article ID 5234061, 9 p. doi: https://doi.org/10.1155/2019/5234061.

23. Gal'chenko V.Y., Vorob'ev M.A. Structural synthesis of attachable eddy-current probes with a given distribution of the probing field in the test zone. *Russian Journal of Nondestructive Testing*, Jan. 2005, vol. 41, no. 1, pp. 29-33. doi: https://doi.org/10.1007/s11181-005-0124-7.

24. Halchenko V.Y., Ostapushchenko D.L., Vorobyov M.A. Mathematical simulation of magnetization processes of arbitrarily shaped ferromagnetic test objects in fields of given spatial configurations. *Russian Journal of Nondestructive Testing*, Sep. 2008, vol. 44, no. 9, pp. 589-600. doi: https://doi.org/10.1134/S1061830908090015.

25. Ostroumov I., Kuzmenko N., Sushchenko O., Zaliskyi M., Solomentsev O., Averyanova Y., Zhyla S., Pavlikov V., Tserne E., Volosyuk V., Dergachov K., Havrylenko O., Shmatko O., Popov A., Ruzhentsev N., Kuznetsov B., Nikitina T. A probability estimation of aircraft departures and arrivals delays. In: Gervasi O. et al. (eds) *Computational Science and Its Applications – ICCSA 2021. ICCSA 2021. Lecture Notes in Computer Science*, vol. 12950, pp. 363-377. Springer, Cham. doi: https://doi.org/10.1007/978-3-030-86960-1_26.

26. Chystiakov P., Chornyi O., Zhautikov B., Sivyakova G. Remote control of electromechanical systems based on computer simulators. *2017 International Conference on Modern Electrical and Energy Systems (MEES)*, Kremenchuk, Ukraine, 2017, pp. 364-367. doi: https://doi.org/10.1109/mees.2017.8248934.

27. Zagirnyak M., Bisikalo O., Chorna O., Chornyi O. A Model of the Assessment of an Induction Motor Condition and Operation Life, Based on the Measurement of the External Magnetic Field. *2018 IEEE 3rd International Conference on Intelligent Energy and Power Systems (IEPS)*, Kharkiv, 2018, pp. 316-321. doi: https://doi.org/10.1109/ieps.2018.8559564.

28. Ummels M. *Stochastic Multiplayer Games Theory and Algorithms*. Amsterdam University Press, 2010. 174 p.

29. Shoham Y., Leyton-Brown K. *Multiagent Systems: Algorithmic, Game-Theoretic, and Logical Foundations.* Cambridge University Press, 2009. 504 p.

30. Xin-She Yang, Zhihua Cui, Renbin Xiao, Amir Hossein Gandomi, Mehmet Karamanoglu. *Swarm Intelligence and Bio-Inspired Computation: Theory and Applications*, Elsevier Inc., 2013. 450 p.

31. Zilzter Eckart. *Evolutionary algorithms for multiobjective optimizations: methods and applications*. PhD Thesis Swiss Federal Institute of Technology, Zurich, 1999. 114 p.

32. Xiaohui Hu, Eberhart R.C., Yuhui Shi. Particle swarm with extended memory for multiobjective optimization. *Proceedings of the 2003 IEEE Swarm Intelligence Symposium*. SIS'03 (Cat. No.03EX706), Indianapolis, IN, USA, 2003, pp. 193-197. doi: https://doi.org/10.1109/sis.2003.1202267.

33. Pulido G.T., Coello C.A.C. A constraint-handling mechanism for particle swarm optimization. *Proceedings of the 2004 Congress on Evolutionary Computation* (IEEE Cat. No.04TH8753), Portland, OR, USA, 2004, vol. 2, pp. 1396-1403. doi: https://doi.org/10.1109/cec.2004.1331060.

34. Michalewicz Z., Schoenauer M. Evolutionary Algorithms for Constrained Parameter Optimization Problems. *Evolutionary Computation*, 1996, vol. 4, no. 1, pp. 1-32. doi: https://doi.org/10.1162/evco.1996.4.1.1.

35. Parsopoulos K.E., Vrahatis M.N. Particle swarm optimization method for constrained optimization problems. *Proceedings of the Euro-International Symposium on Computational Intelligence*, 2002, pp. 174-181.

B.I. Kuznetsov[1], *Doctor of Technical Science, Professor,*
T.B. Nikitina[2], *Doctor of Technical Science, Professor,*
I.V. Bovdui[1], *PhD, Senior Research Scientist,*
O.V. Voloshko[1], *PhD, Junior Research Scientist,*
V.V. Kolomiets[2], *PhD, Associate Professor,*
B.B. Kobylianskiy[2], *PhD, Associate Professor,*
[1] A. Pidhornyi Institute of Mechanical Engineering Problems of the National Academy of Sciences of Ukraine,
2/10, Pozharskogo Str., Kharkiv, 61046, Ukraine,
e-mail: kuznetsov.boris.i@gmail.com (Corresponding author)
[2] Educational scientific professional pedagogical Institute of Ukrainian Engineering Pedagogical Academy,
9a, Nosakov Str., Bakhmut, Donetsk Region, 84511, Ukraine,
e-mail: tatjana55555@gmail.com; nnppiuipa@ukr.net

K. Baazouzi, A.D. Bensalah, S. Drid, L. Chrifi-Alaoui

Passivity voltage based control of the boost power converter used in photovoltaic system

*Introduction. This paper presents a robust nonlinear control of the DC-DC boost converter feeding by a photovoltaic system based on the passivity control. The control law design uses the passivity approach. **Novelty.** The novelty consists in designing a control law for a photovoltaic system using a passivity approach based on energy shaping and associated with damping injection. **Purpose.** The purpose consists to develop a tool for design and optimize a control law of the photovoltaic system in order to improve its efficiency under some conditions such as the variations of the temperature, the irradiation and the parameters. Also, the control law design should be simple with a lower overshoot and a shorter settling time. **Methods.** This work uses the port Hamiltonian mathematical approach with minimization of the energy dissipation in boost converter of the photovoltaic system to illustrate the modification of energy and generate a specify duty cycle applied to the converter. **Results.** The results with MATLAB/SimPowerToolbox® have proven the robustness against parameter variations and effectiveness of the proposed control. **Practical value.** The experimental results, carried out using a dSPACE DS1104 system, are presented to show the feasibility and the robustness of the proposed control strategy against parameter variations.* References 26, tables 3, figures 18.
Key words: **DC-DC converters, interconnection and damping assignment, passivity based control, port controlled Hamiltonian.**

*Вступ. У статті представлено надійне нелінійне керування живленням перетворювача постійного струму, що підвищує, фотоелектричною системою на основі керування пасивністю. У створенні закону управління використовується пасивний підхід. **Новизна.** Новизна полягає у розробці закону управління фотоелектричною системою з використанням пасивного підходу, заснованого на формуванні енергії та пов'язаного з упорскуванням демпфування. **Мета.** Мета полягає в тому, щоб розробити інструмент для проектування та оптимізації закону керування фотогальванічною системою для підвищення її ефективності за деяких умов, таких як зміни температури, опромінення та параметрів. Крім того, будова закону управління має бути простою, з меншим перерегулюванням і коротшим часом встановлення. **Методи.** У роботі використовується математичний підхід Гамільтона до порту з мінімізацією розсіювання енергії у перетворювачі фотоелектричної системи, що підвищує, щоб проілюструвати зміну енергії і створити заданий робочий цикл, що застосовується до перетворювача. **Результати.** Результати з використанням MATLAB/SimPowerToolbox® довели стійкість до змін параметрів та ефективність запропонованого керування. **Практична цінність.** Представлені експериментальні результати, отримані з використанням системи dSPACE DS1104, щоб показати здійсненність та стійкість запропонованої стратегії управління при зміні параметрів.* Бібл. 26, табл. 3, рис. 18.
Ключові слова: **DC-DC перетворювачі, призначення взаємоз'єднань та демпфування, управління на основі пасивності, гамільтоніан, керований портом.**

Introduction. Control theory has overcome the problems of dynamic systems such as uncertain, disturbed and time invariant linear models. Therefore, designing feedback controllers has become a relatively easy and efficient task [1].

However, the above described control theory is no longer applicable in case of nonlinear models. In the few past decades, several nonlinear control and stability methodologies are broadly known in the literature.

The dependence of the linear control on the operating point is raised [2, 3], on the other hand, the sliding mode control drawback is the high and free switching frequency, which generates unconfined voltages or currents [4]. The choice of the candidate function for the stabilizing control based on the Lyapunov criterion of is not obvious for the nonlinear systems it is generally heuristic [5].

The passivity control has been introduced by Romeo Ortega in 1998. It is a controller design procedure rendering the system passive and respecting the desired storage function. This guarantees the stability of the overall system [6-8].

Globally, the Passivity Based Control (PBC) can be classified on two groups, classical passivity control where the storage function is defined (typically quadratic), then design the controller that renders the storage function non-increasing. This approach is similar to a Lyapunov method. In the second passivity control group, the storage function is not defined, but instead selecting the closed-loop desired structure, and then characterizes energy functions compatible with the desired structure. The outstanding examples of this approach are the interconnection and damping assignment (IDA) method [9].

Generally, the passivity control law can be designed according two approaches; the Lagrangian model [8-10] or the Hamiltonian approach [11, 12]. The Lagrangian form is used for mechanical as well as in electrical systems [8]. However, due to the physical characteristics of transistors and diodes used in the DC-DC converters, the Lagrangian formulation is not suitable [2, 13-15].

The goal of the paper is analysis Hamiltonian structure using interconnection and damping assignment method associated to passivity control (IDA-PBC) applied in photovoltaic system. It is a well-established technique to simplify the control law and achieve a desired equilibrium point with minimum storage energy of output voltage.

Subject of investigations. In this work the output voltage from the photovoltaic (PV) system, operate to achieve a desired output voltage of the boost converter by modifying passivity forms of port Hamiltonian model using passivity approach [11, 12]. The design and implementation control law of the output voltage is presented. With the increase of the energy demand the world turned to solar energy which is easy availability, free, inexhaustible source and without CO_2 gas emissions.

In PV panels solar cells are the basic components and it is made of silicon. A solar cell is generally a p-n junction which is made of silicon. It is made up of two different layers when a smaller quantity of impurity atoms added to it. The PV cell is a basic device of the PV system which

converts the irradiations solar to the electrical energy and provide energy to the consumer or feed power to the grid.

Many stages are used in grid connected PV system like PV array, DC to DC converter, DC to AC converter.

The converters used in the PV system are a nonlinear; they have a bilinear model such as the DC-DC boost converter.

In this paper a model is developed through converting common circuit equation of solar cell in to simplified form including the effects of changing solar irradiation and changing temperature by maximum power point tracking (MPPT) algorithm.

The originality of this work consists of the design a control law for a PV system by interconnection and damping assignment.

Modeling, relationships and assumptions. Figure 1 shows the structure of the studied system. The converter is placed between the PV array and load. It can be controlled using microcontroller or digital signal processor (DSP) in order to regulate the output voltage [16, 17].
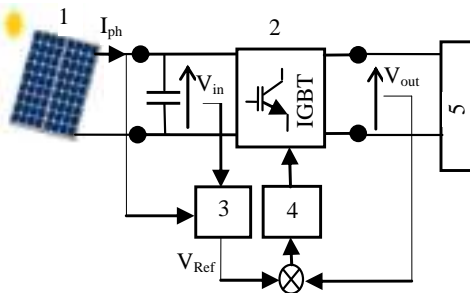
Fig. 1. PV system device with DC-DC boost drive: 1 – PV cell; 2 – DC-DC boost; 3 – MPPT; 4 – IDA-PBC controller; 5 – load

Two approaches have been developed to model the behavior of PV array. The first is based on the equivalent circuit and the second is empirically based models [15].

In the calculation, the following assumptions were made: the one diode equivalent circuit (Fig. 2) is chosen due its simplicity [18].

The main calculation relation is the equation of the PV current I_{pv}:

$$I_{pv} = I_{ph} - \frac{V_{pv} + R_s I_{pv}}{R_{sh}} - I_d (e^{\frac{V_{pv} + R_s I_{pv}}{aV_T}} - 1), \quad (1)$$

where I_d is the current in equivalent diode; a is the diode constant; $V_T = k \cdot T/q$ is the thermal voltage; T is the temperature; k is the Boltzmann constant; q is the charge of electron; I_{ph} indicates the light current wish is proportional to the irradiation G but it is affected by the temperature.

$$I_{ph} = \frac{G}{G_n} \cdot (K_I \Delta T + I_{pv,n}), \quad (2)$$

where $I_{pv,n}$ is the nominal light generated current at (25 °C – 1000 W·m^{-2}), $\Delta T = T - T_n$ is the variation temperature and G_n is the nominal irradiation [W·m^{-2}].

In order to take into account of the saturation current I_s is given by:

$$I_s = \frac{I_{sc,n} + K_I \Delta T}{\left(e^{\frac{(V_{oc,n} + K_V \Delta T)}{aV_T}} - 1 \right)}, \quad (3)$$

where I_{sc} is the short-circuit current; V_{oc} is the open circuit voltage; K_V and K_I are voltage and current coefficients.

The rate parameters of the PV panel are reported in the Table 1.

Table 1
Rate parameters of the PV panel BP SX 100

V_{oc} (open circuit voltage)	32 V
I_{sco} (short circuit current)	5 A
V_{pp} (max point voltage)	24 V
P_{pp} (max point power)	105 W
I_{pp} (max point current)	4.38 A

Figure 2 shows the current and power versus voltage characteristics of a PV module for G = 1000, 800, 600, 400 W/m². For each radiation G the curve has a maximum power point (MPP). To operate the PV system in MPP several techniques have been developed. From Fig. 2 it is noticed that the maximum power has an almost linear relation to the unit of voltage of the network.
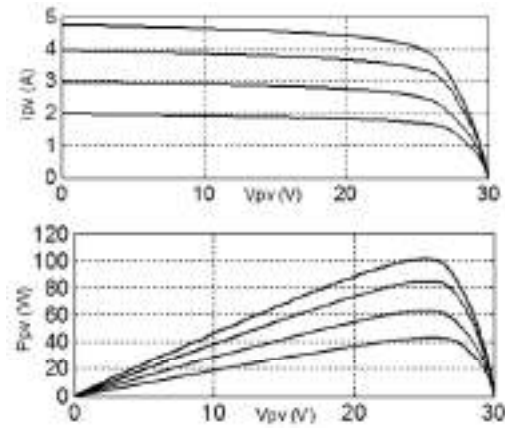
Fig. 2. Current and power versus voltage characteristics

The PV-boost-load system (Fig. 3) using in this section consists of an inductance L, a controlled switch (IGBT), a diode VD and filtering capacitors C. When the switch is on, the boost inductance current increases linearly, the diode VD being blocked. When switch is off, the energy stored in the inductor passes through the diode to the output circuit [19].
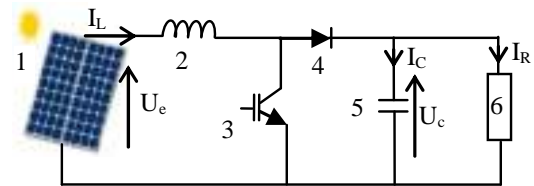
Fig. 3. PV system: 1 – PV panel; 2 – input coil; 3 – IGBT; 4 – diode; 5 – output capacitor; 6 – resistance load

To design the best control law if an appropriate model is chosen. We assume that the continuous conduction mode, the state space average model is given in the following equation [22]:

$$\begin{bmatrix} \dot{x}_1 \\ \dot{x}_2 \end{bmatrix} = \begin{bmatrix} \dfrac{U_e}{L} - \dfrac{x_2}{L} \\ \dfrac{x_1}{C} - \dfrac{x_2}{RC} \end{bmatrix} + \begin{bmatrix} \dfrac{x_2}{L} \\ -\dfrac{x_1}{C} \end{bmatrix} u, \quad (4)$$

where $x_1 = I_L$, $x_2 = U_c$, U_e is the PV voltage, u acts as a control input variable ($0 < u \le 1$).

The ratio U_c and U_e is given as:

$$\frac{U_c}{U_e} = \frac{1}{u} = \frac{1}{1-D}, \quad (5)$$

where D denotes the duty ratio, and U_c voltage is higher than the U_e voltage.

The Pulse Width Modulation (PWM) signals for driving the switching devices can be generated by comparing the sinusoidal control signal with a triangular carrier signal. The control objective is to design a control law for the control input $u(t)$ such that the output voltage of boost (U_c) attains a desired reference. For the desired set point $x^* = (x_1^* \ x_2^d)^T$ we get at equilibrium:

$$\begin{cases} x_1^* = \dfrac{x_2^{d2}}{RU_e} \\ u = 1 - \dfrac{U_e}{x_2^d} \end{cases} . \tag{6}$$

The equation (6) can be written in terms of Port Controlled Hamiltonian (PCH) approach.

Background Port Controlled Hamiltonian. The first work on the PCH has been developed by Dalsmo and van der Schaft in 1992 [20]. It is used to modeling physical systems with lumped-parameter and independent storage elements. Generally, a nonlinear input affine system is described by the following model:

$$\begin{cases} \dot{x} = f(x) + g(x).u \\ y = h(x) \end{cases}, \tag{7}$$

where $f(x)$, $g(x)$ are the Lipschitz functions and x is the states variable such as $\{x \in R^n\}$, $\{h(x) \in C\}$ and $\{(u, y) \in R^{mxn}\}$.

A system (7) is passive if the inflow of electrical power is always nonnegative and has a property of stability with a positive storage function defined as:

$$H \in C : R^n \to R_+ / H(x) = \frac{1}{2} x^T Q x, \forall x.$$

where $Q \geq 0$ is the diagonal matrix and such that for $t_1 \geq t_0$ satisfies the inequality:

$$H(x(t_1)) - H(x(t_2)) \leq \int_{t_0}^{t_1} u^T y \Rightarrow \dot{H} \leq u^T y; \forall(x, u, y).$$

For any nonlinear system described by (7) with a storage function $H(x)$ can be modeled as port controlled Hamiltonian system, which is in the simplest and explicit version of the form (8) [11]:

$$\begin{cases} \dot{x} = [J(x) - R(x)] \nabla H(x) + g(x).u \\ y = g^T(x).\nabla H(x) \end{cases}, \tag{8}$$

where $J(x) = -J^T(x) \in R^{mxn}$ is the interconnection structure matrix, $R(x) = R^T(x) \in R^{mxn} \geq 0$ is the dissipation matrix and $H(x): R^n \to R^+$ is the energy (Hamiltonian) function such as the gradient vector is:

$$\nabla H(x) = \left[\frac{\partial H(x)}{\partial x}\right].$$

From management structure of (8), the acquisition port is $(u^T \ y)$ [8]. Using evaluating the rate of change energy and version of Kalman-Yakubovich-Popov lemma [21-26], we easily see that PCH model is passive because:

$$\dot{H}(x) = \nabla H^T(x)\dot{x} = u^T y - R(x)(\nabla H(x))^2 \leq u^T y.$$

Moreover:

$$\begin{cases} \nabla H^T(x) f(x) = -R(x)(\nabla H(x))^2 \leq 0 \\ y(x) = g^T(x).\nabla H(x) \end{cases}, \tag{9}$$

In previous sections, a suitable model (4) for boost converter with PCH description is expressed [11, 23-25].

We can write (4) in PCH model as

$$\dot{x} = [J(u) - R] \nabla H(x) + G,$$

where:

$$J(u) = \begin{bmatrix} 0 & \dfrac{u-1}{LC} \\ -\dfrac{u-1}{LC} & 0 \end{bmatrix} \in R^{2x2} \qquad R = \begin{bmatrix} 0 & 0 \\ 0 & \dfrac{1}{RC^2} \end{bmatrix} > 0 \in R^{2x2} ;$$

$$G = \begin{bmatrix} \dfrac{U_e}{L} \\ 0 \end{bmatrix} \in R^{2x1}$$

is the constant vector containing the external voltage source.

We assume that the condition $(\omega L \ll 1/(\omega C))$ is satisfied, the boost converter described in (4) is passive since:

$$U_e x_1 - \frac{x_2^2}{R} - y \leq 0.$$

The storage energy:

$$H(x) = \frac{1}{2} x^T Q x; \quad Q = \begin{bmatrix} L & 0 \\ 0 & C \end{bmatrix};$$

$$\nabla H^T(x) = \left[\frac{\partial H(x)}{\partial x_1} \quad \frac{\partial H(x)}{\partial x_2}\right] = [Lx_1 \quad Cx_2];$$

and

$$H(x(t_{i+1})) - H(x(t_i)) \leq \int_{t_i}^{t_{i+1}} x_1 U_e dt$$

where $x_1 \cdot U_e$ is the input power.

The total energy change rate for all $t \geq 0$ is given as:

$$H(x(t)) = H(x(0)) + \int_0^t u^T(\tau) \cdot y(\tau) d\tau - R \cdot \int_0^t \nabla H^2[x(\tau)] d\tau. \tag{10}$$

The storage function $H(x)$ is bounded since (10) shows that we can extract a finite amount of the boost converter energy. The system will eventually stop in a minimum energy point. In fact, the boost converter is a passive system and it can be controlled using the IDA-PBC approach.

The rate of convergence of (10) can be increased by a negative feedback interconnection $u = -k \cdot x$ with $k > 0$ a damping injection gain or modified R via IDA-PBC controller.

Our main idea is to assign the desired closed-loop energy function in the equilibrium point $x^* = (x_1^* \ x_2^d)^T$ using IDA-PBC.

To get the desired output voltage, the following stages must be obtained:

• find a control action $u = \beta(x) + v$ in close-loop and reshaping the amount dissipated energy through by injecting additional damping resistance $r > 0$ to dump the transient oscillation. So:

$$R_d = \begin{bmatrix} r & 0 \\ 0 & \dfrac{1}{RC^2} \end{bmatrix}.$$

• shaping the new potential energy provided by the capacitor is needed.

The new desired energy function, which has a strict (local) minimum at x^*, form is:

$$H_d(x(t)) = H(x(0)) + \int_0^t \beta^T(\tau) y(\tau) d\tau + \int_0^t v^T(\tau) y(\tau) d\tau - R_d \int_0^t \nabla H^2[x(\tau)].d\tau$$

where:

$$H_d(x) = \frac{1}{2} L\left(x_1 - x_1^*\right)^2 + \frac{1}{2}\gamma C\left(x_2 - x_2^d\right)^2; \left.\frac{\partial H_d}{\partial x}\right|_{x=x_d} = 0; \left.\frac{\partial^2 H_d}{\partial x^2}\right|_{x=x_d} > 0.$$

$\gamma > 0$ is the adjustable gain in output potential energy to increasing the rate of convergence of power system.

A block diagram representing IDA-PBC approach is shown in Fig. 4.
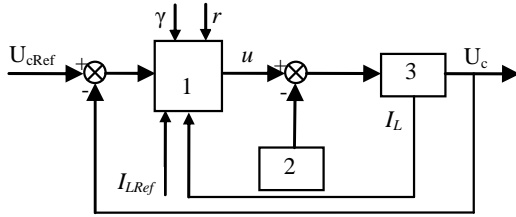
Fig. 4. Scheme of IDA-PBC controller:
1 – IDA-PBC controller; 2 – PWM; 3 – boost with PV cell

The desired target dynamic of (8) is defined as:

$$\dot{x} = (J(u) - R_d).\nabla H_d(x) \cdot \quad (11)$$

Initial conditions and input data. To find a control action (u) in state-feedback for the boost converter, and taking into account all initial conditions ($x(0)$, $u(0)$, $y(0)$) with (11) we make:

$$(J(u) - R_d).\nabla H_d(x) = \left(J(u) - R\right)\nabla H(x) + G. \quad (12)$$

In order to reach a desired voltage x_2^* and for the partial derivative (12) the control law can be found as following:

$$\begin{cases} (u-1)x_2 - \dfrac{u-1}{\gamma}(x_2 - x_2^d) = -rL^2(x_1 - x_1^*) - U_e; \\ -(u-1)x_1 + (u-1)(x_1 - x_1^*) = \dfrac{1}{R}x_2 - \dfrac{1}{R\gamma}(x_2 - x_2^d). \end{cases}$$

So:

$$u = 1 - \gamma \frac{R(x_2^d - U_e)\left(rL^2 x_1 + U_e\right) - rL^2 x_2^{d2}}{R(x_2^d - U_e)\left(x_2^d + (\gamma-1)x_2\right)}. \quad (13)$$

In order to choose the optimal values for r and γ we make the initial condition that $0 < u \leq 1$.

So:

$$\begin{cases} r \geq \dfrac{R(x_2^d - U_e)U_e}{L^2\left(x_2^{d2} - Rx_1(x_2^d - U_e)\right)} \geq 0 \\ \gamma = \dfrac{U_e R x_2^d (x_2^d - U_e)\left(x_2^d - x_2\right)}{Rx_2^d(x_2^d - U_e)\left(rL^2 x_1 + U_e\right) - rL^2 x_2^{d3} - U_e Rx_2^d x_2} \end{cases}.$$

To eliminate steady state error an integral action is added:

$$u = 1 - \gamma \frac{R(x_2^d - U_e)\left(rL^2 x_1 + U_e\right) - rL^2 x_2^{d2}}{R(x_2^d - U_e)\left(x_2^d + (\gamma-1)x_2\right)} + K_p\left(x_2 - x_2^d\right) + K_I \int\left(x_2 - x_2^d\right)$$

where $(K_p, K_I) \in R^{+*2}$.

Stability analysis. To study the stability of the proposed control we use the Lyapunov theory. If we assume that $H_d(x)$ is a candidate function of Lyapunov, the asymptotic stability of set (x_1^*, x_2^d) can be investigated such that:

$$H_d(x) = \frac{1}{2} L\left(x_1 - x_1^*\right)^2 + \frac{1}{2}\gamma C\left(x_2 - x_2^d\right)^2 \geq 0.$$

Quadratic function: $\dfrac{dH_d(x(t))}{dt} = \nabla H_d^T(x)\,\dot{x}(t).$

Using (11):

$$\frac{dH_d(x(t))}{dt} = \nabla H_d^T(x)J(u)\nabla H_d(x) - \nabla H_d^T(x)R_d\nabla H_d(x) \cdot$$

For $J(u) = -J^T(u)$ we get:

$$\frac{dH_d(x(t))}{dt} = -\nabla H_d^T(x)R_d\nabla H_d(x) \Rightarrow$$

$$\Rightarrow \frac{dH_d(x(t))}{dt} = -\left(\left(\frac{\partial H(x)}{\partial x_1}\right)^2 r + \left(\frac{\partial H(x)}{\partial x_2}\right)^2 \frac{1}{RC^2}\right) \leq 0$$

Simulations results. The validation of the theoretical analysis has been carried out by the average boost converter model supplied by PV array using Matlab/Simulink (Fig. 5).
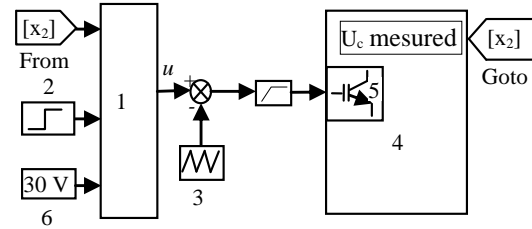
Fig. 5. Simulation diagram of the IDA-PBC:
1 – IDA-PBC controller; 2 – U_{cRef}; 3 – PWM;
4 – boost converter; 5 – IGBT; 6 – input voltage

The parameters of our system are reported in the Table 2. The virtual resistance should be sufficiently large, to ensure a large energy dissipation amount as well as to minimize the ripples of the current.

Table 2
Parameters of DC-DC boost converter

Parameter	Values
Input voltage	$U_e = 30$ V
Inductance	$L = 54$ mH
Capacitor	$C = 4400$ µF
Load resistance	$R = 320$ Ω
Integral gain (I)	$K_I = 1.5$
Proportional gain (P)	$K_P = 4$
Dumping resistance	$r = 4$ Ω
Adjustable gain	$\gamma = 0.5$

In the following, some simulation results are reported in order to show the performances of the proposed controller. The control law is tested with parameters and voltage references variations.

Graphs of changes in output voltage and its reference are shown in Fig. 6.

Referring to Fig. 6, the close loop response adopting IDA-PBC controller exhibit a good tracking of the output voltage to their multivalued reference delivered by PV cell using MPPT algorithm.

Initially the PV voltage is adjusted at 60 V. At time $t = 21.51$ s the reference voltage varies up to 85 V and stabilize in a steady state without error.
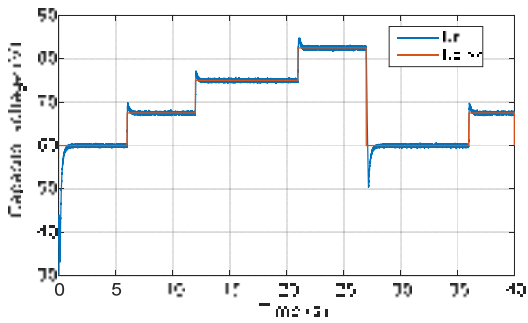
Fig. 6. Simulation results output-voltage during reference voltage variation

Moreover, the reduced duration of the start-up transient operation of the system has been also obtained.

In order to verify the robustness of the proposed method, we will test the performance of IDA-PBC by making variations on parameters system.

According Fig. 7-9 the output voltage does not change with parametric variations; so we deduced the effectiveness robustness of the proposed controller.
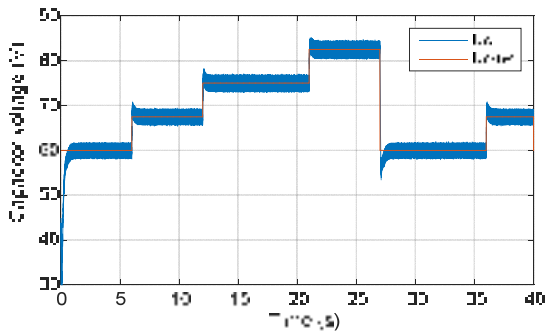
Fig. 7. Output voltage for ΔR = 50 %
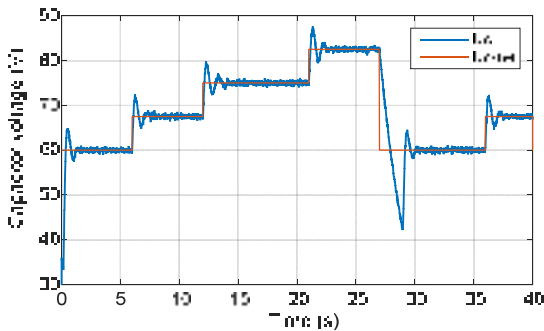
Fig. 8. Output voltage for ΔL = 50 %
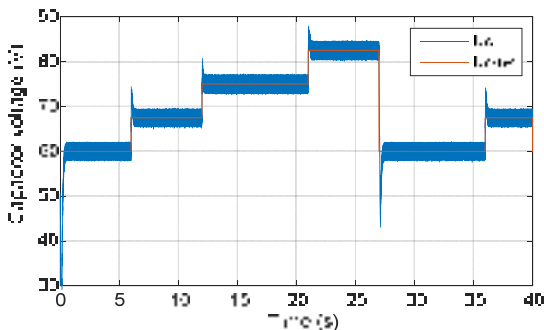
Fig. 9. Output voltage for ΔC = 50 %

Experimental test. To validate the simulations results of proposed control, experiments were conducted on a real system. The layout of the prototype under test is reported in Fig. 10 for obtaining the experimental results.
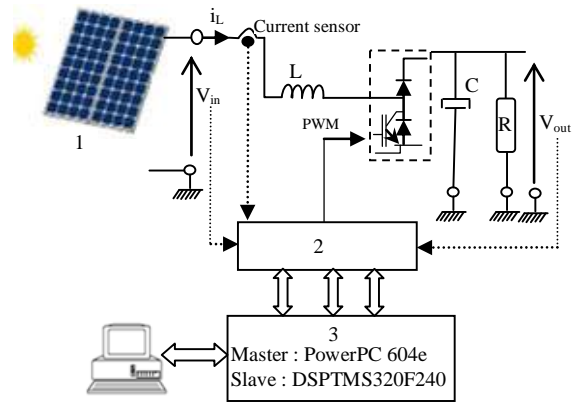
Fig. 10. Laboratory setup structure:
1 – DC source; 2 – interface; 3 – DS1104 dSPACE

The boost converter laboratory structure is based on IGBT modules SKM100GAL123D fed by the DC voltage source. The currents and voltages sensors used are respectively LA-25NP and LV-25P. An interface is used to provide galvanic isolation of all dSPACE DS1103 PPC controller signals (Fig. 11). The main parameters of boost model are reported in Table 3.

Table 3
Experimental parameters of boost converter

Parameter	Values
Input voltage	U_e = 30 v
Inductance	L = 54 mH
Capacitor	C = 4400 µF
Load resistance	R = 320 Ω
Integral gain (I)	K_I = 2
Proportional gain (P)	K_p = 10
Dumping resistance	r = 4 Ω
Adjustable gain	γ = 0.5
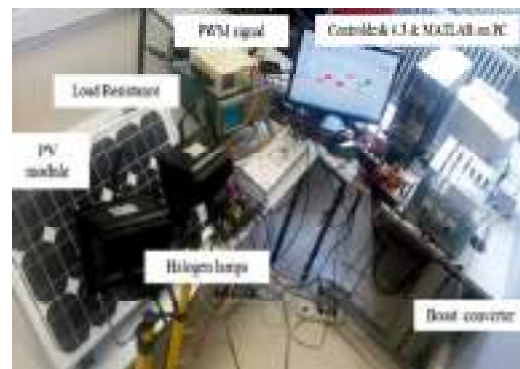
Fig. 11. The hardware setup of the system (LTI laboratory)

Figures 12-15 represents the response output voltage according reference and parameters.
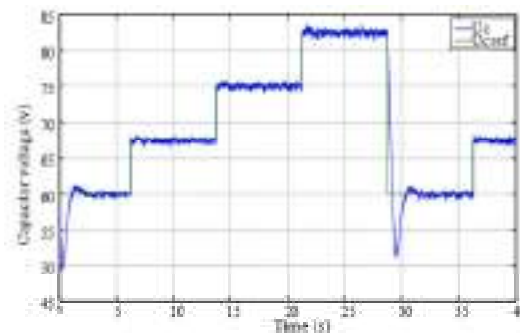
Fig. 12. Output voltage and its reference
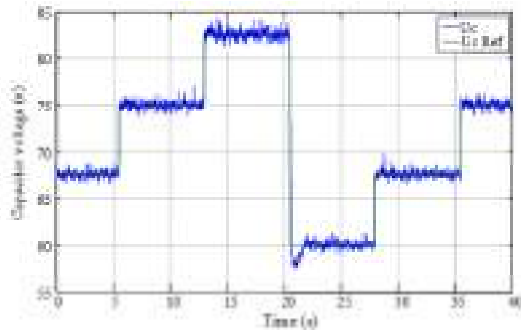
Fig. 13. Output voltage with resistance variation (–50 %)
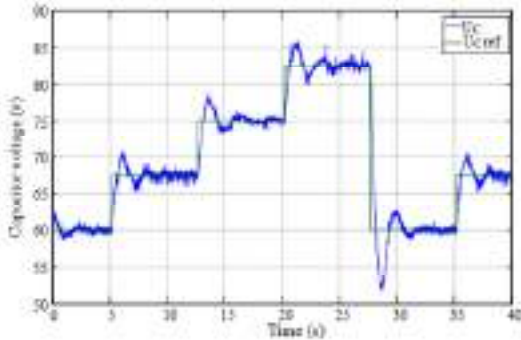
Fig. 14. Output voltage with inductance variation (–50 %)
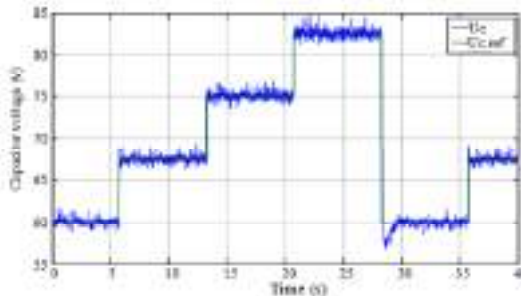
Fig. 15. Output voltage with capacitor variation (–50 %)

The introduced IDA-PBC permits the stability of the system without steady state error (Fig. 16).
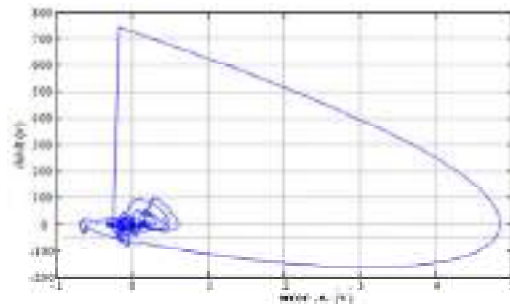
Fig. 16. The trajectory of dynamic error

To validate the proposed control with the classical PI controller a comparative study has been made and the results are presented in Fig. 17, 18.
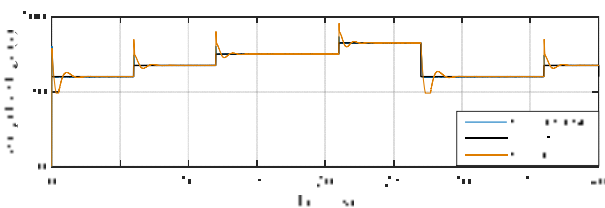
Fig. 17. Output voltage control with PI controller and IDA-PBC
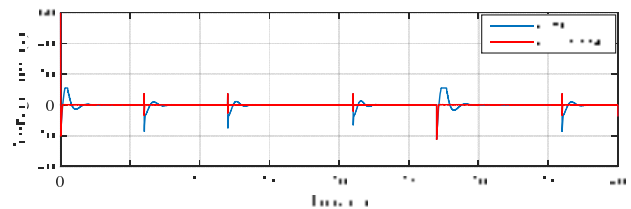
Fig. 18. Dynamic error with PI and IDA-PBC control

Conclusions.

1. The passivity control has been developed to describe energetic properties of dynamical systems and their interconnections; in terms of the input-output behavior and the system is stabilized by an output feedback gain.

2. To design robust controllers via shaping internal energy, we start from the Euler-Lagrange description and then consider instead port-controlled Hamiltonian modeling.

3. To assigning, a desired port controlled Hamiltonian structure in closed-loop the interconnection and damping assignment passivity control technique has turned out to be very successful and has provided solutions of electrical systems.

4. The proposed passivity control has been applied to the DC-DC boost converter and experimental tested on the dSPACEDS1104 system. The general aspects of the performances results are reported and compared with simulation results in order to validate the robustness controller against parameters variation.

5. Our future work revolves around two major challenges: the development of a reliable control of the PV system with fault and the development of controls adapted to the PV system connected to the grid, under constraints.

Conflict of interest. The authors declare that they have no conflicts of interest.

REFERENCES
1. Bennett S. A brief history of automatic control. *IEEE Control Systems Magazine*, 1996, vol. 16, no. 3, pp. 17-25. doi: https://doi.org/10.1109/37.506394.
2. S. Bacha, I. Munteanu, A. Iuliana Bratcu. *Power Electronic Converters Modeling and Control with Case Studies. In Advanced Textbooks in Control and Signal Processing*. Springer London, 2014. 454 p. doi: https://doi.org/10.1007/978-1-4471-5478-5.
3. Petitclair P., Bacha S., Ferrieux J.-P. Optimized linearization via feedback control law for a STATCOM. *IAS '97. Conference Record of the 1997 IEEE Industry Applications Conference Thirty-Second IAS Annual Meeting*, 1997, vol. 2, pp. 880-885. doi: https://doi.org/10.1109/IAS.1997.628965.
4. Montoya D.G., Ramos-Paja C.A., Giral R. Improved Design of Sliding-Mode Controllers Based on the Requirements of MPPT Techniques. *IEEE Transactions on Power Electronics*, 2016, vol. 31, no. 1, pp. 235-247. doi: https://doi.org/10.1109/TPEL.2015.2397831.
5. Sanders S.R., Verghese G.C. Lyapunov-based control for switched power converters. *21st Annual IEEE Conference on Power Electronics Specialists*, 1990, pp. 51-58. doi: https://doi.org/10.1109/PESC.1990.131171.
6. Scherpen J.M.A., Jeltsema D., Klaassens J.B. Lagrangian modeling of switching electrical networks, *Systems & Control Letters*, 2003, vol. 48, no. 5, pp. 365-374. doi: https://doi.org/10.1016/S0167-6911(02)00290-6.

7. Kwasinski A., Krein P.T. Passivity-Based Control of Buck Converters with Constant-Power Loads. *2007 IEEE Power Electronics Specialists Conference*, 2007, pp. 259-265, doi: https://doi.org/10.1109/PESC.2007.4341998.

8. Ortega R., Lonia A., Nicklasson P.J., Sira-Ramirez H. *Passivity-based Control of Euler-Lagrange Systems: Mechanical, Electrical and Electromechanical Applications.* Springer, 1998. 543 p.

9. Petrovic V., Ortega R., Stankovic A.M. Interconnection and damping assignment approach to control of PM synchronous motors. *IEEE Transactions on Control Systems Technology*, 2001, vol. 9, no. 6, pp. 811-820. doi: https://doi.org/10.1109/87.960344.

10. Ortega R., Loria A., Kelly R., Praly L. On passivity-based output feedback global stabilization of Euler-Lagrange systems. *Proceedings of 1994 33rd IEEE Conference on Decision and Control*, 1994, vol. 1, pp. 381-386 doi: https://doi.org/10.1109/CDC.1994.410898.

11. Ortega R., Van der Schaft A., Maschke B., Escobar G. Interconnection and damping assignment passivity-based control of port-controlled Hamiltonian systems. *Automatica*, 2002, vol. 38, no. 4, pp. 585-596. doi: https://doi.org/10.1016/S0005-1098(01)00278-3.

12. Severn R.P., Bloom G.E. *Modern DC to DC Switch Mode Power Converter Circuits*. Van Nostrand Reinhold, New York, 1982.

13. Venkataramanan R., Sabanovic A., Cuk S. Sliding mode control of DC-to-DC converters. *Proceedings - IECON '85, 1985 International Conference on Industrial Electronics, Control and Instrumentation. Industrial Applications of Mini, Micro & Personal Computers*, 1985, pp. 251-258.

14. Middlebrook R.D., Cuk S. A general unified approach to modelling switching-converter power stages. *1976 IEEE Power Electronics Specialists Conference*, 1976, pp. 18-34, doi: https://doi.org/10.1109/PESC.1976.7072895.

15. Montoya D.G., Ramos-Paja C.A., Giral R. Improved Design of Sliding-Mode Controllers Based on the Requirements of MPPT Techniques. *IEEE Transactions on Power Electronics*, 2016, vol. 31, no. 1, pp. 235-247. doi: https://doi.org/10.1109/TPEL.2015.2397831.

16. Du W., Jiang Q., Erickson M.J., Lasseter R.H. Voltage-Source Control of PV Inverter in a CERTS Microgrid. *IEEE Transactions on Power Delivery*, 2014, vol. 29, no. 4, pp. 1726-1734. doi: https://doi.org/10.1109/TPWRD.2014.2302313.

17. Patcharaprakiti N., Premrudeepreechacharn S. Maximum power point tracking using adaptive fuzzy logic control for grid-connected photovoltaic system. *2002 IEEE Power Engineering Society Winter Meeting. Conference Proceedings*, 2002, vol. 1. pp. 372-377. doi: https://doi.org/10.1109/pesw.2002.985022.

18. Ramos-Hernanz J., Uriarte I., Lopez-Guede J.M., Fernandez-Gamiz U., Mesanza A., Zulueta E. Temperature based maximum power point tracking for photovoltaic modules. *Scientific Reports*, 2020, vol. 10, no. 1, p. 3 (12476). doi: https://doi.org/10.1038/s41598-020-69365-5.

19. Nebti K., Lebied R. Fuzzy maximum power point tracking compared to sliding mode technique for photovoltaic systems based on DC-DC boost converter. *Electrical Engineering &*

Electromechanics, 2021, no. 1, pp. 67-73. doi: https://doi.org/10.20998/2074-272X.2021.1.10.

20. Maschke B.M., Van der Schaft A.J. Port-Controlled Hamiltonian Systems: Modeling origins and system theoretic Properties. IFAC Symposia Series, 1993, no. 7, pp. 359-365. doi: https://doi.org/10.1016/b978-0-08-041901-5.50064-6.

21. Mendez-Diaz F., Ramirez-Murillo H., Calvente J., Pico B., Giral R. Input voltage sliding mode control of the versatile buck-boost converter for photovoltaic applications. *2015 IEEE International Conference on Industrial Technology (ICIT)*, 2015, pp. 1053-1058. doi: https://doi.org/10.1109/ICIT.2015.7125236.

22. Hassan M.A., Li T., Duan C., Chi S., Li E.P. Stabilization of DC-DC buck power converter feeding a mixed load using passivity-based control with nonlinear disturbance observer. *2017 IEEE Conference on Energy Internet and Energy System Integration (EI2)*, 2017, pp. 1-6, doi: https://doi.org/10.1109/EI2.2017.8245419.

23. Kassakian J.G., Schlecht M.F., Verghese G.C. *Principles of Power Electronics*. Pearson College Div., 1991. 740 p.

24. Baazouzi K., Bensalah A., Drid S. The PBC technical to control the induction motor. *2014 15th International Conference on Sciences and Techniques of Automatic Control and Computer Engineering (STA)*, 2014, pp. 7-10. doi: https://doi.org/10.1109/STA.2014.7086690.

25. Huang J., Wang H. A Passivity-based Control for DC Motor Drive System with PWM. *TELKOMNIKA Indonesian Journal of Electrical Engineering*, 2012, vol. 10, no. 8, pp. 2267-2271. doi: https://doi.org/10.11591/telkomnika.v10i8.1695.

26. Escobar G., Van der Schaft A.J., Ortega, R. Hamiltonian viewpoint in the modeling of switching power converters. *Automatica*, 1999, vol. 35, no. 3, pp. 445-452. doi: https://doi.org/10.1016/S0005-1098(98)00196-4.

Kamel Baazouzi[1]*, PhD Student of Engineering,*
Abed Djebar Bensalah[1]*, Doctor of Engineering,*
Said Drid[2]*, Professor, Dr.-Ing. of Engineering*,
Larbi Chrifi-Alaoui[3]*, Dr.-Ing. of Engineering*,
[1] Electrical Engineering Department
University of Batna 2,
53, Route de Constantine, Fésdis, Batna 05078, Algeria,
e-mail: Baazouzi.kamel@gmail.com (Corresponding Author),
Abedbensalah@yahoo.fr
[2] Research Laboratory LSPIE,
Electrical Engineering Department,
University of Batna 2,
53, Route de Constantine, Fésdis, Batna 05078, Algeria,
e-mail: saiddrid@ieee.org
[3] Laboratoire des Technologies Innovantes (LTI),
University of Picardie Jules Verne, IUT de l'Aisne,
13 Avenue François Mitterrand 02880 Cuffies-Soissons, France,
e-mail: larbi.alaoui@u-picardie.fr

V.Y. Romashko, L.M. Batrak, O.O. Abakumova

Step-up/step-down regulators in maximum power transmission mode

Introduction. *Switching DC voltage regulators are traditionally used to regulate and stabilize the voltage on the load. Due to the widespread use of non-traditional and renewable sources of electricity, there is a need to select from them the maximum possible amount of electricity. As is known, the maximum power from the power supply to the load will be transmitted provided that the output resistance of the source is equal to the load resistance. If this condition is not met, a matching switching regulator is switched on between the power supply and the load. Most often, for the purpose of matching, pulse regulators of step-up or step-down types are used.* ***Problem.*** *The operation of regulators in the matching mode has a number of features, in comparison with the modes of regulation and stabilization of the output voltage. Thus, since in the maximum power transmission mode the output resistance of the source and the resistance of the load are values of the same order, in any calculation the internal resistance of the source must be taken into account. There are works in which features of work of regulators of step-up and step-down types in a mode of transfer of the maximum power are analyzed. In addition to these types of pulse regulators, there are regulators of step-up/step-down types, which are relatively rarely used for this purpose. First of all it is connected with insufficiently studied abilities of work of such regulators in the specified mode.* ***Goal.*** *The aim of the work is to analyze the features of the operation of pulse regulators of step-up/step-down types in the mode of transmission of maximum power from the power supply to the load, as well as to determine the conditions under which it is possible and appropriate to work in this mode.* ***Methodology.*** *In the work, taking into account the internal resistance of the power supply, the regulation characteristics of the basic circuit of the pulse regulator of the step-up/step-down type are analyzed. The conditions under which the transfer of maximum power from the power supply to the load is ensured are determined.* ***Results.*** *It is shown that the existing variants of the circuits of regulators of the step-up/step-down type can be obtained from the basic circuit by applying the rules of construction of dual electric circuits. Consequently, the basic calculated relations for such circuits can be obtained from the calculated relations of the basic circuit using the principle of duality.* ***Originality.*** *A method for determining and studying the regulation characteristics of pulse regulators, taking into account the internal resistance of the power supply.* ***Practical value.*** *The obtained results allow to determine the conditions under which it is possible and expedient to operate different circuits of regulators in the mode of transmission of maximum power from the power supply to the load. Based on these results, recommendations are given for selecting a suitable range for changing the relative time of the closed state of the controlled switch, depending on the type of power supply used, as well as the method of connecting the controlled switch in the regulator circuit.* References 14, tables 3, figures 8.
Key words: **step-up/step-down regulator, regulation characteristics, maximum power transmission**.

З урахуванням внутрішнього опору джерела живлення проаналізовано регулювальні характеристики імпульсних регуляторів підвищувально-понижувального типу. Визначено умови, за яких забезпечується передавання максимальної потужності від джерела живлення до навантаження. Дано рекомендації щодо вибору доцільного діапазону зміни відносного часу замкненого стану керованого ключа регулятора , у залежності від типу джерело живлення, а також способу підключення керованого ключа в імпульсному регуляторі. Бібл. 14, табл. 3, рис. 8.
Ключові слова: **регулятор підвищувально-понижувального типу, регулювальні характеристики; передавання максимальної потужності.**

Introduction. DC pulse regulators (PRs) are traditionally used to regulate and stabilize the load voltage [1]. With the expansion of the use of non-traditional and renewable energy sources, there is a need to extract from them the maximum possible amount of electricity. As is known [2], the maximum power from the power supply to the load will be transmitted only if the output resistance of the source r is equal to the resistance of its load R. To ensure maximum power transmission in cases where $R \neq r$, between the source and load they connect the PR which matches the output resistance of the source with the resistance of its load. In the presence of the PR, the role of the load source R will be performed by its input resistance. This resistance depends on the load resistance of the regulator R_{LD} as well as the relative time of the closed (open) state of the controlled key t^*: $R = f(R_{LD}, t^*)$. By changing the parameter t^*, it is possible to ensure the condition $R = r$, i.e. the condition of transmitting maximum power from source to load R_{LD}.

In practice, for the purpose of coordination, up or down PRs are most often used [3-5]. The operation of regulators in the matching mode has a number of features compared to the mode of regulation and stabilization of the output voltage. In particular, since in the maximum power transmission mode the output source resistance and the load resistance are of the same order, the internal resistance of the source must be obligatory taken into account in any calculation. In the existing literature [1, 9], when determining the control characteristics of the PRs which operate in the mode of stabilization of the output voltage, it is believed that the internal resistance is much lower than the load resistance. Therefore, the internal resistance of the source is not taken into account. In addition, the internal resistance of the source will affect the coefficient of utilization of electrical energy of the source, and hence the overall efficiency of the system power supply – pulse regulator. In [6] the peculiarities of the operation of the up and down PR in the mode of transmission of maximum power from the power supply to the load are analyzed in detail. In addition to these types of PRs, there are step-up/step-down regulators [7-9] which are relatively rarely used for this purpose. This is primarily due to insufficient study of the features of such regulators in this mode.

The goal of the work is to analyze the features of the step-up/step-down PR in the mode of transmission of maximum power from the power supply to the load, and to determine the conditions under which it is possible and appropriate to operate in this mode.

Analysis of regulatory characteristics. The most important characteristics of any regulator are its regulatory characteristics. In the case of power supply from real sources of electrical energy, due to the presence of internal resistance, the regulatory characteristics will depend on the load resistance. In this regard, the properties of the regulator are described by a family of its regulatory characteristics which determine for different values of load the resistance R_{LD}. Let us analyze the regulatory characteristics of the classical circuit of the step-up/step-down PR (Fig. 1) [9].
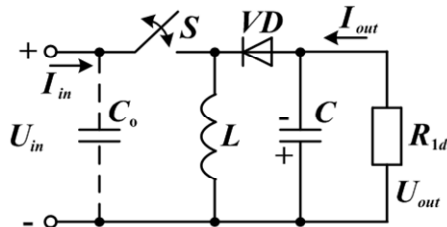
Fig. 1. Basic circuit of the step-up/step-down PR

For simplicity, we assume that the internal resistance of the source r is linear, and the losses in the PR elements are insignificant. To describe the regulatory characteristics, we will use relative values [9].

According to [10], the regulatory characteristic of the PR (Fig. 1) is described by this expression

$$U^* = \frac{t^*\left(1 - t^*\right)}{\left(1 - t^*\right)^2 + r^* t^*}, \quad (1)$$

where $U^* = U/U_{oc}$; $r^* = r/R_{LD}$; $t^* = t_{cl}/T$; U_{oc} is the source's no-load voltage; t_{cl} is the duration of the no-load state of the key S in the period T.

Figure 2 presents a family of regulatory characteristics for several fixed values of relative resistance r^*. The same graph shows the regulatory characteristic for the case of power supply from an ideal voltage source ($r^* = 0$). Let us analyze the obtained characteristics. For an ideal voltage source ($r^* = 0$), with increasing parameter t^* the output voltage U^* will increase indefinitely. In the case of real sources ($r^* \neq 0$), at $t^* = 0$ and $t^* = 1$, the output voltage will be zero, as there is no energy transfer from source to load. At a certain value of the parameter $t^* = t_m^*$, the output voltage, and hence the output power reaches the maximum value P_{max}. The question arises: does this mode of operation correspond to the mode of transmission of maximum power from source to load?
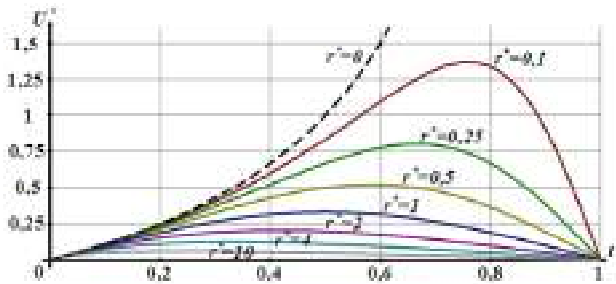
Fig. 2. Regulatory characteristics in the absence of the storage capacitor C_0

As is known [2], in the case of linear internal resistance of the source, its point of maximum power (PMP) has the coordinates $U_{MP}^* = 0.5$; $I_{MP}^* = 0.5$. Therefore, the maximum possible output power of such a source is $P_{MP}^* = U_{MP}^* \cdot I_{MP}^* = 0.25$. The output power of the regulator, at the point of maximum output voltage (Fig. 2), can be determined by the formula $P_{max}^* = U_{max}^{*2}/R_{LD}^* = U_{max}^{*2} \cdot r^*$. The test shows that for any value of the parameter r^* $P_{max}^* < P_{MP}^*$. Therefore, this circuit, for any value of the parameter r^*, does not provide the ability to transfer maximum power from source to load. This is due to the fact that energy is taken from the source only when the key S is closed, i.e. in discrete portions. If the key S is permanently closed ($t^* = 1$), the power supply will operate in short circuit mode, as a result of which energy from the source to the load will not be received. To ensure the continuity of energy extraction from the source, it is necessary to install a storage capacity C_0 of sufficient value at the input of the PR (Fig. 1). Due to the redistribution of currents, in the presence of C_0, the regulatory characteristic will be described by the following expression

$$U^* = \frac{t^*\left(1 - t^*\right)}{\left(1 - t^*\right)^2 + r^* t^{*2}}. \quad (2)$$

For this case, the graphs of the regulatory characteristics are presented in Fig. 3.
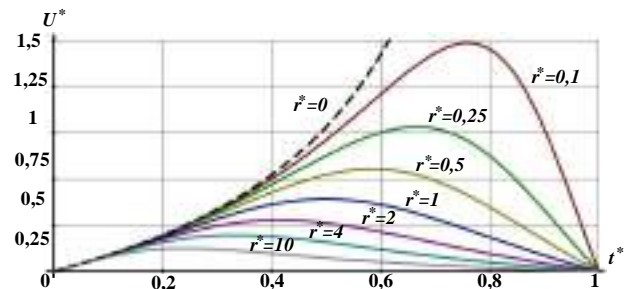
Fig. 3. Regulatory characteristics in the presence of the storage capacitor C_0

The test shows that the output power at the points of maximum output voltage of any of these graphs corresponds to the maximum output power of the source

$$P_{max}^* = P_{MP}^* = 0.25. \quad (3)$$

Therefore, in the presence of capacity C_0, the step-up/step-down regulator provides the possibility of transmission from the source to the load of the maximum possible power. To do this, it is necessary to provide a certain value of the parameter $t^* = t_{MP}^*$. Determine the conditions under which the maximum possible power will be transmitted from the source to the load.

As is known [9], the input and output parameters of the step-up/step-down PR (Fig. 1) are related by the relationships

$$U_{out}^* = U_{in}^* \cdot \frac{t^*}{1 - t^*}; \quad I_{out}^* = I_{in}^* \cdot \frac{1 - t^*}{t^*}. \quad (4)$$

Taking into account that at the linear internal resistance of the source, its output voltage and output current in the PMP $U_{MP}^* = 0.5$; $I_{MP}^* = 0.5$, we can write that in the case of the source operation in the PMP the output voltage and current of the PR

$$U_{out}^* = 0.5 \cdot \frac{t^*}{1 - t^*}; \quad I_{out}^* = 0.5 \cdot \frac{1 - t^*}{t^*}. \quad (5)$$

On the other hand, $U_{out}^* = I_{out}^* R_{LD}^*$, i.e.

$$U_{out}^* = 0.5 \cdot \frac{1 - t^*}{t^*} R_{LD}^*. \quad (6)$$

Equating (5) and (6) we obtain

$$0.5 \cdot \frac{t^*}{1 - t^*} = 0.5 \cdot \frac{1 - t^*}{t^*} R_{LD}^*$$

or

$$t^{*2} / R_{LD}^* = t^{*2} r^* = (1 - t^*)^2. \quad (7)$$

Therefore, the parameter t_{MP}^* can be determined by solving such a quadratic equation

$$t^{*2}(r^* - 1) + 2t^* - 1 = 0. \quad (8)$$

This equation has two roots

$$t_1^* = \frac{\sqrt{r^*} - 1}{r^* - 1}; \quad t_2^* = \frac{1 + \sqrt{r^*}}{1 - r^*}. \quad (9)$$

Taking into account the physical meaning of the parameter t^* we come to the conclusion that only the root t_1^* will be valid, i.e.

$$t_{MP}^* = \frac{\sqrt{r^*} - 1}{r^* - 1}. \quad (10)$$

Table 1 shows the calculated numerical values of the parameter t_{MP}^* for different values of relative resistance r^*. The numerical value for the case $r^* = 1$ is obtained by revealing the uncertainty of the form 0/0.

The results presented in Table 1 are confirmed by the graphs in Fig. 3. Thus, at the PR input (Fig. 1) a storage capacity C_0 of sufficient value is installed, this regulator, in contrast to the up or down PR [6], provides the ability to extract from the power supply maximum power, theoretically, at any value of the load resistance of the regulator R_{LD}.

Table 1

Dependence of the parameter t_{MP}^* on the resistance r^*

r^*	0,05	0,1	0,25	0,5	0,8	1
t_{MP}^*	0,84	0,77	0,67	0,58	0,53	0,5
r^*	1,25	2	4	10	20	
t_{MP}^*	0,48	0,41	0,33	0,24	0,19	

In [6] it is shown that the electric circuits that form the up and down PRs are dual. This, in particular, explains the similarity of their parameters and characteristics. If we apply the principles of construction of dual electrical circuits to the circuit of the considered PR (Fig. 1), we obtain the circuit of the PR shown in Fig. 4, which is well known as the Ćuk circuit [9, 11, 12].
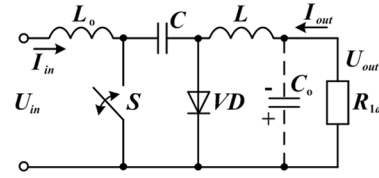
Fig. 4. Step-up/step-down regulator according to Ćuk circuit

Taking into account the principle of duality, the following relations are valid for it

$$U_{out}^* = U_{in}^* \cdot \frac{1 - t^*}{t^*}, \quad I_{out}^* = I_{in}^* \cdot \frac{t^*}{1 - t^*}, \quad (11)$$

where $t^* = t_{OP}/T$, where t_{OP} is the duration of the open state of the key S for the period T.

Similar to the previous circuits, it can be shown that its regulatory characteristic for the output voltage will look like

$$U_{out}^* = U_{in}^* \cdot \frac{t^*(1 - t^*)}{r^*(1 - t^*) + t^{*2}}. \quad (12)$$

Taking into account that for dual circuits the parameter r^* is analogous to the parameter $R_{LD}^* = R_{LD} / r = 1 / r^*$, it can be argued that this circuit will take the maximum power from the source, provided that

$$t^* = t_{MP}^* = \frac{\sqrt{R_{LD}^*} - 1}{R_{LD}^* - 1}. \quad (13)$$

Table 2 shows the calculated numerical values of the parameter t_{MP}^* for different values of relative resistance $r^* = 1 / R_{LD}^*$.

Table 2

Dependence of the parameter t_{MP}^* on the resistance r^* for Ćuk circuit

r^*	0,05	0,1	0,25	0,5	0,8	1
t_{MP}^*	0,19	0,24	0,33	0,41	0,48	0,5
r^*	1,25	2	4	10	20	
t_{MP}^*	0,53	0,58	0,67	0,77	0,84	

Figure 5 shows graphs of the dependence $t_{MP}^* = f(r^*)$ for the PRs the circuit of which is shown in Fig. 1, 4.
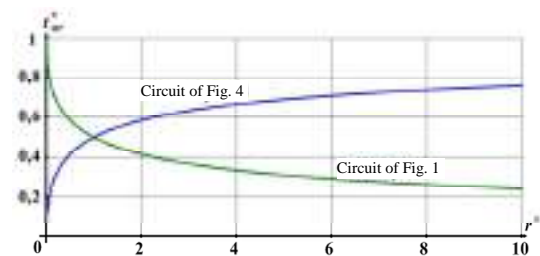
Fig. 5. Dependence of the parameter t_{MP}^* on the resistance r^*

These graphs are a mirror image of each other relative to the corresponding lines which corresponds to $t_{MP}^* = 0.5$. Figure 6 presents graphs of the regulatory characteristics of the regulator (Fig. 4) for different values

of the parameter r^* which confirm the results presented in Table 2.
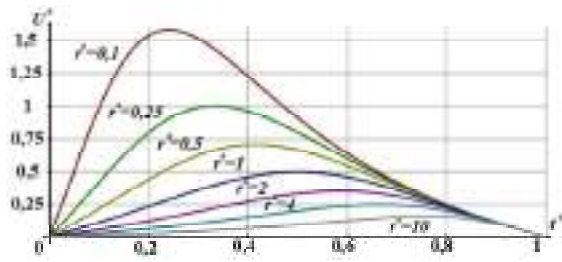
Fig. 6. Regulatory characteristics of Ćuk circuit

Thus, both of these circuits provide the ability to take the maximum power from the power supply, theoretically, at any value of load resistance R_{LD}.

Recommended regulatory ranges. In accordance with the regulatory characteristics (Fig. 3, 6), the output voltage of the regulators reaches its maximum value U_{max}^* provided that $t^* = t_{MP}^*$. The output voltage $U_{out}^* < U_{max}^*$ can be obtained at two different values of the parameter t^*, one of which is greater than t_{MP}^* and the other less. In such cases, as shown in [6], when choosing the regulatory range, it is advisable to take into account the coefficient of utilization of electrical energy of the power supply η.

If the power supply is a voltage source, taking into account (11), the dependence $\eta = f(t^*)$ for the PR (Fig. 4) will look like

$$\eta = U^* = U_{in}^* = U_{out}^* \frac{t^*}{1-t^*}. \tag{14}$$

Therefore, with increasing parameter t^*, η will increase. Therefore, in the case of power supply from the voltage source, it is advisable to change the parameter t^* in the range $t_{MP}^*...1$. If the power supply is a current source, the dependence $\eta = f(t^*)$ for the same circuit will look like

$$\eta = I^* = I_{in}^* = I_{out}^* \frac{1-t^*}{t^*}. \tag{15}$$

Taking into account that $I_{out}^* = U_{out}^* / R_{LD}^* = U_{out}^* r^*$, we obtain that

$$\eta = U_{out}^* r^* \frac{1-t^*}{t^*}.$$

Thus, in the case of power supply from the current source, it is advisable to change the parameter t^* in the range $0...t_{MP}^*$. In addition, the energy efficiency of the source will increase with increasing r^*, i.e. with decreasing load resistance R_{LD}.

Taking into account the duality of the circuits of the considered regulators, we conclude that for the PR (Fig. 1) the recommendations will be the opposite. The analysis of the obtained results, as well as the results presented in [6], shows that to select the appropriate range of regulation of the parameter t^*, it is necessary to take into account two factors:

1) type of electricity source;
2) method of connecting the controlled key S to the RP, relative to the power supply and load.

Table 3 shows the recommended control ranges of the parameter t^*, depending on the type of power supply and the method of connecting the controlled switch S. In practice, this is not always convenient. Therefore, variants of these circuits have been developed in which the polarity of the output voltage coincides with the polarity of the input voltage.

Table 3
Recommended ranges of parameter t^* regulation

Key Scheme		
	$0...t_{MP}^*$	$t_{MP}^*...1$
	$t_{MP}^*...1$	$0...t_{MP}^*$

They are known as ZETA converter (Fig. 7) and SEPIC converter (Fig. 8) [13, 14].
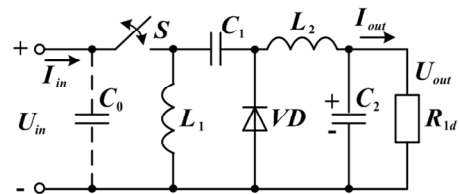
Fig. 7. Regulator type ZETA
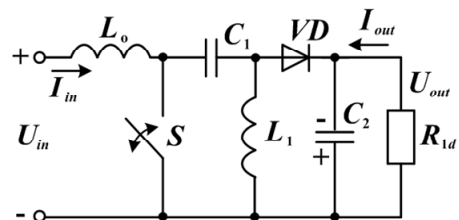
Fig. 8. Regulator type SEPIC

The circuits of these regulators differ from the considered basic circuits (Fig. 1, 4) by the method of construction of the *output* circuit, as well as the presence of additional reactive elements. However, since the most important properties of the regulator are determined by the method of construction of its input circuit, in particular the method of connecting the controlled switch S, the results obtained for the Buck-Boost regulator (Fig. 1) will be valid for the controller type ZETA (Fig. 1) will be valid for the regulator type ZETA (Fig. 7), and the results obtained for the Ćuk regulator (Fig. 4) will be valid for the SEPIC regulator (Fig. 8). In particular, to ensure the possibility of extracting the maximum power from the power supply, capacitor C_0 of sufficient capacity must be installed at the input of the ZETA type regulator (Fig. 7).

Conclusions.

1. Pulse regulators circuits with serial (parallel) connection of the controlled switch S provide the possibility of taking the maximum power from the power supply only if there is a storage capacity C_0 (inductance L_0) at their input.

2. Step-up/step-down pulse regulators provide the ability to take the maximum power from the power supply to the load for almost any value of load resistance R_{LD}.

3. The appropriate range of regulation of the parameter t^* is selected taking into account the type of power supply, as well as the method of connecting the controlled key in the pulse regulator.

Conflict of interest. The authors of the article state that there is no conflict of interest.

REFERENCES
1. Severns R., Blum G. *Impul'snye preobrazovateli postoiannogo napriazheniia dlia sistem vtorichnogo elektropitaniia* [Switching DC voltage converters for secondary power supply systems]. Moscow, Energoatomizdat Publ., 1988. 294 p. (Rus).
2. Bessonov L.A. *Teoreticheskiye osnovy elektrotekhniki. V 2 t. Tom 1. Elektricheskiye tsepi: uchebnik dlya vuzov* [Theoretical Foundations of Electrical Engineering. In 2 vols. Vol. 1. Electric circuits: textbook for universities]. Moscow, Yurayt Publ. House, 2021. 831 p. (Rus).
3. Olalla C., Clement D., Rodriguez M., Maksimovic D. Architectures and Control of Submodule Integrated DC–DC Converters for Photovoltaic Applications. *IEEE Transactions on Power Electronics*, 2013, vol. 28, no. 6, pp. 2980-2997. doi: https://doi.org/10.1109/TPEL.2012.2219073.
4. Anandhi T.S., PremKumar S. Application of DC-DC boost converter for solar powered traffic light with battery backup. *Indian Journal of Science and Technology*, 2015, vol. 8, no. 32, pp. 1-5. doi: https://doi.org/10.17485/ijst/2015/v8i32/84408.
5. Tseng S.-Y., Wang H.-Y. A Photovoltaic Power System Using a High Step-up Converter for DC Load Applications. *Energies*, 2013, vol. 6, pp. 1068-1100. doi: https://doi.org/10.3390/en6021068.
6. Batrak L.M., Romashko V.Y. Switching Regulators Features in the Matching Mode Operation. *Microsystems, Electronics and Acoustics*, 2021, vol. 26, no. 1, pp. 232833–1. doi: https://doi.org/10.20535/2523-4455.mea.232833. (Ukr).
7. Dinniyah F.S., Wahab W., Alif M. (2017). Simulation of Buck-Boost Converter for Solar Panels using PID Controller. *Energy Procedia*, 2017, vol. 115, pp. 102-113. doi: https://doi.org/10.1016/j.egypro.2017.05.011.
8. Shayeghi H., Pourjafar S., Sedaghati F. A Buck-Boost Converter; Design, Analysis and Implementation Suggested for Renewable. Energy Systems. *Iranian Journal of Electrical and Electronic Engineering*, 2021, vol. 17, no. 2, pp. 1862-1862. doi: https://doi.org/10.22068/IJEEE.17.2.1862.
9. Goncharov Y.P., Budonny O.V., Morozov V.G., Panasenko M.V, Romashko V.Y., Rudenko V.S. *Peretovyuvalna technicala. Navchalnyi posibnyk. Chastyna 2* [Power conversion equipment. Text book. Part 2]. Kharkiv, Folio Publ., 2000. 360 p. (Ukr).
10. Romashko V.Y. Regulation characteristics of switching regulators with taking into account the internal resistance of power supply. *Microsystems, Electronics and Acoustics,* 2017, vol. 22, no. 6, p 29-34. doi: https://doi.org/10.20535/2523-4455.2017.22.6.81414. (Ukr).
11. Garza J.G., Chong B., Zhang L. Control of integrated Ćuk converter and photovoltaic modules for maximum power generation. *2012 3rd IEEE International Symposium on Power Electronics for Distributed Generation Systems (PEDG)*, 2012, pp. 175-181. doi: https://doi.org/10.1109/PEDG.2012.6253997.
12. Khan H.R., Kazmi M., Ashraf H.B., Hashir Bin Khalid M., Hasan A., Qazi S.A. An Isolated Power Factor Corrected Cuk Converter with Integrated Magnetics for Brushless DC Ceiling Fan Applications. *Electronics*, 2021, vol. 10, no. 14, p. 1720. doi: https://doi.org/10.3390/electronics10141720.
13. Soedibyo, Amri B., Ashari M. The comparative study of Buck-boost, Cuk, Sepic and Zeta converters for maximum power point tracking photovoltaic using P&O method. *2015 2nd International Conference on Information Technology, Computer, and Electrical Engineering (ICITACEE)*, 2015, pp. 327-332. doi: https://doi.org/10.1109/ICITACEE.2015.7437823.
14. Fakirrao T. Chavan, Shrikant S. Mopari, Panchayya S. Swami. Performance Analysis Of SEPIC And Zeta Converter For Power Quality Improvement. *International Journal of Scientific & Technology Research*, 2019, vol. 8, no. 12, pp. 1925-1929. Available at: http://www.ijstr.org/final-print/dec2019/Performance-Analysis-Of-Sepic-And-Zeta-Converter-For-Power-Quality-Improvement.pdf (Accessed 22 August 2021).

V.Y. Romashko[1]*, Doctor of Technical Science, Professor,*
L.M. Batrak[1]*, PhD, Associate Professor,*
O.O. Abakumova[1]*, PhD, Associate Professor,*
[1] National Technical University of Ukraine
«Igor Sikorsky Kyiv Polytechnic Institute»,
37, Prospect Peremohy, Kyiv-56, 03056, Ukraine,
e-mail: rv790593-eds@lll.kpi.ua;
batrakln5@gmail.com (Corresponding author);
e.o.abakumova@gmail.com

H. Saeed, T. Mehmood, F.A. Khan, M.S. Shah, M.F. Ullah, H. Ali

An improved search ability of particle swarm optimization algorithm for tracking maximum power point under shading conditions

*Introduction. Extracting maximum possible power from solar energy is a hot topic of the day as other sources have become costly and lead to pollution. **Problem.** Dependency on sunlight for power generation makes it unfeasible to extract maximum power. Environmental conditions like shading, partial shading and weak shading are the major aspect due to which the output of photovoltaic systems is greatly affected. Partial shading is the most known issue. **Goal.** There have been many proposed techniques and algorithms to extract maximum output from solar resources by use of photovoltaic arrays but every technique has had some shortcomings that couldn't serve the complete purpose. **Methodology.** Nature inspired algorithms have proven to be good to search global maximum in a partially shaded multipeak curve which includes particle swarm optimization, artificial bee colony algorithm, and flower pollination algorithm. **Methods.** Particle swarm optimization algorithm is best among these in finding global peaks with less oscillation around maximum power point, less complexity, and easy to implement nature. Particle swarm optimization algorithm has the disadvantage of having a long computational time and converging speed, particularly under strong shading conditions. **Originality.** In this paper, an improved opposition based particle swarm optimization algorithm is proposed to track the global maximum power point of a solar photovoltaic module. Simulation studies have been carried out in MATLAB/Simulink R2018a. **Practical value.** Simulation studies have proved that opposition based particle swarm optimization algorithm is more efficient, less complex, more robust, and more flexible and has better convergence speed than particle swarm optimization algorithm, perturb and observe algorithm, hill climbing algorithm, and incremental conductance algorithm.* References 24, tables 4, figures 12.
Key words: **conventional particle swarm optimization, maximum power point, opposition based particle swarm optimization algorithm.**

*Вступ. Отримання максимально можливої потужності із сонячної енергії є надзвичайно актуальним наразі, оскільки інші джерела енергії стали коштовними та призводять до забруднення. **Проблема.** Залежність від сонячного світла для вироблення електроенергії унеможливлює отримання максимальної потужності. Умови навколишнього середовища, такі як затінення, часткове затінення і слабке затінення, є основним аспектом, від якого сильно залежить потужність фотоелектричних систем. Часткове затінення – найвідоміша проблема. **Мета.** Було запропоновано багато методів та алгоритмів для отримання максимальної віддачі від сонячних ресурсів за допомогою фотоелектричних батарей, але кожен метод мав деякі недоліки, які не могли служити досягненню повної мети. **Методологія.** Алгоритми, натхненні природою, виявилися хорошими для пошуку глобального максимуму на частково затіненій кривій з багатьма піками, включаючи оптимізацію рою частинок, алгоритм штучної бджолиної колонії та алгоритм запилення квітів. **Методи.** Алгоритм оптимізації рою частинок найкраще підходить для пошуку глобальних піків з меншими коливаннями навколо точки максимальної потужності, меншою складністю та простотою реалізації. Алгоритм оптимізації рою частинок має недолік, що полягає у тривалому часі обчислень та швидкості збіжності, особливо в умовах сильного затінення. **Оригінальність.** У цій статті пропонується покращений алгоритм оптимізації рою частинок на основі протилежності для відстеження глобальної точки максимальної потужності сонячного фотоелектричного модуля. Розрахункові моделювання проводились у MATLAB/Simulink R2018a. **Практична цінність.** Дослідження за допомогою моделювання довели, що алгоритм оптимізації рою частинок на основі протилежності є більш ефективним, менш складним, надійнішим і гнучкішим і має кращу швидкість збіжності, ніж алгоритм оптимізації рою частинок, алгоритм збурення та спостереження, алгоритм сходження на пагорб та алгоритм інкрементальної провідності.* Бібл. 24, табл. 4, рис. 12.
Ключові слова: **традиційна оптимізація рою частинок, точка максимальної потужності, алгоритм оптимізації рою частинок на основі протилежності.**

Abbreviations

ABC	Artificial Bee Colony	OBL	Opposition Based Learning
FPA	Flower Pollination Algorithm	P&O	Perturb and Observe Algorithm
GMPP	Global Maximum Power Point	PSC	Partial Shading Conditions
IC	Incremental Conductance Algorithm	PSO	Particle Swarm Optimization
IPSO	Improved Particle Swarm Optimization	PSO-OBL	Opposition Based Particle Swarm Optimization Algorithm
MPP	Maximum Power Point	PV	Photovoltaic
MPPT	Maximum Power Point Tracking	PWM	Pulse-Width Modulation

1. Introduction. With increasing demand of renewable source of energy, solar energy is getting more and more attention because of its easy and never ending availability. But operating PV panel at MPPT is a challenging task. So accomplishing this task can make use of PV panels very effective and it will largely reduce the use of non-renewable sources which will have such a huge impact on mankind's lifestyle that it can save a huge amount of money and world resources. However high installation cost and getting lower efficiency are still the challenges that are faced nowadays by researchers [1, 2]. Solar energy plays a vital role in the development of a country. Compared to other renewable sources solar energy generation shows a significantly more dynamic development. Research studies shows that the installed capacity of solar power plants in 2016 was 315 GW [3-6]. For extracting MPPT, there are face several challenges such as temperature and irradiance affects the P-V characteristics of photovoltaic cell. For delivering maximum power to load several conventional algorithms were to tackle MPPT. For instance P&O MPPT method [7], IC MPPT method [8], modified hill climbing method [9], frictional short-circuit current approach [10], ripple correlation control method [11] and sliding mode controller [12] were used. The specialty of these

algorithms is that these give good response for uniform irradiance of solar panel but under PSC these algorithms fails to track the global MPPT.

Goal. This paper present a hybrid technique used to track global max power point very efficiently by using improved particle swarm optimization algorithm. For improving search ability of PSO algorithm, PSO is hybridized with OBL [13], for getting high tracking efficiency, convergence speed and power output. PSO is an outstanding choice for problems of nature of non-linear optimization [14]. To check the robustness of this hybrid techniques, two different PV configurations of are employed.

The PV system consists of PV panels, MPPT controller, DC-DC converter and load (Fig. 1). The output of the PV panels is fed to the converter as well as to the controller. The controller uses its input to regulate the duty cycle of the converter for maximum power point operation.
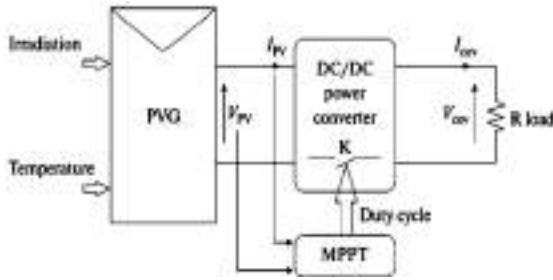
Fig. 1. Block diagram of PV system

This paper is organized as follows. In Section 2 there is description of P-V characteristics under PSC. In Section 3 methodology is describe. In Section 4 test system is presented while in Section 5 simulation results are discussed. In Section 6, comparison is discussed and paper is concluded in Section 7.

2. PV cell's modeling with single-diode equivalent circuit.

2.1. Characteristics of solar cell. Equivalent circuit of PV cell is shown in the Fig. 2 and the output in the form of current is given by:

$$I_{pv} = I_{ph} - I_0 \cdot \left[\exp\left(\frac{q \cdot \left(U_{pv} + I \cdot R_S \right)}{A \cdot K \cdot T} \right) - 1 \right] - \frac{U_{pv} - I \cdot R_S}{R_P}, \quad (1)$$

where I_{pv} is the output current of cell; I_{ph} is the photocurrent; I_0 is the reverse saturation current; q is the charge of an electron; U_{pv} is the work voltage of a PV cell; K is the Boltzmann constant; A is the ideality factor; R_S and R_P are the series and parallel resistances; T is the cell temperature [15].

The different parameters of proposed PV module are shown in Table 1.
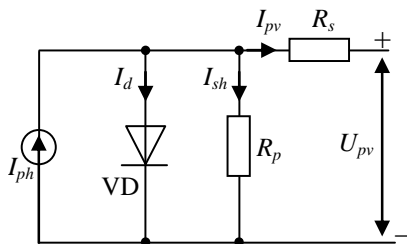
Fig. 2. Single-diode equivalent circuit of PV cell

Table 1
Parameters of Sun Earth Solar Power TPZ250MBZ PV 250 W

Parameters	Variables	Values
Maximum power	P_{MPP}	250 W
Open circuit voltage	V_{oc}	30 V
Short circuit current	I_{sc}	8.3 A
Current of P_{max}	I_{MPP}	8.83 A
Voltage of P_{max}	V_{MPP}	36.8 V
I_{sc} coefficient of temperature	K_I	(0.065±0.015)%/°C
V_{oc} coefficient of temperature	K_V	–(0.32±0.05)%/°C

2.2. Effect of PSC on PV characteristics. In this paper, two different PV configurations are used to check the robustness of proposed technique. The first configuration is 4S2P, which consists of 8 PV modules. Four modules are organized in one string with power of 249 W. The overall power extracted is 1992 W. Second configuration is 3S1P, which consists of 3 PV modules that are arranged in one string. The overall power extracted by second configuration is 747 W [16]. Power extracted by different pattern of PSC is shown in Table 2. The PV configuration (4S2P) proposed in this paper is shown in Fig. 3.

Table 2
Different patterns of 3S1P and 4S2P configurations

4S2P-configuration			3S1P-configuration	
Pattern 1	G11=1 kW·m⁻²	G21=1 kW·m⁻²	Pattern 3	G1= 1 kW·m⁻²
	G12=1 kW·m⁻²	G22=1 kW·m⁻²		G2= 1 kW·m⁻²
	G13=1 kW·m⁻²	G23=1 kW·m⁻²		G3= 1 kW·m⁻²
	G14=1 kW·m⁻²	G24=1 kW·m⁻²		
Pattern 2	G11=1 kW·m⁻²	G21=1 kW·m⁻²	Pattern 4	G1= 1 kW·m⁻²
	G12=900 W·m⁻²	G22=800 W·m⁻²		G2= 900 W·m⁻²
	G13=600 W·m⁻²	G23=700 W·m⁻²		G3= 900 W·m⁻²
	G14=500 W·m⁻²	G24=1 kW·m⁻²		
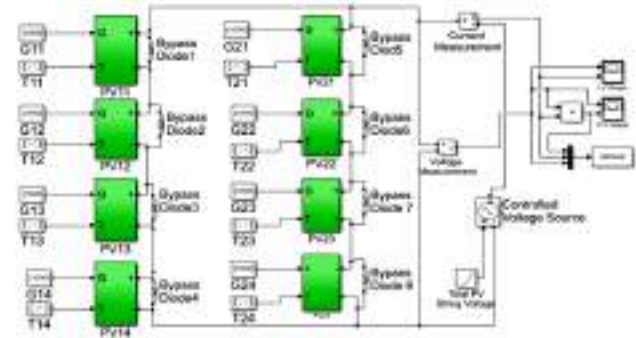
Fig. 3. Proposed PV configuration (4S2P)

3. Methodology.

3.1. PSO algorithm. PSO is an outstanding choice for problems of nature of non-linear optimization. PSO method is inspired by the behavior of swarms, insects and flocks [17]. In the previous decade, PSO is mostly the utmost favored optimization method for MPPT applications. In PSO, the initial particles (duty cycles) are chosen randomly in domain of the bounding limits. These particles are spread in whole search domain. The best among them in each iteration is known to be $P_{\_best}$ and the finest in all repetitions is recognized as $G_{\_best}$. Further, position and velocity of the particles/units are modified in each repetition and the

procedure keeps continuing till it reaches the best position. The motion of PSO particles in arbitrary search domain space are demonstrated in Fig. 4. The velocity and position updates are provided in:

$$X_i^{t+1} = X_i^t + V_i^{t+1};\qquad (2)$$

$$V_i^{t+1} = W \cdot V_i^t + 1 + C_1 \cdot r_1 \cdot \left(P_{besti}^{t+1} - X_i^t\right) + C_2 \cdot r_2 \cdot \left(G_{besti}^{t+1} - X_i^t\right),\quad(3)$$

where W is the inertial weight; X is the position; V is the velocity; C_1 and C_2 are the inertia constants; t is the iteration count.

Equation (4) represents fitness function:

$$P\left(D_i^k\right) > P\left(D_i^{k-1}\right).\qquad (4)$$

Fig. 4. Flowchart of the PSO algorithm

3.2. Opposition Based Learning (OBL). In 2005 Tizhoosh proposed the OBL technique [18] in the field of machine learning. He found that it is easier to find global maxima through opposite solution rather than random solutions and it is 50 % highly probable than original random solutions. OBL produces opposite solutions of original random solutions in each iteration and finds the fitness value of every solution and it is opposite. The one with the lower fitness is retained and other is discarded. The best among current solution space is selected and its opposite is sent to next iteration. This opposition based technique can increase the random search ability of random search methods. It has been used in PSO [19] and differential evolution algorithm [20] to improve their random search domain. The opposite point is defined as follow. Let $q(x_1, x_2, \ldots, x_n)$ is a point in an n-dimensional space, $x_1, x_2, \ldots, x_n \in R$, $x_i \in [a_i, b_i]$. The opposite point $q^*(x_1^*, x_2^* \ldots x_n^*)$ of q is defined as

$$x_i^* = a_i + b_i - x_{ii} = 1 \ldots n .\qquad (5)$$

The opposition based optimization is defined as follow. Let $q(x_1, x_2, \ldots, x_n)$ is a point in n-dimensional space and $q^*(x_1^*, x_2^* \ldots x_n^*)$ is its opposite. For objective fitness function $f(q)$, if $f(q^*) < f(q)q^*$ is kept otherwise q is kept unchanged.

3.3. PSO with OBL. PSO algorithm was presented by Eberhart R. and Kennedy J. in 1995 [21] and is based on the behavior of folk of birds. The present state of a particles that are in continues movement in the possible solution space is described by two variables, the position x_j and the velocity of movement v_j. The state of each particle in n-dimensional solution space, is determined by the position vector $X_j = [x_{j1}, x_{j2}, \ldots, x_{jN}]$ and velocity vector $V_j = [v_{j1}, v_{j2}, \ldots, v_{jN}]$. At the start, the particles are dispersed randomly over the whole possible solution space. Its implementation in PSO is depicted in Fig. 5.

Fig. 5. Particle swarm optimization hybridized with opposition based learning

4. Test systems. Simulation studies for different cases of the PSO and PSO-OBL techniques have been carried out in MATLAB/Simulink R2018a. The system proposed for simulations is shown in Fig. 6. PV module is used followed by a DC-DC buck converter and load. MPPT block is consisting of an MPPT controller and PWM generator. Current and voltage from PV module are presented as input to MPPT controller which produces duty cycles accordingly to run DC-DC converter.

Fig. 6. Proposed system for PV using PSO algorithm

In Fig. 7 PV array configuration of 3S1P is shown, in which a single rail of three series connected modules in used to check partial shading effect.

Fig. 7. 3S1P configuration of PV panel array

Fig. 8. 4S2P configuration of PV panel array

Different cases of partial shading considered for 3S1P are shown in Table 2. Three different modules are given separate values of irradiance and their output P-D curve is generated which generates a 3-peaks curve corresponding to values of irradiance being given as an input. Similarly, 4S2P is shown in Fig. 8 and its different cases for partial shading are shown in Table 2.

5. Simulation results.

5.1. Simulation results of PSO and PSO-OBL for 4S2P configuration. Figures 9, 10 show simulation

results of 4S2P configuration for PSO-OBL in different cases of partial shading as shown in Table 2. The number of iterations used for PSO is 25 while number of iterations used for PSO-OBL is 100 which helps creating opposite candidate solutions and effectively tracks GMPP.

5.1.1. Results of pattern no. 1. In pattern no. 1 the rated power is 1992 W and the power extracted from simulation is also 1992 W. The calculated results show that tracking efficiency will be 100 % and the convergence speed will be 1.021. The P-V curve of rated power and extracted power is shown in Fig. 9.
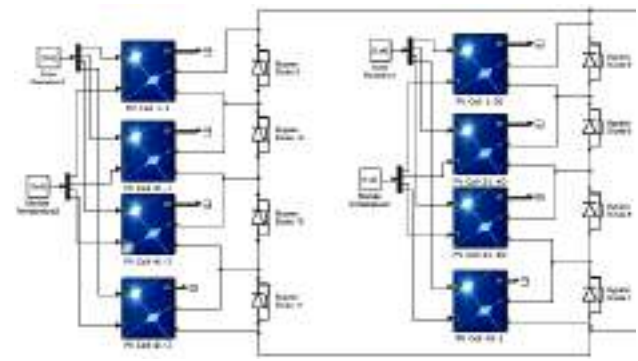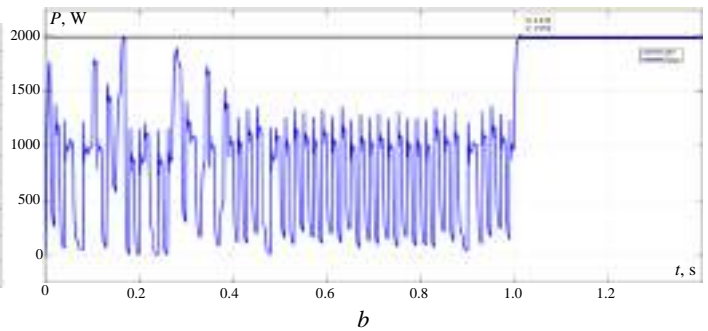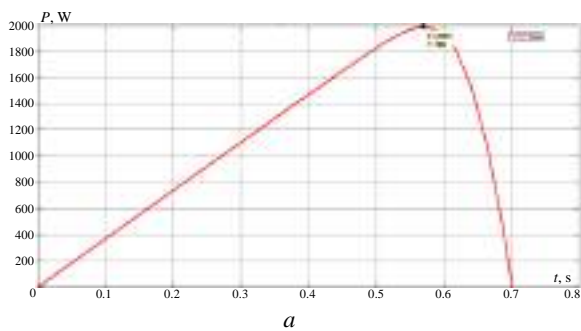
Fig. 9. 4S2P pattern no. 1: *a* – characteristic curve; *b* – P-V curve using PSO-OBL

5.1.2. Results of pattern no. 2. In pattern no. 2 the rated power is 1321 W and the power extracted from simulation is 1320 W. The calculated results show that

tracking efficiency will be 99.81 % and the convergence speed will be 1.008. The P-V curve of rated power and extracted power is shown in Fig. 10.
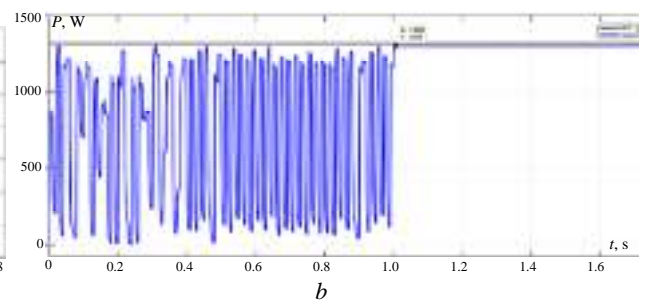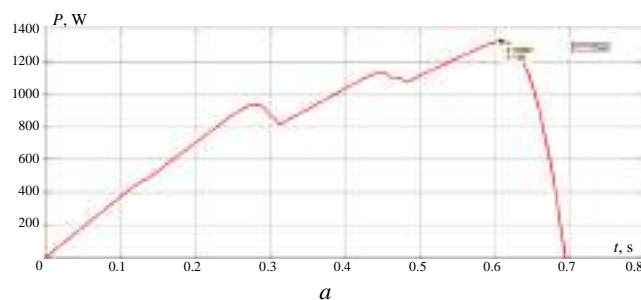
Fig. 10. 4S2P pattern no. 2: *a* – characteristic curve; *b* – P-V curve using PSO-OBL

5.2. Simulation results of PSO for 3S1P configuration. The parent technique (PSO) implementation for 3s1p has shown promising results as agreeing with work [22]. The characteristic curves for different patterns of 3S1P and corresponding P-V curves using PSO are shown in Fig. 11, 12.

5.2.1. Results of pattern no. 3. In pattern no. 3 the rated power is 747 W and the power extracted from simulation is also 747 W. The calculated results show that

tracking efficiency will be 100 % and the convergence speed will be 1.01. The P-V curve of rated power and extracted power is shown in Fig. 11.

5.2.2. Results of pattern no. 4. In pattern no. 4 the rated power is 688.2 W and the power extracted from simulation is 688 W. The calculated results show that tracking efficiency will be 100 % and the convergence speed will be 1.015. The P-V curve of rated power and extracted power are shown in Fig. 12.
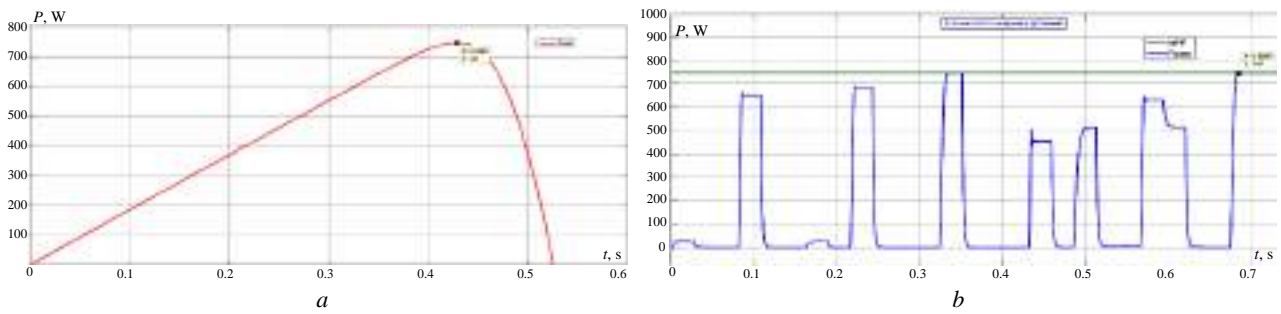
Fig. 11. 3S1P pattern no. 3: *a* – characteristic curve; *b* – P-V curve using PSO
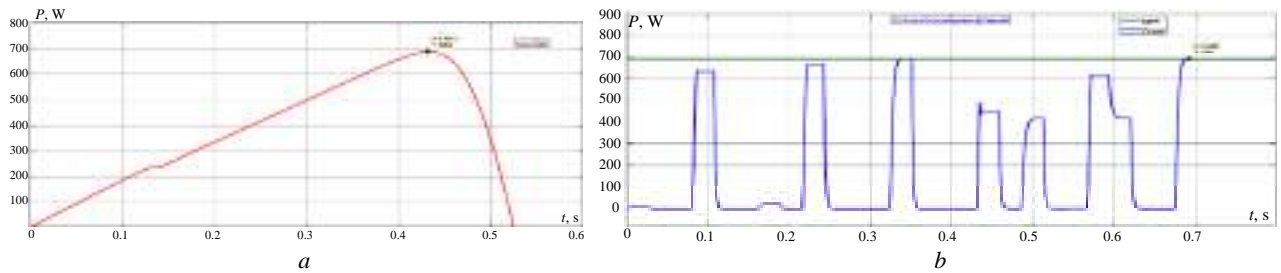
Fig. 12. 3S1P pattern no. 4: *a* – characteristic curve; *b* – P-V curve using PSO

6. Comparison among PSO and PSO-OBL. After performing simulation studies of PSO and PSO-OBL, one can see the clear improved efficiency and effective tracking of GMPP in less t/n ratio (where t/n is the maximum amount of time (or, more specifically, steps) that a function takes to run). This proves that PSO-OBL is better in all conditions as compared to PSO because PSO doesn't perform as well as PSO-OBL and especially when it comes to strong shading PSO-OBL totally outperforms PSO and proves itself to be best to use as MPPT algorithm in all environmental conditions. Tables 3, 4 provide the comparison of both the techniques.

Table 3

Comparison of both techniques

Configuration	Case	Algorithm	t/n	Power	Rated power	Convergence speed	Oscillations at GMPP	Efficiency	BEST algorithm
4S2P	Pattern 1	PSO	0.027	1992	1992	0.6826	0	100	PSO-OBL
		PSO-OBL	0.010	1992		1.021	0	100	
	Pattern 2	PSO	0.027	1317.5	1321	0.6769	0	99.73	PSO-OBL
		PSO-OBL	0.010	1320		1.008	0	99.81	
3S1P	Pattern 3	PSO	0.027	743.1	747	0.6917	0	99.72	PSO-OBL
		PSO-OBL	0.010	747		1.01	0	100	
	Pattern 4	PSO	0.027	688	688.2	0.6811	0	99.97	PSO-OBL
		PSO-OBL	0.010	688		1.015	0	99.97	

Table 4

Comparison of parameters of P&O, IC, PSO and PSO-OBL

Algorithm	Steady state oscillations	Falling to local maximums	Complexity
P&O	✓	✓	✓
IC	✓	✓	✓
PSO	×	×	Less complex
PSO-OBL	×	×	Less complex

7. Conclusions. Environmental conditions limit the functionality of photovoltaic module. A lot of methods have been proposed in literature to address this problem but it never achieved goal due to number of reasons. Partial shading is most known issue. Nature inspired algorithms have proven them to be good to search global maximum in a partially shaded multipeak curve which includes particle swarm optimization, artificial bee colony, flower pollination algorithm etc. Particle swarm optimization is best among these in finding global peak with less oscillation around maximum power point, less complexity and easy to implement nature. Particle swarm optimization has disadvantage of having long computational time and converging speed particularly under strong shading conditions. In this paper, hybrid technique is used to track global max power point very efficiently by using improved particle swarm optimization algorithm. This technique is effective in all shading conditions. Simulation results shows that opposition based particle swarm optimization algorithm is less complex, more efficient, robust, flexible and have better convergence speed than particle swarm optimization and other techniques. Since shading is an unpredictable process so to predict the accuracy and to expect a 100 % output is still an uncertain thing. The increasing demand of energy and ever increasing advancement in technology is making more and more space to bring improvement to maximum power point tracking as well as the improve the transient response of the system [23, 24]. So power extraction with more accuracy in less amount of time is still a scope.

Conflict of interest. The authors declare that they have no conflicts of interest.

REFERENCES

1. Ullah M.F., Hanif A. Power quality improvement in distribution system using distribution static compensator with super twisting sliding mode control. *International Transactions on Electrical Energy Systems*, 2021, vol. 31, no. 9, art. no. e12997 doi: https://doi.org/10.1002/2050-7038.12997.

2. Akbar F., Mehmood T., Sadiq K., Ullah M.F. Optimization of accurate estimation of single diode solar photovoltaic parameters and extraction of maximum power point under different conditions. *Electrical Engineering & Electromechanics*, 2021, no. 6, pp. 46-53. doi: https://doi.org/10.20998/2074-272X.2021.6.07.

3. Hosenuzzaman M., Rahim N.A., Selvaraj J., Hasanuzzaman M., Malek A.B.M.A., Nahar A. Global prospects, progress, policies, and environmental impact of solar photovoltaic power generation. *Renewable and Sustainable Energy Reviews*, 2015, vol. 41, pp. 284-297. doi: https://doi.org/10.1016/j.rser.2014.08.046.

4. European Photovoltaic Industry Association. *Global Market Outlook for Photovoltaics 2014–2018*. Brussels, May 2014. 60 p. Available at: https://helapco.gr/wp-content/uploads/EPIA_Global_Market_Outlook_for_Photovoltaics_2014-2018_Medium_Res.pdf (Accessed 20 August 2021).

5. Rabaia M.K.H., Abdelkareem M.A., Sayed E.T., Elsaid K., Chae K.-J., Wilberforce T., Olabi A.G. Environmental impacts of solar energy systems: A review. *Science of the Total Environment*, 2021, vol. 754, p. 141989. doi: https://doi.org/10.1016/j.scitotenv.2020.141989.

6. Ahmed W., Sheikh J.A., Nouman M., Ullah M.F., Mahmud M.A.P. Techno-economic analysis for the role of single end energy user in mitigating GHG emission. *Energy, Sustainability and Society*, 2021, vol. 11, no. 1, p. 32. doi: https://doi.org/10.1186/s13705-021-00307-3.

7. Hayder W., Abid A., Hamed M. Ben, Sbita L. MPPT based on P&O method under partially shading. *2020 17th International Multi-Conference on Systems, Signals & Devices (SSD)*, 2020, pp. 538-542. doi: https://doi.org/10.1109/SSD49366.2020.9364107.

8. Ali M.N., Mahmoud K., Lehtonen M., Darwish M.M.F. An Efficient Fuzzy-Logic Based Variable-Step Incremental Conductance MPPT Method for Grid-Connected PV Systems. *IEEE Access*, 2021, vol. 9, pp. 26420-26430. doi: https://doi.org/10.1109/ACCESS.2021.3058052.

9. Alajmi B.N., Ahmed K.H., Finney S.J., Williams B.W. Fuzzy-Logic-Control Approach of a Modified Hill-Climbing Method for Maximum Power Point in Microgrid Standalone Photovoltaic System. *IEEE Transactions on Power Electronics*, 2011, vol. 26, no. 4, pp. 1022-1030. doi: https://doi.org/10.1109/TPEL.2010.2090903.

10. Masoum M.A.S., Dehbonei H., Fuchs E.F. Theoretical and experimental analyses of photovoltaic systems with voltage and current-based maximum power-point tracking. *IEEE Transactions on Energy Conversion*, 2002, vol. 17, no. 4, pp. 514-522. doi: https://doi.org/10.1109/TEC.2002.805205.

11. Esram T., Kimball J.W., Krein P.T., Chapman P.L., Midya P. Dynamic maximum power point tracking of photovoltaic arrays using ripple correlation control. *IEEE Transactions on Power Electronics*, 2006, vol. 21, no. 5, pp. 1282-1291. doi: https://doi.org/10.1109/TPEL.2006.880242.

12. Kim I.-S. Sliding mode controller for the single-phase grid-connected photovoltaic system. *Applied Energy*, 2006, vol. 83, no. 10, pp. 1101-1115. doi: https://doi.org/10.1016/j.apenergy.2005.11.004.

13. Patel H., Agarwal V. MATLAB-Based Modeling to Study the Effects of Partial Shading on PV Array Characteristics. *IEEE Transactions on Energy Conversion*, 2008, vol. 23, no. 1, pp. 302-310. doi: https://doi.org/10.1109/TEC.2007.914308.

14. Ben Salah C., Ouali M. Comparison of fuzzy logic and neural network in maximum power point tracker for PV systems. *Electric Power Systems Research*, 2011, vol. 81, no. 1, pp. 43-50. doi: https://doi.org/10.1016/j.epsr.2010.07.005.

15. Syafaruddin, Karatepe E., Hiyama T. Artificial neural network-polar coordinated fuzzy controller based maximum power point tracking control under partially shaded conditions. *IET Renewable Power Generation*, 2009, vol. 3, no. 2, p. 239. doi: https://doi.org/10.1049/iet-rpg:20080065.

16. Roy Chowdhury S., Saha H. Maximum power point tracking of partially shaded solar photovoltaic arrays. *Solar Energy Materials and Solar Cells*, 2010, vol. 94, no. 9, pp. 1441-1447. doi: https://doi.org/10.1016/j.solmat.2010.04.011.

17. Kennedy J. *Particle swarm optimization. Encyclopedia of machine learning*, 2010, pp. 760-766.

18. Tizhoosh H.R. Opposition-Based Learning: A New Scheme for Machine Intelligence. *International Conference on Computational Intelligence for Modelling, Control and Automation and International Conference on Intelligent Agents, Web Technologies and Internet Commerce (CIMCA-IAWTIC'06)*, 2005, pp. 695-701, doi: https://doi.org/10.1109/CIMCA.2005.1631345.

19. Wang H., Wu Z., Rahnamayan S., Liu Y., Ventresca M. Enhancing particle swarm optimization using generalized opposition-based learning. *Information Sciences*, 2011, vol. 181, no. 20, pp. 4699-4714. doi: https://doi.org/10.1016/j.ins.2011.03.016.

20. Li J., Chen T., Zhang T., Li Y.X. A Cuckoo Optimization Algorithm Using Elite Opposition-Based Learning and Chaotic Disturbance. *Journal of Software Engineering*, 2015, vol. 10, no. 1, pp. 16-28. doi: https://doi.org/10.3923/jse.2016.16.28.

21. Poli R., Kennedy J., Blackwell T. Particle swarm optimization. *Swarm Intelligence*, 2007, vol. 1, no. 1, pp. 33-57. doi: https://doi.org/10.1007/s11721-007-0002-0.

22. Obukhov S., Ibrahim A., Aboelsaud R. Maximum Power Point Tracking of Partially Shading PV system Using Particle Swarm Optimization. *Proceedings of the 4th International Conference on Frontiers of Educational Technologies - ICFET '18*, 2018, pp. 161-165. doi: https://doi.org/10.1145/3233347.3233375.

23. Anwar N., Hanif A.H., Khan H.F., Ullah M.F. Transient Stability Analysis of the IEEE-9 Bus System under Multiple Contingencies. *Engineering, Technology & Applied Science Research*, 2020, vol. 10, no. 4, pp. 5925-5932. doi: https://doi.org/10.48084/etasr.3273.

24. Mehdi M.F., Ahmad A., Ul Haq S.S., Saqib M., Ullah M.F. Dynamic economic emission dispatch using whale optimization algorithm for multi-objective function. *Electrical Engineering & Electromechanics*, 2021, no. 2, pp. 64-69. doi: https://doi.org/10.20998/2074-272X.2021.2.09.

Hamdan Saeed[1], MS Scholar,
Tahir Mehmood[1], Professor,
Fadia Ali Khan[2], Lecturer,
Muhammad Shazaib Shah[1], MS Scholar,
Mian Farhan Ullah[3], Lecturer,
Hamid Ali[1], Lecturer,
[1] Department of Electrical Engineering,
University of Engineering and Technology, Taxila, Pakistan,
e-mail: hamdan.saeed@students.uettaxila.edu.pk,
tahir.mehmood@uettaxila.edu.pk,
mshahzaib.Shah@students.uettaxila.edu.pk,
engr.hamidali94@gmail.com
[2] Department of Mechatronics Engineering,
Wah Engineering College, University of Wah,
47040, Wah Cantt, Quaid Avenue, Pakistan,
e-mail: fadia.sohail@wecuw.edu.pk
[3] Department of Electrical Engineering,
Wah Engineering College, University of Wah,
47040, Wah Cantt, Quaid Avenue, Pakistan,
e-mail: farhan.ullah@wecuw.edu.pk (Corresponding Author)

S. Bensiammar, M. Lefouili, S. Belkhelfa

Equivalent cable harness method generalized for predicting the electromagnetic emission of twisted-wire pairs

Introduction. *In this paper, the equivalent cable harness method is generalized for predicting the electromagnetic emissions problems of twisted-wire pairs.* ***The novelty*** *of the proposed work consists in modeling of a multiconductor cable, in a simplified cable harness composed of a reduced number of equivalent conductors, each one is representing the behavior of one group of conductors of the initial cable.* ***Purpose.*** *This work is focused on the development and implementation of simplified simulations to study electromagnetic couplings on multiconductor cable.* ***Methods***. *This method requires a four step procedure which is summarized as follows. Two different cases, of one end grounded and two ends grounded configurations can be analyzed.* ***Results.*** *The results had shown that the model complexity and computation time are significantly reduced, without, however, reducing the accuracy of the calculations.* References 20, tables 1, figures 8.*
Key words: **electromagnetic emission, asymmetric digital subscriber line, crosstalk, equivalent cable harness method, multiconductor transmission line network, power loss, twisted-wire pairs.**

Вступ. *У цій статті метод еквівалентного кабельного джгута узагальнюється для прогнозування задач електромагнітного випромінювання кручених пар дротів.* ***Новизна*** *запропонованої роботи полягає в моделюванні багатожильного кабелю в спрощеному джгуті проводів, що складається зі зменшеної кількості еквівалентних провідників, кожен з яких репрезентує поведінку однієї групи провідників вихідного кабелю.* ***Мета***. *Робота зосереджена на розробці та реалізації спрощеного моделювання для дослідження електромагнітних зв'язків у багатожильних кабелях.* ***Методи***. *Цей метод вимагає чотириступінчастої процедури, яка коротко описана у статті. Можна проаналізувати два різні випадки: конфігурації із заземленням одного кінця та заземлення двох кінців.* ***Результати***. *Результати показали, що складність моделі та тривалість обчислень значно знижуються, проте без зниження точності обчислень.* Бібл. 20, табл. 1, рис. 8.*
Ключові слова: **електромагнітне випромінювання, асиметрична цифрова абонентська лінія, перехресні перешкоди, метод еквівалентного кабельного джгута, мережа багатопровідних ліній передачі, втрати потужності, кручені пари дротів.**

Introduction. For transmission signal in complex telecommunication network one of principle resources of noise that affect the signal quality is due to the crosstalk coupling. The crosstalk among twisted-wire pairs (TWPs) is commonly classified into near end crosstalk (NEXT) and far end crosstalk (FEXT) [1–4]. Furthermore, we distinguished two types of coupling crosstalk, the inductive coupling and the capacitive coupling, the dominant coupling at an arbitrary configuration is due to the termination impedance effects [5, 6].

The survey of literature shows that reducing the number of wires is not a new task. An efficient simplification technique called the «equivalent cable bundle method» (ECBM) has been proposed for modelling electromagnetic (EM) common-mode currents on complex cable bundles for telecommunications networks applications with arbitrary loads [7]. This method, allows, using the theory of Multiconductor Transmission Line Network (MTLN), to take into account the phenomena of propagation and couplings on and between all the wires of the network.

In recent years, the increase in the frequency of disturbances electromagnetic that can potentially attack the wiring network encourages the research to extend digital immunity to high frequencies. This will unfortunately comes up against the limitation in MTLN frequency.

In high frequencies, the use of three-dimensional methods, solving the Maxwell equations in space then proves to be obligatory. However, they require a fine discretization of each conductor of the beam in segments whose length is usually less than one tenth of the wavelength. The computation times then become

prohibitive as soon as the number of conductors of the beam in important.

It must therefore find simplifying hypotheses allowing the complexity to be reduced wiring harness without, however, reducing the accuracy of the calculations [8, 9]. The goal final is to generalize the feasibility of such an approach for twisted-wire pairs.

Purpose of the work is focused on the development and implementation of simplified simulations to study electromagnetic couplings on multiconductor cable.

Presentation of the equivalent cable harness method proposed of complex twisted-wire pairs. Description of the main assumption adopted in this modified procedure for a coupling problem in twisted-wire pairs cable will be detailed in this section.

The proposed geometry consists of a cable composed of twisted-wire pairs, both ends or only one end of the each pair circuit can be grounded.

Note that the twisted-wire pairs used here are connected to the ground plane. We would expect common mode current to be dominant. Therefore, the main assumption of the original ECBM is unchanged [10], we make approach that the impedance loads in such case of twisted-wire pairs can be considered such as a common mode loads and the differential loads in one end of the pairs can be neglected.

The determination of geometrical characteristics of the reduced cable is omitted here because the aim of the method is to predict crosstalk in the pairs that we are interested in his currents and voltages [11, 12].

The modified equivalent cable harness method for modeling crosstalk in frequency domain among twisted-

wire pairs requires a four-step procedure [9], which is summarized as follows.

Step I. The goal of this step is to classify the pairs of the initial cable in different groups according to their termination loads at both ends of each pair. The culprit and victim pairs are classified into two groups separately and they hold its initial characteristics (including its positions, radius, and medium). The common-mode characteristic impedance Z_{mc} is determined by modal transformation in the MTLN formalism in order to obtain the characteristics of all the modes propagating along the cable. Furthermore, the very important condition of the eigenvector associated with the common mode in the matrix $[T_x]$ is verified, this part is more detailed in the original ECBM [8, 10].

Then all the remaining pairs in the complete cable bundle are sorted into groups by comparing the value of the termination loads (near Z_{0i} and far Z_{Li}) to Z_{mc}. The conductors are installed as pairs; each two conductors for one pair are in the same group because the modal analysis is made of twisted-wire pairs configuration. We define the four groups (may be less than four) which can be determined in each configuration in Table 1.

Table 1
Classification of the pairs according to their termination loads

Termination load	Group 1	Group 2	Group 3	Group 4
Near end (0)	$Z_{0i} < Z_{mc}$	$Z_{0i} < Z_{mc}$	$Z_{0i} > Z_{mc}$	$Z_{0i} > Z_{mc}$
Far end (L)	$Z_{Li} < Z_{mc}$	$Z_{Li} > R_{mc}$	$Z_{Li} < Z_{mc}$	$Z_{Li} > Z_{mc}$

Step II. The determination of the per unit length (p.u.l) parameter matrices of an equivalent cable is based on the determination of p.u. parameter matrices of the pairs from which it is consisted.

We consider a short circuit between conductors of one group of «k» conductors (Fig. 1). This assumption allows: firstly to define the group current I_{ec} for the equivalent cable and secondly the group voltage V_{ec} for the equivalent cable.
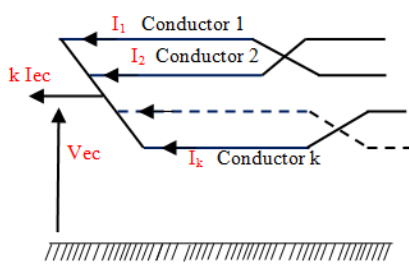
Fig. 1. Mode common current and voltage of k conductors in the same group

To determine the inductance reduced matrix, we need two additional assumptions detailed in [9]:

1) the currents flowing along all the «k» conductors of a cable bundle are decomposed in common mode currents and a differential mode currents. The differential mode current can be neglected [5, 13, 14].

The current and the voltage of «k» conductors in the same group can be written by:

$$I_{ec} = I_1 + I_2 + \ldots + I_k ; \qquad (1)$$

$$V_{ec} = V_1 + V_2 + \ldots + V_k . \qquad (2)$$

Thus, from the telegrapher's equation on the MTLN formalism for lossless line we can obtain the inductance matrix links the currents and the voltages on each conductor on an infinitesimal segment of length:

$$\frac{\partial}{\partial z} \begin{bmatrix} V_1 \\ V_2 \\ \vdots \\ V_k \end{bmatrix} = -j\omega \begin{bmatrix} L_{11} & L_{12} & \cdots & L_{1k} \\ L_{21} & L_{22} & \cdots & L_{2k} \\ \vdots & \vdots & \ddots & \vdots \\ L_{k1} & L_{k2} & \cdots & L_{kk} \end{bmatrix} \begin{bmatrix} I_{c1} \\ I_{c2} \\ \vdots \\ I_{ck} \end{bmatrix} . \qquad (3)$$

2) The common mode currents along all the conductors of a same group are identical:

$$I_{ec} = I_1 = I_2 = \ldots = I_k , \qquad (4)$$

where I_k is the mode common current in the k conductor.

The common-mode characteristic impedance of the harness can be obtained:

$$V_{ck} = \frac{V_{ec}}{k I_{ec}} = \frac{Z_i}{k} , \qquad (5)$$

where Z_i is the common-mode characteristic impedance of each conductor in the group (Fig. 2).
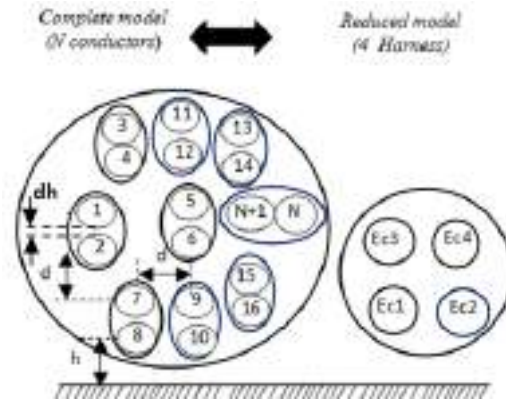
Fig.2. Cross section view of complete and reduced cable

These assumptions may allow finding the final system matrix; we index the conductors of each group as follows:

- N_1 conductors of the first group indexed 1 to x;
- N_2 conductors of the second group indexed $x+1$ to y;
- N_3 conductors of the third group indexed $y+1$ to z;
- N_4 conductors of the fourth group indexed $z+1$ to N.

The final system that allows finding L_{red} can be obtained:

$$\frac{\partial V_1}{\partial x} = -j\omega \begin{bmatrix} \dfrac{\sum_{i=1}^{x} L_{1i}}{N_1} I_{ec1} + \dfrac{\sum_{i=x+1}^{y} L_{1i}}{N_2} I_{ec2} \\ \dfrac{\sum_{i=y+1}^{z} L_{1i}}{N_3} I_{ec3} + \dfrac{\sum_{i=z+1}^{N} L_{1i}}{N_4} I_{ec4} \end{bmatrix} ; \qquad (6)$$

$$\frac{\partial V_N}{\partial x} = -j\omega \begin{bmatrix} \dfrac{\sum_{i=1}^{x} L_{Ni}}{N_1} I_{ec1} + \dfrac{\sum_{i=x+1}^{y} L_{Ni}}{N_2} I_{ec2} \\ \dfrac{\sum_{i=y+1}^{z} L_{Ni}}{N_3} I_{ec3} + \dfrac{\sum_{i=z+1}^{N} L_{Ni}}{N_4} I_{ec4} \end{bmatrix} . \qquad (7)$$

The voltages of each conductor belonging to the same group being equal (2), the insertion of this property in previous equations leads to the following system connecting the voltages and currents of the four groups of conductors [7]:

$$\frac{\partial V_{ec1}}{\partial x} = -j\omega\left[\frac{\sum_{i=1}^{x}\sum_{j=1}^{x}L_{ij}}{N_1^2}I_{ec1} + \frac{\sum_{i=1}^{x}\sum_{j=x+1}^{y}L_{ij}}{N_1 N_2}I_{ec2} +\right.$$

$$\left. +\frac{\sum_{i=1}^{x}\sum_{j=y+1}^{z}L_{ij}}{N_1 N_3}I_{ec3} + \frac{\sum_{i=1}^{x}\sum_{j=z+1}^{N}L_{ij}}{N_1 N_4}I_{ec4}\right]; \quad (8)$$

$$\frac{\partial V_{ec2}}{\partial x} = -j\omega\left[\frac{\sum_{i=x+1}^{y}\sum_{j=1}^{x}L_{ij}}{N_1 N_2}I_{ec1} + \frac{\sum_{i=x+1}^{y}\sum_{j=x+1}^{y}L_{ij}}{N_2^2}I_{ec2} +\right.$$

$$\left. +\frac{\sum_{i=x+1}^{y}\sum_{j=y+1}^{z}L_{ij}}{N_2 N_3}I_{ec3} + \frac{\sum_{i=x+1}^{y}\sum_{j=z+1}^{N}L_{ij}}{N_2 N_4}I_{ec4}\right]; \quad (9)$$

$$\frac{\partial V_{ec3}}{\partial x} = -j\omega\left[\frac{\sum_{i=y+1}^{z}\sum_{j=1}^{x}L_{ij}}{N_1 N_3}I_{ec1} + \frac{\sum_{i=y+1}^{z}\sum_{j=x+1}^{y}L_{ij}}{N_2 N_3}I_{ec2} +\right.$$

$$\left. +\frac{\sum_{i=y+1}^{z}\sum_{j=y+1}^{z}L_{ij}}{N_3^2}I_{ec3} + \frac{\sum_{i=y+1}^{z}\sum_{j=z+1}^{N}L_{ij}}{N_3 N_4}I_{ec4}\right]; \quad (10)$$

$$\frac{\partial V_{ec4}}{\partial x} = -j\omega\left[\frac{\sum_{i=z+1}^{N}\sum_{j=1}^{x}L_{ij}}{N_1 N_4}I_{ec1} + \frac{\sum_{i=z+1}^{N}\sum_{j=x+1}^{y}L_{ij}}{N_2 N_4}I_{ec2} +\right.$$

$$\left. +\frac{\sum_{i=z+1}^{N}\sum_{j=y+1}^{z}L_{ij}}{N_3 N_4}I_{ec3} + \frac{\sum_{i=z+1}^{N}\sum_{j=z+1}^{N}L_{ij}}{N_4^2}I_{ec4}\right]; \quad (11)$$

$$\frac{\partial}{\partial z}\begin{bmatrix}V_{ec1}\\V_{ec2}\\V_{ec3}\\V_{ec4}\end{bmatrix} = -j\omega[L_{red}]\begin{bmatrix}I_{ce1}\\I_{ce2}\\I_{ce3}\\I_{ce4}\end{bmatrix}; \quad (12)$$

$$[L_{red}] = \begin{bmatrix} L_{11r} & L_{12r} & L_{13r} & L_{14r}\\ L_{21r} & L_{22r} & L_{23r} & L_{24r}\\ L_{31r} & L_{32r} & L_{33r} & L_{34r}\\ L_{41r} & L_{42r} & L_{43r} & L_{44r}\end{bmatrix}; \quad (13)$$

$$L_{11r} = \frac{\sum_{i=1}^{x}\sum_{j=1}^{x}L_{ij}}{N_1^2}. \quad (14)$$

The expression of p.u. capacitance matrix for the reduced model $[C_{red}]$ can be obtained with the same reasoning in no homogenous and polar medium.

For a weakly polar medium, one can ignore the dispersion of the dielectric constant and, accordingly, the phase velocity [11]:

$$[C_{red}] = \frac{1}{\upsilon^2}[L_{red}]^{-1}, \quad (15)$$

where $\upsilon = c/\sqrt{\varepsilon_r}$.

So, using the assumptions and approximations set out above, the matrix inductance and capacitance with ($N\times N$) dimension can be reduced into matrix (4×4) which coefficients exerted on and between the conductors.

Step III. The aim of this step is to determine the termination loads to be connected at both ends of the equivalent conductor. Here, all load impedances are considered as pure resistance and are not frequency dependent. There are two kinds of the termination loads, differential-mode loads and common-mode loads:

• *Common-mode loads.* Each load connected to the ground plane at his terminal end (Fig. 3).
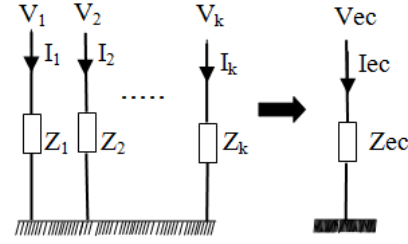
Fig. 3. Equivalent termination common-mode loads

The impedance equivalent Z_{ec} for «k» conductors in the same group ($Z_1, Z_2 \ldots Z_k$), is:

$$\frac{1}{Z_{ec}} = \frac{1}{Z_1} + \frac{1}{Z_2} + \ldots + \frac{1}{Z_k}. \quad (16)$$

• *Differential-mode loads.* We consider the type differential loads connected between conductors from different groups (Fig. 4). The impedance equivalent Z_{d12}, for two conductors (1 and 2) in group 1 and two conductors ($N1+1$ and $N1+2$) in group 2, is:

$$\frac{1}{Z_{d12}} = \frac{1}{Z_{1-N1+1}} + \frac{1}{Z_{2-N1+2}}. \quad (17)$$
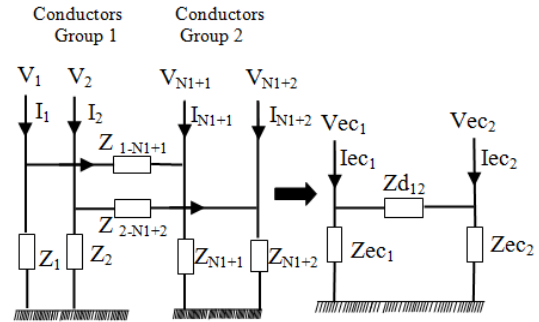
Fig. 4. Equivalent termination differential-mode loads

The type of differential loads connected between conductors in the same group is neglected.

Step IV. The aim of this step is to determine the section geometry (radius, coating radius, permittivity relative of coating, height, distance between harnesses), of each reduced harness using the linear parameter matrices determined at the Step II. This part is more detailed in the original ECBM [8, 10].

For modeling the twist of pairs on complete model the matrix P [1] was used, in the reduced model this matrix is evaluated to take into account only the twisted wires of the pairs which we not apply the method [1].

For the equivalent cable for each group the current and voltage are multiplied by 1 in the matrix P.

In order to determine currents and voltages in both ends of each pair, the excited pair is assumed to be a disturber and the crosstalk in an arbitrary victim pair in term of power loss (PL) is shown.

Note that the values of the power loss crosstalk (PL_{NEXT}, PL_{FEXT}) in decibels can be calculated as follows [15–18]:

$$PL_{NEXT/dB} = -10\log_{10}(|H_{NEXT}(f)|^2);\quad(18)$$

$$PL_{FEXT/dB} = -10\log_{10}(|H_{FEXT}(f)|^2),\quad(19)$$

where H_{NEXT} and H_{FEXT} are the transfer function.

The PL expression can be written as follows:

$$PL_{NEXT,i/dB} = 10\log_{10}[(V_i(x_1)/V_1(x_1))^2];\quad(20)$$

$$PL_{FEXT,i/dB} = 10\log_{10}[(V_i(x_L)/V_1(x_1))^2],\quad(21)$$

where V_i is the voltage in the victim wire which we want calculates his crosstalk; x_1, x_L are the first and the last extremities of the line [19].

Application of the equivalent cable harness method. The mathematical model established will be used for obtaining the power loss near and far (PL_{NEXT} and PL_{FEXT}) in a bundle of twisted wire pairs. Twisted wire-pair is connected by two ends of each pair to the ground plane. Figure 5 illustrates the geometry used, they shows the first case of initial model of twenty-eight pairs denoted from 1 to 56, and the reduced cable of two pairs and two equivalent harness denoted ec$_1$, ec$_2$.
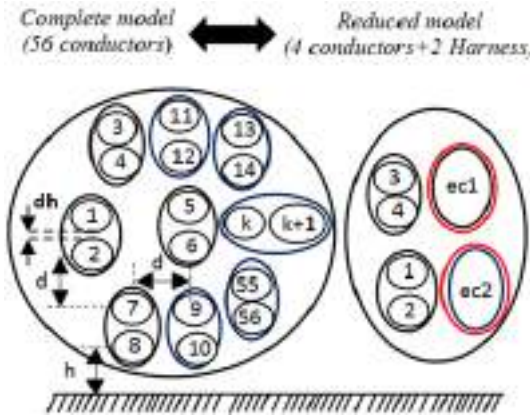
Fig. 5. Complete model cable and reduced model cable twisted-wire pairs cross sectional view

All wires are further assumed to have the same radius $a = 0.523$ mm and polyvinyl chloride coating radius of $b = 0.549$ mm. The length of the wire is $L = 1$ km. The twisted pair consists of $N = 10000$ loops. The height of the first wire (numerated 8 and 10) above ground conductor is $h = 20$ mm, the height is very close to the reference plane, the intention in doing so is to avoid the noise produced by the loop between the receptor circuit and the reference plane.

The other conductors are located just above and next to the first wire with vertical distance of 0.127 mm for the same pair conductors and 3.17 mm for other conductors, the horizontal distance between the wires is $d = 3.17$ mm.

In Fig. 6 the pair one is given as an example, which is connected to the voltage source V_0 at its near end through a load Z_{01} and adapted at its far end through a load Z_{L1}.

The crosstalk will be studied in the frequency range from 1 kHz to 30 MHz with reference to Fig. 6 and in order to make same loads such as in XDSL systems, the loads in the pairs which we are interested are set to $Z_{01} = Z_{L1} = Z_{02} = Z_{L2} = 120$ Ω under the condition, that for a twisted pair the active resistance R of the conductors is much less than the inductive resistance ωL, and the active conductivity G of the

insulation is much less than the capacitive resistance ωC, respectively: $R \ll \omega L$, $G \ll \omega C$ [20].
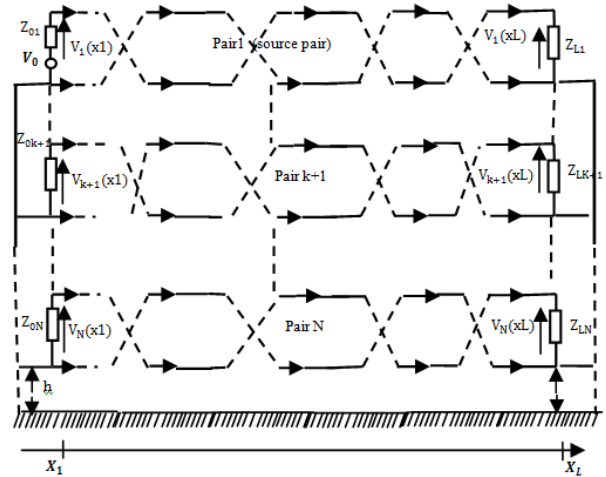
Fig. 6. Model of two ends grounded geometry of twisted-wire pairs longitudinal view

The classification of groups is made according to the comparison with the common-mode loads determined by the modal analysis.

The pairs of the complete cable bundle sorted into four groups as follows (Fig. 5):
- group 1: pairs 1 (conductors 1-2);
- group 2: pairs 2 (conductors 3-4);
- group 3: harness 1 (conductors 5-30);
- group 4: harness 2 (conductors 31-56);

The p.u. parameter matrices $[L_{red}]$ and $[C_{red}]$ of the reduced harnesses cables are calculated in nH/m and pF/m for a 1 km long line respectively:

$$[L_{red}] = \begin{bmatrix} 1.02 & 0.88 & 0.25 & 0.25 & 0.25 & 0.19 \\ & 1.02 & 0.25 & 0.24 & 0.24 & 0.19 \\ & & 1.02 & 0.88 & 0.13 & 0.17 \\ & & & 1.02 & 0.13 & 0.17 \\ & & & & 0.36 & 0.16 \\ & & & & & 0.34 \end{bmatrix};$$

$$[C_{red}] = \begin{bmatrix} 43.74 & -36.56 & -0.53 & -0.47 & -4.13 & -1.21 \\ & 43.74 & -0.47 & -0.52 & -4.64 & -0.71 \\ & & 43.70 & -36.59 & -0.64 & -1.04 \\ & & & 43.72 & -0.65 & -0.64 \\ & & & & 46.10 & -15.20 \\ & & & & & 46.17 \end{bmatrix}.$$

Next before and after applying our equivalent cable harness method the results are compared. The culprit pair is the pair one numerated (1, 2) in Fig. 5, we are interested in the voltage and current of the second pair numerated (3, 4) in Fig. 5.

The near end of conductor one (first pair (culprit pair)) is excited with a constant voltage source of 1 V.

The first pair is activated and we calculate the PL in the second pair (conductor 3). Next, we apply the method and we calculate again the PL on the second pair when the first pair is activated.

Figures 7, 8 show the power loss in the second pair (conductor 3) for *NEXT* and *FEXT* successively for the initial model and the complete model.
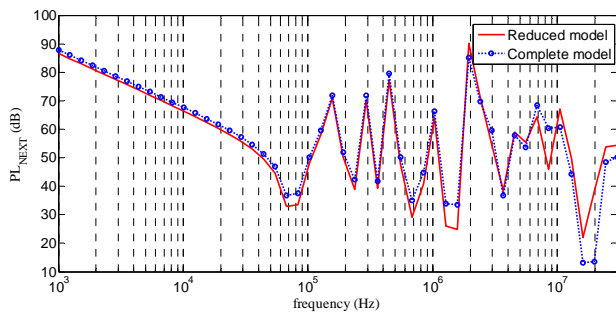
Fig. 7. PL_{NEXT} voltage in the frequency domain on pair two
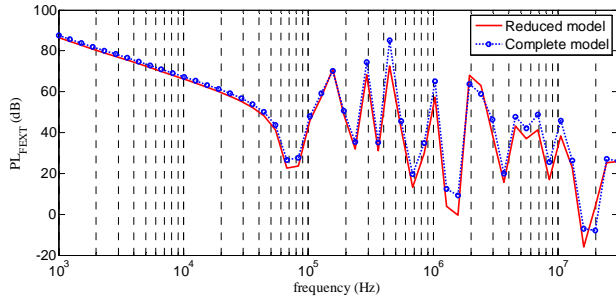
Fig. 8. PL_{FEXT} voltage in the frequency domain on pair two

For this configuration the difference between the two models is a few decibels. In the high frequency some differences are observed which are possibly due to the apparition of the transverse electric and magnetic mode. Results for this case confirm that equivalent cable harness method can be successfully applied in prediction crosstalk in a two ends grounded configuration of twisted-wire pairs cable in frequency domain.

To evaluate currents and voltages at both ends of each pair, the MTLN technique is used [5, 6] because for telecommunications networks the length of the wire is $L = 1$ km and greater than. For automotive applications where the lengths are too shirt (some meters) we can used three-dimensional methods, solving the Maxwell equations in space, how require a fine discretization of each conductor of the beam in segments.

Conclusion.

In this work the equivalent cable harness method was applied at different groups of pairs and voltages for a model of twisted-wire pairs in a cable bundle of telecommunication networks.

The foremost attributes of the modified method are:

• the study of crosstalk is established in the frequency domain from 1 kHz to 30 MHz where the line is electrically long and the transverse electric and magnetic mode is considered;

• the conductor, twisted wire to wire in both configurations studied which affect the terminal loads and give rise to a new approach of the equivalent loads;

• the victim and culprit pairs considered as different groups and were involved in the reduced per unit length parameter matrices.

The crosstalk *NEXT* and *FEXT* are simulated at an arbitrary culprit pair in term of power loss this task allows reduction of complexity and computation time for a complete cable bundle modeling and maintains a fairly good precision, the total computation time is reduced by a factor of 2.8 after equivalence of the complete model by using the method of Multiconductor Transmission Line

Network theory for cable of 28 pairs (56 conductors), which have been performed on a 2.5 GHz processor and a 4 GB RAM memory computer. Numerical simulations presented in this paper validate the efficiency and the advantages of the proposed method.

Conflict of interest. The authors declare that they have no conflicts of interest.

REFERENCES
1. Huang C., Zhao Y., Yan W., Liu Q., Zhou J., Meng Z., Mueed A. Analysis of Crosstalk Problem in Multi-Twisted Bundle of Multi-Twisted Wire Based on BSAS-BP Neural Network Algorithm and Multilayer Transposition Method. *ACES Journal*, 2020, vol. 35, no. 8. Available at: https://aces-society.org/includes/downloadpaper.php?of=ACES_Journal_August_2020_Paper_14&nf=20-8-14 (Accessed 12 June 2021).
2. Yang C., Yan W., Zhao Y., Chen Y., Zhu C., Zhu Z. Analysis on RLCG Parameter Matrix Extraction for Multi-Core Twisted Cable Based on Back Propagation Neural Network Algorithm. *IEEE Access*, 2019, vol. 7, pp. 126315-126322. doi: https://doi.org/10.1109/ACCESS.2019.2935467.
3. Gassab O., Yin W.-Y. Characterization of Electromagnetic Wave Coupling With a Twisted Bundle of Twisted Wire Pairs (TBTWPs) Above a Ground Plane. *IEEE Transactions on Electromagnetic Compatibility*, 2019, vol. 61, no. 1, pp. 251-260. doi: https://doi.org/10.1109/TEMC.2018.2798612.
4. Gassab O., Zhou L., Yin W.-Y. Characterization of Electromagnetic Wave Coupling With a Noncoaxial Cable with Apertures on its Shield. *2020 IEEE MTT-S International Conference on Numerical Electromagnetic and Multiphysics Modeling and Optimization (NEMO)*, 2020, pp. 1-4. doi: https://doi.org/10.1109/NEMO49486.2020.9343565.
5. Song X., Wang J., Li B., Su D. Crosstalk model for shielded bundles of random twisted-wire pairs. *2016 Asia-Pacific International Symposium on Electromagnetic Compatibility (APEMC)*, 2016, pp. 766-769. doi: https://doi.org/10.1109/APEMC.2016.7522860.
6. Liao H., Liu Q., Wu W., Chen L. The Field-Wire Coupling Characteristics of the Twisted-Wire Pairs Illuminated by the Electromagnetic Pulse. *2018 International Applied Computational Electromagnetics Society Symposium - China (ACES)*, 2018, pp. 1-2. doi: https://doi.org/10.23919/ACESS.2018.8669344.
7. Sun Y., Wang J., Song W., Xue R. Frequency Domain Analysis of Lossy and Non-Uniform Twisted Wire Pair. *IEEE Access*, 2019, vol. 7, pp. 52640-52649. doi: https://doi.org/10.1109/ACCESS.2019.2912220.
8. Huo Y., Zhao Y., Li Z. A fast equivalent method for modeling electromagnetic pulse response of cable bundle terminated in arbitrary loads. *Progress in Electromagnetics Research M*, 2017, vol. 53, pp. 177-190. doi: https://doi.org/10.2528/PIERM16120301.
9. Andrieu G., Bunlon X., Koné L., Parmantier J., Démoulin B., Reineixl A. The 'Equivalent Cable Bundle Method': an Efficient Multiconductor Reduction Technique to Model Industrial Cable Networks. In (Ed.), *New Trends and Developments in Automotive System Engineering*. IntechOpen. 2011. doi: https://doi.org/10.5772/13129.
10. Gheddar H., Melit M., Nekhoul B. Hybrid method for crosstalk analysis of multiconductor transmission lines. *2019 19th International Symposium on Electromagnetic Fields in Mechatronics, Electrical and Electronic Engineering (ISEF)*, 2019, pp. 1-2. doi: https://doi.org/10.1109/ISEF45929.2019.9097067.
11. Paul C.R., McKnight J.W. Prediction of Crosstalk Involving Twisted Pairs of Wires-Part II: A Simplified Low-Frequency Prediction Model. *IEEE Transactions on Electromagnetic Compatibility*, 1979, vol. EMC-21, no. 2, pp. 105-114. doi: https://doi.org/10.1109/TEMC.1979.303752.

12. Paul C.R. *Analysis of Multiconductor Transmission Lines, 2nd Edition*. 2007, Wiley-IEEE Press, 800 p.
13. Rotgerink J.L., Schippers H., Leferink F. Low-Frequency Analysis of Multiconductor Transmission Lines for Crosstalk Design Rules. *IEEE Transactions on Electromagnetic Compatibility*, 2019, vol. 61, no. 5, pp. 1612-1620. doi: https://doi.org/10.1109/TEMC.2018.2868985.
14. Distler F., Gold G., Thurn K., Schür J., Vossiek M. Crosstalk simulation of multiple insulated twisted pairs based on transmission line theory. *2017 IEEE 21st Workshop on Signal and Power Integrity (SPI)*, 2017, pp. 1-4. doi: https://doi.org/10.1109/SaPIW.2017.7944033.
15. Fu M., Li G. Applications of equivalent cable bundle method in frequency domain for emission problems of the computer case cable harness. *2017 IEEE 17th International Conference on Communication Technology (ICCT)*, 2017, pp. 1805-1808. doi: https://doi.org/10.1109/ICCT.2017.8359941.
16. Chabane S., Besnier P., Klingler M. A Modified Enhanced Transmission Line Theory Applied to Multiconductor Transmission Lines. *IEEE Transactions on Electromagnetic Compatibility*, 2017, vol. 59, no. 2, pp. 518-528. doi: https://doi.org/10.1109/TEMC.2016.2611672.
17. Xiao P., Du P., Nie B.-L. Simplification technique for modeling electromagnetic radiation of shielding cable bundle. *2018 IEEE International Symposium on Electromagnetic Compatibility and 2018 IEEE Asia-Pacific Symposium on Electromagnetic Compatibility (EMC/APEMC)*, 2018, pp. 1174-1179. doi: https://doi.org/10.1109/ISEMC.2018.8393973.
18. Wang Y., Cao Y.S., Liu D., Kautz R.W., Altunyurt N., Fan J. A Generalized Multiple-Scattering Method for Modeling a Cable Harness With Ground Connections to a Nearby Metal Surface. *IEEE Transactions on Electromagnetic Compatibility*, vol. 61, no. 1, pp. 261-270. doi: https://doi.org/10.1109/TEMC.2018.2806320.
19. Yan J., Li Z., Liu L.L., Gu C.Q. Multiconductor reduction method for modeling crosstalk of complex cable bundles in the vicinity of a 60 degree corner. *Progress in Electromagnetics Research M*, 2013, vol. 28, pp. 201-211. doi: https://doi.org/10.2528/PIERM12121904.
20. Shoory A., Rubinstein M., Rubinstein A., Romero C., Mora N., Rachidi F. Application of the Cascaded Transmission Line Theory of Paul and McKnight to the Evaluation of NEXT and FEXT in Twisted Wire Pair Bundles. *IEEE Transactions on Electromagnetic Compatibility*, 2013, vol. 55, no. 4, pp. 648-656. doi: https://doi.org/10.1109/TEMC.2013.2254716.

Samir Bensiammar [1], *M.Sc. Student*,
Moussa Lefouili [1], *PhD, Professor*,
Soufiane Belkhelfa [1], *M.Sc. Student*,
[1] Mechatronic Laboratory,
University of Jijel, Algeria,
e-mail: bensiammar.samir@umc.edu.dz (Corresponding Author),
lefouili_moussa@yahoo.fr,   sofiankhalf@gmail.com

V.M. Zolotaryov , O.V. Chulieieva, V.L. Chulieiev, T.A. Kuleshova, M.S. Suslin

Influence of doping additive on thermophysical and rheological properties of halogen-free polymer composition for cable insulation and sheaths

Introduction. *The demand for halogen-free fire-resistant compositions for the manufacture of fire-retardant wires and cables is constantly growing.* ***Problem.*** *Therefore, the creation and further processing of these materials is an urgent problem.* ***Goal.*** *The aim of the article is to study the effect of the doping additive on the thermophysical and rheological properties of halogen-free compositions for power cables with voltage 1 kV with the determination of both the temperatures of phase and structural transformations of polymer compositions.* ***Methodology.*** *Experiments investigating the phase transformations were carried out with the help device of thermogravimetric analysis and differential scanning calorimetry TGA/DSC 1/1100 SF of METTLER TOLEDO company. Rheological studies of polymeric materials were conducted by using the method of capillary viscosimetry in the device IIRT–AM.* ***Results.*** *The influence of the doping additive on the formation of the supramolecular structure of the filled polymer compositions for cable products was determined, that resulted in the temperature increase of the decomposition beginning by 11 °C and the end of decomposition by 7 °C.* ***Originality.*** *The effect of a doping additive on reducing the effective melt viscosity of a polymer composition from $6 \cdot 10^4$ to $1 \cdot 10^4$ Pa·s with increasing shear rate has been shown for the first time. The shear rate of the polymer composition containing the doping additive increases from 0.5 to 20 s^{-1} with increasing shear stress.* ***Practical value.*** *The research results provide an opportunity to reasonably approach the development of effective technological processes for the manufacture of the insulation and sheaths of power cables from halogen-free polymer compositions.* References 29, tables 3, figures 8.
Key words: **cable production, doping additive, rheological properties, melting temperature, decomposition onset temperature.**

Попит на вогнестійкі композиції, що не містять галогенів, для виготовлення пожежобезпечних проводів та кабелів безперервно зростає. Тому розробка цих матеріалів є **актуальною** *проблемою.* **Метою** *статті є дослідження впливу легувальної добавки на теплофізичні та реологічні властивості композицій. Теплофізичні властивості визначено з використанням приладу TGA/DSC 1/1100 SF компанії METTLER TOLEDO. Реологічні дослідження полімерних матеріалів проведено методом капілярної віскозиметрії на приладі ИИРТ-АМ. Визначено вплив легувальної добавки на формування надмолекулярної структури наповнених полімерних композицій. Встановлено зниження ефективної в'язкості розплаву полімерної композиції в 6 разів зі зростанням швидкості зсуву в 40 разів при змінненні температури від 150 до 190 °C. Швидкість зсуву полімерної композиції з легувальною добавкою зростає в 40 разів з підвищенням напруження зсуву в 9 разів.* **Результати** *досліджень дають можливість обґрунтовано підходити до розроблення ефективних технологічних процесів виготовлення ізоляції та оболонок силових кабелів. Бібл. 29, табл. 3, рис. 8.*
Ключові слова: **кабельна продукція, легувальна добавка, реологічні властивості, температура плавлення, температура початку розкладу.**

Introduction. In the last few decades, the demand for halogen-free fire-resistant compositions for the manufacture of fire-resistant wires and cables is constantly growing. This is largely due to their advantages in reducing smoke and reducing toxic and corrosive gases during combustion compared to traditionally used halogen-containing non-combustible cable materials. Such compositions are preferably materials containing a polymer based on polyolefins and a significant proportion of inorganic flame retardants, in particular aluminum hydroxide $Al(OH)_3$ [1, 2]. Polyolefins are one of the most flammable materials with high heat of combustion, low oxygen index and high heat dissipation, leaving little or no coke residue [3, 4].

In order to pass various tests for compliance with fire safety standards, compositions with content of the appropriate filler at the level of 60-80 % can be used. Of course, in this case there are quite complex problems regarding the manufacturability and mechanical properties of the compositions, which have to be solved by both manufacturers of cable compounds and manufacturers of cable products [5].

Rheological measurements of polymer melts are widely used in processing technologies of polymer compositions for quality control and process optimization. Another interesting field of rheology is to obtain information about the molecular parameters of polymers and the structure of heterogeneous polymer systems. The publication [6] provides an overview of the influence of molecular weight, molecular weight distribution, the degree of branching on various rheological characteristics. For dispersed polymer systems, such as materials with particles and polymer mixtures, rheological measurements can be used as a simple method of qualitative study of interactions between different phases and changes in geometric structures created by inhomogeneities [7].

Extrusion is the main method of polymer processing in the cable industry. Almost all polymer processing operations require an extruder for melting, mixing and forming products [8, 9]. To understand and optimize the extrusion process, it is first necessary to understand the rheological properties [10]. In other words, it is difficult to understand and optimize the polymer processing operation without first having a complete understanding of the thermoreological behavior of the polymer material over a wide range of time. Moreover, using the rheological properties in both shear and longitudinal flows, it is necessary to determine the appropriate equation that can capture the correct rheological response of the material forced through the capillary and slit extrusion heads [8-11].

Some important rheological properties of polyolefins and their mixtures related to extrusion are discussed in [12-17], including: inlet pressure during extrusion, important for determining the expansion of polymer melts; influence of temperature and pressure on rheological properties [18, 19]; wall penetration of polymers [20-25].

However, for dispersed polymer systems, the relationship between structure and rheological characteristics is not clear, additional research methods should be used to assess the contribution of different structural elements [26]. In [27] the influence of the modifier on the thermophysical properties of fire-resistant composite materials was investigated.

Among the requirements for halogen-free cable polymer compositions is the ability to provide high linear extrusion rates. Thus, the study of the effect of alloying additives on the rheological and thermophysical properties of halogen-free polymer compositions is an urgent problem.

The goal of the work is the study of the effect of the alloying additive on the thermophysical and rheological properties of halogen-free polymer compositions for power cables for voltages up to 1 kV with the determination of the temperatures of phase and structural transformations of polymer compositions.

Polymer cable compositions. Halogen-free fire-resistant polymer compositions were studied: sample 1 and sample 2. The polymer matrix (sample 3) for polymer compositions is a mixture of polyolefins (linear low density polyethylene; polyolefin elastomer and linear low density polyethylene modified with maleic anhydride). Flame retardant filler is alumina trihydrate. The content of flame retardant in polymer compositions is 60 %. The polymer composition in sample 2 contains an alloying additive in an amount of 2 %.

Paraffinic hydrocarbons were used as an alloying additive. The technical properties of the alloying additive are listed in Table 1.

Table 1

Properties of the alloying additive

Indicator	Value
Melt viscosity at temperature 140 °C, Pa·s, 10^3	180-300
Droplet temperature, °C, not less than	103
Penetration hardness, %, not more than	5
Volumetric resistivity at temperature 110 °C and voltage not less than 100 V, Ω·cm, not less than	$1 \cdot 10^{14}$

The polymer composition is made on the compounding line of the X-Compound Company, Switzerland. The line includes the following equipment: compounder/mixer 120-16 L/D, feed extruder GS 140-6 L/D with granulating head, ingredient dosing system, transport systems of ingredients and finished products, granule cooling system.

Equipment and methods. A series of experiments to study phase and structural transformations, thermal oxidative degradation processes were performed using thermogravimetric analysis (TGA) and differential scanning calorimetry (DSC) TGA/DSC 1/1100 SF instrument of the METTLER TOLEDO Company at heating rate of 10 and 50 deg/min.

Operating temperature range is from room temperature to 1100 °C; heating rate is from 0.01 deg/min to 100 deg/min.

Microbalance: the maximum weight during mounting is 1 g. The resolution of the TGA device is 1 μg in the entire weighing range.

DSC measurement range: 1 – ±350 mW; resolution – 0.04 μW.

Determination of temperatures of phase and structural transformations is carried out according to the characteristic points of the description of physical phenomena on DSC diagrams.

The beginning of the melting or vitrification effect is defined as the point of intersection of the baseline with the diagram before the phase transition. The end of the effects is defined as the point of intersection of the baseline with the diagram after the phase transition and the tangent curve, which is drawn to the point of inflection.

Determination of decomposition temperatures of polymer compositions was performed using DSC diagrams obtained using the instrument TGA/DSC 1/1100 SF (temperature rise rate is 10 deg/min). Decomposition start and end temperatures were defined as the points of intersection of the baseline with the diagram before and after the decomposition of the polymer compositions and the tangent to the diagram drawn to the inflection point. Mass loss is defined as the distance on the ordinate axis between the tangent to the TGA diagram and parallel to the abscissa axis at the end of the process.

The study of the rheological properties of polymeric materials was carried out by capillary viscosimetry on the IIRT-AM instrument.

The properties of polymer compositions were determined at temperature of 150-190 °C and loads from 37.24 to 211.82 N. Using the obtained data, the shear stress, shear rate and effective viscosity were calculated.

Shear stress is determined by [28]

$$\tau = (P - P_{in}) \frac{r}{2 \cdot L \cdot \pi \cdot R^2}, \qquad (1)$$

where τ is the shear stress, Pa; P is the force required to ensure the flow through the capillary, N; P_{in} is the input losses, N; R is the radius of the cylinder, cm; r is the radius of the capillary, cm; L is the length of the capillary, cm.

The shear rate is determined by [28]

$$\dot{\gamma} = \frac{4 \cdot Q}{\pi \cdot r^3}, \qquad (2)$$

where $\dot{\gamma}$ is the shear rate, s^{-1}; Q is the material consumption, cm^3/s ($Q = \pi \cdot R^2 \cdot h$, where h is the stationary immersion speed of the piston, cm/s; R is the radius of the cylinder, cm); r is the radius of the capillary, cm.

The effective viscosity is determined by [28]

$$\eta = \tau / \dot{\gamma}, \qquad (3)$$

where η is the effective viscosity, Pa·s.

Graphs of shear stress versus shear rate and effective viscosity versus shear rate and shear stress are plotted.

In order to estimate the energy required for the transition of the system to the so-called transition state, i.e. when the destruction and the establishment of connections are balanced, the activation energy is calculated.

The activation energy of a viscous flow is determined by [28]

$$E_{act} = \frac{R \cdot T_1 \cdot T_2 \cdot \ln(MFR_2 / MFR_1)}{T_2 - T_1}, \qquad (4)$$

where T is the measurement temperature, K; MFR_1 and MFR_2 are the melt flow rates for T_1 and T_2, g/10 min; R is the universal gas constant (8.314 J/(mol·K)).

A series of experiments to determine the electrical strength was performed using an instrument type АИ-70, electrical resistivity – an instrument type KISI-1.

Statistical analysis was performed by the method of disperse analysis (ANOVA) using the model of asymptotic regression according to the integrated Levenberg-Marquardt algorithm with a significance level of α 0.05.

Results of investigations. For the extrusion process of halogen-free polymer compositions, it is important for cable products to investigate their thermophysical characteristics such as: temperatures of phase and structural transformations, decomposition start temperatures. The latter are also important for the operation of cable products at elevated temperatures and short-circuit temperatures. For power cables up to 1 kV with halogen-free insulation, the short-circuit temperature is 170 °C (duration not more than 5 s).

Figures 1, 2 show DSC diagrams of a polymer matrix and a halogen-free polymer composition without and with an alloying additive content.
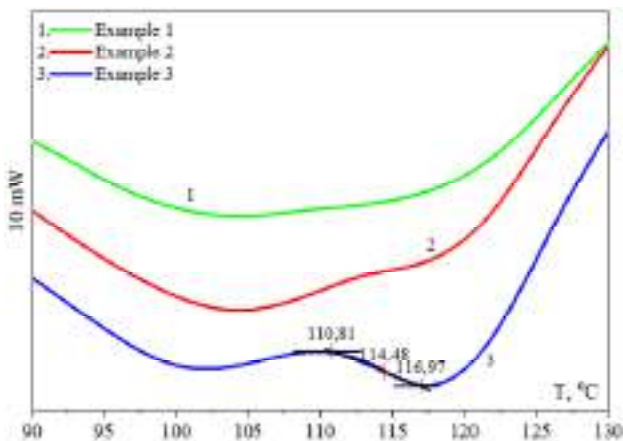
Fig. 1. DSC diagram to determine phase transitions

Temperatures of the beginning and end of decomposition (Fig. 2) vary depending on the composition: for the polymer matrix (curve 3) in the range from 229 °C to 254 °C, for the polymer composition (curve 1) – from 258 °C to 275 °C, and for the polymer composition with an alloying additive (curve 2) – from 269 °C to 282 °C.
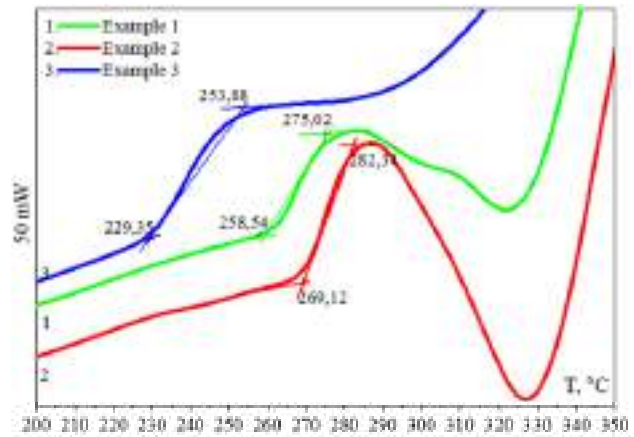
Fig. 2. DSC diagram to determine the beginning and end temperature of the decomposition

Figures 3, 4 show TGA diagrams of a halogen-free polymer matrix and polymer composition without and containing an alloying additive.
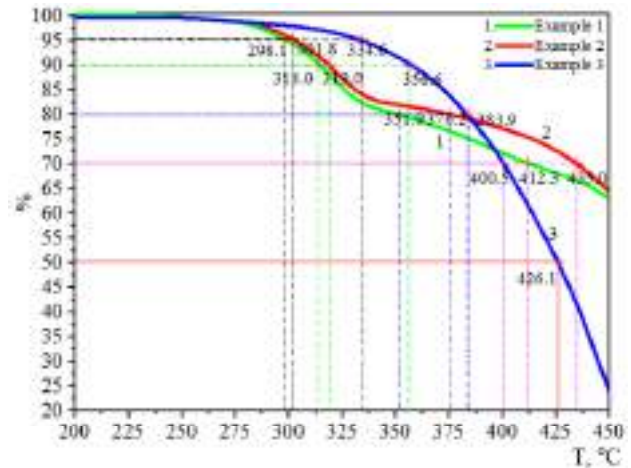
Fig. 3. TGA diagram.
Mass loss in the range from 200 to 450 °C

Table 2 shows the mass loss data determined from the TGA diagram (Fig. 3) for the polymer matrix and polymer composition that do not contain halogens without and with the content of the alloying additive.

Based on the data in Table 2 it is shown that for samples 1, 2 at mass loss from 5 % to 20 %, the temperature is lower (from 298 °C to 376 °C) than for sample 3 (from 334 °C to 383 °C). When the temperature reaches 275 °C (Fig. 3), there is a sharp change in mass loss (curves 1, 2). This is due to the process of dehydration of alumina trihydrate with heat absorption and water release. Sample 3 loses 50 % of the mass at temperature of 426 °C.

Table 2

Mass loss

Mass loss, %	Temperature, °C		
	Sample 1	Sample 2	Sample 3
5	298,1	301,8	334,6
10	314,0	319,0	356,6
20	351,9	376,2	383,9
30	412,3	435,0	400,5
50	–	–	426,1

Analysis of the TGA diagram (Fig. 4) shows that the polymer matrix loses 100 % of its mass at temperature of 525 °C. For samples 1, 2 already at temperature of 560 °C mass loss does not change, the residue is 38 % of the total mass of the polymer composition, which corresponds to the loss of chemically bound water and coincides with the theoretical calculations presented in [29].
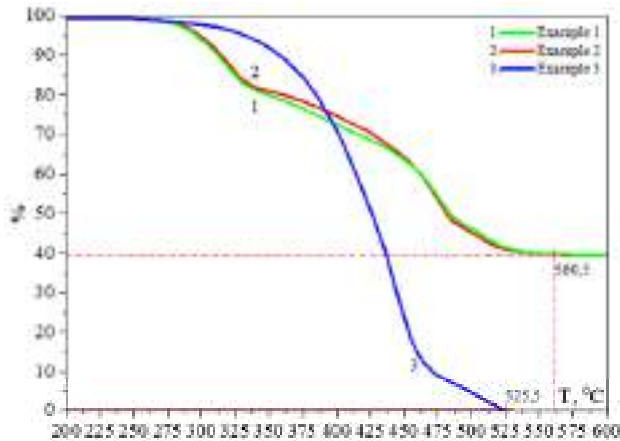
Fig. 4. TGA diagram.
Mass loss in the range from 200 to 600 °C

Analysis of DSC and TGA diagrams (Fig. 1-4) shows that polymer compositions should be used for the manufacture of cable products in which the maximum long-term temperature of the conductive core does not exceed 90 °C, and the maximum temperature at short circuit is 170 °C. At the same time, the optimal temperature range of extrusion of polymer compositions was established. Rheological studies were performed at temperatures of 150, 170 and 190 °C.

Figures 5, 6 present the dependencies of the effective viscosity on the shear rate and the effective viscosity on the shear stress.
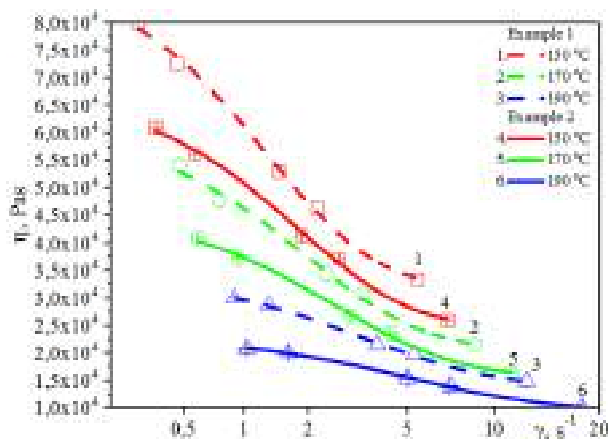
Fig. 5. Dependence of effective viscosity at different temperatures on the shear rate of polymer compositions

In Fig. 5 for the polymer composition of sample 2 there is a more significant decrease in the effective viscosity over the entire temperature range with increasing shear rate compared to the polymer composition of sample 1.

In Fig. 6 there is a decrease in effective viscosity with increasing shear stress for sample 1 from $8 \cdot 10^4$ to

$1.5 \cdot 10^4$ Pa·s, for sample 2 from $6.1 \cdot 10^4$ to $1 \cdot 10^4$ Pa·s. The alloying additive provides efficient distribution of the flame retardant filler in the polymer matrix, resulting in the formation of an ordered supramolecular structure.
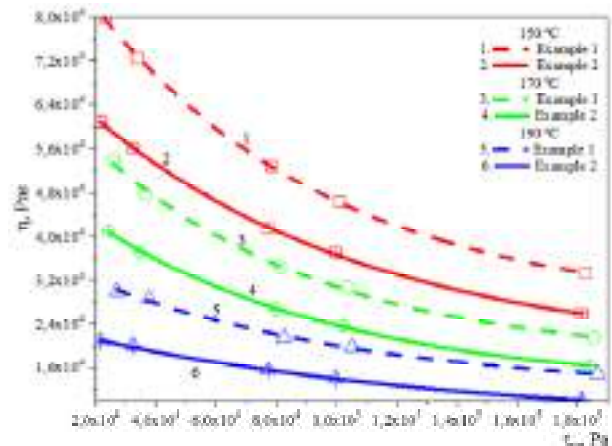
Fig. 6. Dependence of effective viscosity on shear stress of polymer compositions at different temperatures

Figure 7 presents graphical dependencies of shear rate on shear stress (flow curves) for polymer compositions of samples 1 and 2, respectively. The nature of the curves indicates that higher shear stress values are required to achieve higher shear rate values during the flow of polymer compositions. For the polymer composition of sample 2, the flow curves (4, 5, 6) at fixed values of the shear stress are shifted toward higher values of the shear rate compared to the polymer composition of sample 1 (curves 1, 2, 3).
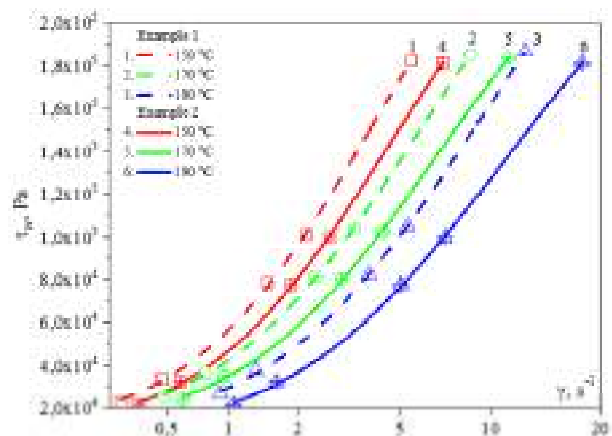
Fig. 7. Dependence of shear stress on the shear rate of polymer compositions at different temperatures

Figure 8 shows the graphical dependencies of the activation energy of the viscous flow on the load for the polymer compositions of sample 1 and sample 2.

The activation energy of a viscous flow determines the energy barriers that are overcome in the elementary act of flow and determines the effect of temperature on the effective viscosity: the higher the activation energy, the greater the effect of temperature on the effective viscosity.

For the polymer compositions of sample 1 and sample 2, the activation energy decreases with increasing load, and the activation energy of the polymer

composition of sample 1 becomes smaller compared to the polymer composition of sample 2.
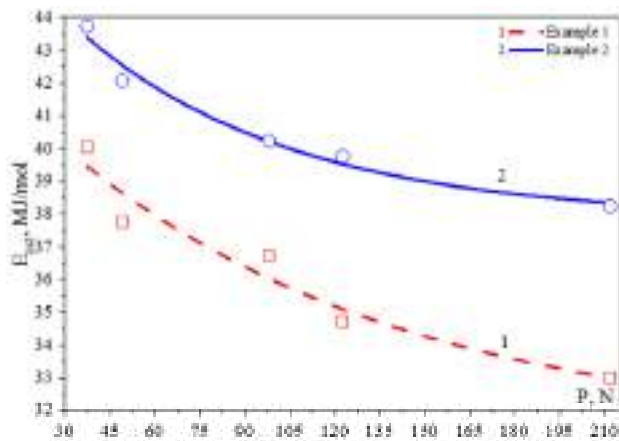
Fig. 8. Dependence of viscous flow activation energy on load for polymer compositions

The electrophysical properties of polymer compositions of sample 1, sample 2, and sample 3 have been studied. The electrical resistivity is determined by the presence of free charges (electrons and ions) and their mobility. Electrical strength is the electric field strength at which a breakdown occurs.

The results of the study are presented in Table 3.

Table 3
Electrophysical indicators of polymer compositions

Indicator	Sample 1	Sample 2	Sample 3
Volumetric resistivity, Ω·cm	$1{,}15 \cdot 10^{15}$	$1{,}32 \cdot 10^{15}$	$1 \cdot 10^{16}$
Electrical strength, kV/mm	45,0	48,5	23,5

It is advisable to compare fire-hazardous polymer compositions that do not contain halogens: sample 1 and sample 2.

From data of Table 3 it can be seen that with the introduction of the alloying additive, the volumetric resistivity increases from $1.15 \cdot 10^{15}$ to $1.32 \cdot 10^{15}$ Ω·cm, the electrical strength increases from 45 to 48.5 kV/mm.

Conclusions.

1. The influence of alloying additive on the formation of supramolecular structure of filled polymer compositions for cable products is determined, due to which the temperature of the beginning of decomposition by 11 °C and of the end of decomposition by 7 °C increases.

2. The expediency of using fire-retardant compositions for the manufacture of cable products, in which the maximum long-term temperature of the conductive core does not exceed 90 °C and the maximum temperature in the event of a short circuit is 170 °C, is shown.

3. For the first timethe effect of an alloying additive on reducing the effective melt viscosity of a polymer composition from $6 \cdot 10^4$ to $1 \cdot 10^4$ Pa·s with increasing shear rate is shown. The shear rate of the polymer composition containing the alloying additive increases from 0.5 to 20 s^{-1} with increasing shear stress.

4. For the first time the influence of an alloying additive on the electrophysical properties of fire-hazardous halogen-free polymer compositions has been studied. With the introduction of the alloying additive, the electrical resistance increases from $1.15 \cdot 10^{15}$ to $1.32 \cdot 10^{15}$ Ω·cm, and the electrical strength increases from 45 to 48.5 kV/mm.

5. The results of research provide an opportunity to reasonably approach the development of effective technological processes for the manufacture of insulation, sheaths of power cables from halogen-free polymer compositions.

Conflict of interest. The authors of the article state that there is no conflict of interest.

REFERENCES
1. Beyer G. *The Global Cable Industry: Materials, Markets, Products.* Wiley Publ., 2021. doi: https://doi.org/10.1002/9783527822263.
2. Meinier R., Sonnier R., Zavaleta P., Suard S., Ferry L. Fire behavior of halogen-free flame retardant electrical cables with the cone calorimeter. *Journal of Hazardous Materials*, 2018, vol. 342, pp. 306-316. doi: https://doi.org/10.1016/j.jhazmat.2017.08.027.
3. Papaspyrides C.D., Kiliaris P. *Polymer Green Flame Retardants*. Elsevier, 2014. doi: https://doi.org/10.1016/C2010-0-66406-6.
4. Nazir R., Gooneie A., Lehner S., Jovic M., Rupper P., Ott N., Hufenus R., Gaan S. Alkyl sulfone bridged phosphorus flae-retardants for polypropylene. *Materials & Design*, 2021, vol. 200, pp. 109459. doi: https://doi.org/10.1016/j.matdes.2021.109459.
5. VISCOSPEED in HFFR compounds: Big impact with minimal dosage. *Compounding World*, October, 2020, pp. 48-49. Available at: https://content.yudu.com/web/1rl19/0A1rl2p/CWOct20/html/print/CW%20October%202020%20pdf%20for%20download.pdf (Accessed 19 November 2021).
6. Munstedt H. Rheological Measurements and Structural Analysis of Polymeric Materials. *Polymers*, 2021, vol. 13, no. 7, p. 1123. doi: https://doi.org/10.3390/polym13071123.
7. Munstedt H. *Rheological and Morphological Properties of Dispersed Polymeric Materials*. Carl Hanser Verlag Publ., 2016. 473 p. doi: https://doi.org/10.3139/9781569906088.
8. Dealy J.M., Wissbrun K.F. *Melt Rheology and Its Role in Plastics Processing – Theory and Applications*. Springer Science & Business Media, 1990, 680 p. doi: https://doi.org/10.1007/978-94-009-2163-4.
9. Agassant J.-F., Avenas P., Carreau P.J., Vergnes B., Vincent M. *Polymer Processing Principles and Modelling*. Carl Hanser Verlag Publ., 2017. 883 p. doi: https://doi.org/10.3139/9781569906064.
10. Barnes H.A. Rheology: Principles, Measurements and Applications. *Powder Technology*, 1996, vol. 86, no. 3, pp. 313. doi: https://doi.org/10.1016/S0032-5910(96)90008-X.
11. Brereton M.G. Dynamics of Polymeric Liquids. *Physics Bulletin*, 1978, vol. 29, no. 1, pp. 26. doi: https://doi.org/10.1088/0031-9112/29/1/038.
12. Mitsoulis E., Hatzikiriakos S.G. Rheological Properties Related to Extrusion of Polyolefins. *Polymers*, 2021, vol. 13, no. 4, pp. 489. doi: https://doi.org/10.3390/polym13040489.
13. Cogswell F.N. Measuring the Extensional Rheology of Polymer Melts. *Transactions of the Society of Rheology*, 1972, vol. 16, no. 3, pp. 383-403. doi: https://doi.org/10.1122/1.549257.
14. Pearson J.R.A. Polymer melt rheology: a guide for industrial practice. *Journal of Non-Newtonian Fluid Mechanics*, 1981, vol. 8. no. 3-4, pp. 365-366. doi: https://doi.org/10.1016/0377-0257(81)80033-X.

15. Zatloukal M. Measurements and modeling of temperature-strain rate dependent uniaxial and planar extensional viscosities for branched LDPE polymer melt. *Polymer*, 2016, vol. 104, pp. 258-267. doi: https://doi.org/10.1016/j.polymer.2016.04.053.

16. Ansari M., Alabbas A., Hatzikiriakos S.G., Mitsoulis E. Entry Flow of Polyethylene Melts in Tapered Dies. *International Polymer Processing*, 2010, vol. 25, no. 4, pp. 287-296. doi: https://doi.org/10.3139/217.2360.

17. Padmanabhan M., Macosko C.W., Padmanabhan M. Extensional viscosity from entrance pressure drop measurements. *Rheologica Acta*, 1997, vol. 36, no. 2, pp. 144-151. doi: https://doi.org/10.1007/BF00366820.

18. Laun H.M. Pressure dependent viscosity and dissipative heating in capillary rheometry of polymer melts. *Rheologica Acta*, 2003, vol. 42, no. 4, pp. 295-308. doi: https://doi.org/10.1007/s00397-002-0291-6.

19. Laun H.M. Capillary rheometry for polymer melts revisited. *Rheologica Acta*, 2004, vol. 43, no. 5, pp. 509-528. doi: https://doi.org/10.1007/s00397-004-0387-2.

20. Brochard F., De Gennes P.G. Shear-dependent slippage at a polymer/solid interface. *Langmuir*, 1992, vol. 8, no. 12, pp. 3033-3037. doi: https://doi.org/10.1021/la00048a030.

21. Hatzikiriakos S.G., Dealy J.M. Wall slip of molten high density polyethylenes. II. Capillary rheometer studies. *Journal of Rheology*, 1992, vol. 36, no. 4, pp. 703-741. doi: https://doi.org/10.1122/1.550313.

22. Brochard-Wyart F., Gay C., de Gennes P.-G. Slippage of Polymer Melts on Grafted Surfaces. *Macromolecules*, 1996, vol. 29, no. 1, pp. 377-382. doi: https://doi.org/10.1021/ma950753j.

23. Hatzikiriakos S. G. Appropriate Boundary Conditions in the Flow of Molten Polymers. *International Polymer Processing*, 2010, vol. 25, no. 1, pp. 55-62. doi: https://doi.org/10.3139/217.2304.

24. Hatzikiriakos S.G. Wall slip of molten polymers. *Progress in Polymer Science*, 2012, vol. 37, no. 4, pp. 624-643. doi: https://doi.org/10.1016/j.progpolymsci.2011.09.004.

25. Hatzikiriakos S.G. Slip mechanisms in complex fluid flows. *Soft Matter*, 2015, vol. 11, no. 40, pp. 7851-7856. doi: https://doi.org/10.1039/C5SM01711D.

26. Sokolov A.V., Roedolf D. Introduction to practical rheology of polymers. *Plasticheskie massy*, 2018, no. 5-6, pp 31-34. doi: https://doi.org/10.35164/0554-2901-2018-5-6-31-34.

27. Chulieieva O., Zolotaryov V. Effect of the modifier on the thermophysical properties of fireproof ethylene-vinyl acetate copolymer composition materials. *Technology Audit and Production Reserves*, 2018, vol. 6, no. 1(44), pp. 23-28. doi: https://doi.org/10.15587/2312-8372.2018.150294.

28. Sadova A.N., Bortnikov V.G., Zaikin A.E. *Praktikum po tekhnologii pererabotki i ispytaniiam polimerov i kompozitsionnykh materialov* [Workshop on processing technology and testing of polymers and composite materials]. 2011, Moscow, KolosS Publ., 191 p. (Rus).

29. Weil E.D., Levchik S.V. *Flame Retardants for Plastics and Textiles*. Carl Hanser Verlag Publ., 2015. doi: https://doi.org/10.3139/9781569905791.fm.

V.M. Zolotaryov [1], *Doctor of Technical Science, Professor,*
O.V. Chulieieva[1], *Doctor of Technical Science,*
V.L. Chulieiev[1], *PhD,*
T.A. Kuleshova[1], *Senior Engineer,*
M.S. Suslin[1], *Engineer,*
[1] PJSC «YUZHCABLE WORKS»,
7, Avtogennaya Str., Khakiv, 61099, Ukraine,
e-mail: zavod@yuzhcable.com.ua;
echuleeva@ukr.net (Corresponding author);
vchuleev@ukr.net; kuleshova.tanushka@gmail.com;
suslin.nikolay@gmail.com

A. Boumassata, D. Kerdoun, O. Oualah

Maximum power control of a wind generator with an energy storage system to fix the delivered power

*Introduction. The power extracted from the wind turbine and delivered to the electrical network must be maximum and constant and the whole system should be have a good compromise between efficiency and cost. In order to attenuate this objective, a doubly fed induction machine, a cycloconverter, a maximum power point tracking algorithm and a flywheel energy storage system constitute a very interesting solution among many others that have been proposed. **Novelty**. The novelty of the proposed work is to use a doubly fed induction machine and a three pulses cycloconverter to reduce the cost and to integrate a flywheel energy storage system between the wind generator and the electrical network to maintain the constancy of the power sent to the network, following the instability of the wind. The proposed work uses a maximum power point tracking algorithm to capture the optimal power available in the wind in order to increase the efficiency of the system. **Results**. A detailed study of the proposed system is presented with the detailed dynamic modeling equations and simulation results are conducted to show the performance and the efficiency of the suggested work. References 21, figures 15.*
Key words: **maximum power point tracking, flywheel energy storage system, doubly fed induction machine, cycloconverter.**

Вступ. Потужність, що видобувається з вітряної турбіни і подається в електричну мережу, має бути максимальною і постійною, а вся система повинна мати хороший компроміс між ефективністю та вартістю. Щоб пом'якшити це завдання, асинхронна машина з подвійним живленням, дуже цікавим рішенням серед багатьох інших, які були запропоновані, є циклоконвертер, алгоритм відстеження точки максимальної потужності та система накопичення енергії маховика. Новизна. Новизна запропонованої роботи полягає у використанні асинхронної машини з подвійним живленням та триімпульсного циклоконвертера для зниження вартості та інтеграції маховикової системи накопичення енергії між вітрогенератором та електричною мережею для підтримки сталості потужності, що відправляється в мережу, враховуючи нестабільність вітру. Запропонована робота використовує алгоритм відстеження точки максимальної потужності для захоплення оптимальної потужності, доступної на вітру, щоб підвищити ефективність системи. Результати. Детальне дослідження запропонованої системи представлено з докладними рівняннями динамічного моделювання, а результати проведеного моделювання показують продуктивність та ефективність запропонованої роботи. Бібл. 21, рис. 15.
Ключові слова: **відстеження точки максимальної потужності, система накопичення енергії маховика, асинхронна машина з подвійним живленням, циклоконвертер.**

Introduction. Wind energy is the fastest growing energy among the new power generation sources in the world [1]. The most important machine used in wind turbine generators for wind energy conversion system is the doubly fed induction machine (DFIM).

The DFIM is an induction machine with wound rotor. It can function like motor or generator. The principal advantage of this machine is that the converter on the rotor side uses 20-30 % of the rated power [2].

Among the converters which make directly the conversion of power without any intermediary of a continuous bus, is the cycloconverter. This converter contains thyristors which make the system less expensive. Cycloconverter is habitually used in large power applications like rolling mills [3, 4], electric traction [5], static Scherbius drives [6] and more. The three pulses cycloconverter is our choice to control the DFIM in both systems (wind generator and flywheel energy storage system (FESS)).

The **purpose** of this work is to extract the maximum power available in the wind and to provide it to the electrical network as a constant as possible with good compromise between cost and efficiency.

In works [7, 8] a flywheel with an asynchronous machine have been integrated between the wind generator and the grid and controlled via an AC-DC-AC converter. In article [9] the author used a flywheel and a synchronous machine as a storage system and controlled by an AC-DC-AC converter. So, in order to achieve this purpose we used, a DFIM and a three pulses cycloconverter to reduce the cost and to support more current, a FESS between the wind generator and the network to maintain the constancy and to prove the quality of the power sent to the network following the instability of the wind, and a maximum power point tracking algorithm to capture the optimal power available in the wind to increase the efficiency of the whole system.

Figure 1 shows the configuration of the proposed and studied system.
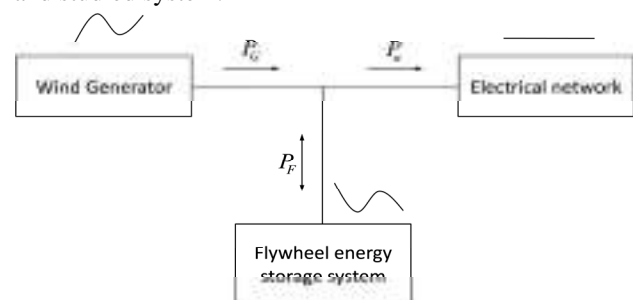
Fig. 1. Studied model

Modeling of the turbine. The mechanical power of the wind turbine P_t is written as [10-12]:

$$P_t = \frac{1}{2} \cdot \rho \cdot R \cdot C_p(\lambda, \beta) \cdot V^3, \qquad (1)$$

where ρ, R, C_p, λ, β and V are respectively the air density, turbine radius, power coefficient, tip speed ratio, pitch angle and the speed of the wind.

C_p is the wind turbine aerodynamic efficiency. It depends on λ and β, where λ is written as:

$$\lambda = \frac{\Omega_t \cdot R}{V}, \qquad (2)$$

where Ω_t is the speed of the turbine.

The power coefficient is defined as [13]:

$$C_p(\lambda,\beta) = (0.35 - 0.00167 \cdot (\beta - 2)) \cdot \sin\left(\frac{\pi \cdot (\lambda + 0.1)}{14.34 - 0.3 \cdot (\beta - 2)}\right) - \quad (3)$$
$$- 0.00184 \cdot (\lambda - 3) \cdot (\beta - 2).$$

Figure 2 shows the curve of C_p obtained via (3). The optimal value of C_p ($C_{p\max} = 0.35$) is for $\lambda = 7.1$ and $\beta = 2°$.
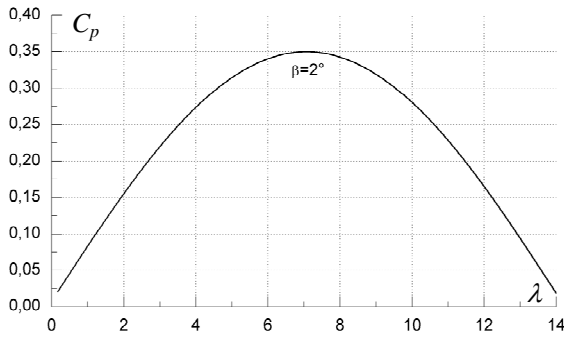
Fig. 2. C_p of the wind turbine

The expression of the mechanical equation is described as follows:

$$J \frac{d\Omega_{mec}}{dt} = T_m - T_{em} - f \cdot \Omega_{mec}, \qquad (4)$$

where J, f are the equivalent inertia and friction coefficient, respectively; Ω_{mec} is the generator's mechanical speed; T_{em} and T_m are the electromagnetic torque and the torque of the turbine referred to the generator, respectively.

Optimal power control. The optimal power characteristics of the wind turbine are strongly nonlinear. For each wind speed (Fig. 3), the system must find the maximum power of what is equivalent to search for the optimal rotor speed (mechanical speed).
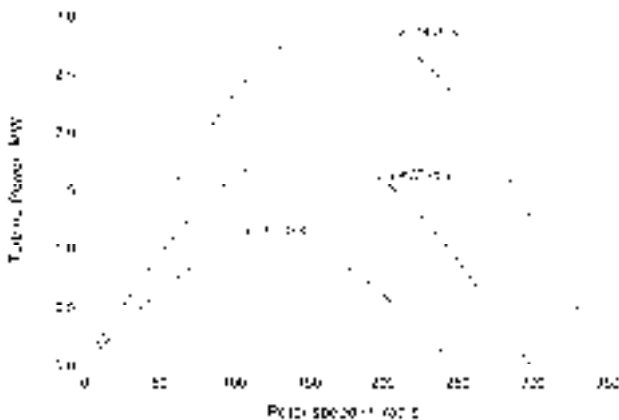
Fig. 3. Power-speed characteristics for different wind speeds

If the rotor speed does not reach its optimal value, the power of the turbine will not be able to reach the optimal power any more. It is possible to regulate the torque of the generator (electromagnetic torque) so as to control the rotor speed so that this one varies with the change of the wind speed (Fig. 4).
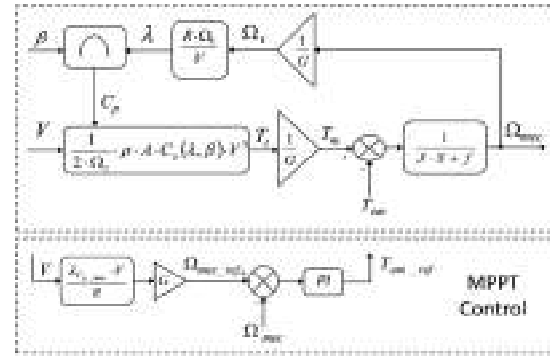
Fig. 4. Optimal power control

From Fig. 4 we can write the reference power as follows:

$$P_{ref} = T_{em\_ref} \cdot \Omega_{mec}. \qquad (5)$$

According to the maximum power point tracking (MPPT) control strategy, the reference power has been generated and delivered to the generator control system, which compares the reference power with the measured output power from the generator to produce the control signals for the power converter. Through the control of the converter, the electrical power of the generator will be equal to its reference, at which the maximum power operation will be achieved.

Modeling of the cycloconverter. The three phase cycloconverter is constituted of 18 thyristors. Each phase is constituted of two converters. The delay angles of those converters are modulated so as to supply an AC output voltage at the required magnitude and frequency.

Figure 5 illustrates the model of three phase-three phase cycloconverter. The function of the switches (Fig. 5) is described as:

$$S_{K_{ij}} = \begin{cases} 1 & S_{K_{ij}} \text{ is closed;} \\ 0 & S_{K_{ij}} \text{ is open,} \end{cases} \qquad (6)$$

where $K \in \{P, N\}$, $i \in \{a, b, c\}$, and $j \in \{A, B, C\}$.

The voltages equation at the output of the three phase cycloconverter can be written in function of $[T]$ as follows [14]:

Fig. 5. Three-phase cycloconverter

$$\begin{bmatrix} v_A \\ v_B \\ v_C \end{bmatrix} = [T] \cdot \begin{bmatrix} v_a \\ v_b \\ v_c \end{bmatrix}; \qquad (7)$$

$$[T] = \begin{bmatrix} (S_{P_{aA}} + S_{N_{aA}}) & (S_{P_{bA}} + S_{N_{bA}}) & (S_{P_{cA}} + S_{N_{cA}}) \\ (S_{P_{aB}} + S_{N_{aB}}) & (S_{P_{bB}} + S_{N_{bB}}) & (S_{P_{cB}} + S_{N_{cB}}) \\ (S_{P_{aC}} + S_{N_{aC}}) & (S_{P_{bC}} + S_{N_{bC}}) & (S_{P_{cC}} + S_{N_{cC}}) \end{bmatrix} \quad (8)$$

where v_a, v_b and v_c are the input voltages; v_A, v_B and v_C are the output voltages.

The voltages at the output of the cycloconverter are commanded using cosine-wave crossing control to produce the firing pulses of the switches. So we will have

three reference waves and three timing waves and a lot of intersection points. We will have 18 control circuits for this cycloconverter one for each switch [14].

Modeling of the DFIM. The electrical expressions of the DFIM are written as [15, 16]:

$$\begin{cases} V_{sdq} = R_s \cdot I_{sdq} + \dfrac{d\phi_{sdq}}{dt} \mp \dot{\theta}_s \cdot \phi_{sqd}; \\ V_{rdq} = R_r \cdot I_{rdq} + \dfrac{d\phi_{rdq}}{dt} \mp \dot{\theta}_r \cdot \phi_{rqd}; \end{cases} \quad (9)$$

$$\begin{cases} \phi_{sdq} = L_s \cdot I_{sdq} + M \cdot I_{rqd}; \\ \phi_{rdq} = L_r \cdot I_{rdq} + M \cdot I_{sqd}, \end{cases} \quad (10)$$

where R_s and R_r are the stator and rotor phase resistances; θ_s and θ_r are the stator and rotor field angles; L_s, L_r and M are the cyclic stator, rotor and mutual inductances, respectively.

The expressions of the active and reactive powers at the output of the DFIM are given as:

$$\begin{cases} P = P_s + P_r; \\ Q = Q_s + Q_r, \end{cases} \quad (11)$$

where P_s, Q_s, P_r and Q_r are the stator (rotor) active and reactive powers, respectively.

The equation of the electromagnetic torque is:

$$T_{em} = p \cdot \left(\phi_{sd} \cdot I_{sq} - \phi_{sq} \cdot I_{sd} \right), \quad (12)$$

where p is the pole pairs number.

Control of the DFIM. For controlling independently the active and reactive powers of the DFIM, the stator flux vector will be aligned with d-axis ϕ_{sd} ($\phi_{sd} = \phi_s$ and $\phi_{sq} = 0$) [17-19] and the expressions of the stator voltages are given by:

$$\begin{cases} V_{sd} = 0; \\ V_{sq} = V_s. \end{cases} \quad (13)$$

The rotor flux equations can be written as:

$$\begin{cases} \phi_{rd} = \sigma \cdot L_r \cdot I_{rd} + \dfrac{M}{L_s} \cdot \phi_{sd}; \\ \phi_{rq} = \sigma \cdot L_r \cdot I_{rq}, \end{cases} \quad (14)$$

with

$$\sigma = 1 - \frac{M^2}{L_s \cdot L_r}, \quad (15)$$

where σ is the leakage coefficient.

We can write the voltages at the rotor according to the rotor currents as follows:

$$\begin{cases} V_{rd} = R_r \cdot I_{rd} + \sigma \cdot L_r \cdot \dfrac{dI_{rd}}{dt} - s \cdot \omega_s \cdot \sigma \cdot L_r \cdot I_{rq}; \\ V_{rq} = R_r \cdot I_{rq} + \sigma \cdot L_r \cdot \dfrac{dI_{rq}}{dt} + s \cdot \omega_s \cdot \sigma \cdot L_r \cdot I_{rd} + s \cdot \dfrac{M \cdot V_s}{L_s}, \end{cases} \quad (16)$$

where s is the machine slip.

The simplified formula of the electromagnetic torque is given as follows:

$$T_{em} = -p \cdot \frac{M}{L_s} \cdot \phi_{sd} \cdot I_{rq}. \quad (17)$$

The expressions of the DFIM powers at the stator are written as follows:

$$\begin{cases} P_s = -V_s \cdot \dfrac{M}{L_s} \cdot I_{rq}; \\ Q_s = \dfrac{V_s^2}{\omega_s \cdot L_s} - V_s \cdot \dfrac{M}{L_s} \cdot I_{rd}, \end{cases} \quad (18)$$

We can simplify the expressions of the output powers of the DFIM as follows:

$$\begin{cases} P = (s-1) \cdot V_s \cdot \dfrac{M}{L_s} \cdot I_{rq}; \\ Q = \dfrac{V_s^2}{\omega_s \cdot L_s} + (s-1) \cdot V_s \cdot \dfrac{M}{L_s} \cdot I_{rd}. \end{cases} \quad (19)$$

The DFIM and the flywheel are the main parts of the flywheel energy storage system. This system stores energy in kinetic form and provides it in electrical form; in other words, the FESS stores energy in kinetic form in the flywheel during motor mode and it provides energy in electrical form during generator mode.

The kinetic energy stocked in the flywheel is defined as follows [9]:

$$E = \frac{1}{2} \cdot J_F \cdot \Omega_F^2 \quad (20)$$

or

$$E = \int P_M \cdot dt, \quad (21)$$

where J_F is the flywheel inertia; Ω_F is flywheel mechanical speed; P_M is the electrical power.

The reference active power provided to the network/FESS from the wind generator is determined by (5) (Fig. 4), and it's written as follows:

$$P_{G\_ref} = T_{em\_ref} \cdot \Omega_{mec}. \quad (22)$$

The expression of the reference active power (electrical power of the FESS) is determined from the difference between the desired power provided to the network and the power generated through the wind generator:

$$P_{M\_ref} = P_{n\_ref} - P_{G\_ref}. \quad (23)$$

The suggested system contains two control blocks: wind generator control block (Fig. 6) and FESS control block (Fig. 7). The first block is devoted to controlling the power provided from the wind generator to the network/FESS; when the power provided to the network from the wind generator is more than the required power at the network, the rest of this power is transferred to the FESS and stocked in the flywheel. The second block is devoted to controlling the power exchanged between the FESS and the network; the FESS stores the power from the wind generator and provides it to the network if the required power of the network is not enough.

The powers' expressions delivered to the network are written as:

$$\begin{cases} P_n = P_G + P_M; \\ Q_n = Q_G + Q_M. \end{cases} \quad (24)$$

The detailed control schemes of the DFIM in both wind generator and FESS are illustrated respectively in Fig. 6, 7.
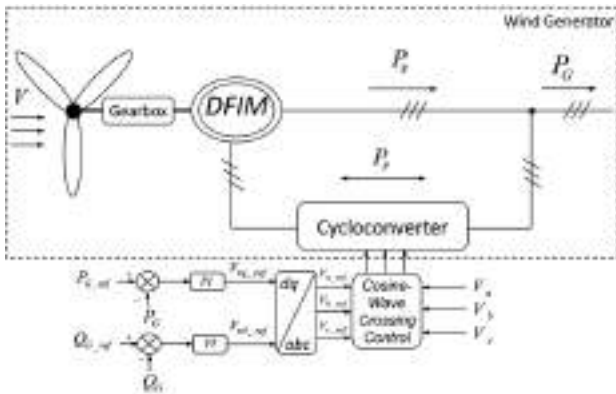
Fig. 6. Wind generator control block
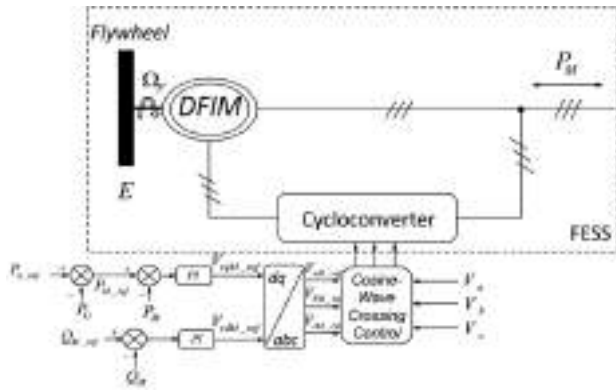
Fig. 7. Wind FESS control block

Simulation results. The model introduced in Fig. 1 was simulated under MATLAB/Simulink and its parameters are given as follows:

• wind generator [20]: number of blades = 3; gear box $G = 70$; blade radius $R = 40$ m; $S_n = 3$ MVA; $U_s = U_r = 690$ V; $f = 50$ Hz; $R_s = 2.97$ mΩ; $R_r = 3.82$ mΩ; $L_s = 12.241$ mH; $L_r = 12.177$ mH; $M = 12.12$ mH; $J = 116$ kg m^2; $p = 2$.

• DFIM (used in the FESS) [21]: $S_n = 1.5$ MVA; $R_s = 0,012$ Ω; $R_r = 0,021$ Ω; $L_s = 13,7037$ mH; $L_r = 13,6751$ mH; $M = 13,5$ mH; $f = 0,0024$; $p = 2$; $J_F \approx 351.5$ kg m^2.

The network requires a constant power of –1.5 MW (the negative value indicates that the network receive power).

The flywheel inertia value was calculated for a speed range between 120 rad/s and 200 rad/s during 3 s and the rated power is 1.5 MW.

Figures 8,a,b demonstrate the operation of the energy storage system.

The initial value of the rotor speed must be corresponding to the initial value of the wind speed.

The generator speed (Fig. 10) follows its reference and varies according to the wind speed variations (Fig. 9). This figure checks the MPPT control.

The active powers of the wind generator and the FESS (Fig. 11,a,b) follow their references correctly. The active power provided to the network given in Fig. 12,a is constant at –1.5 MW and the reactive power (Fig. 12,b) is zero for ensuring unity power factor.

Figure 13 shows the zoom of the voltage and current in the rotor side (FESS) and confirms the control of the cycloconverter.

The speed of the flywheel (Fig. 14) increases when the energy is stored and decreases when the energy is provided (Fig. 15).
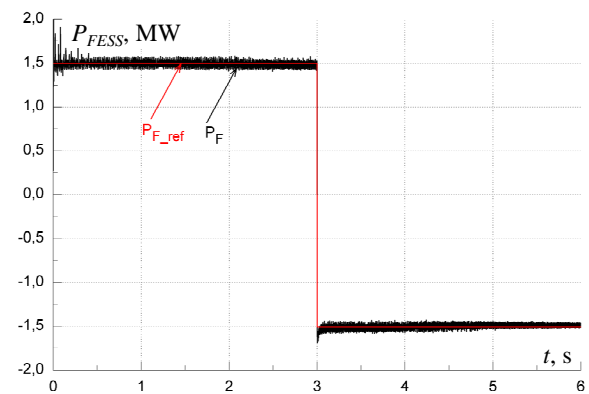
a
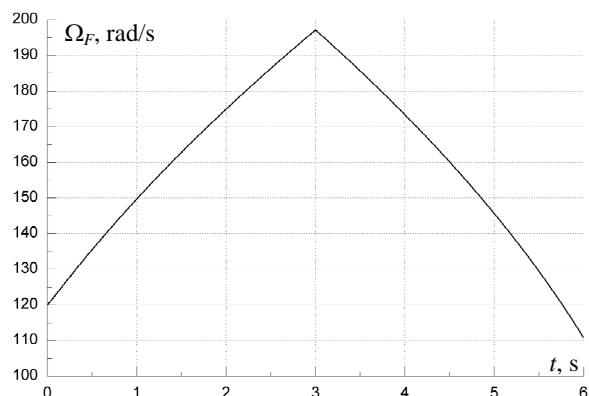
b

Fig. 8. Active power (a) and mechanical speed (b) of the FESS
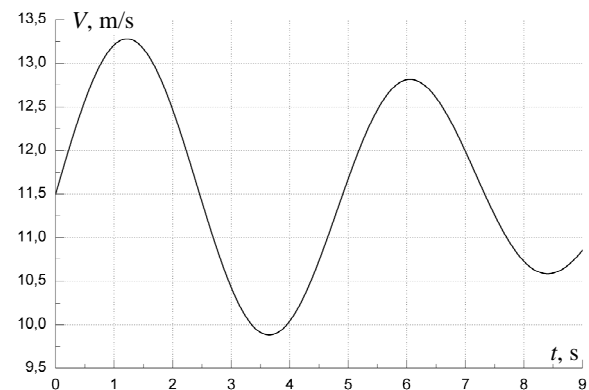
Fig. 9. Wind speed
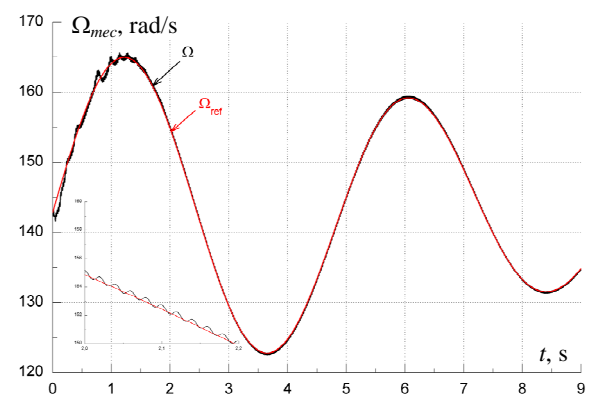
Fig. 10. Generator speed (wind generator)
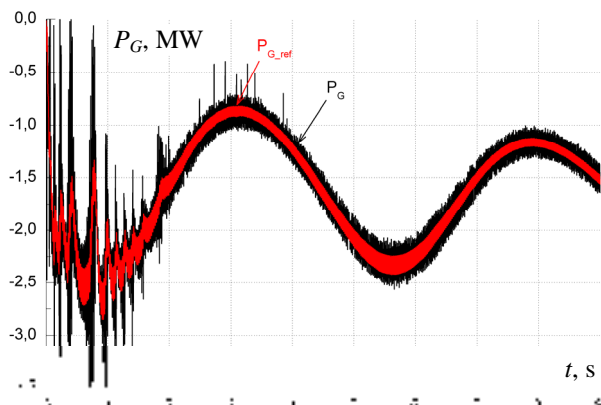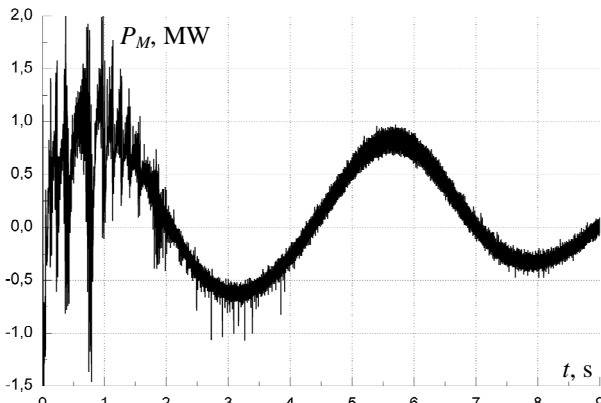
Fig. 11. Active powers of the wind generator (*a*) and the FESS (*b*)
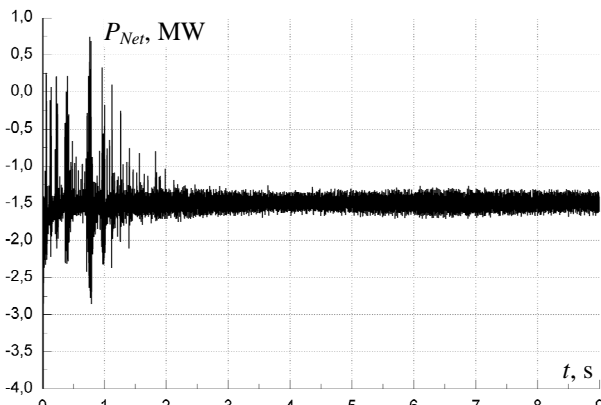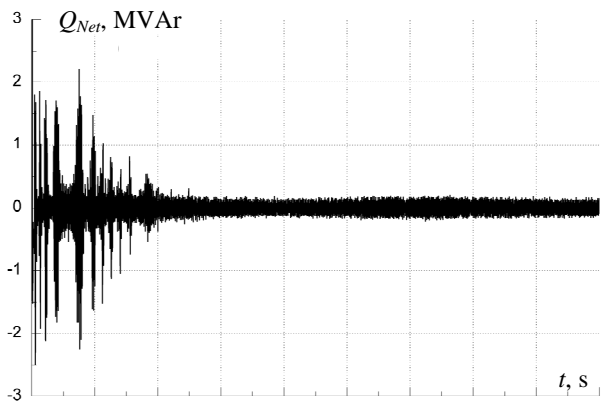
Fig. 12. Network powers
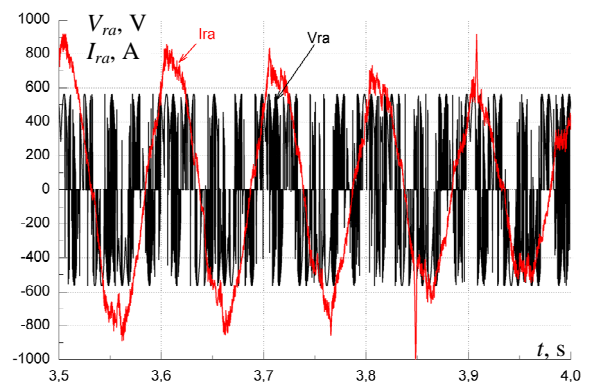
Fig. 13. Rotor phase voltage and current of the DFIM (FESS)
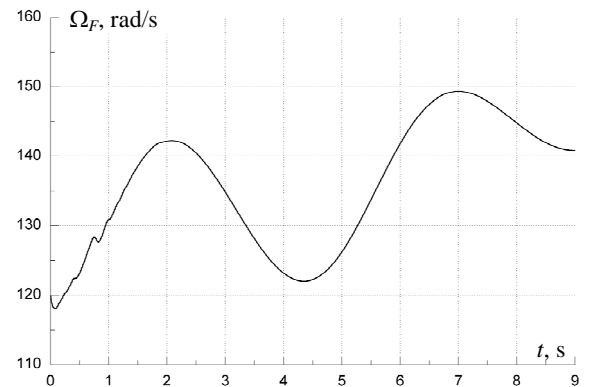
Fig. 14. Speed of the flywheel
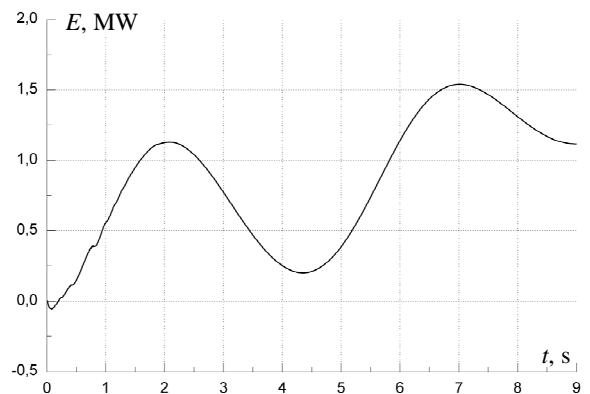
Fig. 15. Energy stocked in the flywheel

Conclusion.

In this article, the wind generator attached with a flywheel energy storage system was studied for different wind speed. The storage system based on doubly fed induction machine and three pulses cycloconverter has been controlled through a reference power as a function of a power generator and a desired network power. Simulation results show, firstly, that the extraction of the maximum power using maximum power point tracking control algorithm was well done. Secondly, they show that the flywheel energy storage system has been capable to store and provide energy, to ensure that the power sent to the electrical network remains constant. Finally, they demonstrate that the wind power fluctuations can be mostly compensated via the storage system. So, the performance and the efficiency of the suggested work have been verified.

Conflict of interest. The authors declare that they have no conflicts of interest.

REFERENCES

1. Beltran B., Ahmed-Ali T., Benbouzid M. High-Order Sliding-Mode Control of Variable-Speed Wind Turbines. *IEEE Transactions on Industrial Electronics*, 2009, vol. 56, no. 9, pp. 3314-3321. doi: https://doi.org/10.1109/TIE.2008.2006949.

2. Longya Xu, Wei Cheng. Torque and reactive power control of a doubly fed induction machine by position sensorless scheme. *IEEE Transactions on Industry Applications*, 1995, vol. 31, no. 3, pp. 636-642. doi: https://doi.org/10.1109/28.382126.

3. Timpe W. Cycloconverter Drives for Rolling Mills. *IEEE Transactions on Industry Applications*, 1982, vol. IA-18, no. 4, pp. 400-404. doi: https://doi.org/10.1109/TIA.1982.4504099.

4. Hagmann R. AC-cycloconverter drives for cold and hot rolling mill applications. *Conference Record of the 1991 IEEE Industry Applications Society Annual Meeting*, 1991, pp. 1134-1140. doi: https://doi.org/10.1109/IAS.1991.178005.

5. Jacovides L.J., Matouka M.F., Shimer D.W. A Cycloconverter - Synchronous Motor Drive for Traction Applications. *IEEE Transactions on Industry Applications*, 1981, vol. IA-17, no. 4, pp. 407-418. doi: https://doi.org/10.1109/TIA.1981.4503968.

6. Smith G.A. Static Scherbius system of induction-motor speed control. *Proceedings of the Institution of Electrical Engineers*, 1977, vol. 124, no. 6, p. 557. doi: https://doi.org/10.1049/piee.1977.0114.

7. Davigny A. *Participation aux services système de fermes d'éoliennes à vitesse variable intégrant du stockage inertiel d'énergie*. Thèse de doctorat, Hautes Études d'Ingénieur, 2007. (Fra).

8. Cimuca G.O. *Système inertiel de stockage d'énergie associé à des générateurs éoliens*. PhD Dissertation, Lille, ENSAM, 2005. (Fra).

9. Leclercq L. *Apport du stockage inertiel associé à des éoliennes dans un réseau électrique en vue d'assurer des services systèmes.* University of Lille in France, 2004. (Fra).

10. Boutoubat M., Mokrani L., Machmoum M. Control of a wind energy conversion system equipped by a DFIG for active power generation and power quality improvement. *Renewable Energy*, 2013, vol. 50, pp. 378-386. doi: https://doi.org/10.1016/j.renene.2012.06.058.

11. Tang C.Y., Guo Y., Jiang J.N. Nonlinear Dual-Mode Control of Variable-Speed Wind Turbines With Doubly Fed Induction Generators. *IEEE Transactions on Control Systems Technology*, 2011, vol. 19, no. 4, pp. 744-756. doi: https://doi.org/10.1109/TCST.2010.2053931.

12. El-Sattar A.A., Saad N.H., El-Dein M.Z.S. Dynamic response of doubly fed induction generator variable speed wind turbine under fault. *Electric Power Systems Research*, 2008, vol. 78, no. 7, pp. 1240-1246. doi: https://doi.org/10.1016/j.epsr.2007.10.005.

13. Gaillard A. *Système éolien basée sur une mada: contibution à l'étude de la qualité de l'énergie électrique et de la continuité de service*. PhD Dissertation, Nancy, 2010. (Fra).

14. Boumassata A., Kerdoun D. Modeling, Simulation and Control of Wind Energy Conversion System based on Doubly Fed Induction Generator and Cycloconverter. *Advances in Electrical and Computer Engineering*, 2014, vol. 14, no. 2, pp. 43-48. doi: https://doi.org/10.4316/AECE.2014.02007.

15. Kairous D., Wamkeue R. DFIG-based fuzzy sliding-mode control of WECS with a flywheel energy storage. *Electric Power Systems Research*, 2012, vol. 93, pp. 16-23. doi: https://doi.org/10.1016/j.epsr.2012.07.002.

16. Kassem A.M., Hasaneen K.M., Yousef A.M. Dynamic modeling and robust power control of DFIG driven by wind turbine at infinite grid. *International Journal of Electrical Power & Energy Systems*, 2013, vol. 44, no. 1, pp. 375-382. doi: https://doi.org/10.1016/j.ijepes.2011.06.038.

17. Poitiers F. Etude et commande de génératrices asynchrones pour l'utilisation de l'énergie éolienne-machine asynchrone à cage autonome-machine asynchrone à double alimentation reliée au réseau. PhD Dissertation, Université de Nantes, 2003. (Fra).

18. Bekakra Y., Ben Attous D. Sliding mode controls of active and reactive power of a DFIG with MPPT for variable speed wind energy conversion. *Australian Journal of Basic and Applied Sciences*, 2011, vol. 5, no. 12, pp. 2274-2286. Available at: http://www.ajbasweb.com/old/ajbas/2011/December-2011/2274-2286.pdf (Accessed 11 May 2021).

19. Jerbi L., Krichen L., Ouali A. A fuzzy logic supervisor for active and reactive power control of a variable speed wind energy conversion system associated to a flywheel storage system. *Electric Power Systems Research*, 2009, vol. 79, no. 6, pp. 919-925. doi: https://doi.org/10.1016/j.epsr.2008.12.006.

20. Gaillard A., Poure P., Saadate S., Machmoum M. Variable speed DFIG wind energy system for power generation and harmonic current mitigation. *Renewable Energy*, 2009, vol. 34, no. 6, pp. 1545-1553. doi: https://doi.org/10.1016/j.renene.2008.11.002.

21. El Aimani S. *Modélisation des différentes technologies d'éoliennes intégrées dans un réseau de moyenne tension*. PhD Dissertation, Ecole Centrale de Lille, 2004. (Fra).

Abderraouf Boumassata [1]*, Dr.,*
Djallel Kerdoun [2]*, Professor,*
Oussama Oualah [2]*, PhD Student,*
[1] Department of EEA, LGECP-Laboratory,
National Polytechnic School Constantine,
BP 75, A, Nouvelle ville RP, Constantine, Algeria,
e-mail: a_boumassata@umc.edu.dz (Corresponding Author)
[2] Department of Electrotechnical, LGEC-Laboratery,
Brothers Mentouri University Constantine 1,
Compus Ahmed Hamani, Zarzara, Constantine, Algeria,
e-mail: Kerdjallel@yahoo.fr, oussama.oulha@umc.edu.dz

S. Bouraghda, K. Sebaa, M. Bechouat, M. Sedraoui

An improved sliding mode control for reduction of harmonic currents in grid system connected with a wind turbine equipped by a doubly-fed induction generator

*Introduction. The implementation of renewable energy resources into the electrical grid has increased significantly in recent years. Wind power is one of the existing resources. Presently, power electronics has become an indispensable tool in wind power plants. **Problem.** However the associated control usually has an impact on increasing the harmonic distortion, especially on the output voltage. **Goal.** This paper proposes a new sliding mode control strategy, applied on a rotor-side of a doubly-fed induction generator. The main goal is to meet the electrical power requirements, while responding to the power quality issues. **Methodology.** The wind energy conversion system must be able to not only track the maximum power point of the wind energy, but also to mitigate the harmonic currents caused by the non-linear loads. To achieve this goal, the power converters are driven by the proposed sliding mode control strategy. The corresponding two gains of the sliding surface are well selected using a particle swarm optimization algorithm. The particle swarm optimization algorithm solves a constrained optimization problem whose fitness function is a prior formulated as the sum of two mean square error criterions. The first criterion presents the tracking dynamic of the reference active power while the second one presents the tracking dynamic of the reference reactive power. **The novelty** lies in the implementation of the particle swarm optimization algorithm in conventional sliding mode control strategy, in which the proposed-improved sliding mode control strategy is developed. The wind energy conversion system control uses the principal of the vector oriented control to decouple the control of the active power from that of the reactive power. **Results.** The improved sliding mode control strategy is applied to control separately theses powers in the presence of non-linear loads. The energy assessment of this strategy is analysed using the wind energy conversion system model based on SimPower software. **Originality.** The obtained simulation results confirm the superiority of the proposed-improved sliding mode control strategy in terms of reference tracking dynamics and suppression of harmonic currents.* References 23, tables 2, figures 11.
Key words: **doubly-fed induction generator; wind energy conversion system; bidirectional converter; particle swarm optimization; sliding mode control.**

*Вступ. Використання відновлюваних джерел енергії в електричній мережі останніми роками значно зросло. Енергія вітру – один із існуючих ресурсів. Нині силова електроніка стала незамінним інструментом вітряних електростанцій. **Проблема.** Проте, відповідне управління зазвичай має вплив на збільшення гармонійних спотворень, особливо у вихідній напрузі. **Мета.** У цій статті пропонується нова стратегія управління ковзним режимом, що застосовується на боці ротора асинхронного генератора з подвійним живленням. Основна мета – задовольнити вимоги до електроенергії, вирішуючи відповідні проблеми з якістю електроенергії. **Методологія.** Система перетворення енергії вітру повинна мати можливість не тільки відстежувати точку максимальної потужності вітру, але й пом'якшувати гармонійні струми, викликані нелінійними навантаженнями. Для досягнення цієї мети силові перетворювачі керуються запропонованою стратегією управління ковзним режимом. Відповідні два коефіцієнти посилення поверхні ковзання добре вибираються з використанням алгоритму оптимізації рою частинок. Алгоритм оптимізації рою частинок вирішує задачу оптимізації з обмеженнями, функція придатності якої заздалегідь сформульована як сума двох критеріїв середньоквадратичної похибки. Перший критерій репрезентує динаміку відстеження еталонної активної потужності, а другий – динаміку відстеження еталонної реактивної потужності. **Новизна** полягає в реалізації алгоритму оптимізації рою частинок у традиційній стратегії управління ковзним режимом, в якій розроблена запропонована покращена стратегія управління ковзним режимом. Управління системою перетворення енергії вітру використовує принцип векторно-орієнтованого управління, щоб відокремити управління активною потужністю від управління реактивною потужністю. **Результати.** Удосконалена стратегія управління ковзним режимом застосовується для роздільного управління цими потужностями за наявності нелінійних навантажень. Енергетична оцінка цієї стратегії аналізується за допомогою моделі системи перетворення енергії вітру на основі програмного забезпечення SimPower. **Оригінальність.** Отримані результати моделювання підтверджують перевагу запропонованої удосконаленої стратегії управління ковзним режимом з точки зору еталонної динаміки стеження та придушення гармонійних струмів.* Бібл. 23, табл. 2, рис. 11.
Ключові слова: **асинхронний генератор із подвійним живленням; система перетворення енергії вітру; двонаправлений перетворювач; оптимізація рою частинок; керування ковзним режимом.**

Abbreviations

APF	Active Power Filter	PRC	Proportional Resonance Control
BTB	Back-To-Back	PSO	Particle Swarm Optimization
DFIG	Doubly-Fed Induction Generator	PWM	Pulse-Width Modulation
DPC	Direct Power Control	RSC	Rotor-Side Converter
DTC	Direct Torque Control	SMC	Sliding Mode Control
GSC	Grid-Side Converter	THD	Total Harmonic Distortion
HSF	High Selectivity Filter	VCS	Vector Control Scheme
MPP	Maximum Power Point	VOC	Vector Oriented Control
MSE	Mean Square Error	WECS	Wind Energy Conversion System
NLL	Non-Linear Loads	WPP	Wind Power Plants
PMSG	Permanent Magnet Synchronous Generator	WT	Wind Turbine

Introduction. The incorporation of renewable energy resources into the electrical grid has increased significantly in recent years. Among of them, the wind energy is one of the existing resources whose potential demand has increased due to domestic and industrial

necessities. This growth is mainly due to the advanced technology used in the design of WECS, reducing the cost of producing electrical energy and enabling it to be competitive with other traditional sources such as fossil fuels, petroleum, natural gas, and so on. A lot of research has focused on DFIG systems in their structures. These have several advantages, including speed control, current harmonic reduction and four-quadrant active and reactive power control. As its rotor speed can be operated at any wind speed, the DFIG system is therefore able to deliver high mechanical power and, in economic terms, it becomes more attractive than other existing conversion systems, thanks to its conversion rate, which is generally around 30% of the nominal power, allowing thus to generate the electrical energy at a lower cost [1].

Currently, power electronics has become an indispensable tool in WPPs to ensure such required specifications such as steady state stability, high energy efficiency, regardless of changing wind conditions. In fact, these tools are often providing many important functionalities to WTs, including the control of several electrical quantities such as stator terminal voltage and frequency, active and reactive power and so on. Nevertheless, the associated control effort usually has an impact on increasing the harmonic distortion, especially on the output voltage of existing converters. As a result, the occurrence of inadequate harmonics has unfortunately become the main issue for the majority of wind energy designers as well as the company managers [2]. The attenuation of the effect of such harmonics on the DFIG system can be performed through proper regulation of the existing converters in the control loop. Similarly, the power quality problem can also be posed of serious challenges where its remedy has been discussed by several researchers [1, 2]. On these grounds, many control strategies have been proposed to overcome these drawbacks. Among them, a control strategy was published in [3] where the WECS is designed to operate partially as an active filter. Also, another control strategy that can be employed to simultaneously generate active and reactive power where an extra active filter is incorporated into a DFIG wind system having a variable speed [1]. Similarly, a modulation technique was proposed in [4] for shunt active filter operation, in which the existing harmonics in the WECS output current are well mitigated. The corresponding feedback control system incorporates a PMSG as well as an AC/DC current converter. Also, a PWM control strategy including a five-leg converter was proposed in [5] where the given performances are compared by those provided by the conventional six-leg topology. The main shortcoming, compared to the six-leg BTB converter, lies in the restriction of increasing the DC link voltage for the same operating point. In parallel, a PRC strategy was developed in [6] for a stationary reference frame to mitigate, as much as possible, the existing harmonics in the rotor current and in torque pulsations. In the same direction, a VCS was suggested in [7, 8] for rotor-side control of a stand-alone generator based on a wound rotor induction machine. The main aim of the proposed control scheme is to keep a constant terminal voltage with stationary frequency at the generator output. In the same way, the

full harmonic component compensation technique of the grid current was adopted in [9]. The corresponding RSC control structure is modified, in which a filtering task is incorporated. Also, an efficiency assessment of the electrical part of the WECS was reported in [10] where the two BTB-PWM inverters, which are supplied with voltage and connected between the stator and rotor, are used to improve the bidirectional power flow. Accordingly, the second inverter, which is disposed on the grid side, serves as an active power filtering to remove the harmonics, generated by the nonlinear load, while providing the required active and reactive power to the DFIG rotor.

Different alternative control strategies have been developed for wind power generation in the electrical grid. Among them, the VOC and the two direct control strategies such as the DTC and the DPC are becoming the most widely used in real world applications [11]. Furthermore, some other nonlinear control strategies have been proposed in the literature where the best known is the SMC, which has proven to be the most attractive during the last decades. This is due to its inherent properties to overcome complex challenges that are caused by the presence of unmolded dynamics, the neglect of high frequency dynamics, the presence of model uncertainties, the variation of model parameters, the presence of load disturbances, and the persistence of the effect of sensor noise. To this purpose, it is important to emphasize that the SMC-based synthesis of a robust controller, taking into account all the previous obstacles, is crucial for the active and reactive power control of the DFIG equipped with a wind turbine [12]. Nevertheless, this control strategy has the capacity to provide good reference tracking dynamics, high robustness in the presence of the preceding factors, and a good tradeoff between the two preceding targets. However, it also presents various misfunctions when strict specifications are considered. Among them, the undesired phenomenon known as «chattering» occurs during the operation of the WECS near its operating point. The drawback that results from this phenomenon is often associated with improper selection of sliding surface gains where trial and error selection is typically performed, leading thus to control inaccuracy, dramatic performance degradation and high thermal loss in power devices. To overcome this problem, the PSO algorithm is introduced in the conventional-SMC-based synthesis where their gains are properly optimized. This can be done by solving the constrained optimization problem whose fitness function is perfectly minimized. The manner of the incorporation of the PSO algorithm in conventional SMC strategy constitutes therefore the main contribution of this paper.

Goal. In this paper, the actual behavior of WECS is primarily modelled near its operating point. Then, the VOC principal is used for decoupling the active power control from the reactive power one. Finally, the improved-SMC-based synthesis is applied to ensure the proper reference tracking dynamics where the suppression of harmonic currents is considered.

System description. The WECS is mainly composed by a DFIG equipped with a wind turbine. Its stator is connected to the grid while the BTB PMW

converter is connected between the DFIG rotor and the grid. The grid-side converter GSC is used to provide bi-directional power flow that is generated from the rotor-side converter RSC, stabilizing thus the DC link voltage and achieving unity power factor. Figure 1 shows the block diagram of a grid-connected DFIG wind turbine.
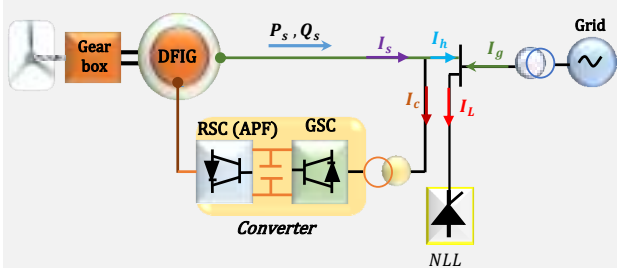
Fig. 1. Block diagram of the grid connected DFIG wind turbine in the presence of NLL

In general, the NLL often unfortunately injects harmonic current into the grid where the desired controller for active and reactive power regulations must be operated as an active filter, in which the existing harmonic currents and voltages are well absorbed. Also, from Fig. 1, the node law imposes that:

$$I_g = I_L - I_h ; \quad (1)$$

$$I_h = I_s - I_c . \quad (2)$$

The stator current I_s of the DFIG is assumed to have a non-sinusoidal waveform close to that of the NLL current I_L. The converter is designed to supply a pure sinusoidal current I_c. Then, the harmonic current I_h thus represents the current that the APF (rotor converter) must generate. Therefore, and in accordance with (1), the grid current I_g will be clear of unwanted harmonic components. To be in agreement with these assumptions, the suggested WECS must generate the same harmonic components as the non-linear current but with opposite phases. This may be performed by investigating the correct control circuit of the rotor converter. Keep in mind that this control circuit may also be used to achieve decoupled control of active and reactive power. The NLL currents must be measured. Following that, the measured load currents (I_{La}, I_{Lb}, I_{Lc}) are converted using the abc to α–β (stationary reference frame) transformation. The NLL current is equal to the sum of the fundamental frequency and various harmonics, as shown below:

$$I_{L\alpha} = I_{L\alpha f} + I_{L\alpha h} ; \quad (3)$$

$$I_{L\beta} = I_{L\beta f} + I_{L\beta h} , \quad (4)$$

where ($I_{L\alpha h}$, $I_{L\beta h}$) and ($I_{L\alpha f}$, $I_{L\beta f}$) are the NLL current's harmonic and fundamental constituents.

Based on (3), (4) and by deducting the load current from its fundamental component, the harmonic components of the NLL current can be expressed. The approach depicted in Fig. 2 can be utilized to distinguish the harmonic of NLL. In this figure, the Park transformation is applied to convert the α–β current components to d–q (synchronous) reference frame. The HSF is used to extract the fundamental component from α–β components. The HSF is a band pass filter as in Fig. 2 [8].

It should be noted that the design of the controller design based on the SMC strategy for tracking both

reference active and reference reactive powers requires prior modeling of all parts involved in the actual WECS behavior, such as wind-turbine part, the rotor-side and stator-side of the converter.
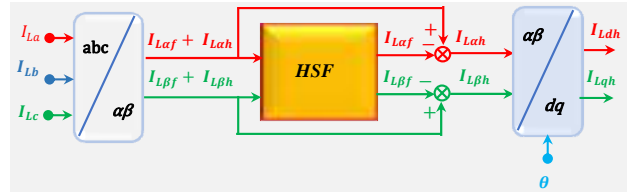
Fig. 2. Harmonic isolation of the whole load harmonic current

Modeling of actual WECS behavior. Modeling of wind turbine. A wind turbine collects the wind through its blades and transmits it to the rotor hub. The kinetic energy of the wind is accordingly converted into mechanical power, generating thus a mechanical torque. Also, the rotor shaft generates an electrical energy and transmits it to the grid. Since the wind energy is found in the form of kinetic energy where its amplitude depends on the air density and the wind speed [12, 13]. The power of the wind P_v being found in the form of kinetic energy when it crosses at the speed V_v, air density ρ and the surface area S. It can be expressed by:

$$P_v = \frac{1}{2} \cdot \rho \cdot S \cdot V_v^3 . \quad (5)$$

The wind turbine can usually only recuperate a part of the preceding power P_v, resulting thus the power P_t that is expressed by:

$$P_t = \frac{1}{2} \cdot \rho \cdot \pi \cdot R^2 \cdot V_v^3 \cdot C_p , \quad (6)$$

where R is the radius of the wind turbine; C_p is the corresponding power coefficient, which is given as a function of the wind speed, the rotation speed and the pitch angle.

Also, C_p is often given as a function of the tip speed ratio λ, which is defined by:

$$\lambda = \frac{\Omega_t \cdot R}{V_v} , \quad (7)$$

where Ω_t is the angular speed of the rotor.

Furthermore, the wind power P_t and the power extracted by the wind turbine P_v are expressed in terms of the power coefficient C_p. Hence, one can obtain:

$$P_t = \frac{1}{2} \cdot C_p(\lambda, \beta) \cdot \rho \cdot S \cdot V_v^3 , \quad (8)$$

where the coefficient $C_p(\lambda,\beta)$ has a theoretical limit, called BETZ limit. It is defined by:

$$C_p(\lambda, \beta) = C_1 \cdot \left(\frac{C_2}{\lambda_i} - C_3 \cdot \beta - C_4 \right) e^{\frac{-C_5}{\lambda_i}} + C_6 \cdot \lambda . \quad (9)$$

The numerical values of the parameters C_k are experimentally given by:

$$\begin{matrix} C_1 = 0.5176; C_2 = 116; C_3 = 0.4; \\ C_4 = 5; C_5 = 21; C_6 = 0.0068, \end{matrix} \quad (10)$$

while the parameter λ_i is expressed by:

$$\frac{1}{\lambda_i} = \frac{1}{(\lambda + 0.08 \cdot \beta)} - \frac{0.035}{\beta^3 + 1} . \quad (11)$$

It is worth noting here that the power conversion coefficient C_p is expressed as a function of the tip speed

ratio λ and the pitch angle β of the rotor blades. Their evolution, depending on λ for different values of β, is illustrated in Fig. 3 [14].

Fig. 3. Evolution of C_p as a function of λ for different β values

From Fig. 3 it seems that the power conversion coefficient C_p reaches its maximum when the pitch angle β is zero and the tip speed ratio λ becomes optimal. Therefore, the corresponding curve is shown in Fig. 4.

Fig. 4. Extraction of the curve defining the maximum power conversion coefficient C_{pmax}

Also, the rotor torque T_t can be computed from the received power P_t and the speed of rotation Ω_t of the turbine. Therefore, the simplified equation that defines the rotor torque is given by:

$$T_t = \frac{\rho \cdot \pi \cdot R^3 \cdot V_v^2}{2} \cdot C_t, \qquad (12)$$

where C_t indicates the torque coefficient, which depends heavily on the power conversion coefficient C_p according to the following equation:

$$C_p(\lambda) = \lambda \cdot C_t(\lambda). \qquad (13)$$

Using the adequate model that resulting from momentum theory requires a priori knowledge of both expressions $C_p(\lambda)$ and $C_t(\lambda)$. Indeed, these two last ones depend essentially on the geometrical characteristics of the blades. Therefore, they are adapted to particular characteristics such as the site where the WECS is located, the desired nominal power, the control type such as pitch or stall, and the WECS operation in variable or fixed speed.

Modeling of DFIG. The DFIG design model is determined by applying the conventional modeling in the Park reference frame. Therefore, the corresponding voltage and flux equations are expressed by [12, 15]:

$$V_{sd} = R_s \cdot i_{sd} + \frac{d\psi_{sd}}{dt} - \omega_s \cdot \psi_{sq};$$

$$V_{sq} = R_s \cdot i_{sq} + \frac{d\psi_{sq}}{dt} + \omega_s \cdot \psi_{sq}; \qquad (14)$$

$$V_{rd} = R_r \cdot i_{rd} + \frac{d\psi_{rd}}{dt} - \omega_r \cdot \psi_{rq};$$

$$V_{rq} = R_r \cdot i_{rq} + \frac{d\psi_{rq}}{dt} + \omega_r \cdot \psi_{rd}; \qquad (15)$$

$$\psi_{rd} = L_r \cdot i_{rd} + L_m \cdot i_{sd};$$

$$\psi_{rq} = L_r \cdot i_{rq} + L_m \cdot i_{sq}; \qquad (16)$$

$$\psi_{sd} = L_s \cdot i_{sd} + L_m \cdot i_{rd};$$

$$\psi_{sq} = L_s \cdot i_{sq} + L_m \cdot i_{rq}. \qquad (17)$$

Also, the electromagnetic torque is expressed by:

$$T_{em} = \frac{3}{2} \cdot \left(\psi_{sd} \cdot i_{sq} - \psi_{sq} \cdot i_{sd} \right) \qquad (18)$$

and both active and reactive powers are expressed by:

$$P_s = \frac{3}{2} \cdot \left(V_{sd} \cdot i_{sd} + V_{sq} \cdot i_{sq} \right); \qquad (19)$$

$$Q_s = \frac{3}{2} \cdot \left(V_{sd} \cdot i_{sq} - V_{sq} \cdot i_{sd} \right), \qquad (20)$$

where V and i are the voltage and current, respectively; R and L are the resistance and inductance, respectively; ψ and ω are the flux and angular speed of the DFIG, respectively; P and Q are the active and reactive powers, respectively.

Also, from (14)-(20), the indexes d and q represent respectively, the electrical components, which are located in the d–axis and the q–axis, while the indexes r, s and m represent respectively the values of the rotor, the stator and the magnetization.

Design controllers for DFIG wind turbine. Design controller for GSC. The proposed control for this converter is the VOC strategy, which employs a rotational reference frame (d–q) oriented to the space vector of the grid voltage (Fig. 5). Thanks to this kind of strategy, it is possible to achieve the two main targets of the converter on the grid side, i.e., the control of the DC bus voltage as well as the power transmission performed by the converter using the controlled reactive power transmission.

Fig. 5. Control loop performed in the grid-side converter (g subscript demonstrates grid-side components)

Accordingly, the difference between the reference DC voltage V_{bus}^* and the measured DC voltage V_{bus} becomes the input of the V_{bus} regulator. Indeed, the i_{dg} regulator is used to remove the discrepancy that is

occurred between the reference current i_{dg}^* and the current i_{dg}. It allows to regulate the active power P_g of the grid. Similar, the i_{qg} regulator is used to control the reactive power Q_g of the grid, in which the difference $i_{qg}^* - i_{qg}$ is removed [16].

For better performance in the dynamic responses, there is additionally one coupling component in each equation that is best incorporated in the control as a feed-forward term, as illustrated in Fig. 5 (at the output of the current controllers) [16]:

$$e_{qf} = -\omega_s \cdot L_f \cdot i_{qg} ; \qquad (21)$$

$$e_{df} = \omega_s \cdot L_f \cdot i_{dg} . \qquad (22)$$

Design controller for RSC The rotor-side converter is designed to control the DFIG output power to grid. It is also used to control the power factor across the DFIG [1]. The stator active and reactive powers serve as the control inputs of the RSC. As mentioned previously, the aim is to operate the DFIG as an APF. The SMC strategy is used for the RSC where the block diagram of RSC is shown in Fig. 6.
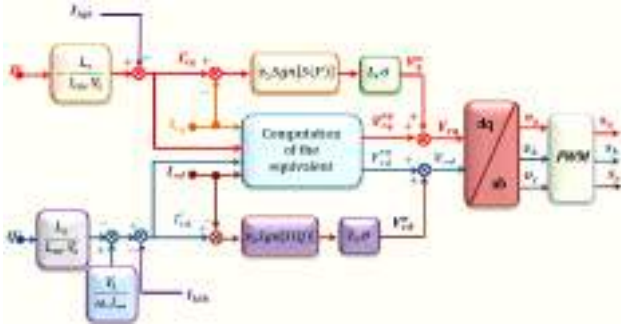
Fig. 6. Control loop performed in the rotor-side converter

Assuming that a reference frame is rotating synchronously with the stator flux and we suppose that the network is stable, the stator flux ψ_{sd} is becoming constant and equal to ψ_s. On the other hand, the stator flux ψ_{sq} becomes zero, i.e., $\psi_{sd} = \psi_s$; $\psi_{sq} = 0$. Also, for the generators utilized in the wind turbine the stator resistance R_s may be ignored, resulting in $V_{sd} = 0$ and $V_{sq} = V_s = \omega_s \cdot \psi_{sq}$.

Conventional SMC strategy The SMC strategy is a very powerful nonlinear tool that has been widely employed by researchers, especially in the last decades [15, 17]. It consists in moving the system behavior along a predetermined sliding surface, where a numeric control signal is applied [12]. Moreover, the state trajectory of the closed-loop system must be oriented towards the sliding surface $S(x) = 0$ and maintained constantly around this surface using the switching logic function U^n. In general, the basic SMC law is commonly expressed by [18, 19]:

$$U_c = U^{eq} + U^n , \qquad (23)$$

where U^{eq} is the equivalent control law that is applied when the existing states of the system are located in the slip plane.

The control law U^n is alternated between $-k$ and $+k$ where $k > 0$. It is defined by:

$$U^n = k \cdot \text{sgn}[S(x)] . \qquad (24)$$

Also, the sigmoid function occurred in (24) is defined by:

$$\text{sgn}[S(x)] = \begin{cases} -1 & \text{if} \quad S(x) < 0; \\ 1 & \text{if} \quad S(x) > 0. \end{cases} \qquad (25)$$

According to the SMC principal, the control law U^n has often stabilized the WECS behavior, in which the given power conversion becomes maximal and the corresponding speed ratio reaches its optimal point λ_{opt}. This closed-loop stability requires often to satisfy the Lyapunov condition that is expressed by:

$$S(x) \cdot \dot{S}(x) < 0 , \qquad (26)$$

where $\dot{S}(x) = \dfrac{dS(x)}{dt}$ denotes the derivative of the sliding surface, which is expressed as a function of the variable to be controlled (x). This last will be considered as either the active power or the reactive power that is delivered by the WECS.

The goal is first to decouple the control of the active power P_s from that of the reactive power Q_s. Then, the desired controller based on the conventional SMC strategy should keep good track of both reference powers P_s^* and Q_s^*, in which a proper suppression of all harmonics occurring in the duty currents should be taken into account. These requirements need detailing some equations such as the rotor currents and their derivatives as well as the sliding surfaces and their derivatives. Furthermore, the relationships between reference stator powers and the reference rotor currents are given by:

$$I_{rq}^* = \frac{-L_s}{V_s \cdot L_m} \cdot P_s^* - I_{Lqh}; \qquad (27)$$

$$I_{rd}^* = \frac{V_s}{\omega_s \cdot L_m} - \frac{L_s}{V_s \cdot L_m} \cdot Q_s^* - I_{Ldh} . \qquad (28)$$

Noted here, that the reference reactive power Q_s^* is set to zero and the reference active power P_s^* can be expressed is related to the synchronous speed ω_s, and the electromagnetic torque T_{em} can be expressed by:

$$P_s^* = \Omega_s \cdot T_{em} . \qquad (29)$$

Moreover, the derivative of rotor currents, in d–axis and q–axis, are expressed by:

$$\frac{dI_{rq}}{dt} = \frac{1}{L_r \cdot \sigma}\left(V_{rq} - R_r \cdot I_{rq} - g \cdot \omega_s \cdot L_r \cdot \sigma \cdot I_{rd} - g \cdot \omega_s \cdot \frac{L_m \cdot V_s}{\omega_s \cdot L_s}\right); \quad (30)$$

$$\frac{dI_{rd}}{dt} = \frac{1}{L_r \cdot \sigma}\left(V_{rd} - R_r \cdot I_{rd} + g \cdot \omega_s \cdot L_r \cdot \sigma \cdot I_{rq}\right),$$

where g and σ are respectively the slip and dispersion coefficient.

In general, the active power becomes directly proportional to the rotor current in q–axis, while the reactive power becomes proportional to the rotor current in d–axis. Accordingly, the control surface of each power is expressed by:

$$S(P) = I_{rq}^* - I_{rq} ; \qquad (31)$$

$$S(Q) = I_{rd}^* - I_{rd} . \qquad (32)$$

Knowing that the appropriate reference tracking dynamics necessitates that all sliding surfaces as well as their derivatives must be equal to zero, i.e., $S(P) = 0$, $S(Q) = 0$, $\dot{S}(P) = 0$ and $\dot{S}(Q) = 0$. These require that the

plot of P_s (with respect to Q_s) is exponentially converged to the one of the corresponding reference powers P_s^* (with respect to Q_s^*). Therefore, all previous sliding surfaces necessarily become attractive and invariant, where the key to the success of the SMC strategy strongly depends on respecting the attractivity relationship of Lyapunov [17], given by (26).

Control law used for active power control This part focuses on finding the two parts of the control law V_{rq}^{eq} (equivalent control vector) and V_{rq}^n (switching part of the control) that constituting the rotor voltage V_{rq}, given in q–axis. Accordingly, the derivative of the sliding surface $\dot{S}(P)$ is computed using (30)-(32), which yields also (33) as follow:

$$\dot{S}(P) = \frac{-L_s}{L_m \cdot V_s} \cdot \dot{P}_s^* - \dot{I}_{Ldh} -$$
$$-\frac{1}{L_r \cdot \sigma} \cdot \left(V_{rq} - R_r \cdot I_{rq} - g \cdot \omega_s \cdot L_r \cdot \sigma \cdot I_{rd} - g \cdot \frac{L_m \cdot V_s}{L_s} \right). \quad (33)$$

From (33) the control law V_{rq} is determined and then decomposed into the two control laws V_{rq}^{eq} and V_{rq}^n, where $V_{rq} = V_{rq}^{eq} + V_{rq}^n$. The resulting rotor voltages in q–axis are given by:

$$V_{rq} = \frac{-L_s \cdot L_r \cdot \sigma}{L_m \cdot V_s} \cdot \dot{P}_s^* - \dot{I}_{Ldh} + R_r \cdot I_{rq} + g \cdot \omega_s \cdot L_r \cdot \sigma \cdot I_{rd} +$$
$$+ g \cdot \frac{L_m \cdot V_s}{L_s} + L_r \cdot \sigma \cdot v_1 \cdot \text{sgn}[S(P)] \quad (34)$$

$$V_{rq}^{eq} = \frac{-L_s \cdot L_r \cdot \sigma}{L_m \cdot V_s} \cdot \dot{P}_s^* - \dot{I}_{Lqh} + R_r \cdot I_{rq} +$$
$$+ g \cdot \omega_s \cdot L_r \cdot \sigma \cdot I_{rd} + g \cdot \frac{L_m \cdot V_s}{L_s}; \quad (35)$$

$$V_{rq}^n = L_r \cdot \sigma \cdot v_1 \cdot \text{sgn}[S(P)]. \quad (36)$$

Control law used for reactive power control Similarly, the derivative of the sliding surface $\dot{S}(Q)$ is first computed and the control law V_{rd} is then extracted as follows:

$$\dot{S}(Q) = \left(\frac{V_s}{L_m \cdot \omega_s} - \frac{L_s}{L_m \cdot V_s} \cdot \dot{Q}_s^* - \dot{I}_{Ldh} \right) -$$
$$-\frac{1}{L_r \cdot \sigma} \left(V_{rd} - R_r \cdot I_{rd} + g \cdot \omega_s \cdot L_r \cdot \sigma \cdot I_{rq} \right); \quad (37)$$

$$V_{rd} = L_r \cdot \sigma \left(\frac{V_s}{L_m \cdot \omega_s} - \frac{L_s}{L_m \cdot V_s} \cdot \dot{Q}_s^* - \dot{I}_{Ldh} \right) + R_r \cdot I_{rd} -$$
$$- g \cdot \omega_s \cdot L_r \cdot \sigma \cdot I_{rq} + L_r \cdot \sigma \cdot v_2 \cdot \text{sgn}[S(Q)] \quad (38)$$

According to (38), the two control laws V_{rd}^{eq} and V_{rd}^n are expressed by:

$$V_{rd}^{eq} = L_r \cdot \sigma \left(\frac{V_s}{L_m \cdot \omega_s} - \frac{L_s}{L_m \cdot V_s} \cdot \dot{Q}_s^* - \dot{I}_{Ldh} \right) +$$
$$+ R_r \cdot I_{rd} - g \cdot \omega_s \cdot L_r \cdot \sigma \cdot I_{rq}; \quad (39)$$

$$V_{rd}^n = L_r \cdot \sigma \cdot v_2 \cdot \text{sgn}[S(Q)]. \quad (40)$$

The block diagram that explains the SMC implementation for active and reactive power controls of the DIFG equipped with a wind turbine is given in Fig. 6.

From (38), (40), it is obvious that the desired reference tracking dynamic requires the proper interaction of all states of the system toward the switching surfaces, i.e., $S(P) = 0$ and $S(Q) = 0$. This still leads to the occurrence of the chattering problem due to the existing of the sigmoid function in both control laws V_{rq}^n and V_{rd}^n, in which the control law V_{rq}^n can either have the gain $-v_1$ or $+v_1$. In the other hand, the control law V_{rd}^n can either have the gain $-v_2$ or $+v_2$. To overcome this challenge, the implementation of the PSO algorithm to optimize the two gains appearing in the two preceding control laws becoming an indispensable key in the design phase of the controllers. This enables to highlight the improved version of the SMC strategy whose details are discussed in the next part.

Improved SMC strategy In this study, the main contribution lies in the selection of the two optimal gains v_1 and v_2 involved in the two control laws V_{rq}^n and V_{rd}^n respectively. The corresponding bounded optimization problem includes the fitness function $J(X)$, expressed as the MSE criterion. It consists of the sum of the two squared errors e_1 and e_2, produced by the simultaneous tracking of the two reference powers P_s^* and Q_s^*. Accordingly, the optimization problem can be expressed by:

$$\min_{X_{\min} \leq X \leq X_{\max}} J(X) = \min_{X_{\min} \leq X \leq X_{\max}} \left\{ \frac{1}{NT} \sum_{i=1}^N \left[e_1^2(X) + e_2^2(X) \right] \right\} \quad (41)$$

where both tracking errors e_1 and e_2 are defined by $e_1(X) = P_s(X) - P_s^*$ and $e_2(X) = Q_s(X) - Q_s^*$ respectively, $X = (X_1, X_2)^T$ denotes the design vector to be optimized where their components are constrained by $-v_1 \leq X_1 \leq +v_1$ and $-v_2 \leq X_2 \leq +v_2$, N and T denote the total number of samples and the sampling time.

The PSO algorithm is implemented in a classical SMC strategy to avoid the fast switching of the two gains v_1 and v_2 from their positive to their negative values. In fact, there is a multitude of unknown gains found between the two positive and negative bounds for each gain of the sliding surface. The objective is therefore mainly to focus on finding the optimal gains during the tracking process of the two reference powers. These optimal gains lead to finding two feasible optimal commands, in which the chattering problem of the SMC strategy is well solved. The optimization process by the PSO algorithm is carried out as follows: The PSO algorithm uses a swarm made up of particles $n_p \in N$ to know in search of the sub-optimal solution $X^* \in N^{q \times 1}$ which minimizes the objective function, called $J(X) \in R$. The position and velocity of particle vectors i^{th} are given respectively by $X_i = (X_{i,1}, X_{i,2}, ..., X_{i,q})^T$ and $V_i = (V_{i,1}, V_{i,2}, ..., V_{i,q})^T$. They are determined by the following iterative expressions [20-22]:

$$V_i^{l+1} = c_0 \cdot V_i^l + c_1 \cdot r_{1,i}^l \cdot \left(X_i^{best,l} - X_i^l \right) +$$
$$+ c_2 \cdot r_{2,i}^l \cdot \left(X_{swarm}^{best,l} - X_i^l \right); \qquad (42)$$
$$X_i^{l+1} = X_i^l + V_i^{l+1},$$

where l is the number of iterations previously provided by the user; c_0, c_1 and c_2 are respectively the inertia factor, the cognitive (individual) and social (group) learning relationships; $r_{1,i}^l$ and $r_{2,i}^l$ are random numbers evenly distributed over the interval [0, 1], $X_i^{best,l}$ and $X_{swarm}^{best,l}$ are respectively the best position obtained previously by the particle and the best position obtained in the whole of the swarm at the current iteration l. In summary, the PSO algorithm can consist of the following steps [21-23]:

• **Step 1:** initialize the n_p particles with positions chosen at random and which should previously be contained in the lower and upper bound vector X_{min} and X_{max};

• **Step 2:** evaluate the fitness function for each position;

• **Step 3:** determine the initial solutions $X_i^{best,0}$ and $X_{swarm}^{best,0}$;

• **Step 4:** check the stop condition. If it is satisfied, the algorithm then converges to the desired optimal gains v_1^{opt} and v_2^{opt}. Otherwise, go to the next step;

• **Step 5:** assign the new values obtained to all particles (updates);

• **Step 6:** go back to step 2.

It should be noted that the PSO algorithm is achieved by obtaining the two optimal gains v_1^{opt} and v_2^{opt}. They are multiplied by the constant value $L_r \cdot \sigma$ and then used for computing the two optimal commands $V_{rq}^{n\,opt}$ and $V_{rd}^{n\,opt}$. Knowing that the two equivalent commands such as V_{rq}^{eq} and V_{rd}^{eq} are a priori computed using (35), (39), respectively. The resulting four preceding optimal commands are used to compute the two optimal rotor voltages V_{rq}^{opt} and V_{rd}^{opt} using (34), (38), respectively.

Simulation results and discussion. The previous system (Fig. 1) was modelled and simulated using SimPower System Demo, MATLAB/Simulink. The proposed control strategy is applied to a WECS equipped with a 2MW DFIG. The system parameters are presented in the Appendix 1. The optimal values obtained are $V_1 = 1550.05211$ and $V_2 = 525.0299$ as shown in the fitness plots (Fig. 7) provided by the algorithm during the extraction process for 20 execution of the code.

Figure 8 is the simulation results for active and reactive power response in case of sliding mode control. In this case study, simulation results show clearly the improvement of active and reactive power demand obtained by applying sliding mode control in term of time response and good reference tracking accuracy.
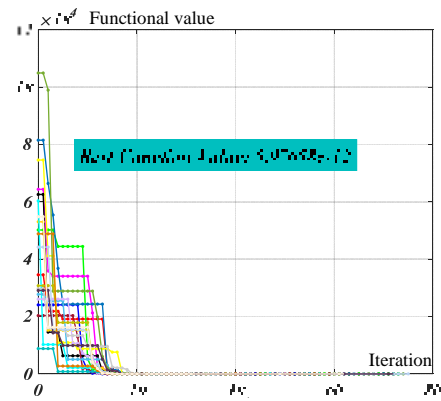
Fig. 7. The obtained fitness curve through PSO
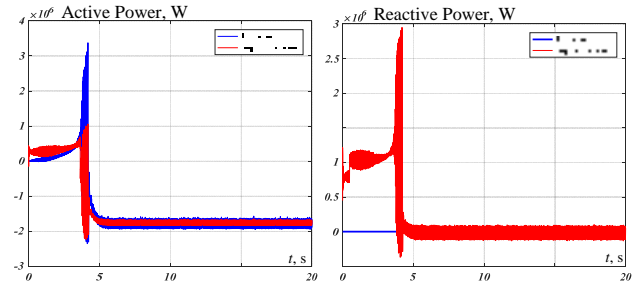
Fig. 8. Active and reactive powers

The most significant harmonic components which will spread in the grid side with a THD as depicted in Fig. 9. After implementing the active filtering technique on the rotor current control loop, the waveform became greatly improved with better harmonic spectrum as displayed in Fig. 10. Referring to the results obtained, THD values are put in the table below (Table 1). The grid side inverter gives an active and reactive power needed by the rotor of DFIG.

Table 1

THD of the grid current

THD without filtering, %	THD after filtering, %
26.22	2.45
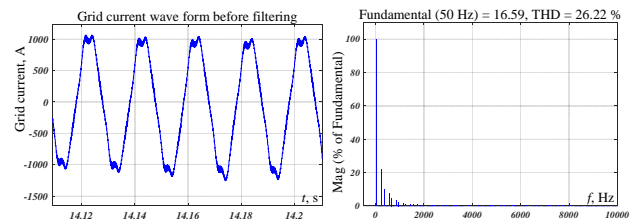
Fig. 9. Grid current wave form and his harmonic spectrum before filtering
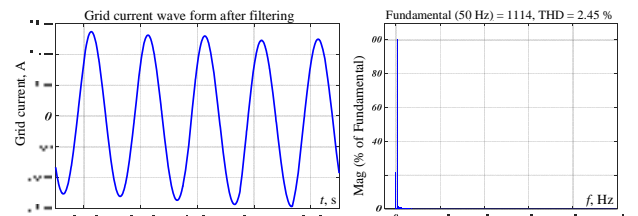
Fig. 10. Grid current wave form and his harmonic spectrum after filtering

The reference harmonic compensating currents is shown in Fig. 10. Concerning V_{dc} regulation, the obtained result is satisfying. In fact, as illustrated in Fig. 11, after a transient state, V_{dc} follows perfectly its reference ($V_{ref} = 1190$ V).
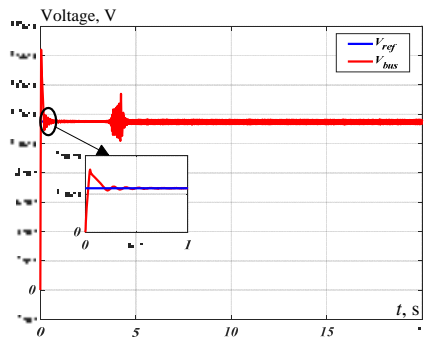
Fig. 11. DC-bus voltage wave form

Conclusions.

In this article, a study concerning a wind turbine based on a doubly-fed induction generator connected to the grid has been elaborated. The goals were to implement a rotor current control loop that would eliminate harmonic currents generated from a coupled nonlinear load using an active filtering concept, while also permitting independent regulation of power flow from and to the generator. For this reason, rotor converter was used as an active power filter. The response was conclusive given the improvements (an almost sinusoidal shape) obtained in the network current. Where we have found that the total harmonic distortion decrease from 26.22 % (before filtering) to 2.45 % (after filtering).

In addition, the other goal was to regulate the common DC bus voltage between the rotor converter and the grid converter. In this study, we discovered that the simulation results show clearly the improvement of active and reactive power demand obtained by applying sliding mode control in term of time response and good reference tracking accuracy.

In summary, the following characteristics of the proposed wind energy conversion system are highlighted in the following points:

1. Possibility to recover the maximum quantity of power from the input wind speed.

2. Using an active power filter to reduce the harmonic currents.

Finally, in order to complete the suggested investigation, the power factor must be corrected. Additionally, the system should be implemented on a real machine in order to explore the impact of the saturation effect on the performance of the generator. These considerations will be investigated in future work.

Conflict of interest. The authors declare that they have no conflicts of interest.

Appendix 1

System parameters [16]

	Parameter	Value		Parameter	Value
Turbine	Radius, m	42	DFIG	Speed range, rpm	900-2000
	Nominal wind speed, m/s	12.5		Pole pairs	2
	Optimum tip speed ratio λ_{opt}	7.2		Magnetizing inductance L_m, mH	2.5
	Maximum power coefficient C_{pmax}	0.44		Rotor leakage inductance L_r, μH	87
	Air density ρ, kg/m^3	1.1225		Stator leakage inductance L_s, μH	87
	Inertia J, kg·m^2	127		Rotor resistance R_r, mΩ	26
	Friction D, N·m·s/rad	0.001		Stator resistance R_s, mΩ	29
DFIG	Nominal stator active power, MW	2	Grid	Grid inductance L_g, mH	0.4
	Nominal torque, N·m	12732		Grid resistance R_g, mΩ	0.02
	Stator voltage, V	690		Grid frequency f, Hz	50
	Nominal speed, rpm	1500		Grid voltage V_g, V	690

REFERENCES

1. Nosratabadi S.M., Gholipour E. Power system harmonic reduction and voltage control using DFIG converters as an active filter. *Turkish Journal of Electrical Engineering & Computer Sciences*, 2016, vol. 24, pp. 3105-3122. doi: https://doi.org/10.3906/elk-1406-35.
2. Dhua D., Yang G., Zhang Z., Kocewiak L.H., Timofejevs A. Harmonic Active Filtering and Impedance-based Stability Analysis in Offshore Wind Power Plants. *Proceedings of 16th Wind Integration Workshop*, 2017, pp. 1-8.
3. Mishra A., Tripathi P.M., Chatterjee K. A review of harmonic elimination techniques in grid connected doubly fed induction generator based wind energy system. *Renewable and Sustainable Energy Reviews*, 2018, vol. 89, pp. 1-15. doi: https://doi.org/10.1016/j.rser.2018.02.039.
4. Hoseinpour A., Masoud Barakati S., Ghazi R. Harmonic reduction in wind turbine generators using a Shunt Active Filter based on the proposed modulation technique. *International Journal of Electrical Power & Energy Systems*, 2012, vol. 43, no. 1, pp. 1401-1412. doi: https://doi.org/10.1016/j.ijepes.2012.06.052.
5. Gonçalves P.F.C., Cruz S.M.A., Mendes A.M.S. Fault-Tolerant Predictive Control of a Doubly-Fed Induction Generator with Minimal Hardware Requirements. *IECON 2018 - 44th Annual Conference of the IEEE Industrial Electronics Society*, 2018, pp. 3357-3362, doi: https://doi.org/10.1109/IECON.2018.8592825.

6. Hosseini Mousavi S.N., Barati H. Direct power control simultaneously in the rotor side converter and grid side converter of DFIG for wind turbines with elimination of network current harmonics. *Journal of Novel Researches on Electrical Power*, 2019, vol. 8, no. 3, pp: 37-51. Available at: http://jeps.iaud.ac.ir/article-1-229-en.pdf (Accessed 20 May 2021).
7. Xu W., Yu K., Liu Y., Gao J., Hua W. Improved Harmonics Elimination for Standalone Brushless Doubly-Fed Induction Generator with Nonlinear Loads. *2018 XIII International Conference on Electrical Machines (ICEM)*, 2018, pp. 243-249. doi: https://doi.org/10.1109/ICELMACH.2018.8506764.
8. Gaillard A., Poure P., Saadate S., Machmoum M. Variable speed DFIG wind energy system for power generation and harmonic current mitigation. *Renewable Energy*, 2009, vol. 34, no. 6, pp. 1545-1553. doi: https://doi.org/10.1016/j.renene.2008.11.002.
9. Kesraoui M., Chaib A., Meziane A., Boulezaz A. Using a DFIG based wind turbine for grid current harmonics filtering. *Energy Conversion and Management*, 2014, vol. 78, pp. 968-975. doi: https://doi.org/10.1016/j.enconman.2013.07.090.
10. Mahieddine H., Zarour L., Lamri L., Lokmane N.A. Developing a grid-connected DFIG strategy for the integration of wind power with harmonic current mitigation. *International Journal of Electrical and Computer Engineering (IJECE)*, 2019, vol. 9, no. 5, pp. 3905. doi: https://doi.org/10.11591/ijece.v9i5.pp3905-3915.
11. Kadri A., Marzougui H., Bacha F. Implementation of direct power control based on stator flux estimation using low-pass

filter estimator for doubly fed induction generator–wind energy conversion system. *Proceedings of the Institution of Mechanical Engineers, Part I: Journal of Systems and Control Engineering*, 2019, vol. 233, no. 7, pp. 764-778. doi: https://doi.org/10.1177/0959651818818895.

12. Rouabhi R., Abdessemed R., Chouder A., Djerioui A. Power Quality Enhancement of Grid Connected Doubly-Fed Induction Generator Using Sliding Mode Control. *International Review of Electrical Engineering (IREE)*, 2015, vol. 10, no. 2, pp. 266. doi: https://doi.org/10.15866/iree.v10i2.5347.

13. Kahla S., Bechouat M., Amieur T., Sedraoui M., Babes B., Hamouda N. Maximum power extraction framework using robust fractional-order feedback linearization control and GM-CPSO for PMSG-based WECS. *Wind Engineering*, 2021, vol. 45, no. 4, pp. 1040-1054. doi: https://doi.org/10.1177/0309524X20948263.

14. Hamouda N., Benalla H., Hemsas K., Babes B., Petzoldt J., Ellinger T., Hamouda C. Type-2 fuzzy logic predictive control of a grid connected wind power systems with integrated active power filter capabilities. *Journal of Power Electronics*, 2017, vol. 17, no. 6, pp. 1587-1599. doi: https://doi.org/10.6113/JPE.2017.17.6.1587.

15. Beltran B., Benbouzid M., Ahmed-Ali T., Mangel H. DFIG-based wind turbine robust control using high-order sliding modes and a high gain observer. *International Review on Modelling and Simulations*, 2011, vol. 4, no. 3, pp. 1148-1155. Available at: https://hal.archives-ouvertes.fr/hal-00630436v2/document (Accessed 20 May 2021).

16. Abad G., López J., Rodríguez M.A., Marroyo L., Iwanski G. *Doubly Fed Induction Machine: Modeling and Control for Wind Energy Generation*. John Wiley & Sons, 2011. 625 p. doi: https://doi.org/10.1002/9781118104965.

17. Abdellah A., Abdelhafid A., Mostafa R. Combining sliding mode and linear quadratic regulator to control the inverted pendulum. *International Review of Automatic Control*, 2013, vol. 6, no. 1, pp. 69-76. Available at: https://www.praiseworthyprize.org/jsm/index.php?journal=ireaco&page=article&op=view&path%5B%5D=11286 (Accessed 20 May 2021).

18. Sadeghi R., Madani S.M., Ataei M., Agha Kashkooli M.R., Ademi S. Super-Twisting Sliding Mode Direct Power Control of a Brushless Doubly Fed Induction Generator. *IEEE Transactions on Industrial Electronics*, 2018, vol. 65, no. 11, pp. 9147-9156. doi: https://doi.org/10.1109/TIE.2018.2818672.

19. Radhwane S., Abdelkader M., Salim D., Aissa K. A fuzzy sliding mode robust control for a field oriented dual star induction machine fed by photovoltaic power supply with MPPT algorithm. *Mediterranean Journal of Measurement and Control*, 2016, vol. 12, no. 4, pp. 654-663. Available at: https://www.researchgate.net/publication/309674107_A_fuzzy_sliding_mode_robust_control_for_a_field_oriented_dual_star_induction_machine_fed_by_photovoltaic_power_supply_with_MPPT_algorithm (Accessed 20 May 2021).

20. Zahedi H., Arab Markadeh G., Taghipour S. Real-time implementation of sliding mode control for cascaded doubly fed induction generator in both islanded and grid connected modes. *Journal of Electrical and Computer Engineering Innovations (JECEI)*, 2020, vol. 8, no. 2, pp. 285-296. doi: https://doi.org/10.22061/jecei.2020.7361.384.

21. Bechouat M., Younsi A., Sedraoui M., Soufi Y., Yousfi L., Tabet I., Touafek K. Parameters identification of a photovoltaic module in a thermal system using meta-heuristic optimization methods. *International Journal of Energy and Environmental Engineering*, 2017, vol. 8, no. 4, pp. 331-341. doi: https://doi.org/10.1007/s40095-017-0252-6.

22. Bechouat M., Soufi Y., Sedraoui M., Kahla S. Energy storage based on maximum power point tracking in photovoltaic systems: A comparison between GAs and PSO approaches. *International Journal of Hydrogen Energy*, 2015, vol. 40, no. 39, pp. 13737-13748. doi: https://doi.org/10.1016/j.ijhydene.2015.05.008.

23. Soufi Y., Bechouat M., Kahla S. Fuzzy-PSO controller design for maximum power point tracking in photovoltaic system. *International Journal of Hydrogen Energy*, 2017, vol. 42, no. 13, pp. 8680-8688. doi: https://doi.org/10.1016/j.ijhydene.2016.07.212.

Skander Bouraghda[1], *PhD, Assistant Professor,*
Karim Sebaa[1], *Professor,*
Mohcen Bechaoua[2,3], *PhD, Associate Professor,*
Moussa Sedraoui[3], *Professor,*
[1] Laboratory of Advanced Electronic Systems (LSEA),
University of Medea, Algeria,
e-mail: skander21440@yahoo.fr (Corresponding Author),
karim.sebaa@gmail.com
[2] Automatic & Electromechanic Department,
University of Ghardaia, Algeria,
e-mail: mohcene.oui@gmail.com
[3] The Telecommunications Laboratory,
8 Mai 1945 – Guelma University, Alegria,
e-mail: sedraoui.moussa@univ-guelma.dz

S. Ghanem, G. Fandi, J. Kyncl, Z. Müller

A novel scheme for control by active and reactive power utilized in gearless variable speed wind turbine system with PMSG connected to the grid

Introduction. As a result of increasing fossil fuel price and state-of-the-art technology, more and more residential and commercial consumers of electricity have been installing wind turbines. The motivation being to cut energy bills and carbon dioxide emissions. ***Purpose.*** *The main goal of this work is developing a control scheme for a variable speed wind turbine generator in order to produce utmost power from varying wind types, and variable wind speed.* ***Novelty.*** *This research paper presents an IGBT power converter control scheme for active power in relation to wind speed and reactive power by adjusting Q-reference (Q_{ref}) value in a gearless variable speed wind turbine with permanent magnet synchronous generator.* ***Methods.*** *An effective modelling and control of the wind turbine with the suggested power converter is executed by utilizing MATLAB/Simulink software. The control scheme consists of both the wind turbine control and the power converter control. Simulation results are utilized in the analysis and deliberation of the ability of the control scheme, which reveals that the wind turbine generator has the capability to actively sustain an electric power grid network, owing to its ability to independently control active and reactive power according to applied reference values at variable wind speed.* ***Practical value.*** *This research can be utilized for assessing the control methodology, the dynamic capabilities and influence of a gearless variable-speed wind energy conversion system on electric power grids. A case study has been presented with a (3·10 MW = 30 MW) wind farm scheme.* References 67, tables 2, figures 19.*
Key words: **wind turbine, wind farm, gearless wind turbine, variable-speed wind turbine, IGBT power converter, multi-pole permanent magnet synchronous generator, full-scale power converter.**

Вступ. Внаслідок зростання цін на викопне паливо та використання найсучасніших технологій, дедалі більше побутових та комерційних споживачів електроенергії встановлюють вітряні турбіни. Мотивація полягає в тому, щоб скоротити рахунки за електроенергію та викиди вуглекислого газу. ***Мета.*** *Основною метою цієї роботи є розробка схеми управління вітряним генератором зі змінною швидкістю для отримання максимальної потужності від різних типів вітру та змінної швидкості вітру.* ***Новизна.*** *У даній дослідницькій роботі представлена схема управління силовим IGBT перетворювачем для активної потужності в залежності від швидкості вітру та реактивної потужності шляхом регулювання значення Q-еталона (Q_{ref}) у безредукторній вітровій турбіні з регульованою швидкістю та синхронним генератором із постійними магнітами.* ***Методи.*** *Ефективне моделювання та керування вітровою турбіною з запропонованим перетворювачем потужності здійснюється з використанням програмного забезпечення MATLAB/Simulink. Схема управління складається з управління вітряною турбіною і з управління силовим перетворювачем. Результати моделювання використовуються для аналізу та обговорення можливостей схеми управління, що показує, що генератор вітрової турбіни здатний активно підтримувати електроенергетичну мережу завдяки своїй здатності незалежно контролювати активну та реактивну потужність відповідно до застосовуваних еталонних значень при змінній швидкості вітру.* ***Практична цінність.*** *Це дослідження може бути використане для оцінки методології управління, динамічних можливостей та впливу безредукторної системи перетворення енергії вітру зі змінною швидкістю на електричні мережі. Наведено тематичне дослідження зі схемою вітряної електростанції (3·10 МВт = 30 МВт).* Бібл. 67, табл. 2, рис. 19.*
Ключові слова: **вітряна турбіна, вітряна електростанція, безредукторна вітряна турбіна, вітряна турбіна з регульованою швидкістю, силовий IGBT перетворювач, багатополюсний синхронний генератор з постійними магнітами, повномасштабний силовий перетворювач.**

Introduction. Presently, there has been progressive advancement in modern renewable wind power plant technology. Specifically, the gearless wind power plant with permanent magnet synchronous generator is utilizing full-scale power converter. Electric power production from renewable energy sources, such as wind, is growingly drawing attraction due to environmental issues, long-term economic advantages and scarcity of conventional energy sources in the near future. The main cost-efficient and practicable disadvantage of wind power is its intermittent characteristics. Wind power requires not only that wind is flowing, all the same it also rely on cut-in and cut-out wind speed that is the wind speeds at which production starts and is brought to a stop in order to keep away from harm. The production of power from the wind on a large-scale, has become an accepted business. It holds substantial prospect for the future, hoping that wind power will become the most accepted choice and form of renewable energy source. Wind energy technology application has come of age, with numerous nations preparing and establishing extensive wind energy farms, with enormous amount of wind turbines. The strength of

wind power technology is that it is clean and inexpensive. As a result of increasing fossil fuel price and state-of-the-art technology, more and more residential and commercial consumers of electricity have been installing wind turbines, the motivation being to cut energy bills and carbon dioxide emissions, and are even vending extra electricity back to the grid network [1-11].

The permanent magnet synchronous generators (PMSGs) are widely utilized in wind turbines owing to their excellent operation and power quality characteristics in the variable speed wind energy transformation systems, its turbine control systems are more complex when weighed with constant speed wind power converter systems. The fixed speed wind turbine implementations are not normally chosen due to their low capabilities and their power quality is not at a required level [12-18]. PMSGs are among the finest solutions for wind power plants. Low-speed multi-pole permanent magnet synchronous generators are free from maintenance and can be utilized in diverse climatic environment. A traditional megawatt-scale wind turbine generator

composes of a low-speed wind turbine rotor, gearbox, and high-speed electric generator. The utilization of gearbox gives rise to several technological issues in a wind turbine generator, as it requires frequent maintenance, it multiplies the weight and total cost of the wind turbine generator, it produces noise, and also multiplies power losses. These issues can be solved by utilizing a substitute, a direct-drive low-speed permanent magnet synchronous generator [18-20]. But a more appropriate solution and way out is to utilize a gearless wind turbine generator.

A multi-pole synchronous generator attached to a power converter can function at low speeds, so that a gear can be excluded. A gearless structure symbolizes a proficient and durable explanation, which can be immensely advantageous mainly for offshore utilizations. Besides, owing to the permanent magnet excitation of the generator the direct current excitation structure can be removed thereby further reducing once more the weight, losses, costs and maintenance demands [20, 21]. The ability of a PMSG wind turbine is consequently evaluated to be higher than alternative ideas [22, 23]. Nevertheless, the drawbacks of the permanent magnet excitation are the excessive costs of permanent magnet constituents and a fixed excitation, which can't be adjusted in accordance with the functional consideration [2].

The dependability of the variable speed wind turbine can be ameliorated notably by utilizing a direct drive PMSG. The PMSG has been given considerable attention in wind power implementation reason being its property of self-excitation, which permits functioning at a high-power factor and high capability [24]. The utilization of permanent magnet in the rotor of the PMSG causes it non-essentially to provide magnetizing current using the stator for constant air-gap flux; the stator current requires just to be torque generating.

Therefore, for the same output, the PMSG will function at a higher power factor due to the absence of magnetizing current. To produce utmost power from varying wind, variable speed functioning of the wind turbine generator is obligatory. This needs a highly-developed control scheme for the generator [25]. A control scheme for the generator side converter with utmost output of a PMSG wind turbine needs to be put in place. The generator side switch mode rectifier is controlled to obtain utmost energy from the wind. This necessitate only one active switching device (IGBT), which is utilized to control the generator torque in order to obtain utmost energy from the wind turbine generator. A full scale IGBT back-to-back voltage source converter, as indicated in Fig. 1 by which the generator is linked to the electric power grid, permits full controllability of the system. As a result of strengthened electric power grid codes, wind turbine generators with full scale power converter will be more utilized in the near future. Since power converter of such wind energy system decouples the generator system from the electric power grid, fault-ride through and grid support can be easily attained [2].
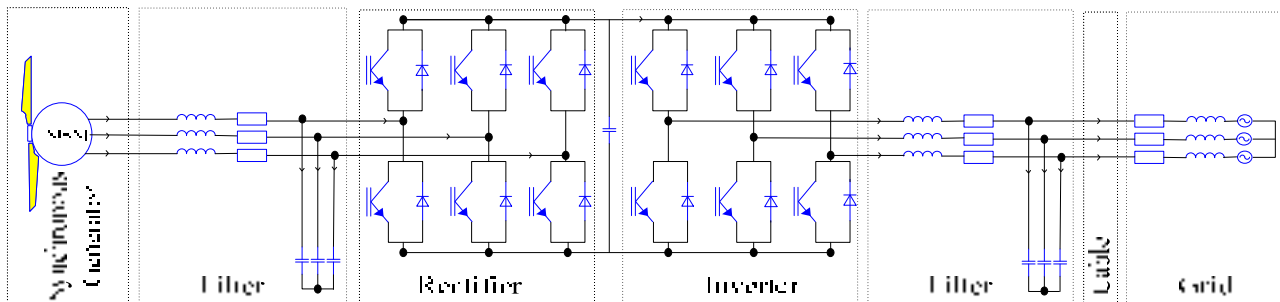
Fig 1. Modeling scheme and control concept of the variable-speed wind plant with multi-pole permanent magnet synchronous generator

The goal of the paper is the development of control scheme for a variable speed wind turbine generator.

An effective model of the whole wind power generator system is performed using Matlab/Simulink software environment. The scheme includes models of the aerodynamic and mechanical sections of the wind turbine generator as well as its electric power and control systems. The PMSG wind turbine generator control methodology is accomplished by harmonized regulation of the power converters and the wind turbine generator control systems. The generator-side and the grid-side has identical power converter control systems, there is also the gearless drive converter and aerodynamics pitch angle control mechanism. The wind turbine generator rating of this research article is 10 MW. A case study of a 3·10 MW = 30 MW wind farm is thereafter presented.

Arrangement of the proposed wind turbine system and mathematical model of the PMSG. The normal schematic arrangement of a variable-speed wind turbine established on a PMSG and full-scale power converter is shown in Fig. 1. It is made up of two main parts. First is the wind turbine generators mechanical part, that is the gearless drive converter and the aerodynamics pitch angle control. Second is the wind turbine generators electrical part that is the multi-pole PMSG full-scale frequency converter and its control mechanism [26]. As can be seen in Fig. 1 the aerodynamic rotor of the wind power arrangement is precisely matched with a gearless generator. The synchronous generator is linked to the electric power grid by means of a full-scale frequency converter scheme, which is utilized to control the speed of the generator and power flow to the grid side of the wind turbine generator arrangement. The permanent magnets are installed on the generator rotor, making provision for fixed excitation of the generator. The power gotten from the generator is fed via the stator windings into the full-scale frequency converter, which changes the varied generator frequency to constant grid frequency. The full-

scale frequency converter structure is made up of a back-to-back voltage source converter, that is the generator-side converter and the grid-side converter joined by means of a DC-link, which is then controlled by IGBT switches. Figure 1 is the proposed variable-speed wind turbine generator under consideration, a PMSG is installed to the electricity grid with the aid of a back-to-back arrangement of converters. The first converter, which is the generator-side converter, is joined to the stator windings of the PMSG. While the second converter, which is the grid side converter is linked to the electricity grid at the point of common coupling with the aid of AC filter. The DC terminals of the two converters are joined together by means of DC shunt capacitor. The power strategy of the converters contains a three-leg voltage source inverter. Nevertheless, diverse control strategies hinged on the systems control function can be applied to the inverter switches [26-33]. Wind turbines can either be Fixed Speed Wind Turbines with Induction Generator (FSWT-IG) or Variable Speed Wind Turbines with Permanent Magnet Synchronous Generator (VSWT-PMSG). The former has the benefits of mechanical manageability, small specific mass, resilient structure, and economical. Nevertheless, its limitations include restricted capacity for power quality control and terminal voltage variation during steady state circumstance, owing to the unmanageable reactive power utilization. The latter is a favourable and appealing variety of wind turbine idea, in which the PMSG can be straightly operated by a wind turbine and attached to the electric power grid network by means of AC/DC/AC power converter. The benefits of the VSWT-PMSG are as follows:

• it neither has gearbox nor brushes, consequently it has higher reliability;

• it has no extra power provision for excitation.

The power converter allows extremely pliable control of active and reactive power in instances of typical and disrupted grid circumstances [2, 17, 21, 34, 35]. PMSGs occupy a significant part in direct drive wind energy production systems for changing mechanical power into electrical power. The dynamic configuration of the PMSG is obtained from the two-phase synchronous reference frame, in which the q-axis is 90° leading of the d-axis in conformance with the orientation of rotation. The harmonization connecting the (d-q) revolving reference structure and the abc-three phase structure is sustained by utilizing a phase locked loop. A detailed mathematical modelling of the PMSG is a necessary condition for the design of the machine control algorithms and the examination of the steady-state and dynamic features of the wind power transformation scheme. Direct drive wind turbine generators, distinguished as highly effective or efficient and requires low maintenance procedures, provides favorable possibilities for future implementations [7, 36-38], particularly offshore applications. In order to do away with the gearbox the generator is constructed for low speed performance maximally between 15-20 rpm. This characteristic has made synchronous generators the only choice for low speed wind turbine utilizations. Synchronous generators magnetic field is provided with rotor excitation, but in the instance of the PMSG the direct current excitation scheme can be removed, which necessitate minimizing losses and exclusion of slip rings and consequently the maintenance requirements of the system [2, 39, 40]. To realize independent control strategy of the active and reactive power, the d-axis and q-axis equivalent circuits is utilized in the drive converter arrangements [41].

The phasor diagram of the PMSG model is shown in Fig. 2. While the mathematical model of the PMSG in both natural (abc) three-phase stationary reference frame and (d, q) synchronously rotating reference frame is developed as follows writing the stator voltage equation (in time domain):

$$u_S = R_S \cdot i_S + L_S \cdot \frac{di_S}{dt} + e . \qquad (1)$$

If (α, β) is the stator coordinate system, we can write (1) in these coordinates:

$$u_S(\alpha,\beta) = R_S \cdot i_S(\alpha,\beta) + L_S \cdot \frac{di_S(\alpha,\beta)}{dt} + e . \qquad (2)$$

Then the voltage and current equations in the rotor coordinate system become:

$$\hat{U}_S(d,q) = U_d + jU_q ; \qquad (3)$$

$$\hat{I}_S(d,q) = I_d + jI_q , \qquad (4)$$

where R_S is the stator resistance; L_S is the stator inductance; U_S is the stator voltage; e is the excited voltage; i_d is the instantaneous real power current; i_q is the instantaneous reactive power current, i_S is the whole current and γ is angular velocity.
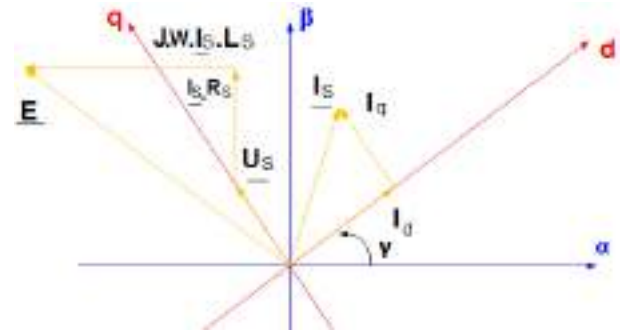
Fig. 2. The phasor diagram of the PMSG model

The equations of the synchronous generator are:

$$\frac{d\Psi_d}{dt} = U_d - R_1 \cdot I_d - \Omega_L \cdot \Psi_q ; \qquad (5)$$

$$\frac{d\Psi_q}{dt} = U_q - R_1 \cdot I_q - \Omega_L \cdot \Psi_d , \qquad (6)$$

where Ψ_d and Ψ_q are the components of the magnetic field; Ω_L is the electrical angular velocity.

So the equations of the magnetic field are:

$$\Psi_d = \Psi_{pm} - L_d \cdot I_d ; \qquad (7)$$

$$\Psi_q = L_q \cdot I_q , \qquad (8)$$

where Ψ_{pm} is the synaptic magnetic field with the rotor.

So the equation of the torque is:

$$M_{MI} = \frac{3}{2} \cdot P_P \cdot \left(\Psi_d \cdot I_q - \Psi_q \cdot I_d \right), \qquad (9)$$

where M_{MI} is the torque of the machine.

We have the mechanical velocity:

$$J \cdot \frac{\mathrm{d}\Omega_m}{\mathrm{d}t} = (M_{MI} - M_W). \qquad (10)$$

So we can calculate the velocity without using measurements by using the following equation:

$$\Omega_m = \frac{1}{J} \cdot \int (M_{MI} - M_W)\mathrm{d}t, \qquad (11)$$

where M_W is the load torque; J is the whole torque inertia.

These principles is used in the mathematical modeling of the PMSG rotor as shown in Fig. 3, which illustrates the schematic diagram of the PMSG rotor utilized in this research work.
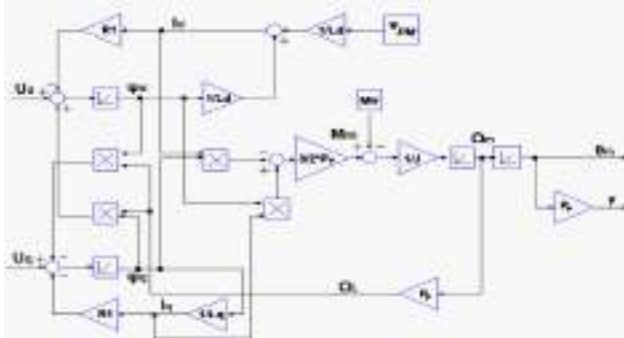
Fig. 3. Schematic diagram of the PMSG rotor

The proposed IGBT power converter control configuration. The power converter control arrangement is split into two controllers: a control scheme for the generator side converter and another control scheme for the grid side converter. The grid side converter should be an active inverter, since it changes DC link voltage to AC grid voltage with fixed frequency of an electric power system, the generator side converter can non-mandatory be made up of passive elements, e.g. a diode rectifier, or active elements such as IGBTs or GTOs. In whatever way, the most advantageous utilization and controllability of a PMSG can be realized if an active inverter is also utilized on the generator side, take for instance the IGBT voltage source converter as suggested in Fig. 1. Nevertheless, IGBT converters are costly and must be guarded or protected from over-currents and over-voltages. IGBTs are composite of bipolar-metal-oxide semiconductor, which possesses the merits of low on-state resistance, voltage regulation of the gate and broad unharmed working locality. IGBTs are as well one of the utmost essential constituents as well as broadly utilized power piece of equipment in power electronics in spans above 1 kV and 1 kW, the most utilized power equipment for commercial implementations are IGBTs. Various control schemes can be implemented with the power converter, including of: unity power factor control; maximum torque control; and the constant stator voltage control of the generator. The standard three phase bridge converter with three legs has been utilized in this research work, each has two switches, that is IGBT with antiparallel diode, operating under pulse width modulation (PWM) with a frequency of about 10 kHz. The rectifier and inverter consist of the same elements and works with the same principle, they are traditionally known as Voltage Sourced Converters (VSC) [2, 28-29, 42-47].

The PMSG frequency rectifier and electric power grid frequency inverter. The organization of the control plan of the frequency inverter for the grid side is displayed below in Fig. 1 the same frequency converter is utilized for the control plan of the generator side. The grid side converter is an active inverter, while the generator side converter is made up of passive diode rectifier, the rectifier and inverter consist of the same elements and works with the same principle. The control signal employed with the IGBTs gate switching is three phase sinusoidal voltage which originated from the d-q axis signal. The grid side inverter controls the DC link capacitor voltage at the set value, so that the active power can be interchanged effectively from the PMSG to the electric power grid. It also controls the reactive power output to the electric power grid in order to control the grid side voltage. In this control scheme, the d-axis of reference frame is oriented along the grid voltage. [36, 48].

Mathematical model of the gearless drive power converter. The drive converter arrangement of a gearless wind turbine generator comprises mainly of the turbine and generator. The major sources of inertia of this system lie in the turbine and generator. The Eigen-frequency of the drive-converter is quite low and within the bandwidth that is usually taken into consideration in power system dynamics simulations, it ranges from 0.1–10 Hz. A wind turbine generator transforms wind power into electrical power. Its functioning attribute is extraordinarily non-identical to that of traditional electrical power sources. The output power of a wind turbine generator can be different over a broad extent between zero and the adjudged ability value, in an unsystematic but continual manner. In multi-pole generators, the same electrical angle indicates a much smaller mechanical angle than in generators with small number of poles. The pitch angle controls the generator speed, meaning that the input in the controller is the error signal connecting the reference generator speed and the measured generator speed. The pitch angle controller places a limit on the rotor speed when the nominal generator power has been attained, by restricting the mechanical power produced from the wind and consequently reinstating the balance connecting electrical and mechanical power [8, 49-52].

The aim of the driving converter utilized in the proposed wind turbine generator scheme is to determine the moment and the time of contact for each switch. The technique of driving is PWM, which utilizes digital signals to control power applications, as well as being sufficiently uncomplicated to change back to analogue with the least possible hardware. Figure 4 gives an idea on how to drive this converter [28, 29]. From Fig. 4 the equations given below in (12)–(14) are generated:

$$I_{ctr1} = \underline{V_1}(t) = 0.5 \cdot AF \cdot \sin(\omega t); \qquad (12)$$

$$I_{ctr2} = \underline{V_2}(t) = 0.5 \cdot AF \cdot \sin\left(\omega t + \frac{2\pi}{3}\right); \qquad (13)$$

$$I_{ctr3} = \underline{V_3}(t) = 0.5 \cdot AF \cdot \sin\left(\omega t - \frac{2\pi}{3}\right), \qquad (14)$$

where I_{ctr1}, I_{ctr2}, and I_{ctr3} are the outputs of the control circuit, and AF is the amplitude function.
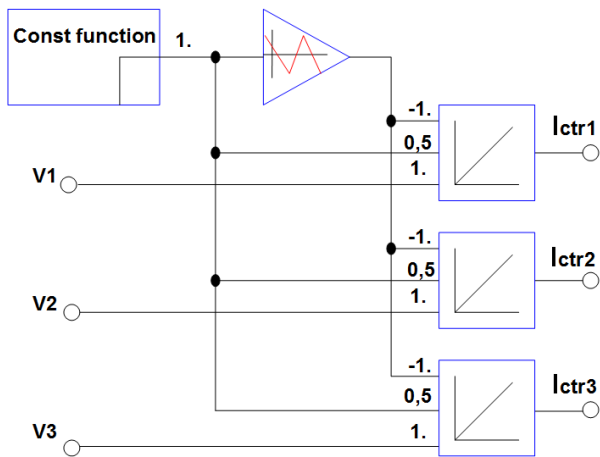
Fig. 4. Generated control currents function structure

PMSG and electric power grid converter control circuits. The constant stator voltage control mechanism is appraised to be of utmost advantage in gearless wind turbine applications, this control structure is applied in the simulation model of the proposed scheme. The DC-link voltage is kept constant to ensure that the generated active power is fed via the DC-link to the electricity grid, all this is done to make sure that no energy is dissipated in the DC-link [2]. Figure 5 illustrates the control circuit of the synchronous generator. It controls the currents of the synchronous generator in the rotor coordinate order and the input quantities which are stator currents (I_{L1}, I_{L2}, I_{L3}) changed into the stator coordinate system (α, β). These currents (I_α, I_β) are rotated from the stator coordinate system to the rotor coordinate system (d, q) by utilizing the vector negative adapter (VD-) technique [28, 46], the electric angle is gotten from the model of the synchronous generator. This then makes the stator currents in the rotor to be in the coordinate system (I_d, I_q) and both the constant and fixed currents are stabilized, which brings about a good assumption for the control mechanism. I_d is utilized to control the reactive power and I_q is utilized to control the synchronous generator torque [45]. Also (I_d, I_q) are compared with reference values ($I_{d.ref}$, $I_{q.ref}$) and the product of the deviation is sent to the PI controller. The output is a continues disengagement process to get driving vectors in the rotor coordinate system ($V_{d.ctr}$, $V_{d.ctr}$). These are then transformed to the stator coordinate system ($V_{\alpha.ctr}$, $V_{\beta.ctr}$) [46] and afterwards it is changed to vectors (V_{ctr1}, V_{ctr2}, V_{ctr3}) in the three-phase system. This process as explained above provides switch-off and switch-on for rectifier IGBT switches.
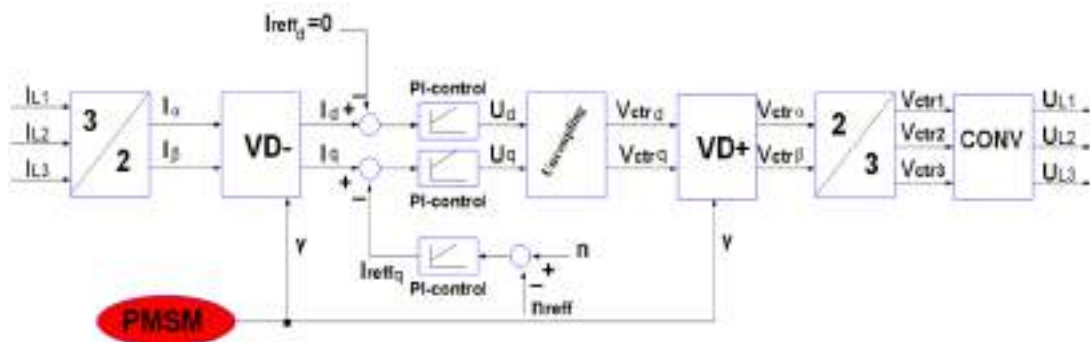
If the DC-link voltage remains constant by utilizing the generator-side converter control, the active power of the generator is conveyed through the DC-link to the grid-side converter. Consequently, the active power produced by the wind turbine can be controlled using the grid side converter. Owing to the converter mechanism used, the reactive power operational point of the generator side and the grid side converter are fully decoupled. This means that the reactive power, which is finally supplied to the electricity grid network, can be independently controlled by the grid side converter. Hence, the same control mechanism is utilized on both the generator and the grid network. The control circuit of the grid network is vividly shown in Fig. 6 [2, 28, 46].

Simulation results of the wind turbine design. To ensure a thorough evaluation of the functioning of the control mechanism for the variable speed wind turbine idea with PMSG, performed in the Matlab/Simulink software environment, a set of simulations with wind speed having the characteristics of no turbulence, no tower shadow etc. is performed. The wind turbine rating used is 10 MW. The nominal power of the wind turbine generator is 10/0.9 = 11.11 MVA. And the reactive power is regulated through the input parameter of Q_{ref} (that is the phase angle between the stator voltage and current of the PMSG) and it is generated in proportion to the nominal power. Three wind speed values have been observed, these are wind speed at points 5 m/s, 10 m/s, and 15 m/s, and Q_{ref} values from 0–1 p.u., from Fig. 7 and Fig. 8, it is observed that as the value of Q_{ref} increases from 0–1 p.u. there is a corresponding increase in the reactive power values i.e. from 0–11.11 MVAr. The active power at wind speed points 5 m/s, 10 m/s, and 15 m/s also increases too in value i.e. 5 m/s = 0.64 MW, 10 m/s = 5.56 MW, 15 m/s = 10 MW respectively. The obtained results for the wind speed and Q_{ref} is shown in Fig. 7, which depicts the graphical illustration of measured reactive and active power values and Fig. 8, showing comparison between measured values of active and reactive power. Hence, the results in Fig. 7,*a* shows that as Q_{ref} increases, there is a corresponding increase only in the reactive power values observed. And in the same vein Fig. 7,*b* shows that as wind speed is increased, there is a corresponding increase only in the active power values observed. Therefore, it can be inferred from simulation results that Q_{ref} has effect only on the observed reactive power values and the turbine wind speed has effect only on the values of active power. For simplicity, the 3D and 2D explanation of the results is further illustrated in Fig. 8,*a*,*b* respectively.

Fig. 5. The control circuit of the synchronous generator
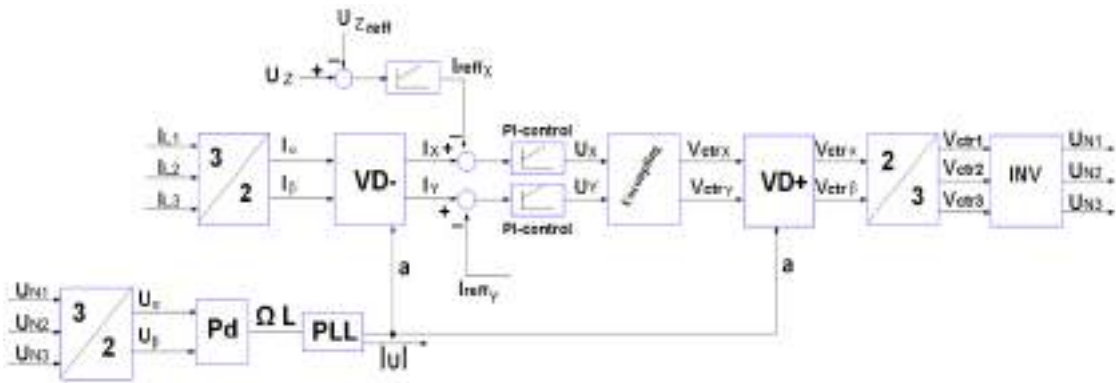
Fig. 6. The control circuit of the grid network
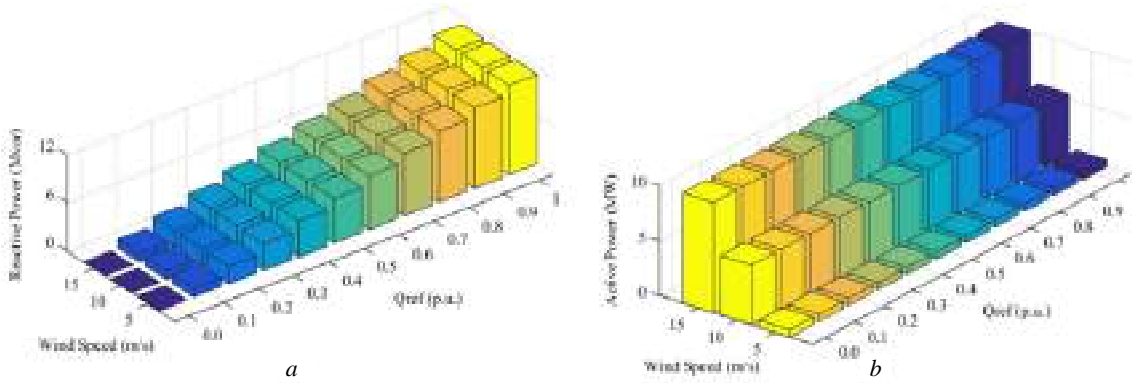
Fig. 7. Graphical illustration of measured values: *a* – reactive power; *b* – active power
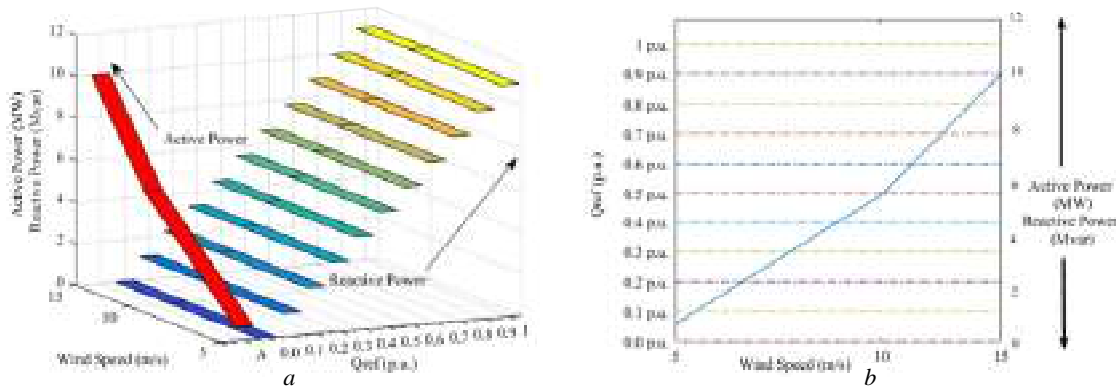
Fig. 8. Comparison between measured values of active and reactive power: *a* – 3D view; *b* – 2D view

Figures 9,*a*,*b* show the output values of reactive power and active power supplied to the network at operational point of 15 m/s and Q_{ref} value of 0.1 p.u. it is observed that the time to reach steady state is $T = 0.25$ s. Also Fig. 10,*a*,*b* show the output values of reactive power supplied to the network at the operational point of 10 m/s and 15 m/s respectively and the observed time to reach steady state for Q_{ref} values of 0.1 p.u. and 0.2 p.u.,

although there were sudden changes in current, the time to reach stable control of the system is very small $T = 0.25$ s. All these show the validity of the system and to further affirm that the proposed system is functional. The symmetrical and sinusoidal voltage wave form of the system is shown in Fig. 11, which further buttress the validity of the system.
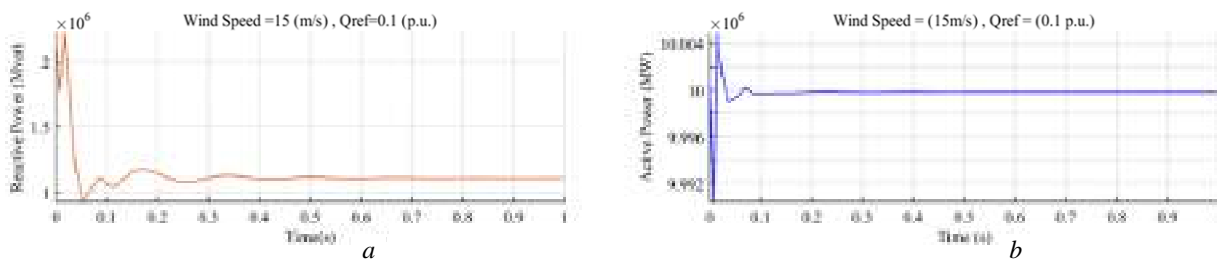
Fig. 9. The output values of reactive (*a*) and active (*b*) power supplied to the grid network at the operational point of 15 m/s
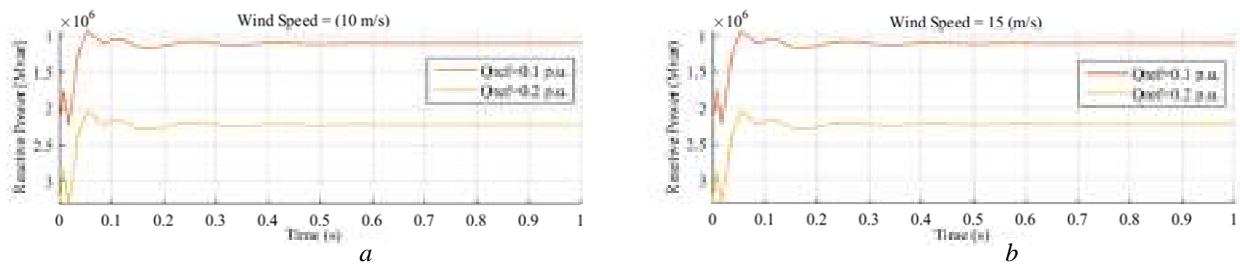
Fig. 10. The output values of reactive power supplied to the grid network at operational point of 10 m/s (*a*) and 15 m/s (*b*)
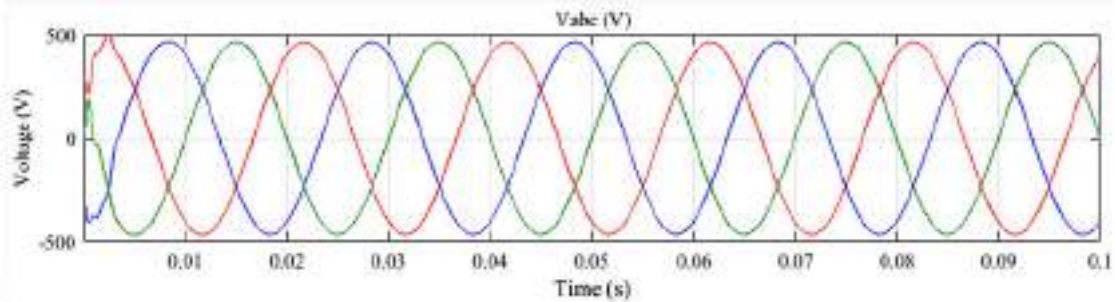
Fig. 11. Symmetrical and sinusoidal voltage wave form of the system

Novelty of simulation scheme. The novelty of this simulation scheme is the use of the Insulated Gate Bipolar Transistor (IGBT) switching device and the Type-4 wind turbine generator. IGBT, Integrated Gate Commutated Thyristor (IGCT) and MOS-Controlled Thyristor (MCT) are the three new designs of power devices. IGBT is the most widespread utilized power electronic equipment at present. An IGBT is fundamentally a hybrid MOS-gated turn ON/OFF bipolar transistor that combines the characteristics of the Metal Oxide Semiconductor Field Effect Transistors (MOSFET), Bipolar Junction Transistor (BJT) and thyristor. The latest advancement in switching devices is playing a very significant part in the evolution of higher power electronics converters for wind power turbines with increased reliability and efficiency. The principal selections are mainly IGBT modules, IGBT press pack, and IGCT press pack. The press-pack technology brings about an increase in reliability, still to be scientifically demonstrated but known from industrial practice, higher power density, that is easier stacking for series connection, and better cooling ability at the price of a higher cost in contrast to power modules. Press-pack IGCT is known to support the advancement of MV power converters and are already state of the art technology in high-power electric drives such as utilized in oil and gas applications, but not yet universally adopted in the wind turbine industry owing to cost issues [53-64]. The Type-4 wind turbine as shown in Fig. 12 presents a great deal of flexibility in its design and operation as the output of the rotating machine is sent to the electricity grid via a full-scale back-to-back frequency converter.
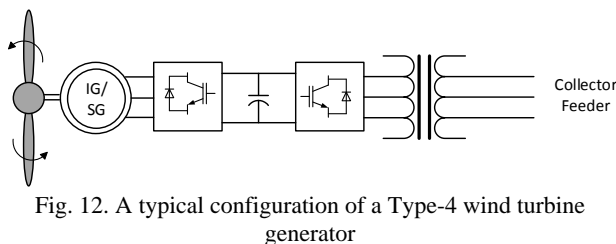
Fig. 12. A typical configuration of a Type-4 wind turbine generator

The wind turbine is permitted to rotate at its optimal aerodynamic speed, which results in a wild alternating current output from the machine. Furthermore, the gearbox might be completely remove or gotten rid of such that the machine spins at a slow wind turbine speed and produces an electrical frequency that is well below that of the electricity grid. This is no issue for a Type-4 wind turbine, as the inverters changes the power, and offer the potentiality of reactive power provision to the electricity grid, much like the Static Synchronous Compensator (STATCOM). The rotating machines of the Type-4 wind turbine built as wound rotor synchronous machines, is comparable to traditional generators found in hydroelectric power plants with control of the field current and high pole numbers, as permanent magnet synchronous machines or as squirrel cage induction machines. Nonetheless, the Type-4 turbine is able to control both real and reactive power flow, irrespective of what kind of machine is utilized [65-67].

Case study. Here, the wind farm rating used is (3·10 MW = 30 MW) 30 MW, three of the 10 MW wind turbine generators designed is utilized in this case study. The reactive power is regulated through the input parameter of Q_{ref} and it is generated in proportion to the nominal power. Three wind speed values are observed at, i.e. points 5 m/s, 10 m/s and 15 m/s respectively. Q_{ref} values is from 0 – 1 p.u., as the value of Q_{ref} increases from 0 – 1 p.u., there is a corresponding increase in the reactive power values i.e. from 0 – 33.33 MVAr. The active power at wind speed points 5 m/s, 10 m/s, and 15 m/s also increases too in value i.e. 5 m/s is 1.92 MW, 10 m/s is 16.68 MW, and 15 m/s is 30 MW. The MV wind farm comprises of a medium-voltage, passive rectification, AC/DC converters, and MV interconnection and distribution system, as illustrated in Fig. 13. While the single line diagram of the wind farm scheme showing its vector components is shown in Fig. 14.
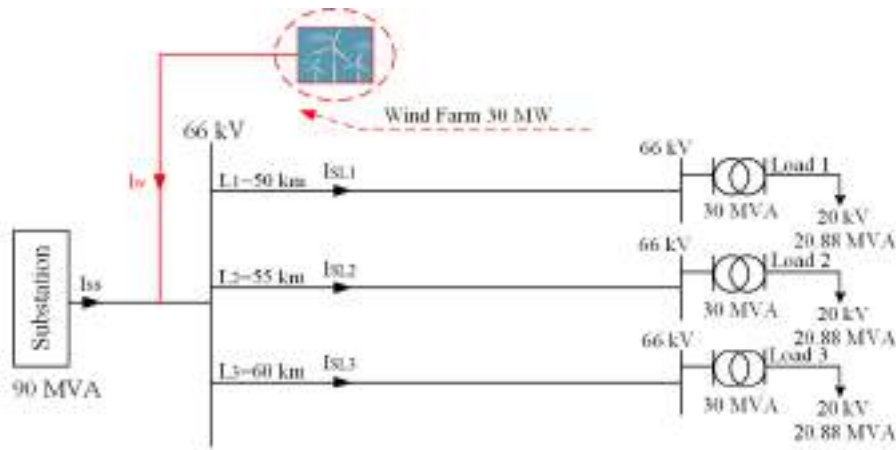
Fig. 13. Scheme of the wind farm connected distribution grid network
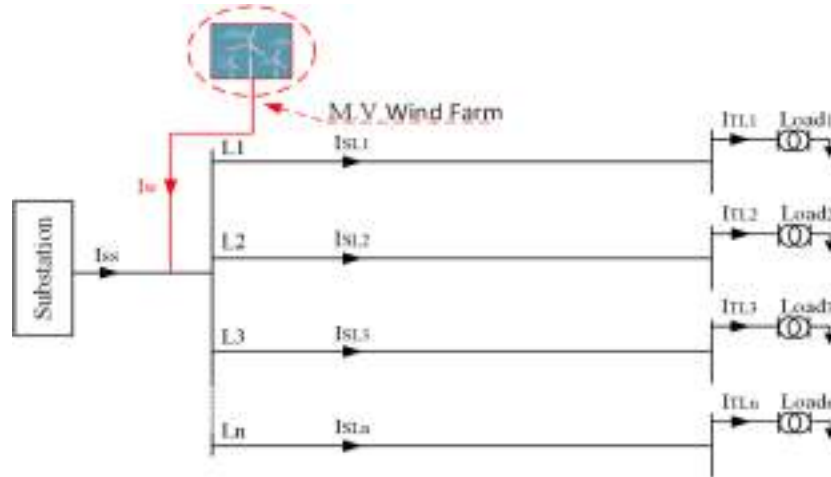
Fig. 14. Single line diagram of the wind farm scheme showing its vector components

The wind energy compensation strategy is connected to the electric power substation as shown in Fig. 14 considering its vector components:

$$I = I_{SS} + I_W, \qquad (15)$$

where I_{SS} is the total substation line current; I_W is the wind farm line current.

The power losses on the line are given by:

$$\Delta P = 3 \cdot I_L^2 \cdot R_{1L}. \qquad (16)$$

And the difference in voltage (voltage drop) of each phase is given by:

$$\Delta V = I_L \cdot Z_L. \qquad (17)$$

From Fig. 14 and (16) the following power equation is deduced:

$$\Delta P_{LLn} = 3 \cdot \left(I_{SLn}^2 \cdot R_{1LLn}\right), \qquad (18)$$

where I_{SLn} is the line current supplied to n^{th} number of power lines from the substation; R_{1LLn} is the resistance of nth number of lines; ΔP_{LLn} is the active power losses of nth number of lines; $n = 1,2,3,...,n$ (n is the number of lines).

Similarly, from Fig. 14 and (17):

$$\Delta V_{LLn} = I_{SLn} \cdot Z_{LLn}, \qquad (19)$$

where ΔV_{ALLn} is the difference in voltage drop on n^{th} number of lines; Z_{LLn} is longitudinal impedance of nth number of lines.

From (18), (19) the matrix equations for power losses and difference in voltage drop of the substation lines are given in (20), (21) respectively:

$$\begin{cases} \Delta P_{LL1} = 3 \cdot \left(I_{SL1}^2 \cdot R_{1LL1}\right) \\ \Delta P_{LL2} = 3 \cdot \left(I_{SL2}^2 \cdot R_{1LL2}\right) \\ \Delta P_{LL3} = 3 \cdot \left(I_{SL3}^2 \cdot R_{1LL3}\right) \\ \vdots \qquad \vdots \qquad \vdots \\ \Delta P_{LLn} = 3 \cdot \left(I_{SLn}^2 \cdot R_{1LLn}\right) \end{cases}, \qquad (20)$$

$$\begin{cases} \Delta V_{LL1} = I_{SS1} \cdot Z_{LL1} \\ \Delta V_{LL2} = I_{SS2} \cdot Z_{LL2} \\ \Delta V_{LL3} = I_{SS3} \cdot Z_{LL3} \\ \vdots \qquad \vdots \qquad \vdots \\ \Delta V_{LLn} = I_{SSn} \cdot Z_{LLn} \end{cases}. \qquad (21)$$

To measure the reactive power Q_G generated from the wind farm, and the active power P_G generated from the wind farm, the Q_{ref} is increased in percentage steps of 5, step 1 is when the wind farm is switched OFF, while for steps 2 to 5 the wind farm is switched ON as depicted in Table 2. Also the values of Q_{ref} is varied from step 2 to step 5 in order to produce reactive power from the wind farm according to the usage of reactive power by the load. The measured reactive power Q_G generated by the wind farm increases, while the measured active power P_G is constant for step 2 to 5 as tabulated in Table 1. The wind farm has supplied reactive power in order to influence the voltage profile of the distribution grid. While the flow of active power is very much essential for the distribution

line to operate. Table 2 shows the measured values of reactive power Q_L, active power P_L and apparent power S_L for one load of step 1 to 5. For step 1, the wind farm is switched OFF, while the wind farm is switched ON for steps 2 to 5. It is seen that the reactive load of the wind farm for one load, increases progressively from step 1 to 5, the active load of the wind farm for one load is constant, and the apparent power for one load of the wind farm also increases in steps of 5 i.e. from step 1 to 5. The percentage rate of increase of generation and using of reactive power is graphically represented in Fig. 15. The rate increase of reactive power generation from wind farm, rate increase of apparent power for one load and the rate increase of reactive power for one load experiences a progressive rise as we move from step 1 to step 5. Thus, from Table 2, and Fig. 15, It will be the same steps for other loads that is L1 = L2 = L3. It can be deduce that reactive power is used to maintain voltage level so that active power can flow to do useful work in an electric power distribution system. Suppose the proposed wind energy distribution system is a weak network with a large reactive load. If we suddenly disconnect the load, we will encounter a peak in the voltage. The systems active power will be utilized to do beneficial task. It is observed that apparent power which is a combination of reactive and active power without reference to phase angle progressively rises, meaning that the wind farm has infused reactive power in order to control and manage the voltage profile of our proposed network. The sending active power at the beginning of lines (P_s), the receiving active power at the end of lines (P_r), the voltage level at the beginning of the lines (U_s), and the voltage level at the end of lines (U_r) where measured in order to determine; Firstly, the power losses (ΔP) of the lines and secondly, the voltage drop (ΔV) on the lines. The measured values of sending and receiving active power, and sending and receiving voltage of lines 1, 2, and 3 for the various steps of the wind farm and loads is shown in Table 2. Also, the sending and receiving active power of the lines is displayed in Fig. 16,*a*,*b*.
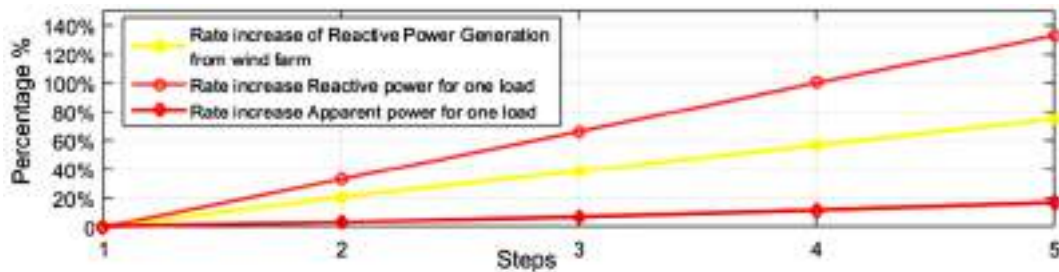
Fig. 15. Percentage rate increase for generation and using of reactive power
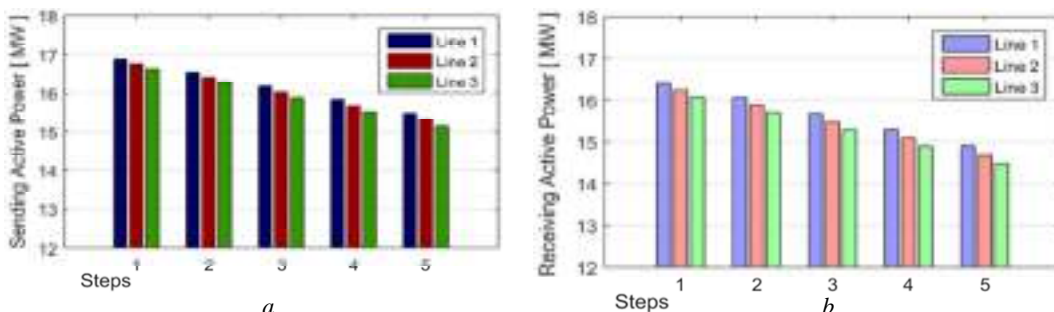
Fig. 16. Sending (*a*) and receiving (*b*) active power of lines

For step 1 to 5 observed, the sending and receiving active power decreases for line 1, 2, and 3 respectively. The diagrams in Fig. 16 show that for each step observed active power losses decreases. While the voltage difference increases from line 1 to line 3 respectively, all these is depicted in Table 1, 2 and Fig. 15.

Therefore, we can say that power losses have been reduced on the electric power distribution system as a result of reactive power compensation near the loads by the wind farm. Considering only the resistive losses in the distribution circuit, and remembering that power losses is directly in proportion to the square of the immensity of the current flow on the line, it is simple to notice that the power losses in one line will rise remarkably more than the decrease of power losses in other different power distribution lines. This demonstrates that a straightforward method to reduce the total losses is to sustain a stable rise in voltage. Here, Fig. 17 depicts that power losses on the lines increases as we move from step 1 to 5, insinuating that the power produced in substation passes from one end to another from complex systems to the end users. It is a fact that the unit of electric power entered by substation usually does not match with the units allocated to the end users. Several percentages of the components are lost in the wind farm electric power distribution system. Figure 18 depicts the percentage voltage on the ref. 66 kV line substation within the range of + or – 10 %, at the ends of lines 1, 2, and 3, that is voltage receiving ends of lines 1, 2, and 3. It is discovered that there is % decrease of voltage ref. 66 kV for line 1 and 2 as we move from step 5 to step 1, but line 3 experiences not too significant change, but only a slight increase as we move from step 5 to step 1. Meaning that the distribution voltage is regulated owing to the wind farm distribution systems ability to supply close to steady voltage over a broad choice of load situations. The diagram in Fig. 19 illustrates the percentage change in voltage and power losses on the lines, and increase of reactive load, and reactive power generation of wind farm. It shows that the listed parameters in i.e. % change in voltage, power losses

on lines, increase of reactive power and reactive power generation of the wind farm gradually increases from negative to positive values, from step 1 to 5 of the lines observed. Meaning that the wind farm connected distribution power system is able to produce and control reactive power according to the usage of reactive loads.
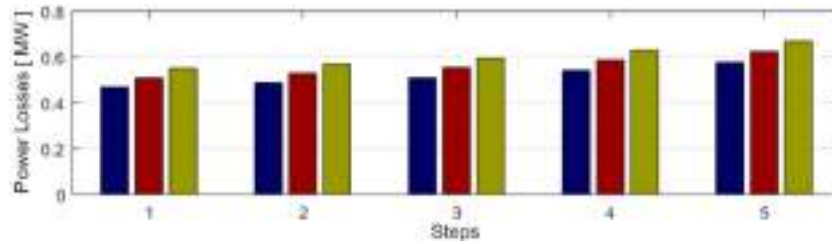
Fig. 17. Power losses of lines
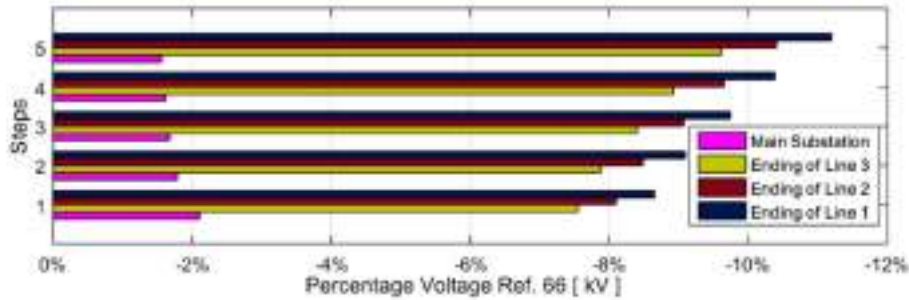
Fig. 18. Percentage voltage ref. 66 kV of lines
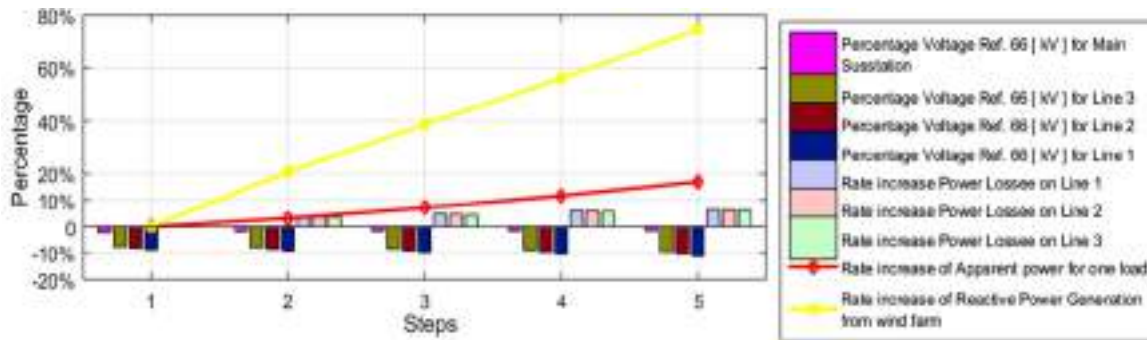
Fig. 19. Percentage change in voltage and power losses of lines, and the increase of reactive load, and reactive power generation of wind farm

Table 1

Measured values of Q_{ref}, active and reactive power of the wind farm

Step	Q_{ref}, p.u.	Rate increase, % Q_{ref}	Reactive power Q_G, MVAr	Active power P_G, MW	Wind farm mode	Speed, m/s
1	0	0 %	0	0	OFF	0
2	0.207	20.7 %	6.941	30	ON	15
3	0.387	38.7 %	12.96	30	ON	15
4	0.567	56 %	19.2	30	ON	15
5	0.747	74.7 %	23.81	30	ON	15

Table 2

Measured values of reactive, active and apparent power of one load

Step	Rate increase, % Q_L	Reactive load Q_L, MVAr	Active load P_L, MW	Apparent load S_L, MVA	Rate increase, % S_L	Wind farm mode	Q_{ref}, p.u.
1	0 %	6	20	20.88	0 %	OFF	0
2	33 %	8	20	21.54	3.161 %	ON	0.207
3	66 %	10	20	22.36	7.089 %	ON	0.387
4	100 %	12	20	23.324	11.704 %	ON	0.567
5	133 %	14	20	24.413	16.92 %	ON	0.747

Conclusions.

The theme of this research paper centres on the design and analysis of the whole control arrangement of a variable speed wind turbine with multi-pole PMSG. Owing to the gearless structure and the permanent magnet excitation of the synchronous generator, it symbolizes an utmost effective and inexpensive or economical maintenance way out, which will be extremely advantageous in offshore wind turbine applications. A complete effectual simulation model is established in the

MATLAB/Simulink software environment. The control of the wind turbine is realized by utilizing the power converter control in harmonization with the pitch control plan. The converter control is an assurance for the variable speed operation to obtain the most favourable power performance. When wind speed is elevated than the rated speed, the pitch angle control operation alters the blade incidence so that the output power of the generator is within the permitted limits. MATLAB/Simulink simulations reveal that the control technique triumphantly controls the variable speed PMSG wind turbine within the limit of standard functional circumstances. The control scheme enables the independent control of active and reactive power according to applied reference values at variable speed. Hence, the proposed gearless wind power plants utilizing the synchronous generator with permanent magnets allows the production of power at variable speeds attaining stability during various wind speed operational points investigated. The rotor coordinate system of the generator allows the control of the synchronous generator magnetic flow and torque separately. The results of this research are an indication of a robust control circuit functionality and stability of the whole activity of the proposed scheme. It can consequently be deduced, that the gearless variable-speed wind turbine PMSG can function in the same way as the traditional wind power plants. The results obtained from the (3·10 MW = 30 MW) wind farm scheme case study agree with other studies carried out worldwide regarding active and reactive power control in MV distribution network connected to wind farm with IGBT power electronics converters as the schemes simulation results reveals an enhanced voltage profile and reduction in power losses.

Conflict of interest. The authors declare that they have no conflicts of interest.

REFERENCES

1. Döşoğlu M.K., Basa Arsoy A. Enhancement of a reduced order doubly fed induction generator model for wind farm transient stability analyses. *Turkish Journal of Electrical Engineering & Computer Sciences*, 2016, vol. 24, pp. 2124-2134. doi: https://doi.org/10.3906/elk-1402-195.
2. Michalke G., Hansen A.D., Hartkopf T. Control strategy of a variable speed wind turbine with multipole permanent magnet synchronous generator. *European Wind Energy Conference and Exhibition 2007, EWEC 2007*, vol. 3, pp. 1371-1378.
3. Merabet A., Keeble R., Rajasekaran V., Beguenane R., Ibrahim H., Thongam J. Power Management System for Load Banks Supplied by Pitch Controlled Wind Turbine System. *Applied Sciences*, 2012, vol. 2, no. 4, pp. 801-815. doi: https://doi.org/10.3390/app2040801.
4. Shaaban M., Usman M.D. Quantitative risk associated with intermittent wind generation. *Turkish Journal of Electrical Engineering & Computer Sciences*, 2016, vol. 24, pp. 3144-3157. doi: https://doi.org/10.3906/elk-1405-102.
5. Izgi E., Kaymak M.K., Öztopal A., Durna B., Şahin A.D. Variations and relations of meteorological parameters between upwind and downwind small-scale wind turbine rotor area. *Turkish Journal of Electrical Engineering & Computer Sciences*, 2016, vol. 24, pp. 1091-1098. doi: https://doi.org/10.3906/elk-1312-147.
6. Stiel A., Skyllas-Kazacos M. Feasibility Study of Energy Storage Systems in Wind/Diesel Applications Using the HOMER Model. *Applied Sciences*, 2012, vol. 2, no. 4, pp. 726-737. doi: https://doi.org/10.3390/app2040726.
7. Ghosh S., Saha P.P.K., Panda P.G.K. Wind Energy Conversion System Connected With Grid Using Permanent Magnet Synchronous Generator (PMSG). *International Journal of Advanced Research in Electrical, Electronics and Instrumentation Engineering*, 2015, vol. 04, no. 01, pp. 120-127. doi: https://doi.org/10.15662/ijareeie.2015.0401011.
8. Karki R., Dhungana D., Billinton R. An Appropriate Wind Model for Wind Integrated Power Systems Reliability Evaluation Considering Wind Speed Correlations. *Applied Sciences*, 2013, vol. 3, no. 1, pp. 107-121. doi: https://doi.org/10.3390/app3010107.
9. Ahmed M.A., Pan J.-K., Song M., Kim Y.-C. Communication Network Architectures Based on Ethernet Passive Optical Network for Offshore Wind Power Farms. *Applied Sciences*, 2016, vol. 6, no. 3, p. 81. doi: https://doi.org/10.3390/app6030081.
10. Fandi G., Igbinovia F.O., Müller Z., Švec J., Tlusty J. Using renewable MV wind energy resource to supply reactive power in MV distribution network. *2015 16th International Scientific Conference on Electric Power Engineering (EPE)*, 2015, pp. 169-173. doi: https://doi.org/10.1109/EPE.2015.7161146.
11. Fandi G., Igbinovia F.O., Švec J., Müller Z., Tlustý J. Advantageous positioning of wind turbine generating system in MV distribution network. *2016 17th International Scientific Conference on Electric Power Engineering (EPE)*, 2016, pp. 1-6. doi: https://doi.org/10.1109/EPE.2016.7521807.
12. Babouri R., Aouchenni O., Aozellag D., Ghedamsi K. Wind farm based on DFIG entirely interfaced with 14-node distribution network: power control and voltage regulation. *Turkish Journal of Electrical Engineering & Computer Sciences*, 2016, vol. 24, pp. 2838-2852. doi: https://doi.org/10.3906/elk-1404-292.
13. Çolak I., Bayındır R., Sefa I., Demirtas M. Design and hybrid energy power system using solar and wind energy. *Proceedings of the 2nd International Conference on Technical and Physical Problems in Power Engineering*, 2004, pp. 776-778.
14. Kabalci E., Irmak E., Çolak I. Design of an AC-DC-AC converter for wind turbines. *International Journal of Energy Research*, 2011, vol. 35, no. 2, pp. 169-175. doi: https://doi.org/10.1002/er.1770.
15. Bana Shari M.B., Mohamadrez Y., Hosseinpou M., Torabzade S. Maximum Power Control of Grid Connected Variable Speed Wind System through Back to Back Converters. *Journal of Applied Sciences*, 2008, vol. 8, no. 23, pp. 4416-4421. doi: https://doi.org/10.3923/jas.2008.4416.4421.
16. Yin M., Li G., Zhou M., Zhao C. Modeling of the Wind Turbine with a Permanent Magnet Synchronous Generator for Integration. *2007 IEEE Power Engineering Society General Meeting*, 2007, pp. 1-6. doi: https://doi.org/10.1109/PES.2007.385982.
17. Hansen A.D. Generators and Power Electronics for Wind Turbines. *In Wind Power in Power Systems*, 2005, pp. 53-78. John Wiley & Sons, Ltd. doi: https://doi.org/10.1002/0470012684.ch4.
18. Oğuz Y., Güney I., Çalık H. Power Quality Control and Design of Power Converter for Variable-Speed Wind Energy Conversion System with Permanent-Magnet Synchronous Generator. *The Scientific World Journal*, 2013, pp. 1-14. doi: https://doi.org/10.1155/2013/783010.
19. Kilk A. Design and Experimental Verification of a Multipole Directly Driven Interior PM Synchronous Generator for Wind Power Applications. *The 4th International Conference «Electric power quality and supply reliability»*, August 29-31, 2004, Pedase, Estonia: Proceedings. Tallinn: Tallinn University of Technology, p. 87-89.

20. Westlake A.J.G., Bumby J.R., Spooner, E. Damping the power-angle oscillations of a permanent-magnet synchronous generator with particular reference to wind turbine applications. *IEE Proceedings - Electric Power Applications*, 1996, vol. 143, no. 3, p. 269. doi: https://doi.org/10.1049/ip-epa:19960285.

21. Polinder H., de Haan S.W.H., Dubois M.R., (Han) Slootweg J.G. Basic Operation Principles and Electrical Conversion Systems of Wind Turbines. *EPE Journal*, 2005, vol. 15, no. 4, pp. 43-50. doi: https://doi.org/10.1080/09398368.2005.11463604.

22. Grauers A. Efficiency of three wind energy generator systems. *IEEE Transactions on Energy Conversion*, 1996, vol. 11, no. 3, pp. 650-657. doi: https://doi.org/10.1109/60.537038.

23. Jöckel S. *Calculations of different generator systems for wind turbines with particular reference to low-speed permanent-magnet machines*. PhD thesis, Technical University Darmstadt, Germany, 2002.

24. Chan T., Lai L.L. Permanent-Magnet Machines for Distributed Power Generation: A Review. *2007 IEEE Power Engineering Society General Meeting*, 2007, pp. 1-6. doi: https://doi.org/10.1109/PES.2007.385575.

25. Haque M.E., Muttaqi K.M., Negnevitsky M. Control of a stand alone variable speed wind turbine with a permanent magnet synchronous generator. *2008 IEEE Power and Energy Society General Meeting - Conversion and Delivery of Electrical Energy in the 21st Century*, 2008, pp. 1-9. doi: https://doi.org/10.1109/PES.2008.4596245.

26. Hansen A.D., Michalke G. Multi-pole permanent magnet synchronous generator wind turbines' grid support capability in uninterrupted operation during grid faults. *IET Renewable Power Generation*, 2009, vol. 3, no. 3, p. 333-348. doi: https://doi.org/10.1049/iet-rpg.2008.0055.

27. Wang P., Wang H., Cai X., Han Z. Passivity-based robust controller design for a variable speed wind energy conversion system. *Turkish Journal of Electrical Engineering & Computer Sciences*, 2016, vol. 24, pp. 558-570. doi: https://doi.org/10.3906/elk-1309-206.

28. Jony K. Beitrag zur Modellbildung dezentraler Elektroenergieversor. 1999 Germany, 50-125.

29. Heier S. *Grid Integration of Wind Energy Conversion System*. Wiley, 2006. 446 p.

30. Brosh P.F. *Moderne Stromrichterantriebe*. Vogel-Buchverlage, 2008. 300 p.

31. Singh B., Al-Haddad K., Chandra A. Active power filter with sliding mode control. *IEE Proceedings - Generation, Transmission and Distribution*, 1997, vol. 144, no. 6, p. 564. doi: https://doi.org/10.1049/ip-gtd:19971431.

32. Fandi G., Švec J., Müller Z. The converter choice and its control circuit design for synchronous generators. *14th International Scientific Conference on Electric Power Engineering*, 2013, Ostrava, Czech Republic, pp. 697-701.

33. Kasem Alaboudy A.H., Daoud A.A., Desouky S.S., Salem A.A. Converter controls and flicker study of PMSG-based grid connected wind turbines. *Ain Shams Engineering Journal*, 2013, vol. 4, no. 1, pp. 75-91. doi: https://doi.org/10.1016/j.asej.2012.06.002.

34. Muyeen S.M., Tamura J., Murata T. *Introduction. In Stability Augmentation of a Grid Connected Wind Farm*. Springer-Verlag, London, UK, 2009, pp. 13-21.

35. Rosyadi M., Muyeen S.M., Takahashi R., Tamura J. A Design Fuzzy Logic Controller for a Permanent Magnet Wind Generator to Enhance the Dynamic Stability of Wind Farms. *Applied Sciences*, 2012, vol. 2, no. 4, pp. 780-800. doi: https://doi.org/10.3390/app2040780.

36. Rafi S.H., Ferdous R.A., Sheikh M.R.I. Modeling and Control Strategy for Variable Speed Wind Turbine Using Permanent Magnet Synchronous Generator. *Rajshahi University Journal of Science and Engineering*, 2015, vol. 43, pp. 89-100. doi: https://doi.org/10.3329/rujse.v43i0.26155.

37. Vijayalakshmi S., Saikumar S., Saravanan S., Sandip R.V., Sridhar V. Modeling and control of a wind turbine using permanent magnet synchronous generator. *International Journal of Engineering Science and Technology*, 2011, vol. 3, no. 3, pp. 2377-2384. Available at: https://www.researchgate.net/publication/50984917_Modelling_and_controlof_a_Wind_Turbine_using_Permanent_Magnet_Synchronous_Generator (Accessed 20 August 2021).

38. Jöckel S. High energy production plus built-in reliability – the new Vensys 70/77 gearless wind turbines in the 1.5 MW class. *European Wind Energy Conference EWEC 2006*, 27 February – 2 March 2006, Athens, Greece. Paper no. 0583.

39. Binder A., Schneider T. Permanent magnet synchronous generators for regenerative energy conversion – a survey. *European Conference on Power Electronics and Applications (EPE) 2005*, 11-14 September 2005, Dresden, Germany, p. 10.

40. Hussein M., Senjyu T., Orabi M., Wahab M., Hamada M. Control of a Stand-Alone Variable Speed Wind Energy Supply System. *Applied Sciences*, 2013, vol. 3, no. 2, pp. 437-456. doi: https://doi.org/10.3390/app3020437.

41. Zhou D., Blaabjerg F., Franke T., Tønnes M., Lau M. Comparison of Wind Power Converter Reliability With Low-Speed and Medium-Speed Permanent-Magnet Synchronous Generators. *IEEE Transactions on Industrial Electronics*, 2015, vol. 62, no. 10, pp. 6575-6584. doi: https://doi.org/10.1109/TIE.2015.2447502.

42. Chinchilla M., Arnaltes S., Burgos J.C. Control of permanent-magnet generators applied to variable-speed wind-energy systems connected to the grid. *IEEE Transactions on Energy Conversion*, 2006, vol. 21, no. 1, pp. 130-135. doi: https://doi.org/10.1109/TEC.2005.853735.

43. Wu R., Blaabjerg F., Wang H., Liserre M., Iannuzzo F. Catastrophic failure and fault-tolerant design of IGBT power electronic converters - an overview. *IECON 2013 - 39th Annual Conference of the IEEE Industrial Electronics Society*, 2013, pp. 507-513. doi: https://doi.org/10.1109/IECON.2013.6699187.

44. Yang S., Bryant A., Mawby P., Xiang D., Ran L., Tavner P. An Industry-Based Survey of Reliability in Power Electronic Converters. *IEEE Transactions on Industry Applications*, 2011, vol. 47, no. 3, pp. 1441-1451. doi: https://doi.org/10.1109/TIA.2011.2124436.

45. Hong S. *Studies on integrated variable-speed constant-frequency wind turbine mode application*. PhD Dissertation, Electric Power Research Institute, Beijing, China, 2003.

46. Teodorescu R., Liserre M., Rodriguez P. *Grid converters for photovoltaic and wind power systems*. Wiley-IEEE Press, 2011. 416 p.

47. Rao S.V., Lokya M., Krishna C.H. A Novel Three-Phase Three-Leg AC/AC Converter Using Nine IGBTS. *International Journal of Modern Engineering Research*, 2012, vol. 2, no. 6, pp. 4323-4334.

48. Fernandez L.M., Garcia C.A., Jurado F. Operating capability as a PQ/PV node of a direct-drive wind turbine based on a permanent magnet synchronous generator. *Renewable Energy*, 2010, vol. 35, no. 6, pp. 1308-1318. doi: https://doi.org/10.1016/j.renene.2009.11.046.

49. Singh A.K., Krisham R., Sood Y. Modeling and control of grid connected variable speed PMSG based wind energy system. *Conference on Advances in Communication and Control Systems 2013 (CAC2S 2013)*, Mumbai, India, pp. 134-139. Available at: https://www.researchgate.net/publication/271241810_Modeling_and_Control_of_Grid_Connected_Variable_Speed_PMSG_Based_Wind_Energy_System (Accessed 20 August 2021).

50. Akhmatov V. *Analysis of dynamic behavior of electric power systems with large amount of wind power*. PhD Thesis, Ørsted, Denmark, Denmark Technical University, 2003.

51. Hansen A.D., Jauch C., Sorensen P., Iov F., Blaabjerg F. *Dynamic wind turbine models in power system simulation tool DIgSILENT*. Risø National Laboratory, Roskilde, Denmark, Technical University of Denmark, 2003. Available at:

https://www.osti.gov/etdeweb/servlets/purl/20437623 (Accessed 20 August 2021).

52. Hansen A.D., Michalke G. Modelling and control of variable-speed multi-pole permanent magnet synchronous generator wind turbine. *Wind Energy*, 2008, vol. 11, no. 5, pp. 537-554. doi: https://doi.org/10.1002/we.278.

53. Blaabjerg F., Liserre M., Ma K. Power Electronics Converters for Wind Turbine Systems. *IEEE Transactions on Industry Applications*, 2012, vol. 48, no. 2, pp. 708-719. doi: https://doi.org/10.1109/TIA.2011.2181290.

54. Rebollo J., Cortés I., Perpiñà X., Millán J. A Review of Si MOS-gated Power Switches and PiN Rectifiers. *Automatika*, 2012, vol. 53, no. 2, pp. 117-127. doi: https://doi.org/10.7305/automatika.53-2.178.

55. Bose B.K. Evaluation of modern power semiconductor devices and future trends of converters. *IEEE Transactions on Industry Applications*, 1992, vol. 28, no. 2, pp. 403-413. doi: https://doi.org/10.1109/28.126749.

56. Mohammed S.A., Abdel-Moamen M.A., Hasanin B. A Review of the State-Of-The-Art of Power Electronics For Power System Applications. *Journal of Electronics and Communication Engineering Research*, 2013, vol. 1, no. 1, pp. 43-52. Available at: https://www.questjournals.org/jecer/papers/vol1-issue1/F114352.pdf (Accessed 20 August 2021).

57. Insulated Gate Bipolar Transistor, Electronics Tutorials. Available at: http://www.electronics-tutorials.ws/power/insulated-gate-bipolar-transistor.html (Accessed 20 August 2021).

58. Rahimo M., Kopta A., Linder S. Novel Enhanced-Planar IGBT Technology Rated up to 6.5 kV for Lower Losses and Higher SOA Capability. *2006 IEEE International Symposium on Power Semiconductor Devices and IC's*, 2006, pp. 1-4, doi: https://doi.org/10.1109/ISPSD.2006.1666064.

59. Rahimo M., Schlapbach U., Kopta A., Vobecky J., Schneider D., Baschnagel A. A High Current 3300V Module Employing Reverse Conducting IGBTs Setting a New Benchmark in Output Power Capability. *2008 20th International Symposium on Power Semiconductor Devices and IC's*, 2008, pp. 68-71, doi: https://doi.org/10.1109/ISPSD.2008.4538899.

60. Ji B., Song X., Sciberras E., Cao W., Hu Y., Pickert V. Multiobjective Design Optimization of IGBT Power Modules Considering Power Cycling and Thermal Cycling. *IEEE Transactions on Power Electronics*, 2015, vol. 30, no. 5, pp. 2493-2504. doi: https://doi.org/10.1109/TPEL.2014.2365531.

61. Busca C., Teodorescu R., Blaabjerg F., Munk-Nielsen S., Helle L., Abeyasekera T., Rodriguez P. An overview of the reliability prediction related aspects of high power IGBTs in wind power applications. *Microelectronics Reliability*, 2011, vol. 51, no. 9-11, pp. 1903-1907. doi: https://doi.org/10.1016/j.microrel.2011.06.053.

62. Alvarez R., Filsecker F., Bernet S. Comparison of press-pack IGBT at hard switching and clamp operation for medium voltage converters. *Power Electronics and Applications (EPE 2011), Proceedings of the 2011-14th European Conference on*, Aug. 30 2011 – Sept. 1 2011. Available at: https://www.researchgate.net/publication/252044893_Comparison_of_press-pack_IGBT_at_hard_switching_and_clamp_operation_for_medium_voltage_converters (Accessed 20 August 2021).

63. Available at: http://www.heraeus.com (Accessed 20 August 2021).

64. Available at: http://www.semikron.com (Accessed 14 June 2021).

65. Camm E.H., Behnke M.R., Bolado O., Bollen M., Bradt M., Brooks C., Dilling W., Edds M., Hejdak W.J., Houseman D., Klein S., Li F., Li J., Maibach P., Nicolai T., Patino J., Pasupulati S.V., Samaan N., Saylors S., Siebert T., Smith T., Starke M., Walling R. Characteristics of wind turbine generators for wind power plants. *2009 IEEE Power & Energy Society General Meeting*, 2009, pp. 1-5. doi: https://doi.org/10.1109/PES.2009.5275330.

66. Rather Z.H., Chen Z., Thøgersen P., Lund P. Dynamic Reactive Power Compensation of Large-Scale Wind Integrated Power System. *IEEE Transactions on Power Systems*, 2015, vol. 30, no. 5, pp. 2516-2526. doi: https://doi.org/10.1109/TPWRS.2014.2365632.

67. Behnke M., Ellis A., Kazachkov Y., McCoy T., Muljadi E., Price W., Sanchez-Gasca J. Development and Validation of WECC Variable Speed Wind Turbine Dynamic Models for Grid Integration Studies. *AWEA's 2007 Wind Power Conference*, Los Angeles, California, June 4-7, 2007. Available at: https://digital.library.unt.edu/ark:/67531/metadc887008 (Accessed 20 August 2021).

Safwan Ghanem[1]*, PhD Student,*
Ghaeth Fandi[1]*, PhD, Assistant Professor,*
Jan Kyncl[1]*, PhD, Associate Professor,*
Zdenek Müller[1]*, PhD, Associate Professor,*
[1] Department of Electrical Power Engineering,
Faculty of Electrical Engineering,
Czech Technical University,
2, Technicka Str., 166 27, Prague, Czech Republic,
e-mail: ghanesaf@fel.cvut.cz;
fandigha@fel.cvut.cz (Corresponding Author);
kyncl@fel.cvut.cz; Zdenek.Muller@fel.cvut.cz

T. Praveen Kumar, S. Ganapathy, M. Manikandan

Improvement of voltage stability for grid connected solar photovoltaic systems using static synchronous compensator with recurrent neural network

Purpose. *This article proposes a new control strategy for static synchronous compensator in utility grid system. The proposed photovoltaic fed static synchronous compensator is utilized along with recurrent neural network based reference voltage generation is presented in grid system network.* ***The novelty*** *of the proposed work consists in presenting a Landsman converter enhanced photovoltaic fed static synchronous compensator with recurrent neural network algorithm, to generate voltage and maintain the voltage-gain ratio.* ***Methods.*** *The proposed algorithm which provides sophisticated and cost-effective solution for utilization of adaptive neuro-fuzzy inference system as maximum power point tracking assures controlled output and supports the extraction of complete power from the photovoltaic panel. Grid is interconnected with solar power, voltage phase angle mismatch, harmonic and voltage instability may occur in the distribution grid. The proposed control technique strategy is validated using MATLAB/Simulink software and hardware model to analysis the working performances.* ***Results.*** *The results obtained show that the power quality issue, the proposed system to overcome through elimination of harmonics, reference current generation is necessary, which is accomplished by recurrent neural network. By recurrent neural network, the reference signal is generated more accurately and accordingly the pulses are generated for controlling the inverter.* ***Originality.*** *Compensation of power quality issues, grid stability and harmonic reduction in distribution network by using photovoltaic fed static synchronous compensator is utilized along with recurrent neural network controller.* ***Practical value.*** *The work concerns the comparative study and the application of static synchronous compensator with recurrent neural network controller to achieve a good performance control system of the distribution network system. This article presents a comparative study between the conventional static synchronous compensator, static synchronous compensator with recurrent neural network and hardware implementation with different load. The strategy based on the use of a static synchronous compensator with recurrent neural network algorithm for the control of the continuous voltage stability and harmonic for the distribution network-linear as well as non-linear loads in efficient manner. The study is validated by the simulation results based on MATLAB/Simulink software and hardware model.* References 29, tables 2, figures 25.
Key words: **static synchronous compensator, photovoltaic fed, adaptive neuro-fuzzy inference system, recurrent neural network.**

Мета. *У статті пропонується нова стратегія управління статичним синхронним компенсатором в енергосистемі. Запропонований статичний синхронний компенсатор з живленням від фотоелектричних елементів використовується разом з генератором опорної напруги на основі нейронної рекурентної мережі, представленим в мережі енергосистеми.* ***Новизна*** *запропонованої роботи полягає у поданні статичного синхронного компенсатора з покращеним фотоелектричним перетворювачем Ландсмана з алгоритмом рекурентної нейронної мережі для генерації напруги та підтримки коефіцієнта посилення за напругою.* ***Методи***. *Запропонований алгоритм, який забезпечує ефективне та економічне рішення для використання адаптивної нейро-нечіткої системи логічного виведення як відстеження точки максимальної потужності, забезпечує контрольований вихід та підтримує вилучення повної потужності з фотогальванічної панелі. Мережа взаємопов'язана із сонячною енергією, у розподільній мережі можуть виникати невідповідність фазового кута напруги, гармоніки та нестабільність напруги. Запропонована стратегія методу управління перевіряється з використанням моделей програмного забезпечення MATLAB/Simulink та апаратного забезпечення для аналізу робочих характеристик.* ***Результати***. *Отримані результати показують, що проблема якості електроенергії, яку запропонована система долає за допомогою усунення гармонік,потребує генерації еталонного струму, що здійснюється рекурентною нейронної мережею. За допомогою рекурентної нейронної мережі більш точно формується еталонний сигнал і відповідно генеруються імпульси для керування інвертором.* ***Оригінальність***. *Компенсація проблем з якістю електроенергії, стабільністю мережі та зниженням гармонік у розподільній мережі за допомогою статичного синхронного компенсатора з фотоелектричним живленням використовується разом із контролером рекурентної нейронної мережі.* ***Практична цінність***. *Робота стосується порівняльного дослідження та застосування статичного синхронного компенсатора з рекурентним нейромережевим контролером для досягнення хорошої продуктивності системи управління системою розподільної мережі. У цій статті представлено порівняльне дослідження традиційного статичного синхронного компенсатора, статичного синхронного компенсатора з рекурентною нейронною мережею та апаратною реалізацією з різним навантаженням. Стратегія, що ґрунтується на використанні статичного синхронного компенсатора з рекурентним алгоритмом нейронної мережі для ефективного контролю стабільності постійної напруги та гармонік для лінійних та нелінійних навантажень розподільної мережі. Дослідження підтверджується результатами моделювання з урахуванням програмно-апаратної моделі MATLAB/Simulink.*. Бібл. 29, табл. 2, рис. 25.
Ключові слова: **статичний синхронний компенсатор, фотоелектричне живлення, адаптивна нейро-нечітка система виведення, рекурентна нейронна мережа.**

Abbreviations

ANFIS	Adaptive Neuro-Fuzzy Inference System	PI	Proportional-Integral
ANN	Artificial Neural Network	P-O	Perturb-Observe
DVR	Dynamic Voltage Restorer	PV	Photovoltaic
FACTS	Flexible AC Transmission System	RNN	Recurrent Neural Network
FFT	Fast Fourier Transform	SEPIC	Single Ended Primary Inductance Converter
FIS	Fuzzy Inference System	SRF	Synchronous Reference Frame
IC	Incremental Conductance	STATCOM	Static Synchronous Compensator
LSTM	Long Short-Term Memory	THD	Total Harmonic Distortions
MPPT	Maximum Power Point Tracking	VSI	Voltage Source Inverter
PCC	Point of Common Coupling		

Introduction. Nowadays, power quality is considered as a major issue in industrial sectors because of increasing sensitive loads [1, 2]. In general, the power quality problems greatly affect the distribution side which results in malfunctioning and failure of sensitive loads

[3]. Majority of power quality issues are caused by non-linear loads and harmonic imbalances [4]. Voltage sag/swell, harmonic distortions, spikes and surges and transient disruptions are the most serious power quality issues that severely affect the power distribution system [5, 6]. Thus in modern power systems, stability enhancement and reactive power compensation are the important actualities; DVR, a FACTS device is widely employed in achieving so. It solves the voltage sag problem in a unique way, however, it only compensates for a specific proportion of sag, and so the power quality problem is not totally eliminated [7-9].

Therefore, one of the excellent FACTS device called STATCOM is utilized in this work which assists in improvising the sag/ swell control, dynamic voltage control, real and reactive power control etc., providing better power quality and voltage stability [10-12]. Due to advanced technologies including incorporation of large-scale renewable distributed generation, enhanced communication as well as control methods, and increased storage capacity, generation of power and distribution networks are facing significant variations. Owing to the static structure, minimal size, and low cost for maintenance, solar PV dependent energy generation systems are widely used by various renewable resources for the generation of power [13]. Since solar PV energy is intermittent, the PV systems are combined with storage systems for energy as well as other sources for renewable energy to ensure trustworthy functioning. This is attained by the parallel connection of DC-DC converters with PV panel [14]. A DC-DC converter is necessary amidst the inverter and the PV panel for avoiding large number of PV panels connected in series manner. This converter is also essential in power generation of PV system for providing electrical isolation [15].

Regarding DC-DC converters, boost converters are used in increasing the PV panel voltage and their incorporation reduces the input ripple current obtained from the solar panel, increasing the panel's reliability and extraction power [16]. Despite these benefits, boost converters have a discontinuous input and output, necessitating a greater number of switching devices. This influences the circuit dynamics by causing fluctuations in the gain of the circuit [17]. To overcome this limitation, a buck-boost converter has been developed, which has a wide input and output voltage range with increased performance. It achieves an additional input feature that increases the dc input voltage range, greatly improving the PV panel's versatility but possesses centralized operation [18]. Zeta converter is also utilized in PV systems which generate minimal ripple current and improved voltage gain but the gain of voltage is sensible with the inductance leakage [19]. CUK converters employed by the PV panel exhibited minimal switching losses together with better voltage regulation and greater efficiency providing versatile operation. However, due to the resulting sharp speed up/down voltage, these converters lagged, impacting the precise utilization [20]. Furthermore, CUK converter utilization is restricted to the medium-low power range, as high-power operation necessitates large input and output inductors, and the converter is harmed when linked to a utility grid due to

grid voltage fluctuations [21, 22]. Moreover, SEPIC converters are utilized in PV systems to generate an output which is non-inverting and is considered as easy to drive due to the referenced switch towards ground node. However, these converters are not finer in terms of cost and efficiency [23]. In order to tackle these issues, Landsman converter is exploited which offers noiseless operation with improved efficiency.

To extract the full quantity of solar power, the DC-DC converter is used in conjunction with a MPPT controller. It is a significant component included in PV systems to improve the efficiency of extracting renewable energy. Numerous schemes for MPPT control are proposed and in most of them, PV voltage is selected as the variable for control because of its enhanced characteristics for stability [24]. P-O is a commonly used MPPT algorithm because of its simplicity and cost-effectiveness. The perturbation's phase size is estimated by the tradeoff amidst MPPT precision and MPPT rate which is little tedious. The use of IC instead of P-O, which is free of oscillations while tracking the maximum power point, yields more precise performance. Despite these benefits, this approach is limited by environmental conditions [25]. These flaws are overcome by employing closed loop control algorithms that balance the DC-link voltages, resulting in minimal distortions and efficiently preserving the grid system's power quality [26]. Closed loop algorithms produce optimal results when dealing with external disruptions, allowing grids to operate in real time but result in high emission costs due to less emission allowance [27]. To overcome these issues, ANFIS is exploited in this approach which combines the benefits of complementary ANN and fuzzy logic algorithms, resulting in better fuzzy controller accuracy and a shorter development time.

Furthermore, the converter's output DC voltage is transformed to AC voltage, which is accomplished by a 3ϕ VSI that is grid connected. The synchronization of grid is regarded as a significant challenge due to issues such as voltage distortions induced by local nonlinear loads and grid disturbances. The basic elements of the common coupling voltage point are evaluated with the consideration of power quality variations for achieving improved synchronization of grid [28, 29]. These grid synchronization frameworks improve control efficiency and interpolate improved grid quality power, resulting in precise outcomes. The control architectures considered are complex hybrid systems that combine classical and modern techniques, such as artificial intelligence and statistical models.

The **goal** of this paper is the synthesis of a recurrent neural network based reference current generation control structure and the identification of the latest trends. The main findings are summarized in the development of increasingly robust controllers for operation with improved efficiency, power quality, stability, safety, and economics. A Landsman converter is exploited which acts as a ripple filter and boosts the oscillating PV voltage. An MPPT controller adopting ANFIS is utilized for providing better accuracy. RNN based reference current generation is utilized for effective harmonic elimination. A 3ϕ VSI for inverting the input DC voltage along with LC filter and AC grid is also employed in STATCOM applications.

Proposed control system. The schematic diagram for the proposed approach is given in Fig. 1, in which the

voltage stability of the power system is enhanced by the implementation of STATCOM. PV power is applied to the STATCOM along a Landsman converter. The point of functioning of PV array is at the maximum power point while the converter power is grid synchronized. For the controlling of Landsman converter, an MPPT controller is connected which tracks the maximum power by evaluating the current as well as voltage obtained from the PV array. It regulates the reference voltage or duty cycle for matching the power to instant power point. The MPPT controller exploits ANFIS and is non-linear and varies in accordance with time. It performs the evaluation of signals and its optimal selection thus mitigating the steady-state error.
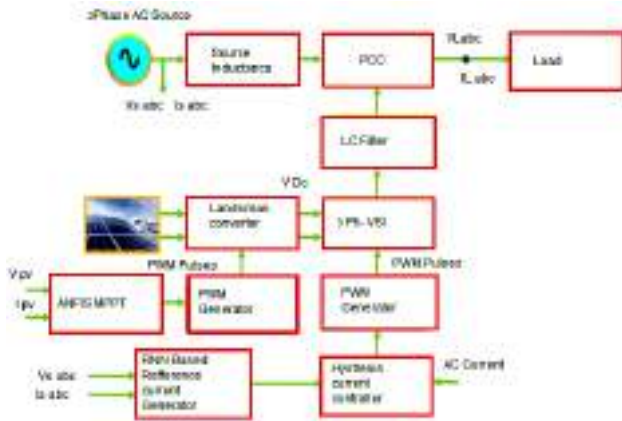
Fig. 1. Schematic diagram of the proposed approach

RNN based reference current generation is utilized in this work, by which the harmonics are eliminated for any change in load and source voltage. Thus, the pulses for controlling the VSI are generated by using hysteresis current controller, thereby providing reactive power compensation and harmonic elimination.

Modeling of PV system. A solar cell is essentially a semiconductor diode that is exposed to irradiance. This solar irradiance comprises of photons having various levels of energy of which few are absorbed in *p-n* junction. The photons with minimum energy level when compared to the solar cell's band gap are unusable. The photons with maximum energy when compared to band gap are utilized in the range similar to band gap. The equivalent circuits generally utilized for the PV cell modeling consists of a single diode offering better tradeoff between simplicity and accuracy and the corresponding diagram is shown in Fig. 2.
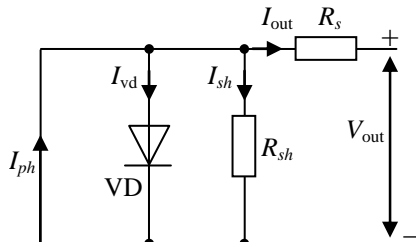
Fig. 2. Equivalent circuit of PV cell

The photo current I_{ph} is based on the solar radiation R and temperature T and is given by

$$I_{ph} = I_{ph}(T_{ref}) \cdot (1 + k_0 \cdot (T - T_{ref}));\qquad(1)$$

$$I_{ph}(T_{ref}) = \frac{R}{R_{ref}} \cdot I_{sc}(T_{ref}),\qquad(2)$$

where $I_{ph}(T_{ref})$ is the photo current corresponding to nominal temperature T_{ref}; R_{ref} is the radiation which is nominal obtained by PV's constructor; k_0 is the constant which is given as

$$k_0 = \frac{I_{sc}(T) - I_{sc}(T_{ref})}{T - T_{ref}},\qquad(3)$$

where I_{sc} is the current across short circuit.

In PV system, the temperature of environment is a nominal one and from (1), (2) for $T = T_{ref}$, the photo current I_{ph} depends on solar radiation and is given as

$$I_{ph} = I_{ph}(T_{ref}) = \frac{R}{R_{ref}} \cdot I_{sc}(T_{ref}).\qquad(4)$$

Equation (5) denotes diode equation in which V_{out} and I_{out} are the current as well as voltage outputs, I_{sat} is the saturation current of the diode VD, V_{th} is the thermal voltage of the diode, R_s is the resistance in series

$$I_d = I_{sat}\left[\exp\left(\frac{V_{out} + I_{out} \cdot R_s}{V_{th}}\right) - 1\right].\qquad(5)$$

The current across parallel resistance is given as

$$I_{sh} = \frac{V_{out} + I_{out} \cdot R_s}{R_{sh}}.\qquad(6)$$

The V-I characteristic equation is given as

$$I_{out} = I_{ph} - I_{sat}\left[\exp\left(\frac{V_{out} + I_{out} \cdot R_s}{V_{th}}\right) - 1\right] - \\ - \left(\frac{V_{out} + I_{out} \cdot R_s}{R_{sh}}\right).\qquad(7)$$

Thus, the modeling of PV system is performed and from (7), the output voltage and the input voltage are evaluated.

Modeling of Landsman converter. Landsman converter is a DC-DC converter which is used to enhance the voltage attained from the PV system providing a noiseless operation. The converter is designed to function in continuous conduction mode irrespective of irradiance level variations. The connection diagram of the proposed Landsman converter is given in Fig. 3.
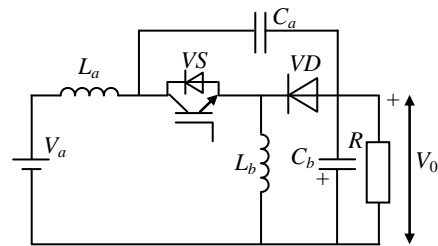
Fig. 3. Landsman converter

The input voltage is given by V_a and the output voltage is given by V_0. The switch is represented as VS and the output resistance is denoted as R. The current across the inductors L_a, L_b and the voltage across C_a are continuous in nature. It has the ability to boost the output and functions in boost mode when the value of duty ratio is greater than 50 %.

Operating mode 1 – switch ON. In operating mode 1, the switch is in ON condition and the voltage of capacitor

C_a termed as V_{Ca} reverse biases the diode. The current across L_b termed as I_{Lb} flows along the switch. Since V_{Ca} is greater than the resultant voltage V_0, and C_a discharges along the switch, transmitting energy to the inductor L_b and the output. Hence, V_{Ca} decreases and I_{Lb} increases and the input supplies energy to the input inductor L_a.

Operating mode 2 – switch OFF. In operating mode 2, the switch is in OFF condition and the forward biasing of diode results in a configuration of circuit as given in Fig. 3. The current across inductor L_b termed as I_{Lb} flows along the diode VD. The inductor L_b transmits its energy retained to output across the diode. Consequently, C_a is charged across the diode with the energy from both the input as well as L_a and hence, V_{Ca} increases while I_{Lb} decreases.

The ripple in the input current I_{La} is calculated by considering the flow of all the ripple component of L_a across C_a. $\Delta\phi$ represents the additional flux and the peak-to-peak ripple current is given by:

$$\Delta I_{La} = \Delta\phi / L_a .\qquad(8)$$

At switch off condition, the current across C_a is given as:

$$I_{Ca} = I_{La} = C_a \cdot \frac{\Delta V_{Ca}}{(1-D)\cdot t_s},\qquad(9)$$

where D is the duty ratio; t_s is the switching period.

The voltage ripple content of V_{Ca} is given as:

$$\Delta V_{Ca} = \frac{I_{La}}{C_a}\cdot(1-D)\cdot t_s .\qquad(10)$$

Substitute (10) in (8):

$$\Delta I_{La} = \frac{1}{2}\cdot\frac{1}{L_a}\cdot\frac{I_{La}}{2\cdot C_a}\cdot(1-D)\cdot t_s\cdot\frac{t_s}{2} =$$
$$= \frac{1}{8\cdot L_a\cdot C_a}\cdot\frac{I_{La}\cdot(1-D)}{f_{sw}^2},\qquad(11)$$

where $f_{sw} = 1/t_s$ is the switching frequency.

Equation (11) is normalized as:

$$\frac{\Delta I_{La}}{I_{La}} = \frac{1}{8\cdot L_a\cdot C_a}\cdot\frac{(1-D)}{f_{sw}^2}.\qquad(12)$$

So, we have:

$$I_{La} = \frac{D}{(1-D)}\cdot I_0 .\qquad(13)$$

where I_0 is the current at the output side.

Substitute (13) in (11)

$$L_a = \frac{D\cdot I_0}{8\cdot f_{sw}^2\cdot C_a\cdot\Delta I_{La}} .\qquad(14)$$

Modelling of MPPT controller. In «neuro-fuzzy» method different learning concepts from the neural network literature are applied to a FIS. Figure 4 shows the model of ANFIS and it possesses the merits of both neural network as well as fuzzy logic controllers. Comparing with existing techniques of MPPT, the ANFIS adopted MPPT controller offers improved accuracy for tracking with high convergence speed.

The three major components present in the ANFIS are a rule based one dealing with choosing fuzzy rules, a database concept representing the membership functions of fuzzy rules and a decision engine for depicting the output adopting inference procedure. Expert awareness
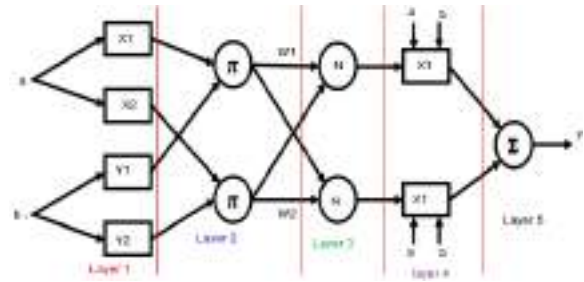
Fig. 4. Proposed ANFIS model

encompasses fuzzy logic principles, while neural network schemes are developed with the data base. Furthermore, the neuro-fuzzy approach appears to be appropriate if the system's data as well as information sources are available. In this approach, ANFIS based MPPT controller is utilized in PV system for tracking optimal power with minimal oscillation and the optimized fuzzy rules are attained by the embedding of the behavior of the complete system.

The outputs are obtained as the linear combination of the corresponding inputs and the fuzzy rules are given below:

1. When $a = X_1$, $b = Y_1$ then $F_1 = i_1a + j_1a + k_1$;
2. When $a = X_2$, $b = Y_2$ then $F_2 = i_2a + j_2a + k_2$;

Layer 1 comprises adaptive nodes capable of generating membership gradings of linguistic labels depending on assumed signals utilizing a proper parameterized membership function given as:

$$O_{1p} = \mu_{X_p}(a) = \frac{1}{1+\left|\frac{a-c_p}{x_p}\right|^{2\cdot y_p}},\qquad(15)$$

where O_{1p} represents the pth node output of initial layer; a is the node input p; X_i is the linguistic label obtained from $X = (X_1, X_2, Y_1, Y_2)$ which represents the fuzzy set and $\{x_p, y_p, z_p\}$ represents the premise parameter set utilized for adjusting the membership function's shape.

Layer 2 comprises nodes which are fixed and designated as Π, further represented as the firing strength of every rule. The fuzzy AND of all inputs is taken as the output of every node:

$$O_{2p} = W_p = \mu_{X_p}(a)\cdot\mu_{Y_p}(b), \; p = 1,2,...\qquad(16)$$

Layer 3 results are firing strengths which are normalized and the pth node output is given by the ratio of the firing strength of pth rule to the total of all rules of firing strengths:

$$O_{3p} = \overline{W_p} = \frac{W_p}{W_1 + W_2} .\qquad(17)$$

Layer 4 outputs are calculated by the adaptive nodes depending on parameters utilizing:

$$O_{4p} = \overline{W_p}\cdot F_p = \overline{W_p}\cdot\left(i_p\cdot a + j_p\cdot b + k_p\right),\quad(18)$$

where $\overline{W_p}$ is the firing strength from the third layer and (i_p, y_p, k_p) are the nodes consequent parameter set.

Layer 5 estimates the overall output of ANFIS from the total of the inputs of nodes:

$$O_{5p} = \sum_{i=1}^{p}\overline{W_p}\cdot F_p = \frac{\sum_{i=1}^{p}W_p\cdot F_p}{\sum_{i=1}^{p}W_p} .\qquad(19)$$

The current, power of the PV system and the duty cycle ratio of the converter are obtained as outputs by ANFIS controller. The input labels permit the ANFIS for generating the converter command which is further fed to the converter for ensuring power adaptation.

RNN based reference current generation. The increased usage of non-linear loads leads to distortions in current and voltage; however, there are several methods to mitigate harmonics. The injection of opposite harmonics in the PCC is one of the effective methods. For this, accurate reference current generation is necessary and this is accomplished in this work by RNN. The illustration of RNN is given in Fig. 5 and the process of harmonics extraction is in Fig. 6.
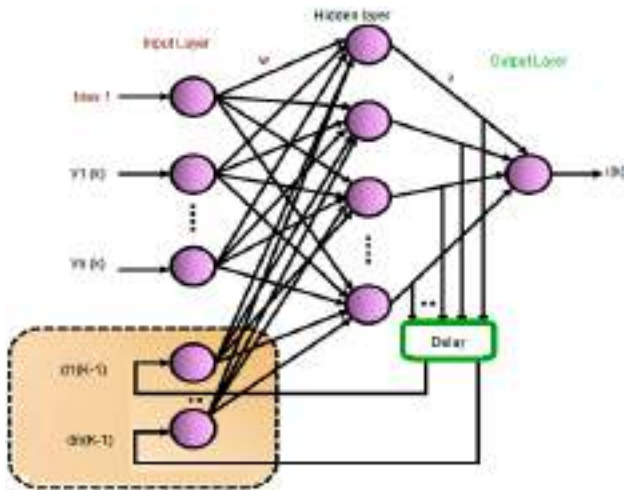
Fig. 5. Structure of RNN
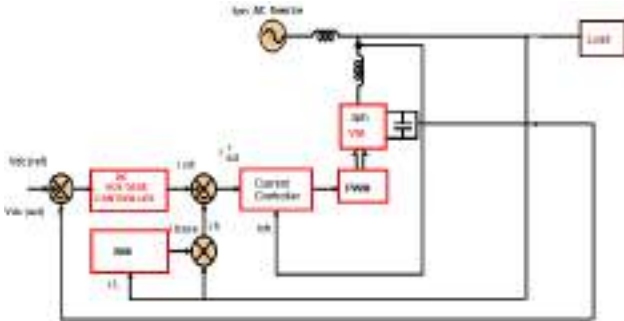
Fig. 6. Reference current generation

The structure of RNN resembles Elman network, in which the hidden layer's output at $(k-1)$, is taken as the additional input for every sample step k. As the feedback is included from the prior step, an additional memory is included so that the neural network has the ability to grasp the dynamic behavior of the system. Back-propagation training is utilized for updating the weights.

By RNN, the harmonic components i_h is extracted from the load current i_L and the expression relating the harmonic component and load current is given as:

$$i_h = i_L - i_{base}, \qquad (20)$$

where the fundamental component is denoted as i_{base}, the reference current i_{sd}^* is generated exactly by RNN thereby eliminating the harmonics.

RNN consists of numerous successive recurrent layers, and these layers are sequentially modeled in order to map the sequence with other sequences. RNN has a strong capability in order to capture the contextual data from the sequence. RNN can operate the sequences with arbitrary length. RNN is the extension of feed forward neural network with the presence of loops in hidden layers. RNN takes the input with the sequence of samples and identifies the time relationship between the samples. The LSTM solves the classification issues by adding the network parameters with the hidden node and releases the state based on the input values. RNN achieves better performance than LSTM by activating the states based on network events. The regular RNN node consists of a single bias and weight. The RNN is evaluated using the gated recurrent unit and LSTM. The one-to-one network configuration is formed using the network parameters, where the time step of each input data generates the output with the specific time step.

- Forget gate layer;
- Input gate layer;
- Output gate layer;
- State gate layer.

The input and the forget gate controls the previous hidden state and the present input state that contributes to the cells state. However, the input, output, and the forget gate activation is scaled using the sigmoid function, and the output of the hidden state is filtered using the hyperbolic function. The optimization of network parameters using the stochastic gradient is achieved based on the sequence of input data. However, the hyperparameters are the structure of the network (size and layers), sequence length, batch size, momentum, and learning rate, respectively. The hyperparameters are set through the stochastic or manual search.

The input of the RNN is the sequence of vectors as $\{y_1, y_2, ..., y_M\}$ the sequence of hidden states as $\{z_1, z_2, ..., z_M\}$ and the output unit as $\{v_1, v_2, ..., v_M\}$ respectively.

The recurrent layer consists of the recurrent function d, which takes the input vector yx and the hidden unit of the previous state zx as the input and generates the hidden state as:

$$zx = d(yx, zx - 1) = \tanh(P \cdot yx + Q \cdot zx - 1). \qquad (21)$$

Moreover, the output units are calculated as:

$$vx = \text{soft} \max(R \cdot zx), \qquad (22)$$

where P, Q, R are the weight matrices; and the activation function tanh indicates the hyperbolic tangent function.

RNN uses the highly complicated function in order to learn and control the information flow in the recurrent layer for capturing the long term dependencies.

Results and discussions. The analysis of PV fed STATCOM assisting harmonics elimination, providing voltage stability is validated through MATLAB environment in this work. The output voltage of the PV system has been enhanced by exploiting the Landsman converter, through which the performance of the system is improved. The DC-link voltage stability is regulated through the ANFIS adopted MPPT controller offering high accuracy with increased speed of convergence. The specifications of PV module and Landsman converter are illustrated in Table 1.

The proposed work is implemented in MATLAB depicted in Fig. 7 and the obtained results are given below.

Specifications PV module and Landsman converter

Parameter name	Value
Cells in a module	36
Modules in series	17
Modules in parallel	4
Open circuit voltage V_{oc}, V	21
Short circuit current I_{sc}, A	7.1
Converter duty ratio D	0.5
Capacitance C_a, μF	4.7
Capacitance C_b, μF	1000
Inductance L_a, mH	0.9
Inductance L_b, mH	5.4
Capacitance C_f, μF	650
Resistance R_c, Ω	0.03
Inductance L_f, mH	0.7
Resistance R_f, Ω	0.01
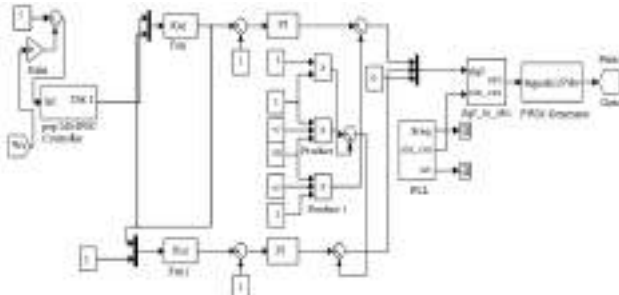
Fig. 7.Control block of RNN

Figure 8 indicates the waveform for solar irradiation. Its increase leads to the increase of output current as well as voltage. This results in maximum power output in this mode of operation.

Figure 9 indicates the waveform for temperature. The increase in operating temperature results in the marginal increase of output current, but leads to decrease in output voltage and hence results in the decrease of net output power.
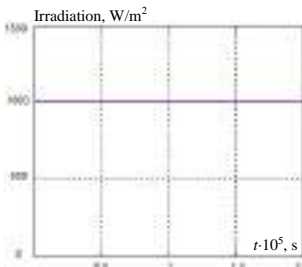
Fig. 8. Waveform for solar irradiation
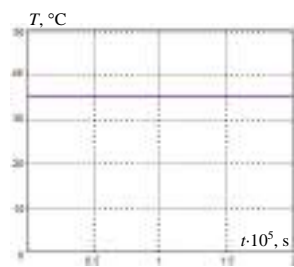
Fig. 9. Waveform for temperature

Figures 10, 11 denote the waveforms for output voltage and output current in PV panel respectively. The output voltage obtained is a constant DC voltage with varying time.
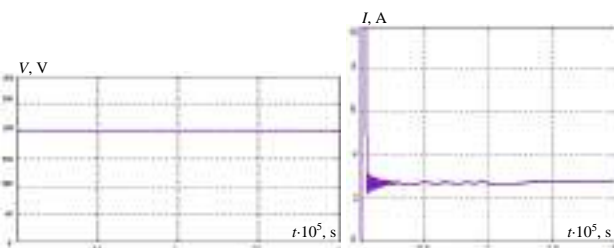
Fig. 10. Output voltage waveform for PV panel

Fig. 11. Output current waveform for PV panel

Figures 12, 13 denote the output voltage waveform as well as output current waveform for a switched boost Landsman converter. The adopted ANFIS based MPPT extracts maximum power from the PV panel and is fed to the converter which further minimizes the ripples.
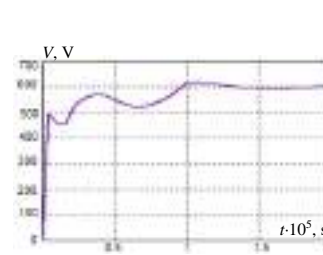
Fig. 12. Output voltage waveform for switched boost Landsman converter
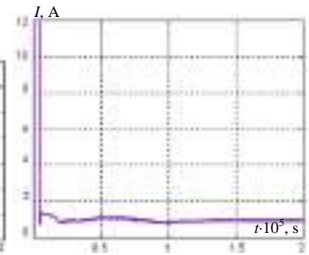
Fig. 13. Output current waveform for switched boost Landsman converter

Figure 14 denotes the AC output voltage waveform for VSI with varying magnitude and frequency. The comparison of reference signal is performed with a carrier waveform of increased frequency for controlling the inverter's AC output voltage.

Figure 15 indicates the output voltage waveform for grid which is sinusoidal in nature with constant voltage and frequency.
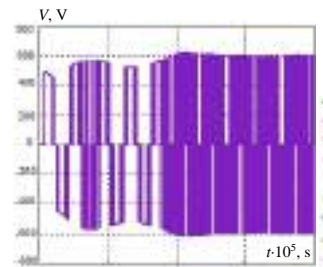
Fig. 14. Output voltage waveform for VSI
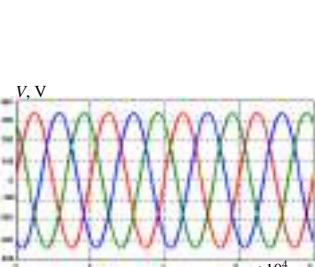
Fig. 15. Output voltage waveform for grid

Figure 16 indicates the output current waveform for grid which is sinusoidal in shape during its operation maintaining constant voltage and frequency. The grid current THD (Fig. 17) has been observed as 3.5 %, which satisfies the IEEE standard.
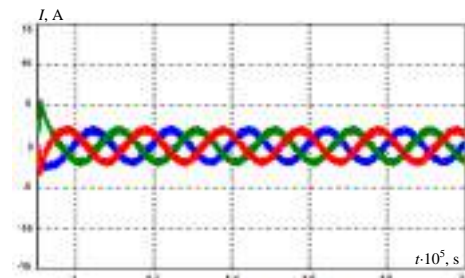
Fig. 16. Output current waveform for grid

Fundamental (50 Hz) = 10.45, THD = 3.5 %
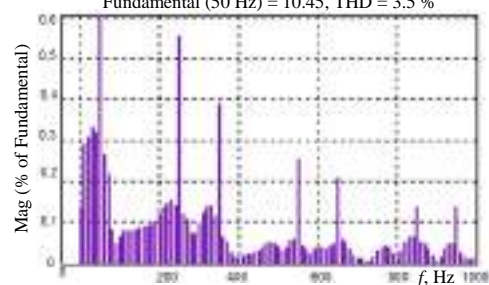
Fig. 17. Grid current THD

The performance of the converter is analyzed in terms of its efficiency and voltage gain ratio. In both the aspects the proposed Landsman converter provides better results as shown in Fig. 18, with a maximum efficiency of 92 % and gain of 10.
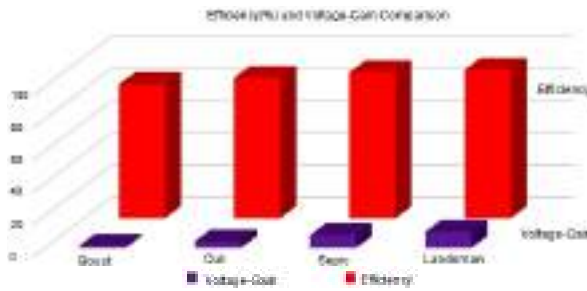
Fig. 18. Comparison of efficiency and voltage-gain for Landsman converter

The tracking efficiency of the proposed MPPT algorithm is revealed to be more effective when analogized with conventional algorithms like P-O, IC and fuzzy. The tracking efficiency (Fig. 19) of P-O algorithm, IC, fuzzy and ANFIS are observed as 81 %, 84 %, 89 % and 92 % respectively.
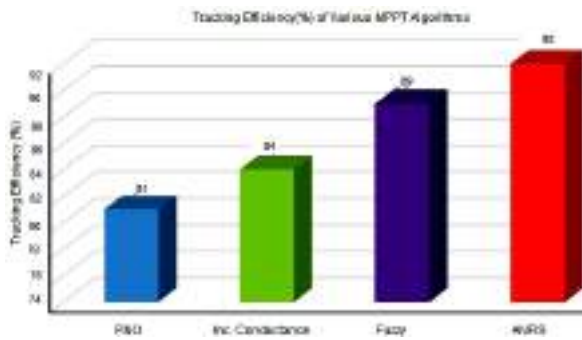
Fig. 19. Comparison of tracking efficiency

DC-link voltage control plays a key role in determining the overall performance of the system, by which the voltage stability is ensured. Better settling time and THD is accomplished by using the proposed RNN based reference current generation whereas the PI controller and SRF theory delivers relatively low values depicted in Table 2.

Table 2
Comparison of settling time and THD

	PI	SRF	RNN
Settling time, s·10^{-5}	3.2	2.7	1.75
THD	4.7 %	4.2 %	3.5 %

Experimental setup. The PV array integrated utility grid using high gain converters hardware setup shown in Fig. 20. The operation of the STATCOM under two different cases.

Method 1. In this method the outer loop and inner loop of the grid used is PI voltage regulator and PI current controller.

Method 2. In the method the outer voltage loop used in PI voltage regulator and inner current loop used as RNN current controller. The above different methods to assure the controller performance at different system parameters, the local loads on grid side and solar irradiance has been changed as follows:
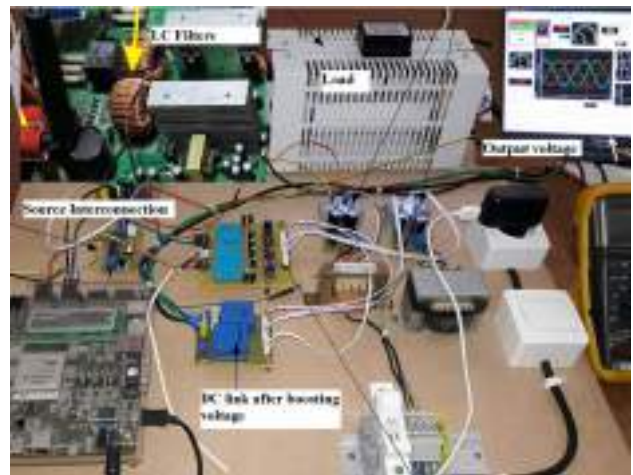
Fig. 20. Hardware setup for grid connected solar PV systems using STATCOM

1. Without any break 10 kW inductive load is applied and 0.8 s with 5 kW one more inductive load is applied.

2. Duration of 0.4 s to 0.6 s solar irradiance is changed from 1000 W/m^2 to 600 W/m^2.

In hardware circuit, displays the voltage and current before the boost converter of PV terminal. The current is changed with respect to change in irradiance of the solar PV panel. The PV array voltage level is changed by using high gain.

The proposed RNN controller shows better harmonic reduction than existing PI current controller. Moreover, the voltage stability of the system maintain with solar PV interconnected with distribution grid even under dynamic changes.

The load current of solar interconnected PV system is shown in Fig. 21.

For various operating condition the single stage grid connected system was studied and the off mode grid with solar PV system for disconnected source voltage depicted in Fig. 22.

The isolation condition of 1000 W/m^2 is 400 V PV model power for reactive power by the inverter output shown in Fig. 23.

In this case the isolation level on the PV panel was varied as shown in the Fig. 24.

The FFT analysis of output voltage for the grid interconnected THD is depicted in Fig. 25 and the reduced THD is 4.24 %.
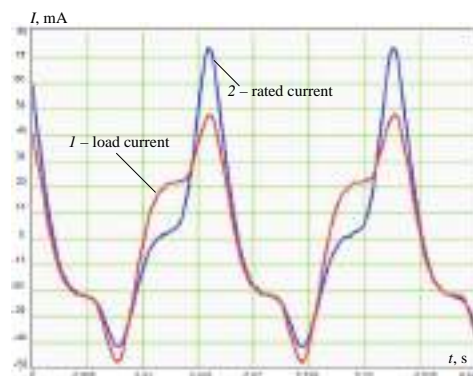
Fig. 21. Load current
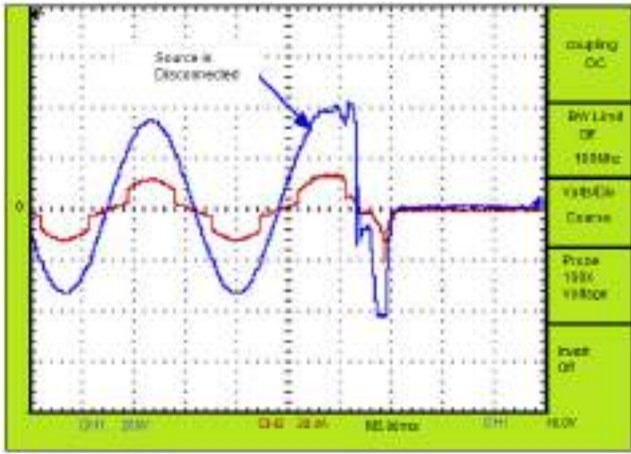
Fig. 22. Disconnected source voltage
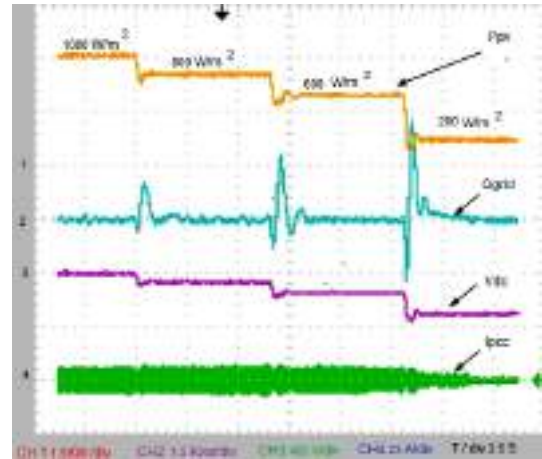
Fig. 23. PV module power P_{pv}, reactive power Q_{grid} supplied by inverter, DC link voltage V_{dc}, current at the PCC I_{pcc} for variable isolation
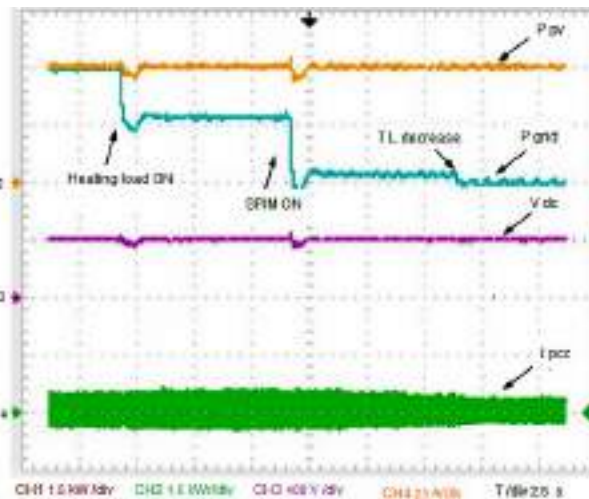
Fig. 24. PV module power P_{pv}, active power P_{grid} supplied by inverter, DC link voltage V_{dc}, current at the PCC I_{pcc} for switching ON of local load
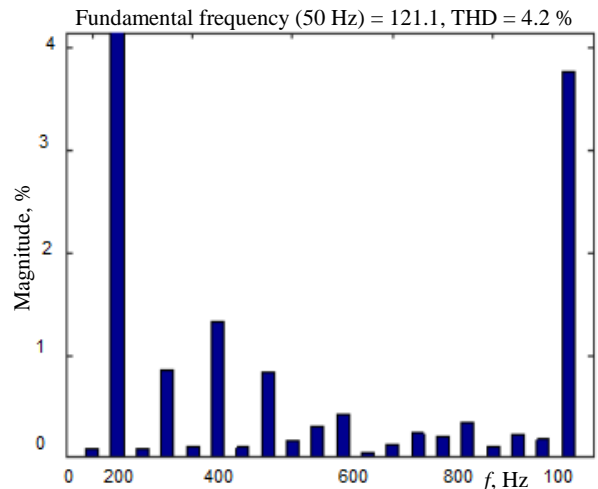
Fundamental frequency (50 Hz) = 121.1, THD = 4.2 %
Fig. 25. The performance of FFT analysis of output voltage for THD

The observation.

1. The proposed model, active power, reactive power injected for different isolation level, the inverter DC link voltage and current fed to the grid.

2. The THD level of the current is found to be below 5 %.

3. The reactive power is maintained at zero level in order to ensure the unity power factor operation.

4. Reactive power injected by the system voltage regulation at the terminal of the inverter the can be adjusted.

5. The system for a strong interconnection grid system, the performance of the controller is much better and faster as compared to that for a weak interconnected grid system.

While implementing the practical consequences, there will be a ripple current significant rise whenever the inverter feeds non-linear load, and its majority of concern is magnetizing current. The hardware prototype sampling time, harmonics will be slightly higher than its simulation results. It can be suppressed by either increasing the number of levels of inverter or designing a filter.

Conclusions.

In this paper, an efficient way of regulating voltage stability and mitigating harmonics is addressed by using a photovoltaic fed static synchronous compensator with recurrent neural network. Static synchronous compensator is basically shunt connected, which provides reactive power compensation and voltage stability. DC-DC converters has been incorporated with photovoltaic systems and Landsman converter has been utilized in this work along with adaptive neuro-fuzzy inference system maximum power point tracking for tracking the maximum power from the photovoltaic, along with DC-link voltage regulation. The chosen converter provides better efficiency and voltage-gain ratio when compared with other converters. Recurrent neural network assists in the generation of reference signal, so that the harmonics that occur in the system are effectively mitigated. The validation of the proposed work is carried out through simulation in MATLAB and also tested with hardware model. It has been observed that the total harmonic distortions is minimized to 5 % which suits IEEE standard.

Conflict of interest. The authors declare that they have no conflicts of interest.

REFERENCES
1. Chowdhury B.H. Optimizing the integration of photovoltaic systems with electric utilities. *IEEE Transactions on Energy Conversion*, 1992, vol. 7, no. 1, pp. 72-78. doi: https://doi.org/10.1109/60.124544.
2. Yazdani A., Dash P.P. A Control Methodology and Characterization of Dynamics for a Photovoltaic (PV) System Interfaced With a Distribution Network. *IEEE Transactions on Power Delivery*, 2009, vol. 24, no. 3, pp. 1538-1551. doi: https://doi.org/10.1109/TPWRD.2009.2016632.
3. Babu V., Ahmed K.S., Shuaib Y.M., Manikandan M. Power Quality Enhancement Using Dynamic Voltage Restorer (DVR)-Based Predictive Space Vector Transformation (PSVT) With Proportional Resonant (PR)-Controller. *IEEE Access*, 2021, vol. 9, pp. 155380-155392. doi: https://doi.org/10.1109/ACCESS.2021.3129096.

4. Babu V., Ahmed K.S., Shuaib Y.M., Mani M. A novel intrinsic space vector transformation based solar fed dynamic voltage restorer for power quality improvement in distribution system. *Journal of Ambient Intelligence and Humanized Computing*. 2021. doi: https://doi.org/10.1007/s12652-020-02831-0.

5. Li C., Burgos R., Wen B., Tang Y., Boroyevich D. Stability Analysis of Power Systems With Multiple STATCOMs in Close Proximity. *IEEE Transactions on Power Electronics*, 2020, vol. 35, no. 3, pp. 2268-2283. doi: https://doi.org/10.1109/TPEL.2019.2931891.

6. Hou X., Sun Y., Han H., Liu Z., Su M., Wang B., Zhang X. A General Decentralized Control Scheme for Medium-/High-Voltage Cascaded STATCOM. *IEEE Transactions on Power Systems*, 2018, vol. 33, no. 6, pp. 7296-7300. doi: https://doi.org/10.1109/TPWRS.2018.2865127.

7. Kumar N., Singh B., Panigrahi B.K., Xu L. Leaky-Least-Logarithmic-Absolute-Difference-Based Control Algorithm and Learning-Based InC MPPT Technique for Grid-Integrated PV System. *IEEE Transactions on Industrial Electronics*, 2019, vol. 66, no. 11, pp. 9003-9012. doi: https://doi.org/10.1109/TIE.2018.2890497.

8. Anand I., Senthilkumar S., Biswas D., Kaliamoorthy M. Dynamic Power Management System Employing a Single-Stage Power Converter for Standalone Solar PV Applications. *IEEE Transactions on Power Electronics*, 2018, vol. 33, no. 12, pp. 10352-10362. doi: https://doi.org/10.1109/TPEL.2018.2804658.

9. Li R., Shi F. Control and Optimization of Residential Photovoltaic Power Generation System With High Efficiency Isolated Bidirectional DC–DC Converter. *IEEE Access*, 2019, vol. 7, pp. 116107-116122. doi: https://doi.org/10.1109/ACCESS.2019.2935344.

10. Babu V., Basha S.S., Shuaib Y.M., Manikandan M., Enayathali S.S. A novel integration of solar fed dynamic voltage restorer for compensating sag and swell voltage in distribution system using enhanced space vector pulse width modulation (ESVPWM). *Universal Journal of Electrical and Electronic Engineering*, 2019, vol. 6, no. 5, pp. 329-350. doi: https://doi.org/10.13189/ujeee.2019.060504.

11. Ahmad M.W., Gorla N.B.Y., Malik H., Panda S.K. A Fault Diagnosis and Postfault Reconfiguration Scheme for Interleaved Boost Converter in PV-Based System. *IEEE Transactions on Power Electronics*, 2021, vol. 36, no. 4, pp. 3769-3780. doi: https://doi.org/10.1109/TPEL.2020.3018540.

12. Chandrasekar B., Nallaperumal C., Padmanaban S., Bhaskar M.S., Holm-Nielsen J.B., Leonowicz Z., Masebinu S.O. Non-Isolated High-Gain Triple Port DC–DC Buck-Boost Converter With Positive Output Voltage for Photovoltaic Applications *IEEE Access*, 2020, vol. 8, pp. 113649-113666. doi: https://doi.org/10.1109/ACCESS.2020.3003192.

13. Huang Q., Huang A.Q., Yu R., Liu P., Yu W. High-Efficiency and High-Density Single-Phase Dual-Mode Cascaded Buck–Boost Multilevel Transformerless PV Inverter With GaN AC Switches. *IEEE Transactions on Power Electronics*, 2019, vol. 34, no. 8, pp. 7474-7488. doi: https://doi.org/10.1109/TPEL.2018.2878586.

14. Andrade A.M.S.S., Schuch L., da Silva Martins M.L. High Step-Up PV Module Integrated Converter for PV Energy Harvest in FREEDM Systems. *IEEE Transactions on Industry Applications*, 2017, vol. 53, no. 2, pp. 1138-1148. doi: https://doi.org/10.1109/TIA.2016.2621110.

15. Padmanaban S., Priyadarshi N., Bhaskar M.S., Holm-Nielsen J.B., Hossain E., Azam F. A Hybrid Photovoltaic-Fuel Cell for Grid Integration With Jaya-Based Maximum Power Point Tracking: Experimental Performance Evaluation. *IEEE Access*, 2019, vol. 7, pp. 82978-82990. doi: https://doi.org/10.1109/ACCESS.2019.2924264.

16. Han B., Lai J.-S., Kim M. Dynamic Modeling and Controller Design of Dual-Mode Cuk Inverter in Grid-Connected PV/TE Applications. *IEEE Transactions on Power Electronics*, 2018, vol. 33, no. 10, pp. 8887-8904. doi: https://doi.org/10.1109/TPEL.2017.2779843.

17. Manikandan M., Basha A.M. ODFF: Optimized Dual Fuzzy Flow Controller Based Voltage Sag Compensation for SMES-Based DVR in Power Quality Applications. *Circuits and Systems*, 2016, vol. 7, no. 10, pp. 2959-2974. doi: https://doi.org/10.4236/cs.2016.710254.

18. Moradi-Shahrbabak Z., Tabesh A. Effects of Front-End Converter and DC-Link of a Utility-Scale PV Energy System on Dynamic Stability of a Power System. *IEEE Transactions on Industrial Electronics*, 2018, vol. 65, no. 1, pp. 403-411. doi: https://doi.org/10.1109/TIE.2017.2721902.

19. Venkatramanan D., John V. Dynamic Modeling and Analysis of Buck Converter based Solar PV Charge Controller for Improved MPPT Performance. *2018 IEEE International Conference on Power Electronics, Drives and Energy Systems (PEDES)*, 2018, pp. 1-6, doi: https://doi.org/10.1109/PEDES.2018.8707505.

20. Zhou Y., Ho C.N.M., Siu K.K.-M. A Fast PV MPPT Scheme Using Boundary Control With Second-Order Switching Surface. *IEEE Journal of Photovoltaics*, 2019, vol. 9, no. 3, pp. 849-857. doi: https://doi.org/10.1109/JPHOTOV.2019.2899470.

21. Bana P.R., Panda K.P., Padmanaban S., Mihet-Popa L., Panda G., Wu J. Closed-Loop Control and Performance Evaluation of Reduced Part Count Multilevel Inverter Interfacing Grid-Connected PV System. *IEEE Access*, 2020, vol. 8, pp. 75691-75701. doi: https://doi.org/10.1109/ACCESS.2020.2987620.

22. Li F., Qin J., Kang Y. Closed-Loop Hierarchical Operation for Optimal Unit Commitment and Dispatch in Microgrids: A Hybrid System Approach. *IEEE Transactions on Power Systems*, 2020, vol. 35, no. 1, pp. 516-526. doi: https://doi.org/10.1109/TPWRS.2019.2931293.

23. Cantillo A., De Nardo A., Femia N., Zamboni W. Stability Issues in Peak-Current-Controlled SEPIC. *IEEE Transactions on Power Electronics*, 2011, vol. 26, no. 2, pp. 551-562. doi: https://doi.org/10.1109/TPEL.2010.2066288.

24. Swain S., Subudhi B. Grid Synchronization of a PV System With Power Quality Disturbances Using Unscented Kalman Filtering. *IEEE Transactions on Sustainable Energy*, 2019, vol. 10, no. 3, pp. 1240-1247. doi: https://doi.org/10.1109/TSTE.2018.2864822.

25. Kewat S., Singh B. Grid Synchronization of WEC-PV-BES Based Distributed Generation System Using Robust Control Strategy. *IEEE Transactions on Industry Applications*, 2020, vol. 56, no. 6, pp. 7088-7098. doi: https://doi.org/10.1109/TIA.2020.3021060.

26. Abdul R.A. Solar PV System for Water Pumping Incorporating an MPPT based Bat Optimization Circuits and Systems. *Journal of Advanced Research in Dynamical and Control Systems*, 2020, vol. 12, no. 01-Special Issue, pp. 786-794. doi: https://doi.org/10.5373/JARDCS/V12SP1/20201130.

27. Moyo R.T., Tabakov P.Y., Moyo S. Design and Modeling of the ANFIS-Based MPPT Controller for a Solar Photovoltaic System. *Journal of Solar Energy Engineering*, 2021, vol. 143, no. 4, p. 041002. doi: https://doi.org/10.1115/1.4048882.

28. Grossi E., Buscema M. Introduction to artificial neural networks. *European Journal of Gastroenterology & Hepatology*, 2007, vol. 19, no. 12, pp. 1046-1054. doi: https://doi.org/10.1097/MEG.0b013e3282f198a0.

29. Kalaiarasi N., Nagalakshmaiah E., Dash S.S., Paramasivam S. Development and analysis of ANN based MPPT and SL Z-source inverter for photovoltaic systems. *International Journal of Control Theory and Applications*, 2016, vol. 9, no. 39, pp. 313-323. Available at: https://serialsjournals.com/abstract/39638_cha-36.pdf (Accessed 11 May August 2021).

Thota Praveen Kumar[1]*, Research Scholar,*
Somaskandan Ganapathy[1]*, Professor,*
Mani Manikandan[2]*, Professor,*
[1] Annamalai University,
Chidambaram, Tamil Nadu, 608002, India,
e-mail: thotap@rediffmail.com (Corresponding author),
ganapathy1967@gmail.com
[2] Jyothishmathi Institute of Technology and Science,
Karimnagar, Telangana, 505481, India,
e-mail: cm.manikandan@gmail.com

Передплатний індекс: 01216